SAPIENZA
UNIVERSITÀ DI ROMA

TOR VERGATA
UNIVERSITÀ DEGLI STUDI DI ROMA

INAF
ISTITUTO NAZIONALE
DI ASTROFISICA
NATIONAL INSTITUTE
FOR ASTROPHYSICS

PH.D. IN ASTRONOMY, ASTROPHYSICS
AND SPACE SCIENCE

CYCLE XXXII

Unresolved stellar populations in high redshift galaxies

Marianna Torelli

A.Y. 2018/2019

Supervisor : Prof. Giuseppe Bono

Co-Supervisor : Prof. Adriano Fontana

Coordinator : Prof. Paolo De Bernardis

Deputy Coordinator : Prof. Nicola Vittorio

Summary

Stellar populations in high-redshift galaxies cannot be resolved in single stars, this means that we need of observed integrated quantities, like magnitudes and spectra, to investigate their stellar content. Stellar populations synthesis models are fundamental and powerful tools to model the integrated properties of unresolved systems. Key information concerning galaxy formation and evolution can be provided by using physical parameters, like stellar mass, age, star formation rate, metal and dust content. This is the reason why evolutionary stellar population synthesis models are already widely used in codes performing fits of the spectral energy distributions (SEDs) of massive sample of high redshift galaxies observable in large photometric and spectroscopic surveys. However, the accuracy of the inferred parameters depends on the reliability of the adopted models. Major uncertainties come from the stellar ingredients and from assumptions adopted in stellar evolutionary models. Therefore, it is crucial to calibrate these models on systems for which we have accurate and independent information about physical parameters, like age and metal content. In this context, Galactic globular clusters (GGCs) play a key role: their stellar population is characterized by uniform age and metallicity and also, it can be resolved in each fundamental stellar evolutionary phases.

Thus, the main aim of this work is to empirically calibrate stellar population synthesis models against a sample of ~ 70 GGCs for which we have unprecedented accurate multi-band photometry from far-UV to mid-IR.

Firstly, we analysed a fundamental stellar evolutionary phase, namely the horizontal branch (HB) phase, characterized by stars burning helium in their core and hydrogen in a surrounding shell. We took advantage of our sample of GGCs combining the homogeneous and accurate optical ground-based V and I photometry with HST/$F606W$ ($\sim V$) and HST/$F814W$ ($\sim I$) space-based photometry. We introduced a new HB index, τ_{HB}, defined as the ratio between the areas subtended by the cumulative number distribution in magnitude and in colour of all HB stars. We found a linear correlation between τ_{HB} and the absolute ages of the clusters in our sample. We also found a quadratic anti-correlation with [Fe/H] which becomes linear after the removal of age effect in τ_{HB} values. Moreover, we were able to identify a sub-sample of eight "second parameter" clusters, peculiar according

to their τ_{HB} values and showing bluer HB morphology when compared to typical clusters of similar metallicity.

After analysing the GGCs, we investigated the HB morphology in a sample of 19 nearby Local Group dwarf spheroidal (dSph) galaxies: eight of them are Milky Way satellites, nine are Andromeda satellites, while two of them are isolated galaxies. For the Milky Way dwarfs, we have data in ground-based $UBVRI$ data, while for the rest of the sample we have photometry in HST/$F475W$ ($\sim B$) or HST/$F606W$ ($\sim V$) and HST/$F814W$ ($\sim I$). We found that nearby dSphs cover a limited range in HB morphologies, indeed they range from $HBR' \sim 1$ (Andromeda III) $HBR' \sim 2.5$ (Ursa Minor) and from $\tau_{HB} \sim 1$ (Leo II) to $\tau_{HB} \sim 5$ (Ursa Minor). This indicates that HB morphologies are systematically redder than in GGCs. Moreover, they display a modest variation both in metallicity and age, thus suggesting a relevant environmental effect when moving from GGCs ($M = 10^4 - 10^6 M_{\odot}$) to dSphs ($M = 10^7 - 10^9 M_{\odot}$).

To complete our investigation concerning the resolved stellar populations, we exploited our GGC multi-band photometry to calibrate stellar population synthesis models. Indeed, we employed integrated observed/synthetic data in GALEX/FUV, GALEX/NUV bands and HST/$F275W$. In the optical range we used homogeneous and accurate $UBVRI$ ground-based and HST/$F606W$ and HST/$F814W$ space-based photometry. Moreover, we used the first Pan-STARRS data release in $grizy$ filters. In the near-IR wavelengths, we employed the $JHKs$ photometry from 2MASS, while in the mid-IR we calculated synthetic integrated magnitudes in four IRAC filters on board of SPITZER. We performed an empirical calibration of Bruzual & Charlot (2003) stellar population synthesis model. In particular, we compared the inferred cluster ages from SED fitting to the ones obtained through photometric techniques found in the literature. We found a difference of ΔAge between $3Gyr$ and $10Gyr$ for most of the clusters in the sample. Moreover, ΔAge seems to have a mild correlation with metallicity, in the sense that it seems to decrease as metallicity increases. Finally, we compared the rest-frame colours predicted by Bruzual & Charlot (2003) model to the ones obtained by other stellar population synthesis models. We found that, in the optical-NIR wavelength range, they agree quite well with observations. On the contrary, in the FUV band, they systematically under-estimate colours in the metal-rich regime ([Fe/H]>-1), while they over-estimate NIR colours in the metal-poor regime ([Fe/H]<-1).

After having analysed the resolved simple (GGCs) and composite (dSph galaxies) stellar populations, we dedicated our efforts to investigate the unresolved stellar populations in high redshift galaxies through the galaxy stellar mass function (GSMF), which is a fundamental statistical tool to investigate the stellar mass assembly in galaxies from the re-ionization era to present time. We compute the GSMF through the non-parametric $1/V_{max}$ method in $0.2 < z < 4.0$. We combined the five CANDELS fields (GOODS-South, GOODS-North, EGS, COSMOS, UDS), the Frontier Fields Parallels (Abell 2744, MACSJ0416, MACSJ0717, MACSJ1149)

and the Ultravista/COSMOS field for a total area of 1.65 deg^2. This sample allows us to explore the GSMF from low masses ($\sim 10^8 M_\odot$) to a very high-mass end ($\sim 10^{12} M_\odot$), thanks to both deep photometry and large area. Our total GSMF is in good agreement with the one estimated in previous works by different authors. As shown by previous studies, we found a progressive steepening of the faintest region of the function, while its "knee" shows a slight decrease with redshift. Finally, we analysed the GSMF of star-forming and quiescent populations. We found that, while the GSMF of the star-forming population has a shape similar to total one, thanks to our deep photometry, we are able to observe a bi-modality in the quiescent GSMF. This bi-modality seems to be connected, according to empirical and theoretical evidence available in the literature, with different physical mechanisms able to cease the star formation.

Finally, in the context of a more extended project in which we plan to re-calibrate SPSMs on high redshift galaxies, we decided to firstly investigate the impact of the SPSM calibration on the GSMF of quiescent galaxies. Indeed, we would expect to find an age difference in stellar populations of quiescent galaxies similar to the one found for GGCs. In fact, these stellar systems are dominated by old (t>10 Gyr) stellar populations, therefore, an error on inferred ages could also affect the quiescent GSMF at low redshifts. To overcome this problem, we identified a new prescription in our SED fitting code to avoid too young, non-physical age estimates for quiescent galaxies. The new recipe provided accurate both re-calibrated stellar masses and GSMF. The age estimates, as expected, mildly (< 0.1dex) affects the GSMF at low redshift ($z < 1.5$) and only at the lowest mass end ($M < 10^8 M_\odot$).

Contents

1 Stellar Populations **17**
- 1.1 Resolved stellar populations . . . 17
  - 1.1.1 Old simple stellar populations . . . 17
  - 1.1.2 Young simple stellar populations . . . 21
- 1.2 Composite stellar populations . . . 22
- 1.3 Unresolved stellar populations . . . 24
  - 1.3.1 Simple stellar populations . . . 24
  - 1.3.2 Stellar populations synthesis technique . . . 29
  - 1.3.3 Composite stellar populations . . . 39
  - 1.3.4 Spectral evolution . . . 40
  - 1.3.5 SED Fitting . . . 42

2 Horizontal Branch morphology: A new photometric parametrization **50**
- 2.1 Introduction . . . 51
- 2.2 Globular cluster sample . . . 54
- 2.3 The *HBR* morphology index . . . 56
- 2.4 L1 and L2 HB morphology indices . . . 65
- 2.5 A new HB morphology index: τ_{HB} . . . 69
- 2.6 Comparison between space- and ground-based data . . . 76
- 2.7 Correlation of τ_{HB} with cluster metallicity, age, and helium content 80
- 2.8 Comparison with synthetic horizontal branch models . . . 89
- 2.9 Conclusions . . . 90

3 Horizontal Branch photometric parametrization on nearby dwarf spheroidal galaxies **95**
- 3.1 Dwarf spheroidal galaxy sample . . . 97
- 3.2 The *HBR* morphology index for dwarf spheroidal galaxies . . . 98
- 3.3 τ_{HB} estimate in $I, B–I$ diagram . . . 105
- 3.4 Photometric parametrization of the HB morphology in dwarf spheroidal galaxies . . . 108

3.5 Conclusions . . . 111

4 Calibration of stellar population synthesis models on Galactic Globular Clusters 114
4.1 Globular cluster integrated magnitudes . . . 115
4.1.1 Optical bands . . . 115
4.1.2 Ultraviolet bands . . . 117
4.1.3 Infrared bands . . . 123
4.2 Globular cluster spectral energy distributions . . . 123
4.3 Model calibration . . . 128
4.4 Conclusions . . . 142
4.5 Notes on individual clusters . . . 144

5 The galaxy stellar mass function 145
5.1 Dataset . . . 146
5.1.1 CANDELS . . . 146
5.1.2 Frontier Fields parallels . . . 147
5.1.3 UltraVista . . . 147
5.2 The galaxy stellar mass function derivation . . . 151
5.2.1 Stellar masses . . . 151
5.2.2 The galaxy stellar mass function estimate . . . 152
5.3 The galaxy stellar mass function of star-forming and quiescent populations . . . 162
5.4 GGC calibration effects on quiescent GSMF . . . 168
5.5 Conclusions . . . 170

6 Conclusions 173

Appendices 179

A Notation for chemical composition 179

B Stellar evolution 181
B.1 From theory to observations . . . 184

C Peculiar globular clusters 186

D Notes on individual outliers 187

E Additional CMDs of dSph galaxies 189

References 196

List of Figures

1.1 Isochrones computed with BaSTI. Left: isochrones for different ages (t=10,11,12 Gyr, see legend) and same chemical composition (Z=0.0001). Right: isochrones for different metallicities (Z=0.01, 0.001, 0.0001, see legend) and same age (t = 12 Gyr). 18
1.2 Representation of the vertical and horizontal methods for the age estimate (Demarque, 1997). 19
1.3 Isochrones in the VBV diagram for different ages for young SSPs (Salaris & Cassisi, 2005). 21
1.4 CMD of the stars in the solar neighbourhood (Salaris & Cassisi, 2005). 23
1.5 CMD of a CSP divided in grid of cells of 0.1 mag in colour and 0.5 mag in magnitude (Salaris & Cassisi, 2005). 23
1.6 Time evolution of magnitudes in selected photometric bands (Salaris & Cassisi, 2005). 25
1.7 Examples of colour-colour diagrams. 26
1.8 Different index-index diagrams from Cassisi & Salaris (2013) for scaled-solar populations (solid and short-dashed lines) with [Fe/H] from -1.79 to 0.40 and α-enhanced (long-dashed and dotted lines) with [Fe/H] from -1.84 to +0.05. Ages span from 1.25 to 14 Gyrs, increasing from top to bottom. Metallicities increase from left to right. 28
1.9 Different extinction laws: Milky Way (Cardelli, $R_V = 3.1$), Calzetti and SMC. 33
1.10 Salpeter, Chabrier and Kroupa IMFs. (Crosby et al., 2013) 36
1.11 Four different parametrized SFHs (SFR as a function of age)(Schaerer et al., 2013). 38
1.12 Possible non parametric SFHs from Leja et al. (2019). 38
1.13 SED of a SSP of $Z = 1Z_{\odot}$ at different ages: 1 Myr (blue), 10 Myr (cyan), 100 Myr (green), 1 Gyr (red), 100 Gyr (violet) (Greggio & Renzini, 2011). 40
1.14 SED of a 12 Gyr population for different assumption on the effective temperature of the HB stars (Greggio & Renzini, 2011). 42

1.15 SED of a 1 Gyr population for different assumption on SFH: inverted-τ model (green), peaked model (orange), constant (blue), τ model (red), SSP model (magenta)(Greggio & Renzini, 2011). 43
1.16 SED of a 13 Gyr population for different assumptions on SFH, as in Figure 1.15(Greggio & Renzini, 2011). 44
1.17 Relation between SFR_{IR+UV} and SFR_{fit} in different redshift bins from Santini et al. (2009). Red line defines the region SFR_{IR+UV}=SFR_{fit}. 47
1.18 M/L from different models in various bands (Maraston, 2005). . . . 49
1.19 Total stellar mass from Ma05 and BC03 models. (Maraston, 2005) . 49

2.1 Sky distribution of ground-based (black dots) and space-based (red dots) data for the cluster NGC 5053. North is up and east is to the left. 57
2.2 Cluster NGC 5286 *I*, *V–I* CMD based only on ACS-*HST* data. . . . 58
2.3 Cluster NGC 5286 *V*, *B–I* CMD. The left panel shows all stars. The central panel shows our candidate cluster stars. The right panel shows the candidate field stars. Candidate cluster and field stars have been selected following the method described in the main text. 59
2.4 Difference between Harris (1996) values (2003 version) for *HBR* and our measurements as a function of [Fe/H]. 61
2.5 Observed *HBR′* values as a function of metal content. The metallicity scale is from Carretta et al. (2009) (see the Appendix for more details). The error bar in the lower left corner gives the uncertainty of the metal content (0.1 dex). 63
2.6 Observed *HBR′* values as a function of the cluster ages (gigayears (Gyr)) provided by VandenBerg et al. (2013); Leaman et al. (2013). The error bar in the lower left corner gives the uncertainty in the cluster ages (± 0.5 Gyr). 64
2.7 L1 and L2 indices as a function of the metal content (Carretta et al., 2009). The different symbols and colours identify the different cluster groups defined in Milone et al. (2014): G1 (red crosses) for metal-rich globulars ([Fe/H]>-1.0), G2 (green triangles) for clusters with [Fe/H]<-1.0 and L1 ≤ 0.4, G3 (blue circles) for globulars with L1 ≥ 0.4. 67
2.8 L1 and L2 indices as a function of the cluster age (Gyr) from VandenBerg et al. (2013); Leaman et al. (2013). The different symbols and colours identify the different cluster groups defined in Milone et al. (2014): G1 (red crosses) for metal-rich globulars ([Fe/H]>-1.0), G2 (green triangles) for clusters with [Fe/H]<-1.0 and L1 ≤ 0.4, G3 (blue circles) for globulars with L1 ≥ 0.4. 68

2.9 Run of the normalized CND with respect to the *I* magnitude for three globular clusters (lower panels), chosen as representative of three different metallicity regimes (NGC 6341, NGC 5272, and NGC 104). Upper panels show the horizontal branch of the three chosen globulars in *I*,*V*–*I* CMDs. 71

2.10 Run of the normalized CND with respect to *V*–*I* for the same three globular clusters (lower panels) of Fig. 2.9. Upper panels show the horizontal branch of the three chosen globulars in *I*, *V*–*I* CMDs. . . 72

2.11 The indices $A_{CND}(I)$ and $A_{CND}(V–I)$ vs. the HBR' morphology index. 73

2.12 Our new HB morphology index τ_{HB} vs. HBR'. 74

2.13 L1 (top) and L2 (bottom) indices as a function of τ_{HB} for the globulars in our sample. The different symbols and colours identify the different cluster groups defined in Milone et al. (2014): G1 (red crosses) for metal-rich globulars ([Fe/H]>-1.0), G2 (green triangles) for clusters with [Fe/H]<-1.0 and L1 $\leq$ 0.4, G3 (blue circles) for globulars with L1 $\geq$ 0.4. 75

2.14 Top: relative difference between the global HBR' and the HBR' values only based on ground-based data versus the global index. Note that in the estimate of the global index the priority in selecting the photometry was given to space-based (ACS at *HST*) data. Bottom: as the top panel, but the relative difference is between the global index and the HBR' index only based on space-based data. The standard deviation of the estimates is represented by the error bar at the top left corner of the panels. At the top right corners we display the mean relative difference. 77

2.15 Top: relative difference between the global τ_{HB} and the τ_{HB} index only based on ground-based data versus the global index. Note that in the estimate of the global index the priority in selecting stars was given to space-based (ACS at *HST*) data. Bottom: as the top panel, but the relative difference is between the global index and the τ_{HB} index only based on space-based data. The standard deviation of the estimates is represented by the error bar at the bottom left corner of the panels. At the top right corners we display the mean relative difference. 78

2.16 Variation of τ_{HB} as a function of cluster metallicity (Carretta et al., 2009). The red line shows the quadratic best fit, the blue lines show 1.5 σ levels. Red squares display the outliers, which are those objects located at more than 1.5 σ from the quadratic fit. In the left corner the error bar shows the 0.1 dex error on the metal content. 81

2.17 CMDs (I, V–I) for three pairs of GGCs in the sample. Left panels: Clusters belonging to the outlier group. Right panels: CMDs of clusters with similar [Fe/H] as the outlier ones, but following the main τ_{HB}-[Fe/H] relation. 83
2.18 Our index τ_{HB} as a function of cluster ages obtained from different authors. Top: cluster ages from VandenBerg et al. (2013); Leaman et al. (2013). The error bar in the lower left corner shows the conservative ±0.5 Gyr error on the GGC ages. Bottom: ages from Salaris & Weiss (2002) based on the metallicity scale provided by Carretta & Gratton (1997). In both panels red squares are the same second parameter clusters shown in Fig. 2.16 and discussed in this section. Red lines determine the best-fit to each data sample, blue lines the $\pm1\sigma$ levels. 84
2.19 [Fe/H] vs. $\tau_{HB,12\ Gyr}$. The red line identifies the linear best-fit function of the plane, and red squares mark the eight second parameter clusters (see text for details). 86
2.20 Residuals of the corrected $\tau_{HB,12\ Gyr}$ as a function of the metal content (Carretta et al., 2009) versus the spread in helium content ∂Y estimated by Milone et al. (2018). Red squares identify the second parameter globulars. 88
2.21 The new HB morphology index, $\tau_{HB,12\ Gyr}$, as a function of cluster iron abundance (Carretta et al., 2009). The two lines display synthetic HB models at fixed cluster age (12 Gyr), but either with a canonical helium content ($\partial Y = 0$, blue line) or with an internal spread in He of $\partial Y = 0.03$ (black line). The coloured triangles identify three models for [Fe/H]=-1.6 for three different combinations of ∂Y and ΔM (see legend). Red squares mark the eight second parameter clusters. The error bar on the left corner gives the 0.1 dex error on the metal content. 91

3.1 Sculptor V, B–I CMD of the entire catalogue (left panel), candidate galaxy (central panel) and candidate field (right panel) stars. 99
3.2 Carina V, B–I CMD of the entire catalogue (left panel), candidate galaxy (central panel) and candidate field (right panel) stars. 100
3.3 Andromeda III I, B–I CMD. 101
3.4 Observed HBR' values as a function of metal content for GGCs (black dots) and our sample of dSph galaxies (coloured squares, see legend in the upper right corner). The error bars on dSph [Fe/H] values show the dispersion of metallicity distributions. 102
3.5 Observed HBR' values as a function of the absolute age for GGCs (black dots) and our sample of dSph galaxies (coloured squares, see legend in the upper right corner). 103

3.6 [Fe/H] vs $\tau_{HB}(IVI)$ (left panel) and $\tau_{HB}(IBI)$ (right panel). Red lines show the best-fit relations in both panels, red squares mark the 2ndP clusters already identified in Chapter 2, while green squares show other three possible clusters in $\tau_{HB}(IBI) - [Fe/H]$ diagram, peculiar for their $\tau_{HB}(IBI)$ values. 106

3.7 Age vs $\tau_{HB}(IVI)$ (left panel) and $\tau_{HB}(IBI)$ (right panel). Red lines show the best-fit relations in both panels, red squares identifies the 2ndP clusters already defined in Chapter 2, while green squares show the three possible outliers identified in $\tau_{HB}(IBI) - [Fe/H]$ diagram. The error bar in the lower left corner shows the conservative ± 0.5 Gyr error on the GGC ages. 107

3.8 [Fe/H] vs $\tau_{HB}(IVI)$ (left panel) and $\tau_{HB}(IBI)$ (right panel) estimated for dwarf spheroidal galaxies. Blue shaded regions show the 1.5σ (left panel) and 1.0σ (right panel) areas from GGCs. Red lines are the best-fit relations from GGC analysis. Black dots identifies MW satellites, blue squares show the Andromeda satellites [M31], while the magenta triangles represent isolated galaxies in the Local Group [LG]. 109

3.9 Age vs $\tau_{HB}(IVI)$ (left panel) and $\tau_{HB}(IBI)$ (right panel) estimated for dwarf spheroidal galaxies. Blue shaded areas show the 1.0σ levels from GGCs. Red lines are the best-fit relations from GGC analysis. Black dots identifies MW satellites, blue squares show the Andromeda satellites [M31], while the magenta triangles represent isolated galaxies in the Local Group [LG]. The error bar in the lower left corner shows the conservative ± 0.5 Gyr error on the dSph galaxy ages. 110

4.1 Proper motion distribution for NGC 362. Red square identifies the centre of the cluster. 116

4.2 Upper panel: *VVI* CMD of the observed (grey dots) and synthetic (blue from MS to RGB-tip, red for AGB+HB phases) for NGC 6218 stars. Bottom panel: number distribution of the observed (green) and synthetic (red) HB stars. 118

4.3 Upper panel: *VVI* CMD of the observed (grey dots) and synthetic (blue from MS to RGB-tip, red for AGB+HB phases) for NGC 6121 stars. Bottom panel: number distribution of the observed (green) and synthetic (red) HB stars. 119

4.4 Upper panel: *VVI* CMD of the observed (grey dots) and synthetic (blue from MS to RGB-tip, red for AGB+HB phases) for NGC 6624 stars. Bottom panel: number distribution of the observed (green) and synthetic (red) HB stars. 120

4.5 SEDs for each cluster in our sample for six different bins in metallicity. Red lines show the photometric SEDs for the 2ndP clusters identified in Chapter 2, while the black ones define the SEDs for the "typical" GGCs. Each SED is normalized to the *V*-band. 125
4.6 Fits of the normalized SEDs shown in Figure 4.5 for three different bins in metallicity (see legend). 127
4.7 Multi-wavelength SED fitting of NGC 104. 128
4.8 Multi-wavelength SED fitting of NGC 1261. 129
4.9 Multi-wavelength SED fitting of NGC 5024. 129
4.10 Multi-wavelength SED fitting of NGC 4590. 130
4.11 Difference between the age estimated by VandenBerg et al. (2013); Leaman et al. (2013) and the inferred values from SED fitting by *zphot* as a function of [Fe/H]. 131
4.12 Difference between the age estimated by VandenBerg et al. (2013); Leaman et al. (2013) and the inferred values from SED fitting by *zphot* as a function of [Fe/H] excluding the MIR photometry. 133
4.13 Rest-frame colours as a function of the age in Gyr. Red lines identifies our BC03 models for [Fe/H] value fixed to -0.7. Dots represent the observed points for globular clusters with [Fe/H] similar to -0.7. Blue dots identify the globulars in this metallicity bin located in the region with $\Delta Age < 3.0$ in Figure 4.11. 134
4.14 Rest-frame colours as a function of the age in Gyr. Red lines identifies our BC03 models for [Fe/H] value fixed to -1.7. Dots represent the observed points for globular clusters with [Fe/H] similar to -1.7. Blue dots identify the globulars in this metallicity bin located in the region with $\Delta Age < 3.0$ in Figure 4.11. 135
4.15 Rest-frame colours as a function of the age in Gyr. Red lines identifies our BC03 models for [Fe/H] value fixed to -2.3. Dots represent the observed points for globular clusters with [Fe/H] similar to -2.3. Blue dots identify the globulars in this metallicity bin located in the region with $\Delta Age < 3.0$ in Figure 4.11. 136
4.16 Comparison between our BC03 (red) and Conroy & Gunn (2010b) FSPS (green) models in optical and *NIR* wavelengths. Black dots show the observed colours of our sample of GGCs. 138
4.17 Comparison between our BC03 (red) and Conroy & Gunn (2010b) FSPS (green) models in *UV* wavelengths. Black dots show the observed colours of our sample of GGCs. 139
4.18 *MIR* colours as a function of metallicity. Red lines identify our BC03 models, black dots show the observed colours of our sample of GGCs. We show with red dots the 2ndP cluster colours. 140

5.1 CANDELS fields. 148

5.2 Frontier Fields areas. Top left: A2744 cluster (on the left) and parallel (on the right). Top right: M0416 cluster (on the right) and parallel (on the left). Bottom left: M0717 cluster (on the left) and parallel (on the right). Bottom right: M1149 cluster (top) and parallel (bottom). 149
5.4 Redshift distribution of the galaxies in the different fields. In black the total distribution of the entire sample. 151
5.5 Mass distribution of the galaxies in the different fields as a function of redshift. The red line identifies the mean stellar mass in each field. 153
5.6 Observed K_s flux (lower scale) and K_s magnitudes (upper scale) as a function of the best-fit stellar masses estimated by Fontana et al. (2004) The diagonal lines identify the stellar mass the galaxies can attain according to their K_s magnitude. The solid line shows the minimum mass, the dashed line shows the maximum mass for dusty sources, while the dashed-dotted line is the maximum mass for dust-free objects. The dotted line is the completeness limit on stellar masses, while the shaded area identifies the fraction of galaxies lost due to incompleteness effect. 155
5.7 Mass distribution as a function of redshift for galaxies in the GOODS-S field (black dots). The red solid line identifies the completeness curve for the sample. 156
5.8 Individual and total GSMF in each redshift bin. Dot coloured symbols identify the GSMF for each field of the sample (see legend), black stars show the *total* GSMF of the joined fields. 157
5.9 Total GSMF estimated in this work (black dots) compared to some of the results published in the literature: Santini et al. (2012) (brown hexagons), Ilbert et al. (2013) (green diamonds), Muzzin et al. (2013) (yellow pentagons), Tomczak et al. (2014) (red squares), Davidzon et al. (2017) (cyan triangles). In the legend we also display the redshift intervals in which the GSMF was computed if different from this work. 158
5.10 GSMF single Schechter (blue line) and Double Schechter (red line) best-fit functions. 159
5.11 Single Schechter function best-fit parameters as a function of the redshift. 160
5.12 GSMF of CANDELS/GOODS-S field assuming an exponential declining (red dots) and a delayed (green squares) SFH. 162
5.13 UVJ selection for sources in all ten fields in the seven different redshift bins. Darker areas identify higher densities of galaxies. Red lines show the separation between star-forming and quiescent populations. 164

5.14 Total GSMF of star-forming (blue) and quiescent (red) populations in seven different redshift bins. 165
5.15 GSMF Schechter fits for total (left), star-forming (middle) and quiescent (right) populations as a function of the redshift. 166
5.16 Local GSMF from Baldry et al. (2012) described through a double Schechter function 167
5.17 Quiescent galaxy calibrated ages using the prescription described in the main text as a function of the ages inferred not using the prescription. Red line shows the bisector of the diagram. 169
5.18 Quiescent galaxy calibrated stellar masses using the prescription described in the main text as a function of the masses inferred not using the prescription. Red line shows the bisector of the diagram. . 170
5.19 Comparison between the total GSMF quiescent (red dots) population investigated in the previous section and the one obtained after the application of the correction prescription for young ages (green squares). 171

B.1 Evolutionary tracks of five stars with different mass on the HRD (Freedman & Kaufmann, 2007). 181

E.1 Leo II *V*, *B–I* CMD of the entire catalogue (left panel), candidate galaxy (central panel) and candidate field (right panel) stars. 190
E.2 Sextans *V*, *B–I* CMD of the entire catalogue (left panel), candidate galaxy (central panel) and candidate field (right panel) stars. 191
E.3 Andromeda I *I*, *B–I* CMD. 192
E.4 Andromeda XXVIII *I*, *B–I* CMD. 193
E.5 Cetus *I*, *B–I* CMD. 194
E.6 Tucana *I*, *B–I* CMD. 195

List of Tables

2.1 Globular Clusters in the sample with parameters used in this work. 55
2.2 Parameters and observational HB morphology indices for the GGCs in the sample. 62
2.3 Examples of globular pairs of similar metallicity and HBR', but different values in τ_{HB}. 76
2.4 Best fit parameters for the linear functions fitting the τ_{HB}-Age relations used in this work 85

3.1 Dwarf spheroidal galaxies in the sample with parameters used in this work. 98
3.2 Parameters and observational HBR' values for the dSph galaxies in the sample. 104
3.3 Parameters and observational HB morphology indices for the dSph galaxies in the sample. 112

4.1 Parameters used to calculate synthetic bands. 122
4.2 Integrated magnitudes corrected for reddening for each cluster in our sample in different photometric bands. 124
4.3 Integrated magnitudes corrected for reddening for seven 2ndP clusters in our sample in different photometric bands with and without considering the EHB stars. 126

5.1 Area and magnitude limits of the investigated fields. 154
5.2 Best-fit parameters for the Single and Double Schechter functions. . 156
5.3 Best-fit parameters for star-forming, quiescent and total populations. 168

Chapter 1

Stellar Populations

Stars are considered to be the building blocks of galaxies allowing to understand their history. Stellar populations are determined by their age and metallicity (see Appendix A to have information about the astronomical nomenclature for metallicity). In this Chapter, we will give a review of the main methods and techniques currently used to investigate them.

1.1 Resolved stellar populations

1.1.1 Old simple stellar populations

A simple stellar population (SSP) is an assembly of stars of the same age, born during a single burst of star formation and with the same initial chemical composition. Observational counterparts are globular clusters, even though many observations have revealed the existence of multiple populations (with similar [Fe/H] values and difference in ages of $\sim$ 1-2 Gyr) (Bertelli et al., 2003; Bedin et al., 2004; Mackey et al., 2008; Milone et al., 2008), open clusters and elliptical galaxies. The theoretical colour-magnitude diagram (CMD[1], see Appendix B to have information concerning the main stellar evolutionary phases and their location on the CMD) of an SSP can be described by an isochrone, representing the evolution of stars with same age but different initial mass.

For each point along the isochrone we can determine, at fixed age, luminosity, effective temperature (T_{eff}) and mass. In order to obtain observable quantities, the isochrone must be translated into an observed CMD through specific bolometric corrections (Appendix B.1).

Left panel of Figure 1.1 shows isochrones for different values of age but same chemical composition. We note that the bolometric luminosity of the turn-off (TO) point decreases with the increasing of age, due to the fact that mass of the

[1] *A plot showing the magnitude in a given photometric band as a function of a colour index (the difference between the magnitudes in two different bands).*

star decreases when it evolves at the TO. For t>6 Gyr, the relation between the age and the TO luminosity is almost linear, following $dLog(L/L_{\odot})(TO) \sim -4.1 \cdot 10^{-2}(dex/Gyr)$ (Cassisi & Salaris, 2013). Moreover, the TO becomes redder when age increases. These features make the TO a good tool to estimate the age of a SSP. Moreover, the sub giant branch (SGB) slope increases when age increases, while the luminosity of the red giant branch (RGB) tip does not depend on the age value.

On the contrary, right panel of Figure 1.1 shows isochrones with same age but different chemical compositions. We note that the isochrones become bluer and brighter for higher metallicities (the radiative opacity decreases when the heavy element abundance increases). The strongest sensitivity to metallicity variation is shown by the RGB, which becomes redder and more tilted when Z increases. This means that, as the TO for the age, the RGB can be used as in indicator of the SSP metallicity value, comparing the observed CMD of a population with isochrones of different chemical compositions.

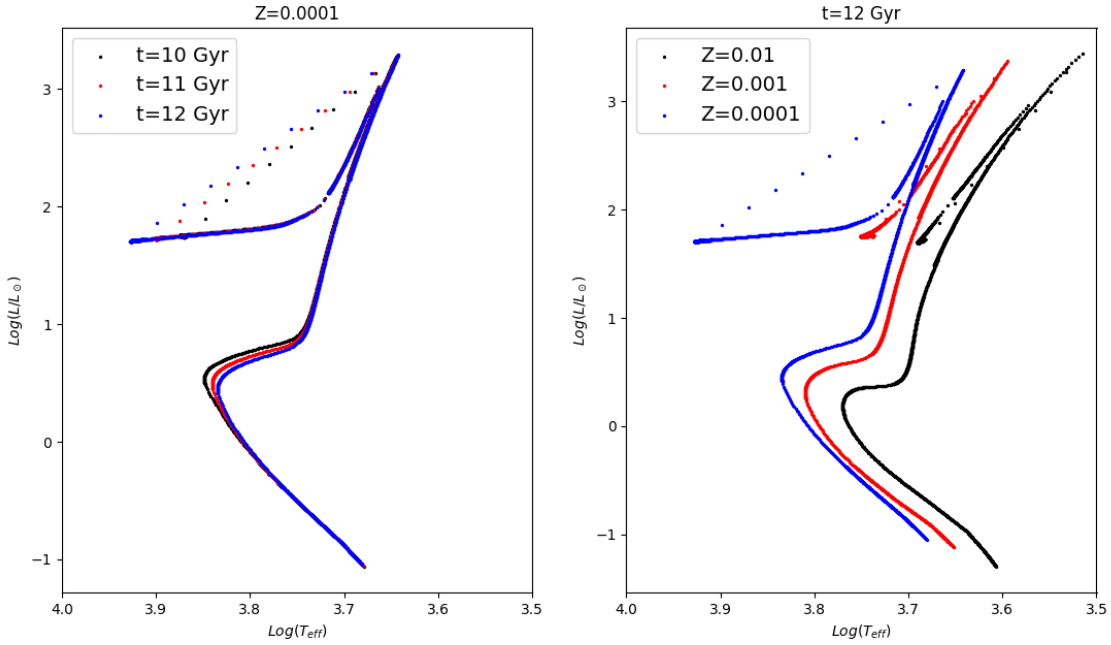

Figure 1.1: Isochrones computed with BaSTI. Left: isochrones for different ages (t=10,11,12 Gyr, see legend) and same chemical composition (Z=0.0001). Right: isochrones for different metallicities (Z=0.01, 0.001, 0.0001, see legend) and same age (t = 12 Gyr).

Age estimate: the vertical and horizontal methods

In the previous section, we have shown that we can use the position of the TO point to determine the age of a SSP. The simplest way to do this would be the comparison between isochrones of different ages with the observed CMD of a stellar population, for example a globular cluster. However, to overcome the problems due to reddening and distance effects, we usually use empirical methods employing differential quantities like magnitude difference between the Zero-Age Horizontal Branch (ZAHB) level and TO or the difference in colour between the TO and the base of the RGB.

In the *vertical method* we estimate the age of the SSP comparing the observed $\Delta V = V_{TO} - V_{ZAHB}$ with the theoretical one. ΔV is the difference in V magnitude between the TO point and the ZAHB level, around $Log(T_{eff}) = 3.85 \cdot (B-V) \sim 0.3$ (Salaris & Cassisi, 2005).

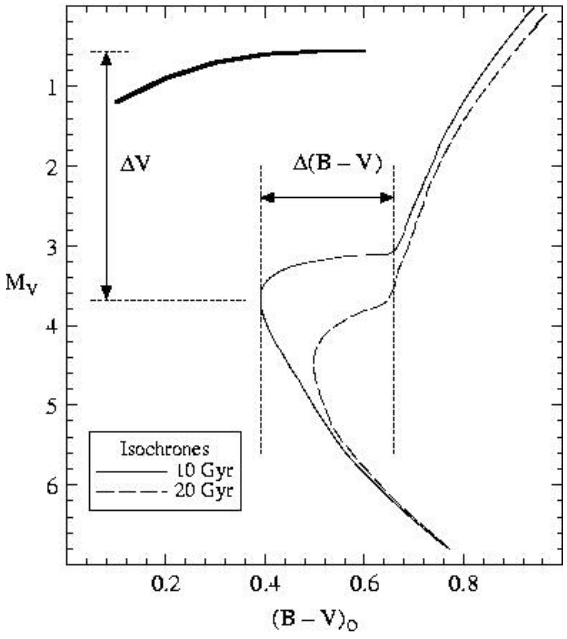

Figure 1.2: Representation of the vertical and horizontal methods for the age estimate (Demarque, 1997).

Since the ZAHB level is unaffected by age, at fixed metallicity, changes in ΔV are exclusively due to changes in TO luminosity for age effects, in particular, ΔV increases when age increases.

In general, the vertical method uses the V-band since in these wavelength the ZAHB level is mostly horizontal.

Uncertainties arise when the ZAHB level is not horizontal, for example for bolometric correction dependency on temperature or for reddening effect. Moreover,

we could run into complications because of a poorly populated horizontal branch (HB) or a HB populated only in its bluer region.

In general, at fixed metallicity, a variation of 0.1 mag in V leads to a variation of $\sim$ 1 Gyr in the age estimate, while a 0.4 dex variation in the cluster [Fe/H] causes an age uncertainty of 1 Gyr. This means that the vertical method can be considered as unaffected by metallicity uncertainties (Salaris & Cassisi, 2005).

The *horizontal method* makes use of $\Delta(B-V) = (B-V)_{RGB}-(B-V)_{TO}$, the difference in colour between the base of the RGB and the TO point, where $(B-V)_{RGB}$ is the mean colour of RGB stars located 2.5 mag above the TO (Salaris & Cassisi, 2005).

$\Delta(B-V)$ changes with age thanks to the variation of $B-V$ colour of the TO point, which becomes redder with the increasing of the SSP age. As for the vertical method, also $\Delta(B-V)$ has a weak sensitivity to the metallicity. A graphical representation of vertical and horizontal methods is shown in Figure 1.2.

HB colour and the second parameter problem

In general, the mass loss along the RGB can be described through the Reimers formula, $dM/dt \propto \eta/M$, with a fixed mean η value and a spread $\Delta\eta$. In this way, we can determine the ZAHB level and the evolution of the HB stars. Once we fix η and $\Delta\eta$, the HB morphology is mainly controlled by metallicity: if we increase the metal content, at fixed age, we obtain a redder HB, populated by colder stars. Therefore, the metallicity is the main, "first" parameter determining the HB star distribution. However, if we fix the metallicity and vary the age, the HB morphology becomes redder for a decreasing in age values. This means that if we compare two clusters with same metallicity and one of them has a redder HB, we expect that it is younger.

The HB morphology is often described using the horizontal branch ratio (HBR) defined by Lee (1989); Lee et al. (1994): $HBR = (B-R)/(B+R+V)$, where B is the number of HB stars bluer than the blue (hot) edge of the RRL instability strip, V is the number of RR Lyrae stars, and R is the number of HB stars redder than the red (cold) edge of the RRL instability strip.

This parameter degenerates for clusters with extremely blue or red HB morphologies, and hence, for extreme metal-poor or extreme metal-rich clusters.

The HB morphology is affected by the so-called "second parameter problem", due to the fact that we can observe pairs of globular clusters with same metallicity (e.g., NGC 288-NGC 362) and age within the errors, but different HB morphologies.

This problem, still unsolved, will be widely treated in the next chapter.

Metallicity and reddening estimates

As previously described, the RGB colour and slope offer a good tool to determine the metallicity of the analysed SSP. Due to uncertainties in theoretical isochrones,

we usually employ empirical relationships to link [Fe/H] with observational CMDs (Salaris & Cassisi, 2005):

$$\begin{aligned}
&[Fe/H] = -0.24S + 0.28, \sigma = 0.12;\\
&[Fe/H] = -0.85\Delta V_{1.4} + 0.77, \sigma = 0.16;\\
&[Fe/H] = -2.12(V-I)^2_{-3.5} + 8.81(V-I)_{-3.5} - 9.75, \sigma = 0.15;\\
&[Fe/H] = -3.34(V-I)^2_{-3.0} + 12.37(V-I)_{-3.0} - 11.91, \sigma = 0.15
\end{aligned} \tag{1.1}$$

where S is the slope of the line connecting the RGB at the ZAHB level and a point 2.5 brighter in the VVI diagram, $\Delta V_{1.4}$ is the difference in magnitude between the HB and the de-reddened RGB at $V-I = 1.4$. $(V-I)_{-3.5}$ and $(V-I)_{-3.0}$ are the RGB colours at $M_I = -3.5$ and $M_I = -3.0$, respectively. Finally, σ is the uncertainty on [Fe/H]. In this way we can determine the [Fe/H] abundance from the SSP photometry.

1.1.2 Young simple stellar populations

Age estimate

A SSP younger than $\sim 4Gyr$ is defined as "young" SSP, whose classical observational counterparts are Galactic open clusters. Young SSP isochrones for different ages (0.1, 0.5 and 1.8 Gyr) are shown in Figure 1.3.

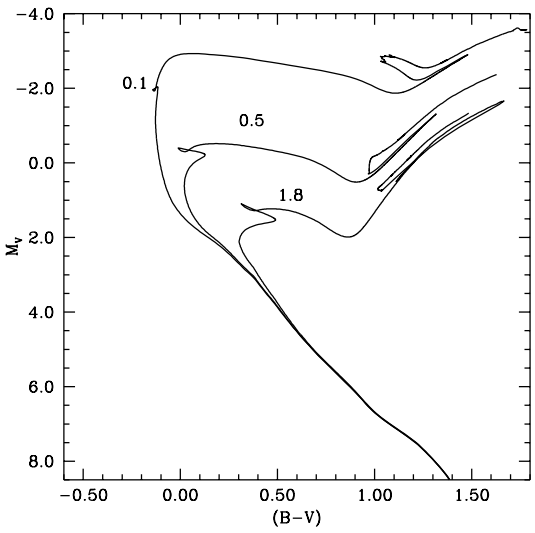

Figure 1.3: Isochrones in the VBV diagram for different ages for young SSPs (Salaris & Cassisi, 2005).

Comparing Figure 1.3 to 1.1 one, we note that the TO point in young isochrones are different to the ones shown in old SSP ones: this is due to the fact that young age main sequence (MS) stars burn hydrogen through the CNO cycle and this

causes the appearance of the overall contraction (the "hook" visible at the TO isochrone point). Moreover, the TO luminosity is higher because massive stars are still on the MS.

In SSP with age between 0.5 and 4 Gyr, stars undergo the He-burning in a red clump (RC) close to the RGB. The He-burning is so fast that causes a significant mass loss. If the age is lower than 0.5 Gyr, stars burn helium in bluer regions of the CMD describing the blue loops we can observe in Figure 1.3.

As already found for old SSPs, the TO point can be used as age indicator also for younger populations, since the beginning of the He-burning phase in the stellar cores can be easily connected to the isochrone age. Also the effects of metallicity variations shown in Figure 1.1 are similar.

However, since the RGB and SGB are very fast and, hence, depopulated, estimating the young SSP age through the horizontal method is in practice impossible. The vertical method could be in principle used if a sizeable sample of RC stars exists.

Metallicity and reddening estimates

For young SSPs, we can estimate metallicity and reddening using the same methods described for old SSPs. In this case we can also employ a tool provided by the Strömgren *ubvy* photometry. Indeed, for SSPs younger than 10-100 Myr the MS stars populating the CMD below the TO point have masses between 3 and $20M_{\odot}$ and show a well defined and standard sequence in the c_1by diagram, where $c_1 = (u-v)-(v-b)$. This sequence does not depend on metallicity for $[Fe/H] > -1$ and due to the fact that in this diagram the reddening vector is almost horizontal ($c_1(0) = c_1 - 0.20 * E(b-y)$), it is easy to estimate the reddening simply shifting the observed star colours along $c_1(0)$ until they reach the standard sequence.

1.2 Composite stellar populations

Composite stellar populations (CSPs) consist of stars formed at different ages and different chemical compositions. Natural observational counterparts are galaxies, which often show two or more populations and in many cases they are still forming stars. Figure 1.4 (Salaris & Cassisi, 2005) shows the *VBV* CMD of the stars in the solar neighbourhood displaying the presence of a CSP due to the coexistence of both young (MS, in the brighter region of the diagram) and old (RGB, SGB) objects.

The main tool to understand and analyse CSPs is the star formation history (SFH) which gives the total stellar mass formed through time (star formation rate (SFR)) with a certain initial chemical composition.

This means that we can describe the SFH as the function $\Gamma(\Phi(t)\Psi(t))$ where $\Phi(t)$ is the SFR and $\Psi(t)$ is the the age-metallicity relation. Since the stars continue to

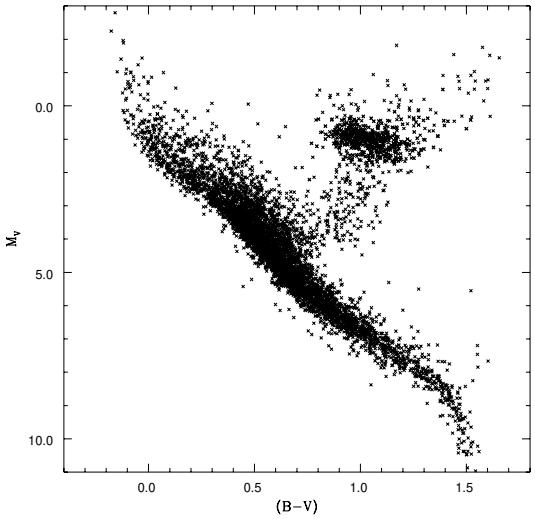

Figure 1.4: CMD of the stars in the solar neighbourhood (Salaris & Cassisi, 2005).

affect the interstellar medium chemical composition for their entire life, $\Phi(t)$ and $\Psi(t)$ are not independent.

If the SFR and the IMF are known, the stellar evolutionary theory is able to estimate the age-metallicity relation, giving the information about the SFH and hence allowing to predict the evolution of the CSP.

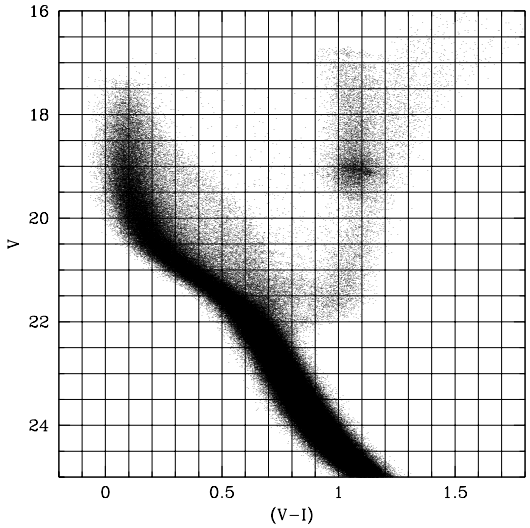

Figure 1.5: CMD of a CSP divided in grid of cells of 0.1 mag in colour and 0.5 mag in magnitude (Salaris & Cassisi, 2005).

The SFH of a CSP can be determined from the direct observations of the single stars. One of the most common methods is the sampling of the observed CMD (see for example Figure 1.5). Firstly, the CMD is divided in N cells both in magnitude and in colours. The width of the cells is usually chosen so that each of them contain a good sample of stars. Then, synthetic CMDs for simple stellar populations with an homogeneous distributions of age (n) and metallicities (m) are created, spanning the intervals in Δt and ΔZ, respectively. In this way, a total of nxm synthetic models is created. The choice of Δt and ΔZ depends on the statistics and the photometric errors upon the observed CMD, but also on the uncertainties affecting the theoretical models.

The minimization of a merit function from the comparison between observed and theoretical CMDs provides the best model for the SFR and the age-metallicity relation, and hence, for the SFH.

Obviously, many assumptions have to be done: the assumed IMF is realistic and not dependent on age and metallicity, the available stellar models are accurate to theorise the populations in the observed CMDs, data are assumed to have high quality photometry.

1.3 Unresolved stellar populations

In the local Universe we can analyse the stellar populations taking advantage of the properties of their individual stars in a specific evolutionary phase. Indeed, age, metallicity and initial helium abundance can be inferred from the CMD.

On the contrary, observations of distant galaxies provide us integrated quantities for colours, magnitudes and spectra since we cannot resolve the single stars of the population, i.e., the stellar population is *unresolved*.

1.3.1 Simple stellar populations

Analytically, the integrated flux F_λ^I from a simple unresolved stellar population (USP) of age t and metallicity Z can be defined as (Salaris & Cassisi, 2005):

$$F_\nu^I(t, Z) = \int_{m_l}^{m_u} f_\lambda(t, m, Z)\phi(m)dm \tag{1.2}$$

where m_l and m_u are the lower and upper limits on masses, normally the mass of the lowest-mass and of the highest-mass stars alive in the SSP, respectively (m_u can be approximated to the mass at the TO point). $\phi(m)$ is the IMF and f_λ is the flux of the stellar population. This means that the observed total flux is the sum of the fluxes from the single stars inside the population, modulated by the IMF, which describes the number of stars formed with a mass M and $M + \Delta M$.

The integrated magnitude in a specific band A can be written as:

$$M_A(t,Z) = -2.5log\left(\int_{m_l}^{m_u} 10^{-0.4M_A(m,t,Z)}\phi(m)dm\right) \tag{1.3}$$

so that, it is the sum of the star fluxes within the wavelength band. Finally, the integrated colours are defined as the difference between integrated magnitudes in two different bands.

Integrated magnitudes and colours

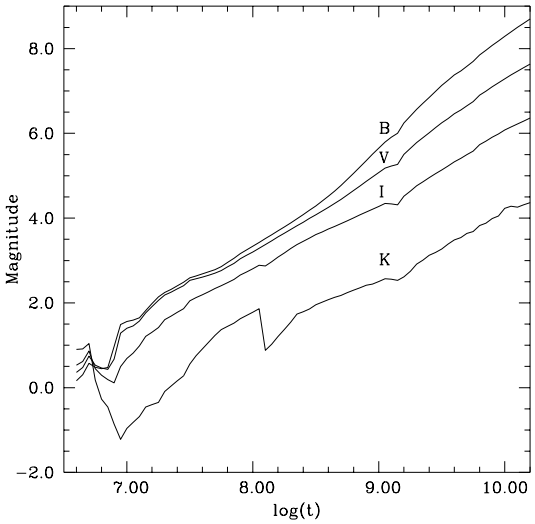

Figure 1.6: Time evolution of magnitudes in selected photometric bands (Salaris & Cassisi, 2005).

Figure 1.6 shows the time evolution of the integrated magnitudes in B, V, I, K photometric bands for a population of solar metallicity.

In general, the magnitudes fade with time because of the depletion of the MS stars for $t > 10Gyr$. In the K-band we have a sudden increase in luminosity due to the asymptotic giant branch (AGB) population growth at $t \sim 200Myr$, where B, V, I-bands experience a boost due to the increase of He-burning stars (HB phase for low-mass stars and blue-loop for intermediate mass stars).

To analyse the USP, the use of integrated colours is more helpful since, unlike the integrated magnitudes, they are independent on the stellar population distance and, in principle, on the mass.

Figure 1.7 shows three different colour-colour diagrams (CCDs) from Salaris & Cassisi (2005). In Figure 1.7a the lines (solid, dashed and dotted) identify different metallicities while the dots define different ages. At young ages the lines in these CCDs arrange with a complicated pattern due to the non monotonic relation between age and metallicity.

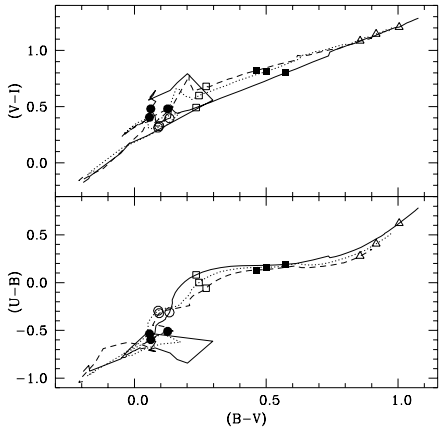

(a) Colour-colour diagrams from Salaris & Cassisi (2005). Different symbols identify different ages: 30 Myr (filled circles), 100 Myr (open circles), 350 Myr (open squares), 1 Gyr (filled squares), 10 Gyr (open triangles).

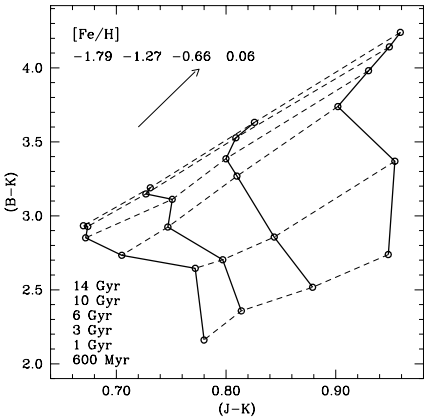

(b) Colour-colour diagram from Salaris & Cassisi (2005) for selected ages and metallicities (see labels). Solid lines display constant metallicities, the dashed ones identify the constant ages.

Figure 1.7: Examples of colour-colour diagrams.

Indeed, the lines overlap while points lay on the same line: this means that these observed colour pairs for a given SSP can be reproduced with different metallicities for different ages. This is the so-called "age-metallicity degeneracy", which can be broken using specific CCDs, like the one displayed in Figure 1.7b, where the colour $(B-K)$ seems to be sensitive to the age, while $(J-K)$ to the metallicity. Indeed, $(B-K)$ is sensitive to the TO magnitude and colour, usually used to photometrically determine the age of the resolved stellar populations. Moreover, the emission in J and K, and so the colour $(J-K)$, is dominated by the AGB and/or RGB stars, whose position in the diagram depends on the initial metallicity.

This combination of colours is able to disentangle the effects due to metallicity from the ones due to the age. Indeed, we observe that the solid lines, identifying constant metallicities, do not overlap with the dashed lines, identifying constant ages.

Absorption-feature indices

Integrated spectra of unresolved populations (with resolution $R < 1nm$) can be used to constrain stellar ages and chemical compositions. In fact, they are characterized by several absorption features depending on the abundance of different specific chemical elements in stellar atmospheres and on the number of stars in a specific evolutionary state.

The absorption feature strengths (and so, equivalent widths) can be measured

through a system of indices. To define an index we have to measure the relative flux in a central wavelength range covering the selected absorption feature, and two flanking intervals (side-bands) that provide a reference level (pseudo-continuum) from which the strength of the absorption feature is evaluated.

Indices for narrow lines are usually expressed in Angstroms, while those for molecular bands in magnitudes:

$$I_{\text{Å}} = \int_{\lambda_1}^{\lambda_2} \left(1 - \frac{F_{I,\lambda}}{F_{C,\lambda}}\right) d\lambda \tag{1.4}$$

$$I_{mag} = -2.5log\left[\left(\frac{1}{\lambda_2 - \lambda_1}\right) \int_{\lambda_1}^{\lambda_2} \frac{F_{I,\lambda}}{F_{C,\lambda}} d\lambda\right] \tag{1.5}$$

The Lick index system (Worthey et al., 1994) provided most of the evolutionary information about old stellar populations since it was created.

It was established by observations of ∼ 500 sources with the image dissector scanner (IDS) and Cassegrain spectrograph on the 3 m Shane Telescope at Lick Observatory.

Originally, they covered the wavelength range 4000-6400 Å with a resolution between 8 and 10 Å for roughly 500 stellar spectra and they were estimated using Equations 1.4 and 1.5 from the non flux-calibrated spectra. Now, they are mostly estimated using Equations 1.4 and 1.5 on flux-calibrated integrated spectra of a resolution > 8 Å, and therefore, they are not exactly in the Lick system (Lick-type indices), but we usually do not make any difference between them.

Worthey et al. (1994) defined the first set of 21 indices, and then 4 indices where included to cover the Balmer line series in the optical range (Worthey & Ottaviani, 1997).

In general, indices from the Lick system provide index-index diagrams that are useful to break the age-metallicity degeneracy and to independently estimate age, [Fe/H] and [α/Fe] for a stellar population.

Different examples are shown in Figure 1.8. In the right upper panel of Figure 1.8 we have H_β-Fe5406 index diagram for different ages, metallicities and for both scaled-solar and α-enhanced mixtures. H_β index is a good tracer for age thanks to its high sensitivity to the T_{eff} of TO stars, while Fe5406 traces iron abundance ([Fe/H]) and it is not sensitive to α enhancement. As we can see from the diagram, the lines are roughly orthogonal, meaning that the age-metallicity degeneracy can be easily broken with this index combination.

On the contrary, H_β index is slightly affected by α enhancement: at constant [Fe/H], it shows a systematic decrease at the lower [Fe/H] values. Increasing [Fe/H], the decrease of the index becomes even smaller.

Moreover, to investigate old stellar systems, magnesium feature at ∼ 5200Å is often used (Buzzoni, 2015). The feature is a blend of the atomic Mg_b triplet (5178 Å) and the vibrational band of MgH molecule. The magnesium complex

is sampled by three Lick indices, Mg_1, Mg_2 and Mg_b. The first one probes the molecular contribution, Mg_b index is useful to investigate the atomic triplet, while Mg_2 connect the other two. The indices Mg_b and Mg_2 of early-type galaxies provide higher metallicities than indices like Fe5270 and Fe5335, probably because stellar populations in these objects have higher Mg/Fe (in general α/Fe ratios) than the solar values (Thomas et al., 2003). This causes shorter star formation time scales (< 1 Gyr), not described by current models of galaxy formation yet.

The left upper panel in Figure 1.8 the H_β-Mg_b grid. It displays how Mg_b index is sensitive to the α enhancement degree, because of its dependence on the abundance of the α element Mg.

We can create new indices from different combinations. For example if we combine Fe5406 and Mg_b, we have the new index $[MgFe] = \sqrt{< Fe > \times Mg_b}$, with $< Fe >= 1/2(Fe5270 + Fe5335)$.

Left lower panel in Figure 1.8 shows the H_β-[MgFe] diagram: [MgFe] seems to be not affected by α-enhancement level, while,at fixed [MgFe], H_β increases with the α-enhancement. Finally, from Fe5406-[MgFe] grid (right lower panel in Figure 1.8), we can estimate the α enhancement degree. Indeed, in this case the age/metallicity lines are completely degenerate, but the scaled-solar and α-enhanced sequences are well separated. Therefore, thanks to a combination of three diagrams (for example H_β-Fe5406, H_β-[MgFe], Fe5406-[MgFe]), we can independently compute age, metallicity and α enhancement degree.

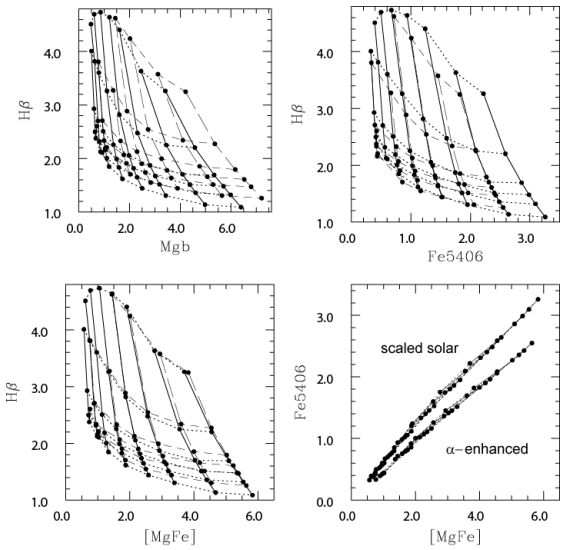

Figure 1.8: Different index-index diagrams from Cassisi & Salaris (2013) for scaled-solar populations (solid and short-dashed lines) with [Fe/H] from -1.79 to 0.40 and α-enhanced (long-dashed and dotted lines) with [Fe/H] from -1.84 to +0.05. Ages span from 1.25 to 14 Gyrs, increasing from top to bottom. Metallicities increase from left to right.

1.3.2 Stellar populations synthesis technique

Stellar populations synthesis models (SPSMs) are usually adopted to theoretically investigate the evolutionary status of the USPs in galaxies.

Two approaches currently exist. The *inverse approach* compares the observed integrated magnitudes/colours and spectra to the results of SPSMs. In this way it constrains the SFH characterizing the population. The *direct approach* uses a theoretical model converting a predicted SFH into integrated properties. These expected quantities are then compared to the observed ones.

All the ingredients we need to produce SPSMs will be reviewed in the following sections.

Stars

Isochrones An isochrone is a line describing stars of the same age in the Hertzsprung-Russel diagram (HRD). Theoretical models describe the evolution of the stars from the early (hydrogen burning limit $M \sim 0.1 M_{\odot}$) to the final ($M \sim 100 M_{\odot}$) stages. Therefore, isochrone libraries have to cover wide ranges in age, chemical mixture and evolutionary phases.

In the following the most common models currently used are reviewed.

Padova models (Bertelli et al., 1994)— They firstly characterized the evolution of the stars in the mass range ΔM=0.15$M_{\odot}$-7$M_{\odot}$ and metallicity range of ΔZ=0.0004-0.07 (Girardi et al., 2002). The updated version PAdova and TRieste Stellar Evolution Code (PARSEC, Bressan et al., 2012) supplies the evolutionary phases from the pre-main sequence (PMS) ($M = 0.1 M_{\odot}$) to the massive ($M = 12 M_{\odot}$) stages and an improvement of the input physics description (opacities, equation of state, rates of nuclear reactions). Thermally-pulsing asymptotic giant branch (TP-AGB) stars, characterized by a very short life and cold temperatures, need a significant and accurate treatment. They are one of the most important contribution to the integrated flux of stellar populations, especially in NIR bands where their high luminosities can alter the mass to light ratio (M/L) estimates in galaxies (Cassisi & Salaris, 2013).

The first *Padova* isochrone libraries including the treatment of TP-AGB phase are provided in Marigo et al. (2008), while the complete analysis of thermal pulse cycles is described in the newest stellar isochrones PARSEC-COLIBRI (Marigo et al., 2013, 2017), covering a wide range of initial metallicities (0.0001<Z<0.06). They take into account the effect of diffusion, dredge-ups and hot-bottom burning. They provide new models for pulsation able to describe changes of stellar parameters, long period variability and dust production.

BaSTI models (Pietrinferni et al., 2004)— At first they characterized stellar evolution of stars with mass range between $0.5 M_{\odot}$ and $10 M_{\odot}$ while [Fe/H] ranges between -2.27 and 0.40 with scaled solar distribution. Recently, thanks to an

update (Pietrinferni et al., 2013) they are able to describe even extremely metal-poor ($Z = 10^{-5}$) and super-metal-rich (Z = 0.05) objects, with both scaled-solar and α-enhanced ($[\alpha/Fe] = 0.4$) distributions. A particular attention is put on the initial He mass fraction Y, ranging from 0.245 to 0.4, and on the mass loss rate.

The latest version BaSTI-IAC (Hidalgo et al., 2018) provides improvements on input physics (solar metal mixture, opacities, nuclear reaction rates, bolometric correction) and on the overshooting efficiency. The new models describe the evolutionary stages of the stars in the mass range $0.1M_{\odot} \leq M \leq 15M_{\odot}$, initial metallicity $-3.20 \leq [Fe/H] \leq +0.45$ with an helium enrichment ratio of $dY/dZ = 1.31$. The isochrone ages cover a range between 20 Myr and 14.5 Gyr.

Pisa Evolutionary Library (PEL) database (Castellani et al., 2003a; Cariulo et al., 2004) provides models for Magellanic Cloud stellar populations and for metal-poor stars. Magellanic Cloud models are computed in the mass range $0.8M_{\odot} \leq M \leq 8M_{\odot}$, from the MS to the C-burning or to the TP-AGB phase. The isochrones cover ages from $\sim 100Myr$ to $\sim 15Gyr$. Additional models which include overshooting during the H burning are also available. The metal-poor stellar population models extend the previous set to stars with Z=0.0002, 0.0004, 0.0006, 0.001 with assumptions about the initial He content. The mass range is $0.6M_{\odot} \leq M \leq 11M_{\odot}$ covering ages from 20 Myr to 20 Gyr.

Geneva models (Schaller et al., 1992)— These models are characterized by masses from $0.8M_{\odot}$ to $120M_{\odot}$ and metallicities from Z=0.001 to 0.1. They include evolutionary phases from the pre-main sequence (Bernasconi & Maeder, 1996) to the end of the carbon burning for massive stars (Meynet et al., 1994). Therefore, they cannot be used to analyse the evolutionary status of low-mass stars.

Obviously, all the different models are affected by several uncertainties, relevant for modelling the population spectral energy distributions (SEDs). For example, they are all one dimensional codes, so they can approximately describe convection, rotation, mass loss, pulses and binary interactions, all three dimensional processes (Conroy, 2013).

Stellar spectral libraries Stellar spectral libraries convert surface gravity $g(Z) = \frac{GM}{R^2}$ ($[cm/s^2]$) and effective temperature $T_{eff}(Z)$ values obtained from stellar evolution models into observable SEDs. The SPS models usually combine different spectral libraries which can be either theoretical or empirical. Pros and cons of both type of stellar spectral libraries will be discussed in the following.

Theoretical libraries Theoretical libraries are characterized by a wide parameter space and by the fact that their produced spectra are not affected by observational problems like atmospheric absorption. These libraries obviously depend on the choice on the input parameters and the approximations made to compute models.

One of the most important issues is the treatment of atomic/molecular lines, which seriously affects spectra reproduction of the Sun (inaccurate atomic lines

list, Kurucz, 2011) and of the cooler stars (uncertainties on molecular lines, Allard et al., 2011). Indeed, the predicted lines usually come from model calculations and not from laboratory measurements. Therefore, their central wavelength and strengths are often defined with an high uncertainty.

Several theoretical libraries are available.

CoMARCS models (Aringer et al., 2009)— They provide a quite good description of carbon rich stars, the late evolution of low and intermediate-mass stars. Determining the physical parameters and mass loss of these objects is important to understand the chemical enrichment in galaxies, and so, to model their IR flux. CoMARCS models are characterized by T_{eff} between 2400 and 4000 K, surface gravities from log(g) = 0.0 to -1.0 ($[cm/s^2]$), metallicities from 0.0134 to 0.00134 and C/O ratios between 1.05 and 5.0.

MARCS (Gustafsson et al., 2008) and ***PHOENIX*** (Brott & Hauschildt, 2005)— They model atmospheres and molecular lines for cold stars. The first one describes stars with T_{eff} ranging from 2500 K and 8000 K, log(g) between -1 and 5 ($[cm/s^2]$), C/O ratios between 0.09 and 5.0. The second library models stars with T_{eff} ranging from 2700 K and 10000 K, log(g) between -0.5 and 5.5 ($[cm/s^2]$), metallicities from -4.0 to 0.5 with variations of α elements.

Smith models (Smith et al., 2002)— This library describes the ionizing O and Wolf-Rayet stars with expanding model atmospheres for five metallicities from 0.05 to 2.

ATLAS models (Castelli & Kurucz, 2003)—The library describe stellar atmospheres with T_{eff} ranging from 3500 K to 50000 K, log(g) between 0.0 and 5.0 ($[cm/s^2]$) and with [M/H]=0.0,-0.5,-0.5 with an α enhancement of +0.4 dex, -1.0,-1.5.

Empirical libraries Empirical spectral libraries do not depend on the treatment of theoretical models like convection or atomic/molecular lines, but they are affected by observational constraints like atmospheric absorption, spectral resolution, flux calibration. Contrary to theoretical libraries, they do not cover a wide range in parameters. Indeed, due to the fact that they are based on star observations in the solar neighbourhood, we lack of information about rare objects, like low-metallicity hot MS, Wolf-Rayet (WR) or TP-AGB stars.

ELODIE library (Prugniel & Soubiran, 2001, 2004) covers a very large wavelength range (400 to 680 nm) and atmospheric parameters space (T_{eff} from 3000 K to 60000 K, log(g) from -0.3 to 5.9 and [Fe/H] from -3.2 to +1.4.). Two resolutions (R=42000 and R=10000) are available. Its flux calibration is limited by the use of an echelle spectrograph.

INDO-US (Valdes et al., 2004) contains spectra for 1273 stars, with spectral coverage of 346-946.4 nm and a broad coverage of atmospheric parameters.

STELIB (Le Borgne et al., 2003) is a library of 249 stellar spectra in the wavelength range 320-950 nm. The included stars are characterized by various spectral

types, luminosities and wide range in metallicity ([Fe/H] from -1.90 to +0.47).

MILES (Sánchez-Blázquez et al., 2006) provides the greatest atmospheric parameters coverage for 985 stars. Most of them are field stars in the solar neighbourhood, but it also includes open and globular cluster stars with different ages and metallicities. G8-K0 metal-rich stars ([Fe/H] from +0.02 to +0.5) with temperatures between 5200 and 5500 K, some stars with temperatures above 6000 K and metallicities higher than +0.2, and hot dwarf stars with low metallicities are available.

Kesseli et al. (2017) published a library obtained with the spectra from the Sloan Digital Sky Survey. It contains spectra for stars with metallicities from -2.0 to +1.0, separated into main-sequence (dwarf) stars and giant stars. Its wavelength coverage is from 365 to 1020 nm with a resolution better than 2000.

One of the major problem of empirical libraries is the irregular coverage in the HRD. In general the lower main sequence and the red giant branch are well covered over a wide range in metallicity. On the contrary, since hotter and younger ($< 1Gyr$) stars are rare in the solar neighbourhood, their coverage is really challenging for empirical spectral libraries.

Another problem is represented by the determination of log(g), T_{eff} and [Fe/H]. The major uncertainties ($\sim 100K$) exist for T_{eff}, reflecting on the estimation of several absorption feature lines, including hydrogen Balmer lines and iron and magnesium, useful to study stellar populations of early-type galaxies.

In the solar neighbourhood the low metallicity stars are α-enhanced ([Mg/Fe] $\sim$ 0.0 at [Fe/H] $\sim$ 0.0 and [Mg/Fe] $\sim$ 0.4 at [Fe/H]<-1.0). This represents another issue since, in the models, all the low metallicities have to be corrected for the [α/Fe] bias.

Dust

All galaxies, especially star-forming ones, contain interstellar dust. It obscures light in the UV-NIR and emits in the IR bands. Dust attenuation and emission are often modelled as distinct components since they depend on different properties of a galaxy (the geometry of dust grains and the radiation field, respectively).

Attenuation Attenuation by dust is usually described by reddening and total obscuration.

The reddening can be parametrized through the colour excess $E(B-V)$. It describes the wavelength dependence of the dust effects, taking into account that shorter wavelength photons are more readily scattered and absorbed by dust.

The total obscuration is in general parametrized by $A(V)$. It measures the total light absorbed or scattered by dust out of our line of sight. Several laws ($A(\lambda)/A(V)$, see Figure 1.9) exist describing the total obscuration for single stars in the Milky Way and in the Large and Small Magellanic Clouds (Cardelli et al., 1989), but

obviously in a galaxy we have different optical depths for each star and stellar population, depending on position and age.

We can describe the dust obscuration in a galaxy as (Walcher et al., 2011):

$$I(\lambda) = I_{star}(\lambda)e^{-a_\lambda \Delta\tau} \tag{1.6}$$

where a_λ is the reddening law and $\Delta\tau$ is the thickness.

Dust attenuation in starbust galaxies is usually described by the Calzetti law (Calzetti et al., 2000), a simple $1/\lambda$ polynomial function. In general a power law $a_\lambda \propto \lambda^{-0.7}$ can reproduce the observed attenuation in galaxies (Charlot & Fall, 2000).

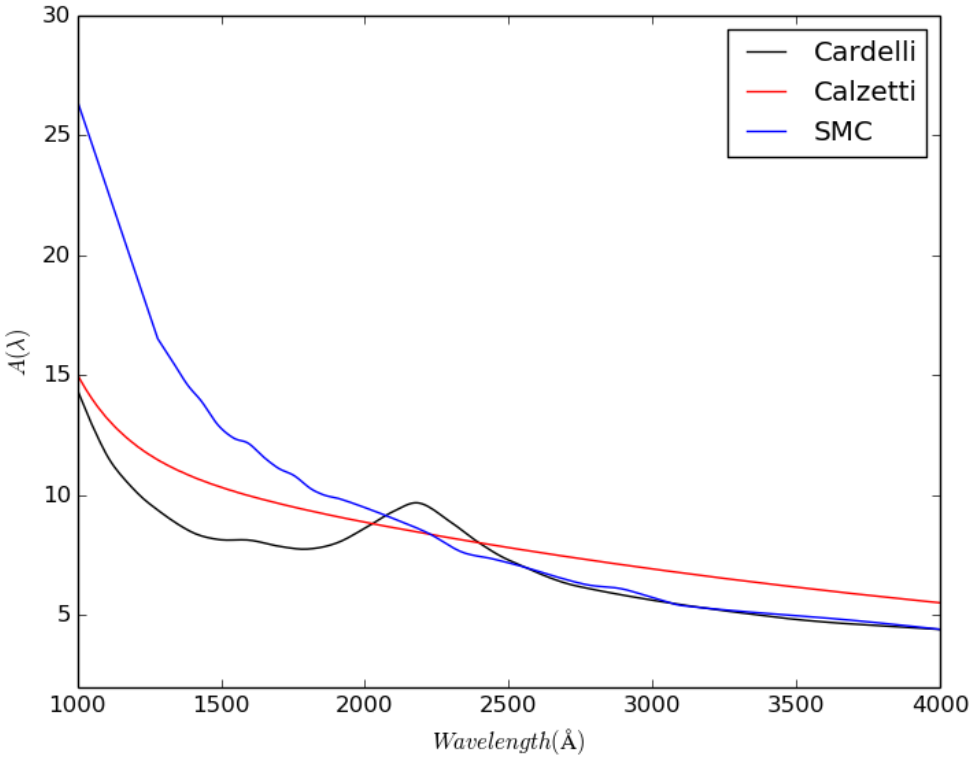

Figure 1.9: Different extinction laws: Milky Way (Cardelli, $R_V = 3.1$), Calzetti and SMC.

Emission The IR wavelengths of galaxy SEDs are dominated by the emission of dust grains. Three different types can exist: graphitic/amorphous carbon grains, amorphous silicate grains and polycyclic aromatic hydrocarbons (PAHs). At short wavelengths ($\lambda < 20\mu m$) the emission ($\sim 1/3$ of IR flux) is dominated by PAHs. The most prominent PAH emission features at 3.6 μm, 6.2 μm, 7.7 μm, 8.6 μm,

11.3 μm are well modelled (Desert et al., 1990; Draine & Li, 2007), while at longer wavelengths ($\lambda > 50\mu m$) grains of $T \sim 15 - 20K$ dominate the emission ($\sim 2/3$ of IR flux). Dale et al. (2001) developed simple models for dust emission. They combined different emission curves for large and small grains to reproduce IR empirical spectra of star forming galaxies.

Initial Mass Function

The IMF, $\phi(m)$, is defined as the initial mass distribution at the time of birth of the stars in a stellar system. Since the evolution of the single stars depends mainly on their mass, analysing the IMF allows to determine some of the stellar population properties.

The quantity $\phi(m)dm$ is the relative number of stars born with masses in the range $m \pm dm/2$.

Normalizing as:

$$\int_{m_l}^{m_u} m\phi(m)dm = 1M_\odot \tag{1.7}$$

$\phi(m)dm$ is defined as the number of stars born with masses in $m \pm dm/2$ for every new solar mass formed. In general $m_l \sim 0.08M_\odot$, since below this mass value the hydrogen burning cannot take place, and $m_u \sim 100M_\odot$, since the stars with masses greater than this value are unstable against the radiation pressure.

If we consider M_* as the total mass of the formed stars, we can define the total number of the stars formed in the mass range as:

$$dN(m) = \frac{M_*}{M_\odot}\phi(m)dm \tag{1.8}$$

while the total mass of the stars as:

$$dM(m) = \frac{M_*}{M_\odot}m\phi(m)dm \tag{1.9}$$

For convenience, we use the IMF in the logarithmic form:

$$\xi(m)dlogm = \phi(m)dm \rightarrow \xi(m) = ln(10)m\phi(m) \tag{1.10}$$

For the Galaxy, the first and most common empirical IMF form is the simple power-law model defined by Salpeter (1955):

$$\phi(m)dm \propto m^{-\alpha} \tag{1.11}$$

with $\alpha = 2.35$ for stars with mass $0.4M_\odot \leq m \leq 10M_\odot$.

In general the functional form could vary within the same galaxy and from galaxy to galaxy. Observations seem to show that the IMF has roughly the same form in every location of the Milky Way and so it is usually assumed as universal.

In the solar neighbourhood the observed IMF deviates from the Salpeter simple power law only at the lowest mass ($m < 1M_\odot$) end, where it becomes flatter, and at the highest mass end, where it is steeper. Therefore, according to the observational results, other forms could be used. Observing the field stars in the solar neighbourhood, Kroupa (2001) defined a broken power-law:

$$\phi(m) \propto \begin{cases} m^{-2.7} & (1.0M_\odot \leq m \leq 100M_\odot) \\ m^{-2.3} & (0.5M_\odot \leq m \leq 1.0M_\odot) \\ m^{-1.3} & (0.08M_\odot \leq m \leq 0.5M_\odot) \\ m^{-0.3} & (0.01M_\odot \leq m \leq 0.08M_\odot) \end{cases}$$

which is similar to the Salpeter IMF for $m > 0.5M_\odot$, while Chabrier (2003) determined the lognormal form for the IMF:

$$\xi(m) \propto \begin{cases} m^{-1.35} & (m \leq 1.0M_\odot) \\ e^{-[log(m/0.2M_\odot)]^2/0.6} & (m \geq 1.0M_\odot) \end{cases}$$

A comparison between these three different functional forms for IMF is shown in Figure 1.10. From this Figure it is evident that for $m \leq 1M_\odot$ the three different IMFs follow a power low, with the Chabrier one emphasizing high mass stars.

Since outside the Galaxy only the brightest and massive stars are observable, we can determine only the high mass end of the IMF. Therefore, within the uncertainties, the IMF is considered similar for the different galaxies and so, universal.

The IMF variations with parameters like stellar density, metallicity and age are not theoretically determined, so the IMF is one of the main source of uncertainties in the stellar population SED models.

Star Formation History

The SFH $\Psi(t)$ is a function describing when the stars in a galaxy formed. It is a priori unknown and so, it has to be modelled. In general we can use parametrized (see e.g., Carnall et al., 2019, and references therein), non parametric (see e.g., Leja et al., 2019, and references therein) and simulated (Brammer et al., 2008a; Pacifici et al., 2012) SFH models.

The most widely used parametrized model is the exponentially declining SFH (τ model):

$$\Psi(t) = \tau^{-1} e^{-(t-T_0)/\tau} \tag{1.12}$$

where τ is the characteristic duration of the star formation. According to this model, the star formation has its maximum value for $t = T_0$ and then exponentially declines within τ time-scale.

Studying high redshift mock galaxies SEDs, Lee et al. (2009a) assessed that best fit SFRs inferred using a single component SFH are underestimated of a factor of

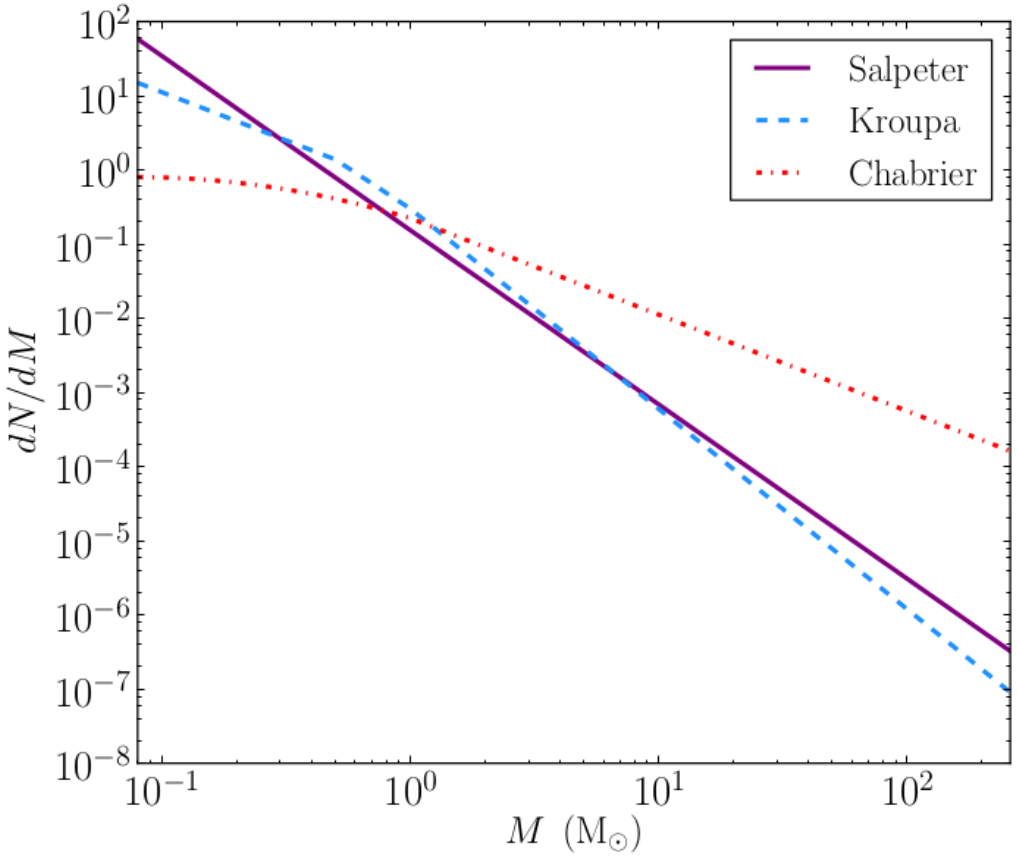

Figure 1.10: Salpeter, Chabrier and Kroupa IMFs. (Crosby et al., 2013)

two compared to the values from a two component SFH (young bursty+ old long lasting). This could be due to the fact that these galaxies have rising SFHs instead of declining models. Therefore, other parametrized models have been suggested (Figure 1.11).

For example, Maraston et al. (2010) suggested exponentially increasing SFHs:

$$\Psi(t) = \tau^{-1} e^{t/\tau} \tag{1.13}$$

to predict the star formation in high redshift star forming galaxies. Lee et al. (2010) proposed instead the delayed τ models:

$$\Psi(t) = \frac{(t - T_0)}{\tau} e^{-(t-T_0)/\tau} \tag{1.14}$$

able to reproduce the predicted rising SFHs for large values of τ.

Unfortunately, these simple parametrized models are not always able to match with galaxy observations. Indeed, from comparison to simulations and mock galaxies, they result to be too unsophisticated to describe those events which are complex and crucial for star formation, like bursts, quenching and active galactic nuclei (AGN) feedback. A possible solution is modelling SEDs with non parametric SFHs. In this case the function is divided in bins of age and the fit is implemented through the mass fraction in each bin (see Figure 1.12 for possible examples). They are able to provide complex SFHs, but they are reliable only if the galaxies are built with the same SPSMs used in fitting techniques.

Another possibility is the use of SFH libraries from hydrodynamic models of galaxy formation (Finlator et al., 2007). The advantage is that the model can more likely contain realistic SFHs compared to simple analytic models. For physical parameters like stellar mass and SFR, their simulated galaxies have similar values to the simple SFH models ones, but with substantially smaller uncertainties.

Pacifici et al. (2012) used semi-analytic models for SFHs computing larger samples of SFHs, but the results are sensitive to the choice of priors.

Codes

SPM codes assemble isochrones, stellar spectra, IMF, the effect of dust and metallicity enrichment to model a stellar population.

Different SPM libraries are available in literature.

GALAXEV (BC03 hereafter, Bruzual & Charlot, 2003) is characterized by a wide range in wavelength (91 Å - 160 μm), age (0-20 Gyr) and metallicity (Z=0.0001-0.05). It uses STELIB libraries (resolution R = 3 Å for λ=3200-9500 Åand R=20 Å for the other wavelengths). Salpeter and Chabrier IMFs and three different evolutionary tracks (two from Padova and the other from Geneva tracks) are available. The update version by Charlot & Bruzual 2007 has a special treatment of TP-AGB stars following the prescriptions by Marigo & Girardi (2007); Marigo et al. (2008).

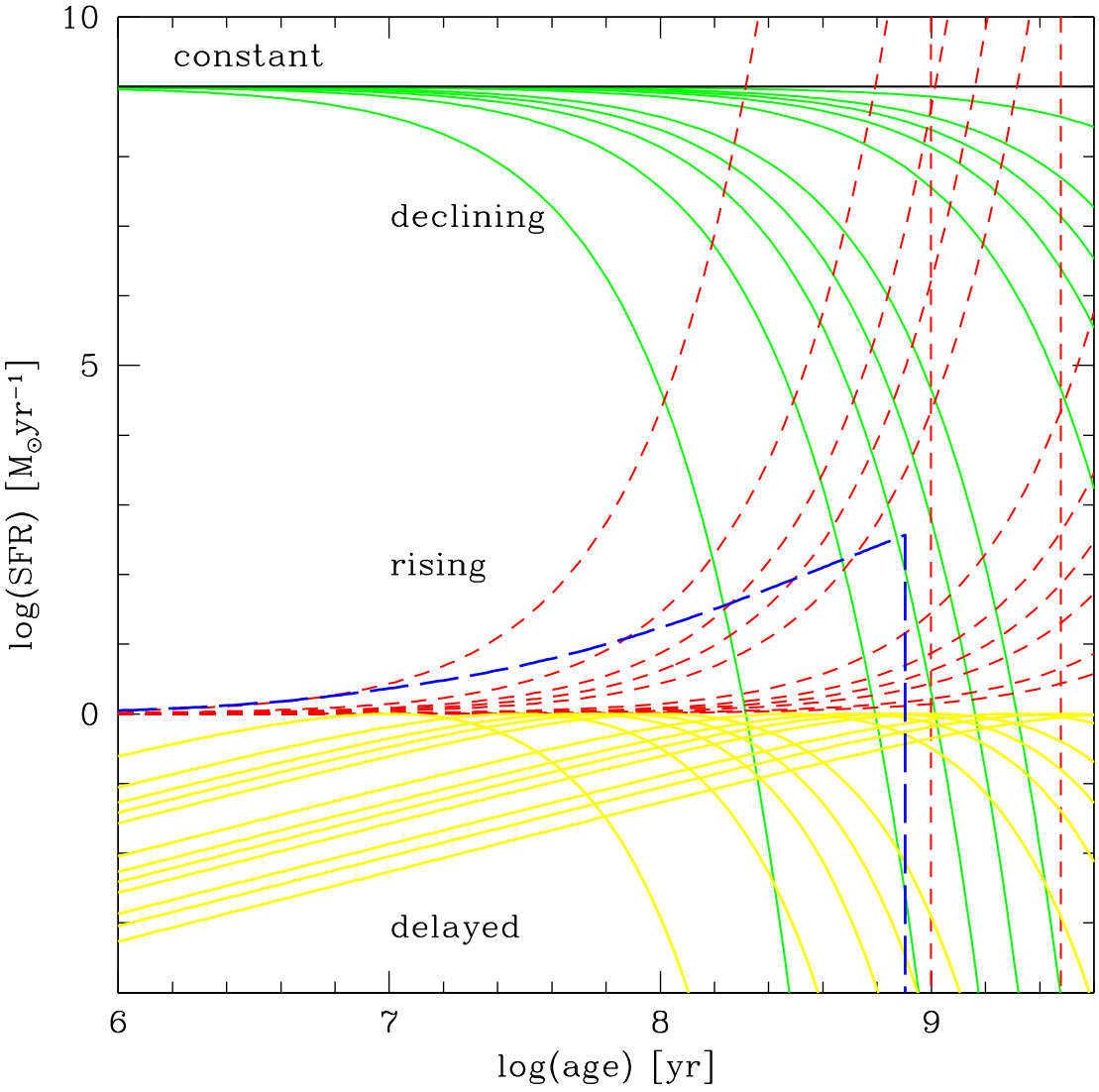

Figure 1.11: Four different parametrized SFHs (SFR as a function of age)(Schaerer et al., 2013).

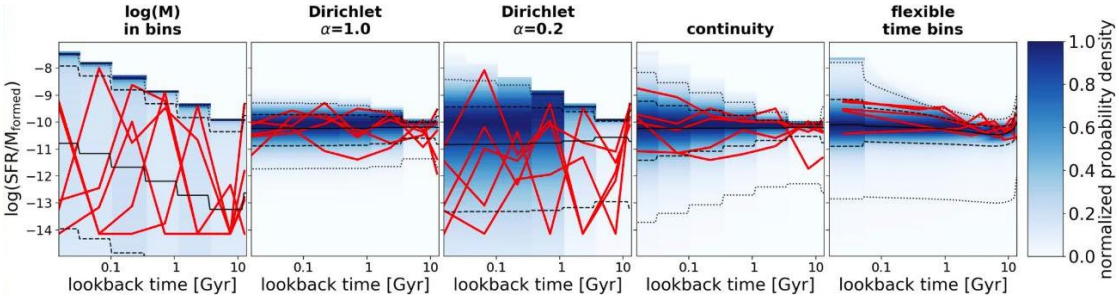

Figure 1.12: Possible non parametric SFHs from Leja et al. (2019).

PÉGASE (Fioc & Rocca-Volmerange, 1999) models spectra of galaxies from UV to NIR wavelengths, isochrone ages are in the range 0-20 Gyr. The code uses the stellar evolutionary tracks from the Padova group in the metallicity range $0.0001 \leq Z \leq 0.1$, while the stellar spectra are those from Lejeune et al. (1997). The IMF can be defined by the user through a combination of different power laws. An updated version *PÉGASE.3* (Fioc & Rocca-Volmerange, 2019) is now available to fit galaxy SEDs FIR/sub-mm wavelengths. It also includes the computation of nebular metallic and IR lines.

Ma05 (Maraston, 1998, 2005) is a model based on fuel consumption theorem and so the main ingredient of the synthesis is the amount of hydrogen and/or helium mass burned in each evolutionary phase.

These models have a wide range in metallicity (Z=0.0001-0.07), age (1000 yr-15 Gyr). Salpeter and Kroupa IMFs are available. They use Padova and Geneva tracks for different ages and/or metallicities. Stellar spectra come from BaSel library, with resolution R=5-10 Åin R and V bands, R=20-100 Åin NIR bands.

GALaxy EVolution (GALEV) (Kotulla et al., 2009) models describe the chemical and spectral evolution over cosmological scales. Metallicities are from 0.02 to 2.5, ages from 4 Myr to 16 Gyr. They use BaSeL libraries and Salpeter, Scalo, Kroupa IMFs. Isochrones are taken from Padova and Geneva tracks.

Flexible Stellar Population Synthesis (FSPS, Conroy & Gunn, 2010a) allows the user to compute the stellar population models in a flexible way taking into account different IMFs and metallicities. It includes the BaSTi and Padova isochrone libraries, the BaSeL spectra and O stars, WR stars, and post-AGB stars treatment from Smith et al. (2002); Rauch (2003).

1.3.3 Composite stellar populations

Stellar systems in the real Universe can be rarely described by a SSP: it is widely observed that also globular clusters are characterized by multiple populations formed at different epochs. In this case we can define these objects as CSPs

This means that the flux of a CSP is modulated by its SFH and chemical enrichment (Greggio & Renzini, 2011):

$$F_\lambda(X_i, t) = \int_o^t f_\lambda(X_i, t - t')\psi(t')dt' \tag{1.15}$$

where $f_\lambda(t)$ is the spectrum of a SSP, X_i is the chemical composition (in this case constant with time), $\psi(t)$ is the SFH of the population.

Clearly, galaxies are the perfect examples of observed CSP, characterized by complex SFHs, metal enrichment and environment exchanges.

Galaxies in fact contain stars with wide ranges in mass, age and chemical composition whose distribution changes with time. Consequently, we have to take into account the stellar evolution and different star formation histories while modelling galaxy SEDs at low and high redshift.

1.3.4 Spectral evolution

Simple stellar populations

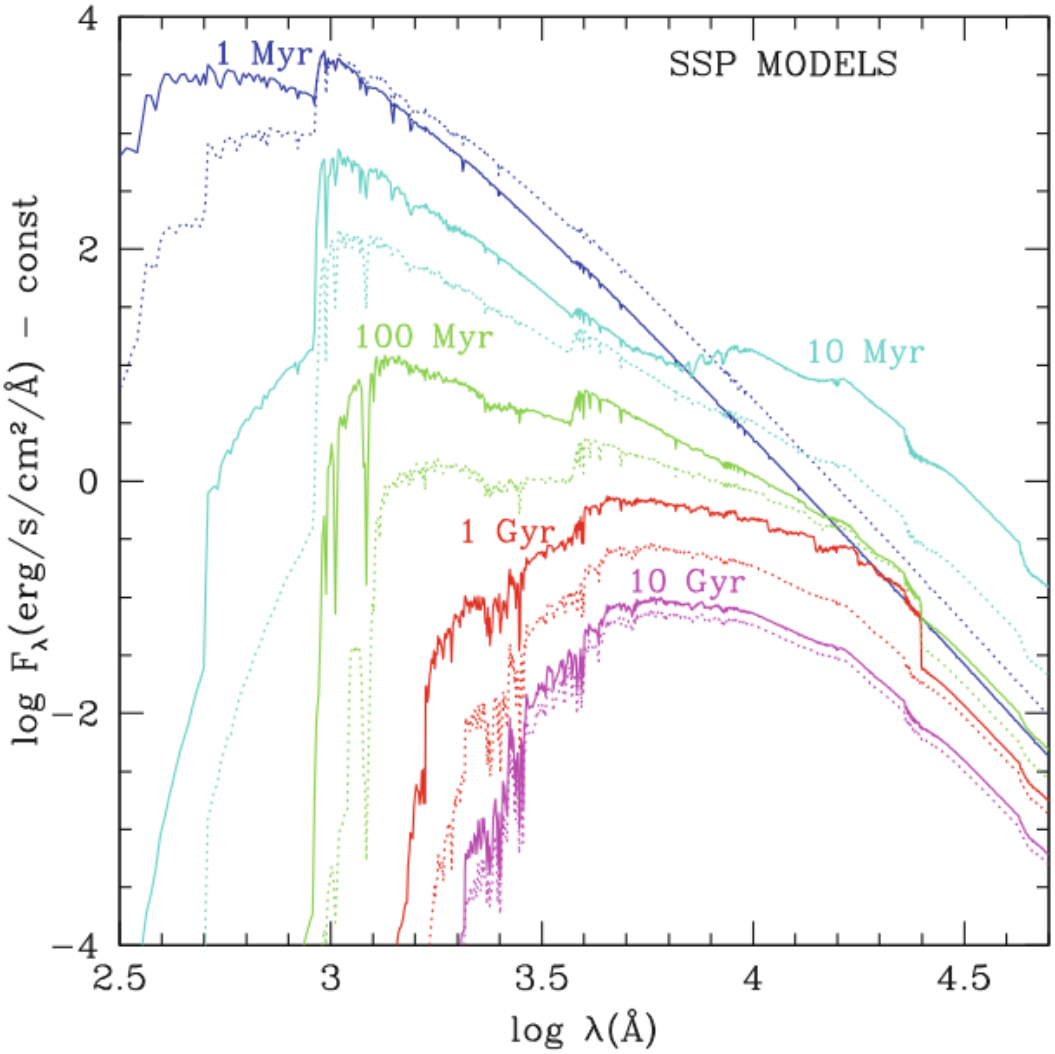

Figure 1.13: SED of a SSP of $Z = 1Z_{\odot}$ at different ages: 1 Myr (blue), 10 Myr (cyan), 100 Myr (green), 1 Gyr (red), 100 Gyr (violet) (Greggio & Renzini, 2011).

Figure 1.13 (Greggio & Renzini, 2011) shows the spectral evolution of a SSP with $Z = Z_{\odot}$ at different ages from $1Myr$ to $10Gyr$. When the population is $\sim 1Myr$ old (blue line), its massive stars are on the MS: the SED is almost constant except for a prominent Lyman break (912 Å) due to the photon absorption by the hydrogen gas.

At the age of $\sim 10Myr$ (cyan line), massive MS stars have already left this

phase, so that we have a depression of the flux for $\lambda < 1500$Å (the slope of the ultraviolet flux flattens), while the most massive stars are already dead. In the mean time, the other stars are evolving to the RGB phase, causing the increasing of the emission in the NIR bands.

We observe this trend while the population ages up to $100Myr$ (green line), when a Balmer break (3646Å), due to the arising A-type MS stars, becomes prominent and Balmer lines start to arise.

Moreover, we observe a general increasing of the NIR emission, due to the contribution of TP-AGB stars. Along with this, several metal lines appear while the Balmer break weakens, merging with the 4000 Å break.

At $1Gyr$ (red line), we have the maximum contribution of TP-AGB stars and the appearance of the first molecular lines

At $10Gyr$ (violet line), the molecular lines have almost disappeared with the fuel consumption of TP-AGB stars, while we observe the formation of metallic (magnesium and iron) lines in the optical bands.

We note that the UV flux rapidly fades if we compare it to the NIR emission. Indeed, the UV flux is mainly caused by the hot HB stars, whose lifetime is strictly connected to their effective temperatures, as shown in Figure 1.14. It displays a 12 Gyr SSP SED for different HB morphologies: a blue HB dramatically contributes to the UV emission of the population, a flat distribution of HB stars ($T_eff \sim 4000K - 40000K$) produces a flat UV flux. On the contrary, a red HB morphology does not contribute to the UV emission, generating a more prominent NIR rising (Greggio & Renzini, 2011).

Composite stellar populations

Analysing the observed SED of a CSP, we need to take into account the right parametrization of the SFH (several different SFH models have been already described in Sect. 1.3.2).

Figure 1.15 displays the spectra of a $1Gyr$ stellar population for different assumptions of SFHs, producing the same total stellar mass. In addition, it also shows the spectrum of a SSP, which has passively evolved for 1 Gyr. We note that the four CSP spectra have almost the same shape, while the major differences arise in the UV and optical bands, where they are forming stars: we have the maximum emission from the inverted-τ model and the minimum one from the τ model. Towards the IR bands, the difference between the spectra decreases since they are modelled to give birth to the same total stellar mass, even though in these wavelengths the fluxes still have differences of the order of ~ 2

Figure 1.16 (Greggio & Renzini, 2011) shows the spectra for a 13 Gyr CSP considering different SFH models, as in Figure 1.15. Also in this case, we observe major differences in the UV and optical wavelengths, while in IR they are almost undistinguishable also in comparison with the SSP spectrum.

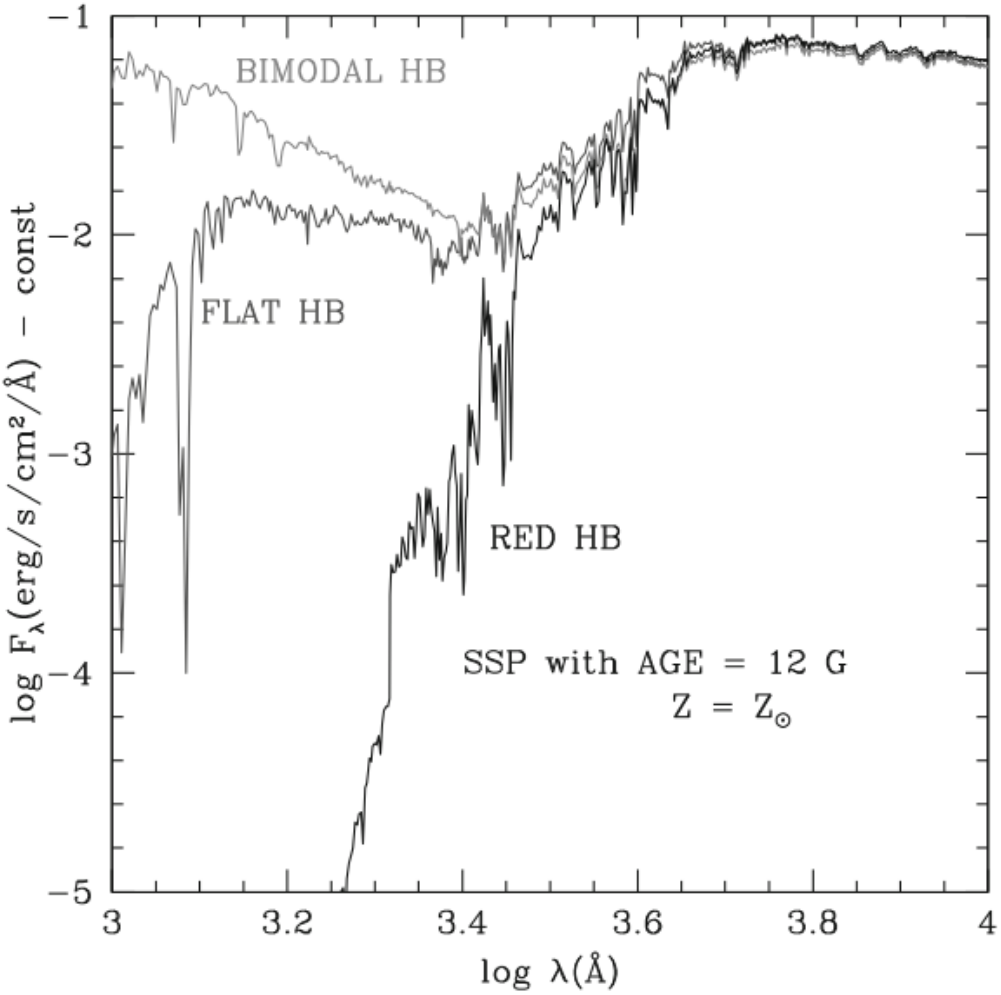

Figure 1.14: SED of a 12 Gyr population for different assumption on the effective temperature of the HB stars (Greggio & Renzini, 2011).

From the figures, it is evident that the NIR is a good indicator of the total stellar mass, but the fact that we observe populations with different SFHs displaying similar NIR spectra (similar mass) is a warning to use it as unique indicator.

1.3.5 SED Fitting

SED fitting allows to analyse an observed galaxy SED extracting simultaneously several properties of the source, like photometric redshifts, age, stellar mass, dust and SFRs. Each of these properties allows to constrain and understand the physics and the evolution of galaxies from high to low redshift.

It is a crucial technique since our current knowledge of the Universe is mainly

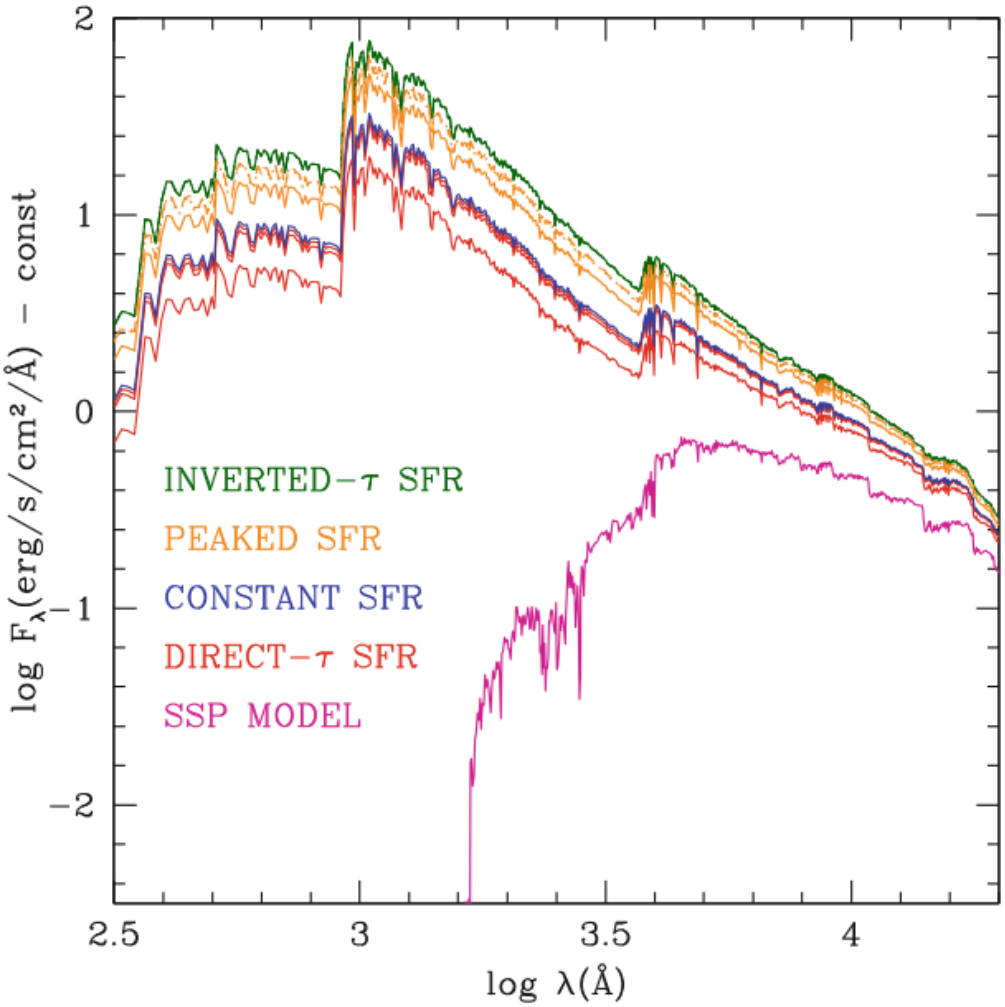

Figure 1.15: SED of a 1 Gyr population for different assumption on SFH: inverted-τ model (green), peaked model (orange), constant (blue), τ model (red), SSP model (magenta)(Greggio & Renzini, 2011).

based on the physical quantities inferred from galaxy SEDs.

Tools

Since the first SED fitting techniques were developed (Faber, 1972), huge progress has been done in this field thanks to the improvement both in quality and volume of the data.

Different tools and method are available in the literature.

BAGPIPES (Bayesian Analysis of Galaxies for Physical Inference and Parameter EStimation, Carnall et al., 2018) is a Python tool to fit spectroscopic and photometric galaxy data from far-UV to far-IR. It uses a nested sampling algo-

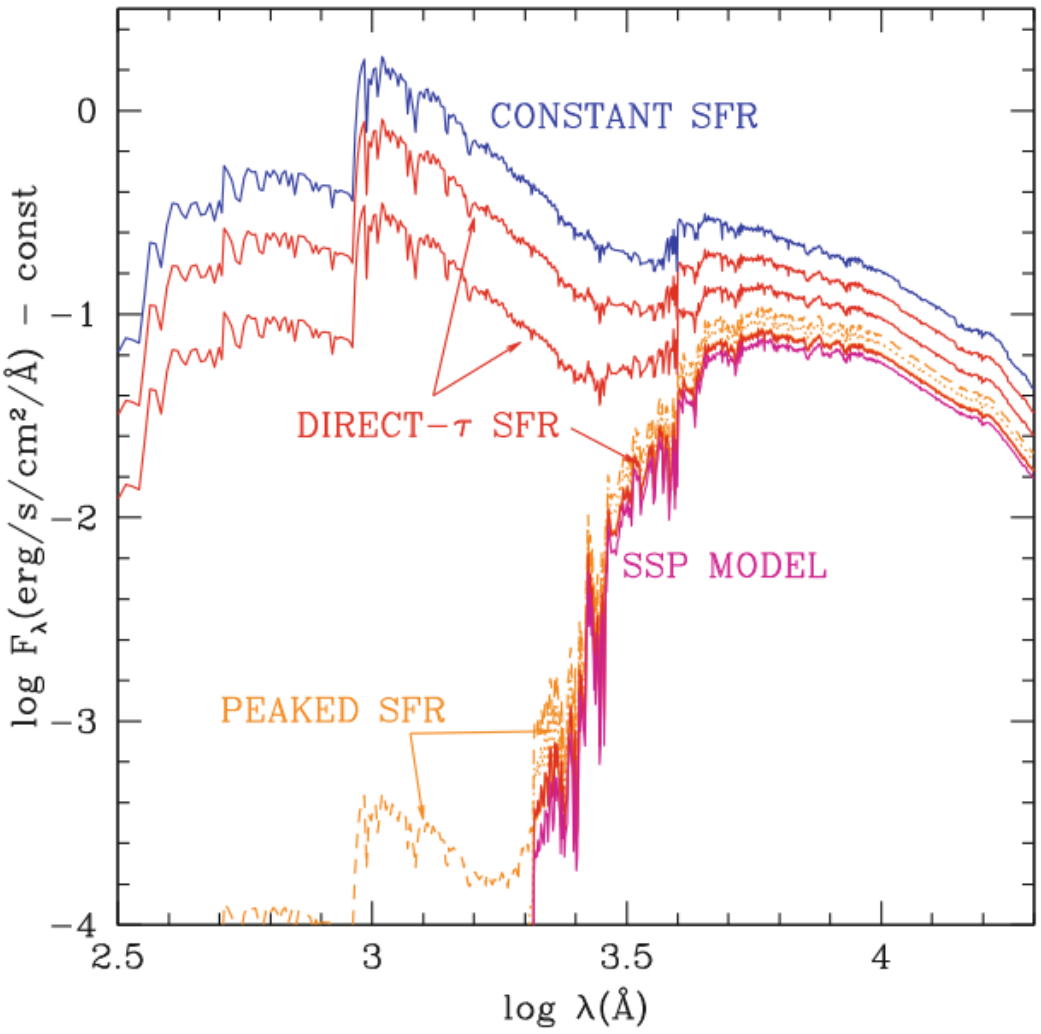

Figure 1.16: SED of a 13 Gyr population for different assumptions on SFH, as in Figure 1.15(Greggio & Renzini, 2011).

rithm to fit the galaxy spectra through a Bayesian approach. BAGPIPES uses the 2016 version of BC03 (Bruzual & Charlot, 2003), with a Kroupa (2001) IMF. The SFH can be built as a single function, a sum of different functional forms or customized through an array of SFR values. The available SFHs are: delta, constant, exponentially declining, delayed exponentially declining, log-normal and double power law functions.

BEAGLE (BayEsian Analysis of GaLaxy sEds, Chevallard & Charlot, 2016) models photometric and/or spectroscopic observations of galaxies adopting a Bayesian approach to infer galaxy physical parameters from observed SEDs. It includes the

latest version of the SPS code by Bruzual & Charlot (2003), the Chabrier (2003) IMF and parametric e non parametric descriptions of both SFH and chemical enrichment history of the galaxy. Indeed, in this picture the SFH is defined as a series of bins in star formation, in which mass fraction and metallicity are adjusted to reproduce the observation. BEAGLE also includes IGM and ISM model descriptions.

CIGALE (Code Investigating GALaxy Emission, Burgarella et al., 2005) is a code modelling the observed galaxy SEDs from far-UV to far-IR. It uses a minimum chi-square algorithm and a Bayesan method to derive the probability of each of the inferred parameters.

EAZY (Brammer et al., 2008b) is a code to estimate high-quality photometric redshifts from the observed galaxy SEDs. It uses a non-negative least squares algorithm.

FAST (Fitting and Assessment of Synthetic Templates Kriek et al., 2009) is an IDL code to fit photometric, spectroscopic, or both, observations of galaxies. It is compatible with EAZY, such that the extracted photometric redshifts from EAZY and its input file can be used by FAST. The tool includes Bruzual & Charlot (2003) and Maraston (2005) SPMs, Salpeter (1955), Kroupa (2001) and Chabrier (2003) IMFs. The inferred parameters are determined using a chi-square algorithm.

Zphot (Giallongo et al., 1998; Fontana et al., 2000) is a Fortran code for SED fitting extracting photometric redshifts and physical parameters of galaxies. The user can write a configuration file choosing from a variety of input models and options. Both empirical and synthetic stellar models are available; exponential declining, inverted, delayed, constant and finite length SFHs are accepted with a flexible range in time-scales. Nebular emission is based on Schaerer & de Barros (2009) prescription; one or a combination of models between Milky Way, Large Magellanic Cloud, Small Magellanic Cloud and Calzetti et al. (2000) laws can be chosen to add dust as free parameter. IGM absorption and a variety of IMFs are included.

Zphot performs chi-square minimization scanning the template SEDs to identify the best fit model to the observed photometry (magnitudes or fluxes, from UV to NIR wavelengths). It can work at a fixed redshift, in a redshift interval, at the best-fit redshift.

Inferred parameters and uncertainties

Photometric Redshifts One of the problems of extracting parameters from the extragalactic sources SEDs is redshift estimate (*photometric redshifts, photo-z*). This estimate is different from the other ones because more reliable and independent measures exist from spectroscopy. Therefore, it allows us to empirically calibrate and test SED methods. Two approaches exist to estimate photo-z. The empirical one uses a subset of spectroscopic redshifts to describe the redshift distribution as a function of magnitudes and colours, calibrating the relation itself.

On the contrary, template methods use libraries of observed spectra of galaxies or SED models. Shifting them to any redshift and convolving with the transmission curves of photometric filters, they create a template for redshift estimators.

Both methods create routines (based on χ^2 minimization or machine learning algorithms) to estimate photo-z.

Despite their simplicity, first empirical methods (Connolly et al., 1995; Brunner et al., 1997; Wang et al., 1998) provided accurate redshifts and uncertainties, using low-order polynomial fitting functions. Obviously, since the templates come from observed galaxies, these methods suffer of the effects of filter band-passes and flux calibrations.

Moreover, the redshift estimation is accurate only when the objects in the templates and in the observed catalogues have the same observables. This means that the method is more uncertain for objects with fainter magnitudes than the training ones. Finally, the training subsets have to cover large samples in redshift, galaxy type, colour and magnitude.

Since the first methods were created, new computational intensive algorithms have been used. Collister & Lahav (2004), for example, implemented artificial neural networks for their code ANNz.

Machine learning algorithms can determine the magnitude/colour and redshift correlations to a very high level. They are able to work with huge datasets (for example SDSS, Ball et al., 2008) and extrapolate very precise estimates of photo-z.

Template methods are usually involved to investigate new surveys, lacking of spectroscopic redshifts. These techniques suffer of several problems, like the mismatch between models and observed galaxies or the treatment of AGNs, emission lines, dust. Moreover, the template set has to be large enough to represent all the galaxies in the sample.

The maximum likelihood method is the most common one for template fitting. The best fit redshifts and templates are the ones which maximize the likelihood function (or minimize the χ^2) when comparing the observed magnitudes with model templates. The uncertainty on the redshifts are usually estimated propagating through photometric errors (e.g. *hyperz* code, Bolzonella et al., 2000).

To overcome the problem of possible colour-redshift degenaracy due to the large number of galaxies in the template libraries, we can use the Bayesan inference. Therefore, we include our prior knowledge about some properties, like the evolution of age with redshift or the shape of redshift distribution to better constrain the probability distribution function.

This method is used in several public codes like BPZ (Benitez, 2000), *kphotoz* (Blanton et al., 2003), ZEBRA (Feldmann et al., 2006), *Le Phare* (Arnouts et al., 1999; Ilbert et al., 2006, 2009) and EAzY (Brammer et al., 2008a).

Star Formation Rate SFR can be estimated using well-established relations with monochromatic indicators. Emission from new born stars is absorbed and re-

emitted by dust. Therefore, dust emission in mid-IR bands is in general the most sensitive tracer of SFR. Moreover, considering that unabsorbed photons emit in the UV wavelengths, a widely used SFR indicator is often a combination of IR and UV luminosity.

SFR can also be estimated from SED fitting. Its measure is based on several assumptions: galaxy SED is considered as purely stellar SED which can be described by a single attenuation law. The estimate is affected by some degeneracies that cannot be completely removed, like the one existing between age, metallicity and dust.

Because of the age-dust-metallicity degeneracy, SFRs from SED fitting have larger uncertainties than those from IR tracers.

Figure 1.17 shows relation between SFR_{IR+UV} and SFR_{fit} in different redshift bins from Santini et al. (2009). Red line defines the region SFR_{IR+UV}=SFR_{fit}. As

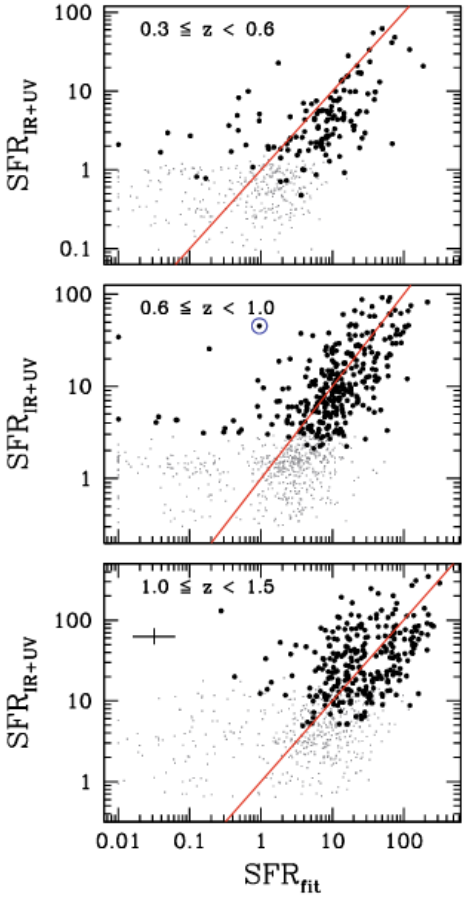

Figure 1.17: Relation between SFR_{IR+UV} and SFR_{fit} in different redshift bins from Santini et al. (2009). Red line defines the region SFR_{IR+UV}=SFR_{fit}.

we can see, in general there is consistency between the two estimators.

According to Santini et al. (2009), small inconsistencies for $SFR_{fit} > SFR_{IR+UV}$ objects could arise from incorrect fitting of red galaxies. Indeed, for these objects SED fitting techniques could infer large amount of dust to a dust-free population. On the contrary, galaxies with $SFR_{fit} < SFR_{IR+UV}$ could be dusty star forming galaxies fitted with a dust-free SED. Moreover, in this case the higher IR emission could be caused by processes not visible in UV/optical wavelengths.

Masses and M/L ratios Stellar masses are calculated as the product of the mass to light ratio M/L with the luminosity L. Uncertainties on L come from data quality, those on stellar masses depend on SED fitting. To minimize the errors upon stellar masses we can choose a reference band in which dust absorption and stellar populations properties, like age and metallicity, do not have strong effects on M/L.

NIR wavelengths (H band, 1.65 μm) are in general used to estimate stellar masses, especially because they are the most useful to constrain metallicities allowing to investigate possible degeneracies between Z and M/L.

Many uncertainties affect the M/L derivation. One of the most important is represented by the stellar evolutionary phases, examined for the first time by Maraston et al. (2006).

Different SPMs models take into account different libraries and approximations and so, predict different results.

Figure 1.18 shows a comparison of M/L from different models in different bands. The bolometric M/L from BC03 are larger than Maraston's ones because of the more delayed development of the RGB phase in Padova tracks, used in BC03, than BaSTI ones, used in Ma05. Due to the fact that in BC03 the contribution of TP-AGB is very low, these models infer larger values of $(M/L)_K$ for younger ages. At older ages, the $(M/L)_K$ estimates are instead smaller probably because of the cooler temperatures for RGB stars when compared to the Maraston's treatment.

$(M/L)_{bol}$ and $(M/L)_K$ by Worthey et al. (1994) are smaller because of larger bolometric and NIR luminosities. In general models from Vazdekis et al. (1996) are similar to the BC03 ones since they use the same isochrone tracks.

In general M/L ratios estimations from SED fitting are accurate at the ~ 0.3 dex level for a fixed IMF.

Figure 1.19 displays the stellar mass of an evolving stellar population with initial mass $M > 1M_{\odot}$ and solar metallicity, from Ma05 and BC03 models. Solid lines identify the model adopting the Salpeter IMF, while the dotted lines models adopting the Kroupa IMF. Considering a Salpeter IMF, in 15 Gyr the stellar mass decreases of a factor of roughly 30 %. On the contrary, due to the less power in the low mass range of the Kroupa IMF, models predict smaller stellar masses.

In general, low redshift galaxies are characterized by more uncertain M/L ratios, due to the different TP-AGB phase treatments included in different models.

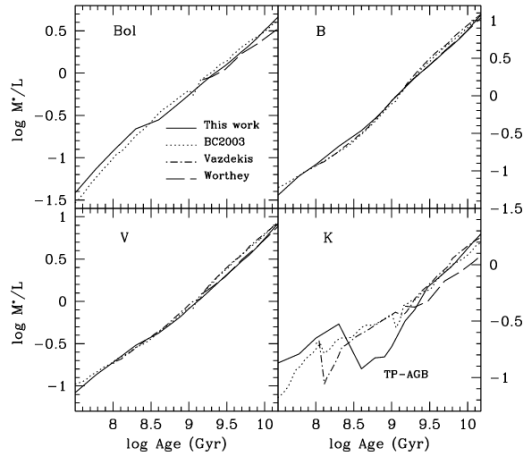

Figure 1.18: M/L from different models in various bands (Maraston, 2005).

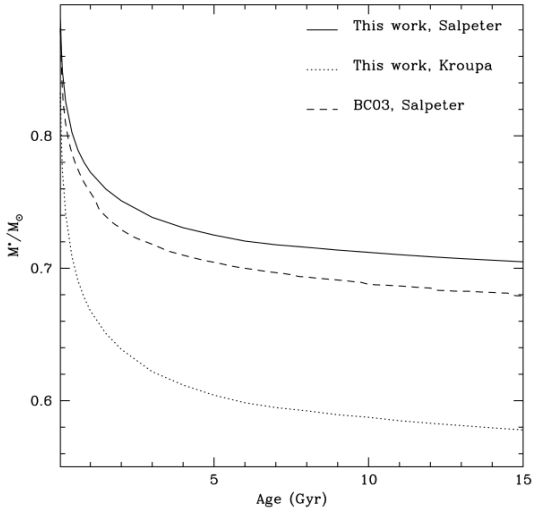

Figure 1.19: Total stellar mass from Ma05 and BC03 models. (Maraston, 2005)

On the contrary, M/L ratios for high redshift galaxies suffer of the uncertainties caused by the SFH forms.

Galaxies with high SFRs could have a population of "hidden" older stars with high M/L ratios. Different SFH functional forms give different estimates of M/L. For example with a two component SFH (young+old), we have larger stellar masses than the one estimated using a one component SFH model (Papovich et al., 2001).

Chapter 2

Horizontal Branch morphology: A new photometric parametrization

In the analysis of resolved stellar populations, we firstly decided to deeply investigate one of the main stellar evolutionary stages, namely the HB phase, in which old stars are burning helium in their core and hydrogen in a shell. The HB luminosity level together with the MSTO offers a fundamental tool to analyse and estimate the age of Globular Clusters, giving us the opportunity to put a lower limit to the age of the Universe.

In particular, we define a new photometric HB morphology index, overcoming some of the limitations and degeneracies affecting similar indices available in the literature (e.g., HB ratio, Chapter 1). Moreover, we analyse the 2nd Parameter problem (Chapter 1), i.e., the observed variation of HB morphologies in clusters with similar ages. The results presented in this Chapter have been published in Torelli et al. (2019).

Abstract Theory and observations indicate that the distribution of stars along the horizontal branch of Galactic globular clusters mainly depends on the metal content. However, the existence of globular clusters with similar metal content and absolute age but different horizontal branch morphologies, suggests the presence of another parameter affecting the star distribution along the branch.

To investigate the variation of the horizontal branch morphology in Galactic globular clusters, we define a new photometric horizontal branch morphology index, overcoming some of the limitations and degeneracies affecting similar indices available in the literature. We took advantage of a sample of 64 Galactic globular clusters, with both space-based imaging data (*Advanced Camera for Surveys survey of Galactic globular clusters*) and homogeneous ground-based photometric catalogues in five different bands (U,B,V, R, I). The new index, τ_{HB}, is defined as the ratio between the areas subtended by the cumulative number distribution in magnitude (I) and in colour (V–I) of all stars along the horizontal branch. This new index shows a linear trend over the entire range in metallicity (-2.35

≤ [Fe/H] ≤ -0.12) covered by our Galactic globular cluster sample. We found a linear relation between τ_{HB} and absolute cluster ages. We also found a quadratic anti-correlation with [Fe/H], becoming linear when we eliminate the age effect on τ_{HB} values. Moreover, we identified a subsample of eight clusters that are peculiar according to their τ_{HB} values. These clusters have bluer horizontal branch morphology when compared to typical ones of similar metallicity. These findings allow us to define them as the 'second parameter' clusters in the sample. A comparison with synthetic horizontal branch models suggests that they cannot be entirely explained with a spread in helium content.

2.1 Introduction

Globular clusters are stellar systems that play a fundamental role in constraining the formation and evolution of galaxies (Searle & Zinn, 1978; VandenBerg et al., 2013; Leaman et al., 2013) and cosmological parameters. Dating back more than half a century (Sandage, 1953), the absolute ages of Galactic globular clusters (GGCs) have been used to provide a lower limit to the age of the Universe (see e.g. Salaris & Weiss, 2002; Dotter et al., 2011; Monelli et al., 2015; Richer et al., 2013, and references therein) and estimate of the primordial helium abundance (see e.g. Zoccali et al., 2000; Salaris & Cassisi, 2005; Villanova et al., 2012). GGCs are also laboratories to investigate evolutionary (Chaboyer et al., 2017; Dotter et al., 2007; Brown et al., 2010; Weiss et al., 2004) and pulsational (Bono & Stellingwerf, 1994; Bono et al., 1999; Marconi et al., 2015) properties of old, low-mass stars. In this context, advanced evolutionary phases (red giant [RGs] and horizontal branch [HB] stars) have several advantages when compared with main sequence (MS) stars. They are a few magnitudes brighter and within the reach of spectroscopic investigations at the 8-10m class telescopes. This means that they can be used for investigating the cluster dynamical evolution and interaction with the Galactic potential (Pancino et al., 2007; Zocchi et al., 2017; Calamida et al., 2017; Lanzoni et al., 2018). Moreover, their chemical abundances (iron peak, α-, neutron capture elements) can be measured with high accuracy both in the optical (Carretta et al., 2014) and in the near-infrared (NIR) regime (D'Orazi et al., 2018).

Despite a general consistency between theory and observations concerning hydrogen and helium burning phases, we continue to face a number of long-standing open questions. Amongst them the morphology of the HB plays a pivotal role. Stars along the HB are low-mass (M ≈ 0.50-0.80 $\mathbf{M}_{\odot}$), core-helium-burning stars and their distribution along the HB depends, at fixed initial chemical composition, on their envelope mass. Indeed, the envelope mass when moving from the red HB (RHB) to the extreme HB (EHB) decreases from M_{env} ≈0.30 $\mathbf{M}_{\odot}$ to M_{env} ≈0.0001 $\mathbf{M}_{\odot}$, while the effective temperature increases from ≈ 5,500 **K** to ≈30,000 **K**.

The current empirical and theoretical evidence indicates that the HB morphology is affected by the initial metal content. Metal-poor clusters are mainly char-

acterized by a blue HB morphology. This means that in these clusters HB stars are mainly distributed along the blue, hot, and extremely hot region. Metal-rich GGCs are generally characterized by a red HB morphology, that is, HB stars in these clusters are mainly distributed in the red (cool) region.

Although this theoretical and empirical framework appears well established, there is solid evidence that GGCs with similar chemical compositions display different HB morphologies. This suggests that the HB morphology was affected by at least a 'second parameter' (see. e.g. Sandage & Wildey, 1967, and references therein). This problem was defined as the 'second parameter problem' and the clusters affected by this problem were called second parameter clusters.

During the last half-century several working hypotheses have been suggested to explain the second parameter problem. They include variations of the initial helium content (van den Bergh, 1967; Sandage & Wildey, 1967), dynamical effects related to the cluster mass (e.g. Recio-Blanco et al., 2006), the cluster age (e.g. Searle & Zinn, 1978), dynamical evolution (e.g. Iannicola et al., 2009), or a combination of two or more of these – for example age and/or metallicity plus helium content, as suggested by Freeman & Norris (1981); Gratton et al. (2010).

To quantify the extent of this second parameter problem, Lee (1989); Lee et al. (1994) suggested an HB morphology index based on star counts along the HB. It is defined as the difference between the number of stars that are bluer (B) and redder (R) than the RR Lyrae (RRL) instability strip, divided by the sum of the number of blue, red, and variable (V) stars: $HBR = \frac{B-R}{B+R+V}$. This HB morphology index has been quite popular, because it can be easily estimated from the theoretical and the observational point of view (star counts). However, it is prone to intrinsic degeneracies in both the metal-poor and the metal-rich regimes, in the sense that when the observed HB is bluer or redder than the RRL strip, HBR stays constant, irrespectively of the exact distribution of stars along the HB.

Similar HB morphology indices have been suggested in the literature, but using different cuts in colour. In particular, Buonanno (1993) suggested splitting HB stars bluer than the RRL instability strip into two blocks: stars hotter than the RRL instability strip and cooler than $(B\text{-}V)$=-0.02 were called B1, while those hotter than $(B\text{-}V)$=-0.02 were called B2. The new index had the key advantage of removing the degeneracy of the HBR index in the metal-poor regime, but it was still affected by degeneracies in the metal-rich regime.

Considering that almost all GGCs show the presence of multiple populations, Milone et al. (2014) introduced two new indices for describing the HB morphology. L1 is the difference in colour between the red giant branch (RGB) and the coolest red point of the HB, while L2 is the colour extension of the HB. These two indices allowed the authors to identify three different GGC groups from the L1-[Fe/H] diagram, and to find correlations of L1 with cluster age and metallicity. In addition, they found a variation of L2 with cluster luminosity (mass) and with helium content. This latter correlation is connected with the presence of multiple

populations in globular clusters and it could be an additional ingredient to explain the HB colour extension. These two parameters are interesting, because they are correlated with the physics characterizing the HB stars. However, their definition seems to be very sensitive to the choice of the key points selected in colour magnitude diagrams (HB luminosity level, RGB).

In this work, we introduce a new HB morphology index based on the ratio between the areas subtended by the cumulative number distribution (CND) of star counts along the observed cluster HB in magnitude (I-band) and in colour (V–I): $\tau_{HB} = A_{CND}(I)/A_{CND}(V–I)$. This new index has been calculated in a large sample (64) of GGCs, for which both space- and ground-based optical photometric catalogues are available. For the same sample of GGCs, we have also estimated the classical ***HBR*** index and performed a detailed comparison with τ_{HB}. We present evidence that our new index, in contrast with similar indices available in the literature, shows a well-defined correlation with cluster age and an anti-correlation with cluster iron abundance.

The structure of the chapter is the following. We present in Sect. 2.2 our sample of GGCs with their photometric coverage. We also describe the method adopted for the separation between candidate cluster and field stars based on the comparison of star spectral energy distributions (SEDs). Section 2.3 deals with the classical HB morphology index ***HBR***. We analyse its pros and cons and calculate its values for the entire cluster sample, together with its dependence on age and metallicity, while in Sect. 2.4 we do the same analysis for the L1 and L2 indices. In Sect. 2.5 we introduce our new HB morphology index, τ_{HB}, calculate its values for our GGC sample, and discuss pros and cons compared to ***HBR***. In Sect. 2.6 we analyse and compare the relative difference between the classical HB morphology index and τ_{HB} estimates when considering just space- or just ground-based observations. The correlation of our new index with the absolute age and the metallicity of the individual clusters is addressed in Sect. 2.7. Here we also identify the second parameter clusters in our sample that show very different estimates in τ_{HB} compared to the ones attained by globulars with similar [Fe/H] values. In Sect. 2.8 we compare τ_{HB} with synthetic HB models specifically computed for this work. The summary of the results and a brief discussion concerning future developments of the project are outlined in Sect. 2.9. In Appendix C we list specific information on individual GGCs for which the photometric properties are uncertain either due to the lack of ground-based or space-based data, because the photometry does not cover the entire cluster area (tidal radius), or because of the small number of HB stars. In Appendix D we also included a few notes for the GGCs we defined as 'outliers' in the analysis of the HB morphology.

2.2 Globular cluster sample

In this work we use a sample of 64 GGCs for which optical images are available from both space-based (Advanced Camera for Surveys (ACS)/Wide Field Channel (WFC) on board the Hubble Space Telescope (*HST*)) and ground-based observations. The relevant parameters for our cluster sample are listed in Table 2.1. We took advantage of the photometric catalogues provided by Sarajedini et al. (2007); Dotter et al. (2011) in the context of the Hubble Space Telescope Treasury project, *An ACS Survey of Galactic Globular Clusters* [1]. This survey is based on a single ACS pointing across the centre of each cluster, observed through two complete orbits, one for the $F606W$ ($\sim V$) and one for the $F814W$ ($\sim I$). Cluster NGC 6715 represents an exception since it was observed for two orbits in each filter (Anderson et al., 2008). Thanks to these data we can avoid the crowding problems in the central regions of the clusters (the red region in Fig. 2.1 shows the field coverage for one of the globulars in the sample, NGC 5053) and reach very faint magnitudes ($I \sim 26.0$, see ACS colour-magnitude diagram (CMD) in Fig. 2.2).

To cover a significant fraction of the body of each cluster we adopted the multi-band (U, B, V, R, I) optical catalogues provided by one of the authors (PBS, see for example Stetson et al., 2005, 2014a, 2019), based on images collected with several ground-based telescopes. The ground-based data allow us to reach the tidal radius for most of the globulars. The blue line in Fig. 2.1 shows the tidal radius of NGC 5053. There are a few clusters (see Appendix C) for which we cannot reach the tidal radius with our data while still covering the main body of the cluster. For 47 GGCs we have data in all available photometric bands from both space- and ground-based facilities.

Thanks to the fact that all the clusters in the sample have data in B, V, I bands (except for NGC 6426, NGC 6624, NGC 6652, Lynga 7, and Palomar 2, see Appendix C), we based the cluster and field stars' separation on the SED of the stars in these bands, following the procedure described in Di Cecco et al. (2015); Calamida et al. (2017). We selected first the bona fide cluster stars considering only the central region, since we expect that it is less contaminated by field stars. Then we compared the SEDs of these stars to the ones in the total catalogue, to separate cluster stars from the field. We note that for stars with space data only we did not make any selection, because we expect negligible contamination by field stars in the ACS field of view (FoV). Therefore, in this case we took advantage of the entire ACS catalogues.

Moreover, when we had measurements in the V and I bands from both ACS and ground-based telescopes, we preferred the first ones for their higher signal-to-noise ratio (S/N) values. We used the ACS coverage for the central region of our globulars within the ACS FoV ($\sim 4arcmin$), while outside up to the tidal radius we adopted the ground-based observations.

[1] *Photometry available at* https://www.astro.ufl.edu/~ata/public_hstgc/

Table 2.1: Globular Clusters in the sample with parameters used in this work.

ID	Name	Ra (J2000)[(a)]	Dec (J2000)[(a)]	*U*	*B*	*V*	*R*	*I*	*F606W*	*F814W*	$r_t(')^{(a)}$	HBR[(a)]	Age(Gyr)[(b)]	E(B-V)[(c)]	[Fe/H][(d)]	$\mu^{(b)}$
NGC 0104	47 Tuc	00:24:05.67	-72:04:52.6	✓	✓	✓	✓	✓	✓	✓	42.9	-0.99	11.75 ± 0.25	0.03	-0.76 ± 0.02	13.25
NGC 0288		00:52:45.24	-26:34:57.4	✓	✓	✓	✓	✓	✓	✓	12.9	0.98	11.50 ± 0.38	0.01	-1.32 ± 0.02	14.87
NGC 0362		01:03:14.26	-70:50:55.6	✓	✓	✓	✓	✓	✓	✓	16.1	-0.87	10.75 ± 0.25	0.03	-1.30 ± 0.04	14.70
NGC 1261		03:12:16.21	-55:12:58.4	✓	✓	✓	✓	✓	✓	✓	7.3	-0.71	10.75 ± 0.25	0.01	-1.27 ± 0.08	16.02
NGC 1851		05:14:06.76	-40:02:47.6	✓	✓	✓	✓	✓	✓	✓	11.7	-0.36	11.00 ± 0.38	0.04	-1.18 ± 0.08	15.31
NGC 2298		06:48:59.41	-36:00:19.1	✓	✓	✓	✓	✓	✓	✓	6.5	0.93	-	0.22	-1.96 ± 0.04	-
NGC 3201		10:17:36.82	-46:24:44.9	✓	✓	✓	✓	✓	✓	✓	28.5	0.08	11.50 ± 0.38	0.26	-1.51 ± 0.02	13.29
NGC 4147		12:10:06.30	+ 18:32:33.5	✓	✓	✓	✓	✓	✓	✓	6.3	0.55	12.25 ± 0.25	0.03	-1.78 ± 0.08	16.33
NGC 4590	M 68	12:39:27.98	-26:44:38.6	✓	✓	✓	✓	✓	✓	✓	30.3	0.17	12.00 ± 0.25	0.06	-2.27 ± 0.04	16.05
NGC 4833		12:59:33.92	-70:52:35.4	✓	✓	✓	✓	✓	✓	✓	17.9	0.93	12.50 ± 0.50	0.33	-1.89 ± 0.05	-
NGC 5024	M 53	13:12:55.25	+18:10:05.4	✓	✓	✓	✓	✓	✓	✓	21.8	0.81	12.25 ± 0.25	0.03	-2.06 ± 0.09	16.31
NGC 5053		13:16:27.09	+17:42:00.9	✓	✓	✓	✓	✓	✓	✓	13.7	0.50	12.25 ± 0.38	0.02	-2.30 ± 0.08	16.19
NGC 5272	M 3	13:42:11.62	+28:22:38.2	✓	✓	✓	✓	✓	✓	✓	38.2	0.08	11.75 ± 0.25	0.01	-1.50 ± 0.05	14.99
NGC 5286		13:46:26.81	-51:22:27.3	✓	✓	✓	✓	✓	✓	✓	8.4	0.80	12.25 ± 0.38	0.29	-1.70 ± 0.07	15.04
NGC 5466		14:05:27.29	+28:32:04.0	✓	✓	✓	✓	✓	✓	✓	34.2	0.58	12.50 ± 0.25	0.02	-2.31 ± 0.09	16.09
NGC 5904	M 5	15:18:33.22	+02:04:51.3	✓	✓	✓	✓	✓	✓	✓	28.4	0.31	11.50 ± 0.25	0.04	-1.33 ± 0.02	14.26
NGC 5927		15:28:00.69	-50:40:22.9	✓	✓	✓	✓	✓	✓	✓	16.7	-1.00	10.75 ± 0.38	0.51	-0.29 ± 0.07	14.20
NGC 5986		15:46:03.00	-37:47:11.1	✓	✓	✓	✓	✓	✓	✓	10.5	0.97	12.25 ± 0.75	0.34	-1.63 ± 0.08	-
NGC 6093	M 80	16:17:02.41	-22:58:33.9	✓	✓	✓	✓	✓	✓	✓	13.28	0.93	-	0.21	-1.75 ± 0.08	-
NGC 6101		16:25:48.12	-72:12:07.9	✓	✓	✓	✓	✓	✓	✓	7.3	0.84	12.25 ± 0.50	0.10	-1.98 ± 0.07	-
NGC 6121	M 4	16:23:35.22	-26:31:32.7	✓	✓	✓	✓	✓	✓	✓	32.5	-0.06	11.50 ± 0.38	0.50	-1.18 ± 0.02	11.07
NGC 6144		16:27:13.86	-26:01:24.6		✓	✓	✓	✓	✓	✓	33.3	1.00	12.75 ± 0.50	0.71	-1.82 ± 0.05	-
NGC 6171	M 107	16:32:31.86	-13:03:13.6	✓	✓	✓	✓	✓	✓	✓	17.4	-0.73	12.00 ± 0.75	0.45	-1.03 ± 0.02	13.43
NGC 6205	M 13	16:41:41.24	+36:27:35.5	✓	✓	✓	✓	✓	✓	✓	25.2	0.97	12.00 ± 0.38	0.02	-1.58 ± 0.04	14.39
NGC 6218	M 12	16:47:14.18	-01:56:54.7	✓	✓	✓	✓	✓	✓	✓	17.6	0.97	13.00 ± 0.50	0.17	-1.33 ± 0.02	13.52
NGC 6254	M 10	16:57:09.05	-04:06:01.1	✓	✓	✓	✓	✓	✓	✓	21.5	1.00	11.75 ± 0.38	0.29	-1.57 ± 0.02	-
NGC 6304		17:14:32.25	-29:27:43.3						✓	✓	13.3	-1.00	11.25 ± 0.38	0.52	-0.37 ± 0.07	13.81
NGC 6341	M 92	17:17:07.39	+43:08:09.4	✓	✓	✓	✓	✓	✓	✓	15.2	0.91	12.75 ± 0.25	0.02	-2.35 ± 0.05	14.66
NGC 6352		17:26:29.11	-48:25:19.8		✓	✓		✓	✓	✓	10.5	-1.00	10.75 ± 0.38	0.35	-0.62 ± 0.05	13.36
NGC 6362		17:31:54.99	-67:02:54.0		✓	✓	✓	✓	✓	✓	16.7	-0.58	12.50 ± 0.25	0.07	-1.07 ± 0.05	14.36
NGC 6366		17:27:44.24	-05:04:47.5	✓	✓	✓	✓	✓	✓	✓	15.2	-0.97	11.00 ± 0.50	0.75	-0.59 ± 0.08	12.40
NGC 6388		17:36:17.23	-44:44:07.8		✓	✓		✓	✓	✓	6.2	-	-	0.41	-0.45 ± 0.04	-
NGC 6397		17:40:42.09	-53:40:27.6	✓	✓	✓	✓	✓	✓	✓	15.8	1.00	13.00 ± 0.25	0.19	-1.99 ± 0.02	-
NGC 6426		17:44:54.65	+03:10:12.5						✓	✓	13.2	0.58	-	0.35	-2.15	-
NGC 6441		17:50:13.06	-37:03:05.2	✓	✓	✓	✓	✓	✓	✓	8.0	-	-	0.61	-0.44 ± 0.07	-
NGC 6496		17:59:03.68	-44:15:57.4	✓	✓	✓	✓	✓	✓	✓	5.3	-1.00	10.75 ± 0.38	0.23	-0.46 ± 0.07	14.93
NGC 6535		18:03:50.51	-00:17:51.5	✓	✓	✓		✓	✓	✓	8.4	1.00	12.75 ± 0.50	0.41	-1.79 ± 0.07	13.88
NGC 6541		18:08:02.36	-43:42:53.6	✓	✓	✓		✓	✓	✓	29.6	1.00	12.50 ± 0.50	0.16	-1.82 ± 0.08	-
NGC 6584		18:18:37.60	-52:12:56.8		✓	✓	✓	✓	✓	✓	9.4	-0.15	11.75 ± 0.25	0.11	-1.50 ± 0.09	15.54
NGC 6624		18:23:40.51	-30:21:39.7						✓	✓	20.6	-1.00	11.25 ± 0.50	0.26	-0.42 ± 0.07	14.47
NGC 6637	M 69	18:31:23.10	-32:20:53.1		✓	✓		✓	✓	✓	8.4	-1.00	11.00 ± 0.38	0.17	-0.59 ± 0.07	14.70
NGC 6652		18:35:45.63	-32:59:26.6			✓		✓	✓	✓	4.5	-1.00	11.25 ± 0.25	0.11	-0.76 ± 0.14	14.90
NGC 6656	M 22	18:36:23.94	-23:54:17.1	✓	✓	✓	✓	✓	✓	✓	29.0	0.91	12.50 ± 0.50	0.33	-1.70 ± 0.08	-
NGC 6681	M 70	18:43:12.76	-32:17:31.6	✓	✓	✓	✓	✓	✓	✓	7.9	0.96	12.75 ± 0.38	0.11	-1.62 ± 0.08	14.78
NGC 6717	Pal 9	18:55:06.04	-22:42:05.3		✓	✓	✓	✓	✓	✓	9.9	0.98	12.50 ± 0.50	0.25	-1.26 ± 0.07	14.17
NGC 6723		18:59:33.15	-36:37:56.1		✓	✓		✓	✓	✓	10.5	-0.08	12.25 ± 0.25	0.16	-1.10 ± 0.07	14.23
NGC 6752		19:10:52.11	-59:59:04.4	✓	✓	✓	✓	✓	✓	✓	55.3	1.00	12.50 ± 0.25	0.06	-1.55 ± 0.01	-
NGC 6779	M 56	19:16:35.57	+30:11:00.5	✓	✓	✓	✓	✓	✓	✓	8.6	0.98	12.75 ± 0.50	0.25	-2.00 ± 0.09	-
NGC 6809	M 55	19:39:59.71	-30:57:53.1	✓	✓	✓	✓	✓	✓	✓	16.3	0.87	13.00 ± 0.25	0.09	-1.93 ± 0.02	13.62
NGC 6838	M 71	19:53:46.49	+18:46:45.1	✓	✓	✓	✓	✓	✓	✓	9.0	-1.00	11.00 ± 0.38	0.33	-0.82 ± 0.02	12.67
NGC 6934		20:34:11.37	+07:24:16.1	✓	✓	✓	✓	✓	✓	✓	8.4	0.25	11.75 ± 0.25	0.11	-1.56 ± 0.09	16.05
NGC 6981	M 72	20:53:27.70	-12:32:14.3	✓	✓	✓	✓	✓	✓	✓	9.2	0.14	11.50 ± 0.25	0.06	-1.48 ± 0.07	16.05
NGC 7006		21:01:29.38	+16:11:14.4	✓	✓	✓	✓	✓	✓	✓	6.3	-0.28	-	0.08	-1.46 ± 0.06	-
NGC 7078	M 15	21:29:58.33	+12:10:01.2	✓	✓	✓	✓	✓	✓	✓	21.5	0.67	12.75 ± 0.25	0.11	-2.33 ± 0.02	15.03
NGC 7089	M 2	21:33:27.02	-00:49:23.7	✓	✓	✓	✓	✓	✓	✓	21.5	0.96	11.50 ± 0.25	0.04	-1.66 ± 0.07	15.41
NGC 7099	M 30	21:40:22.12	-23:10:47.5	✓	✓	✓	✓	✓	✓	✓	18.3	0.89	13.00 ± 0.25	0.05	-2.33 ± 0.02	14.60
ARP 2		19:28:44.11	-30:21:20.3	✓	✓	✓		✓	✓	✓	12.7	0.86	12.00 ± 0.38	0.11	-1.74 ± 0.08	17.25
IC 4499		15:00:18.45	-82:12:49.3	✓	✓	✓	✓	✓	✓	✓	12.4	0.11	-	0.22	-1.62 ± 0.09	-
Lynga 7		16:11:03.65	-55:19:04.0						✓	✓	-	-1.00	-	1.06	-	-
Pal 2		04:46:05.91	+31:22:53.4		✓	✓	✓	✓	✓	✓	6.8	-	-	1.21	-1.29 ± 0.09	-
Rup 106		12:38:40.2	-51:09:01		✓	✓	✓	✓	✓	✓	5.0	-0.82	-	0.17	-1.78 ± 0.08	-
Terzan 7		19:17:43.92	-34:39:27.8		✓	✓	✓	✓	✓	✓	7.3	-1.00	-	0.09	-0.12 ± 0.08	-
Terzan 8		19:41:44.41	-33:59:58.1	✓	✓	✓	✓	✓	✓	✓	4.0	1.00	13.00 ± 0.38	0.15	-	17.14

Notes: List of the Globular Clusters in the sample with parameters used in this work: J 2000 coordinates, data availability in ground-based and space-based bands, tidal radius in arcmin, *HBR* index, Age in Gyr, colour excess E(B-V), [Fe/H], apparent visual distance modulus μ.

References: (a)Harris (1996);(b)VandenBerg et al. (2013);(c)Dutra & Bica (2000); (d)Carretta et al. (2009).

An example of our selection is shown in Fig. 2.3, which displays the V, B–I CMD of NGC 5286 for total (left panel), cluster (central panel), and field (right panel) stars. We can appreciate from the figure that the joint catalogues allow us to cover the entire evolution of the stars in the globulars, from the faint part of the MS to the brighter region of the RGB-tip and asymptotic giant branch (AGB) in the CMD.

2.3 The *HBR* morphology index

As already discussed in Sect. 2.1, the traditional HB morphology index is defined as

$$HBR = \frac{B - R}{B + R + V}, \tag{2.1}$$

where B is the number of HB stars bluer than the blue (hot) edge of the RRL instability strip, V is the number of RR Lyrae stars, and R is the number of HB stars redder than the red (cold) edge of the RRL instability strip. This HB morphology index has several advantages when compared with other observables (HB luminosity level, colour distribution) connected with the helium burning phases.

First, when considered with the comparison between predicted and observed HB luminosity levels, HB star counts are independent of uncertainties affecting the cluster distance and are minimally affected by uncertainties in cluster reddening and the possible occurrence of differential reddening. Moreover, the comparison between the predicted and observed number of HB stars is less prone to uncertainties affecting the transformations of theoretical predictions into the observational plane.

In the comparison between theory and observations, the HBR index accounts for the global distribution of stars along the HB. On the other hand, the comparison between the predicted and observed HB luminosity levels is mainly restricted to the RRL instability strip, that is, the truly horizontal region of the HB. However, a minor fraction of GGCs hosts a sizeable sample of RRLs to properly define the HB luminosity level.

One of the main cons of the HBR index is that it describes a global property of HB stars. This means that it does not trace the detailed stellar distribution along the HB. It is also affected by severe degeneracies both in the metal-poor and in the metal-rich regimes. This means that a significant fraction of GGCs attain values close either to 1 (blue HB morphology) or to -1 (red HB morphology), irrespective of the exact colour distribution of stars.

Despite the stated limitations we calculated values of the HBR index for our GGC sample. For each cluster we defined two boxes including candidate blue (B) and red (R) HB stars. The colour ranges for the boxes were fixed using either predicted or empirical edges for the RRL instability strip. Stars located in the

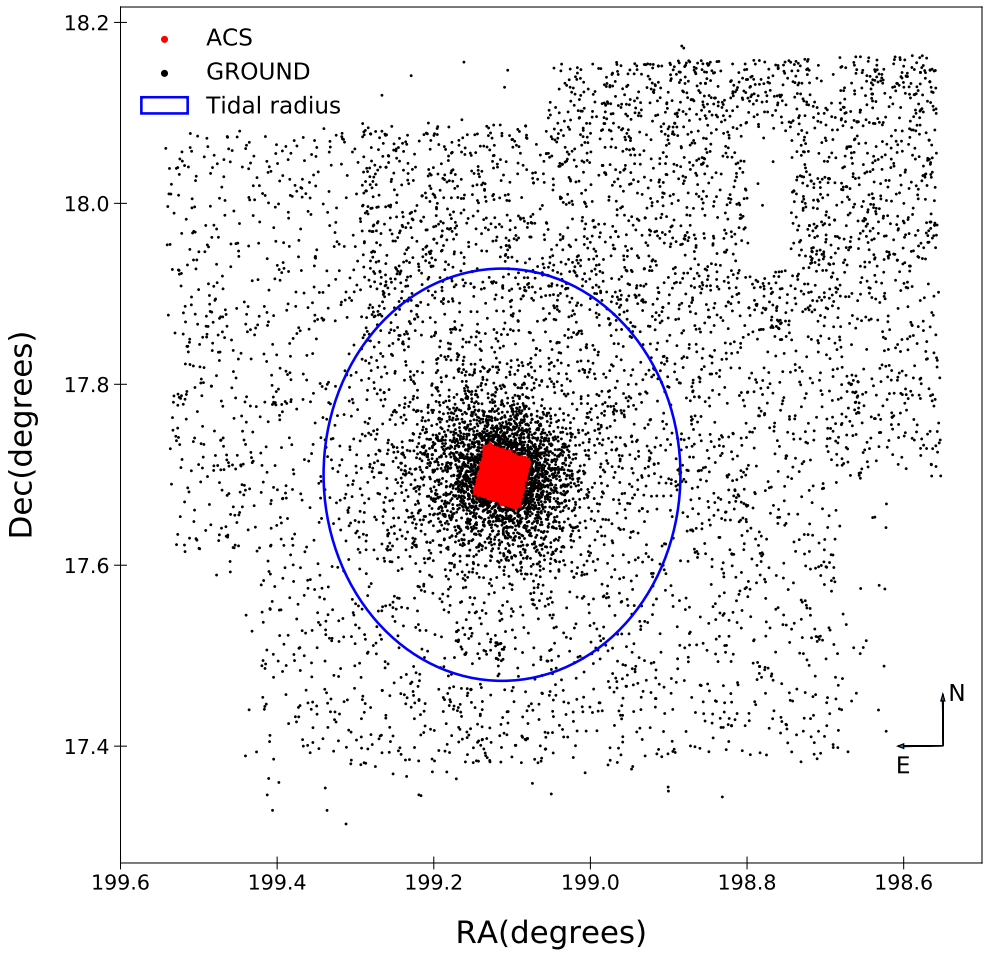

Figure 2.1: Sky distribution of ground-based (black dots) and space-based (red dots) data for the cluster NGC 5053. North is up and east is to the left.

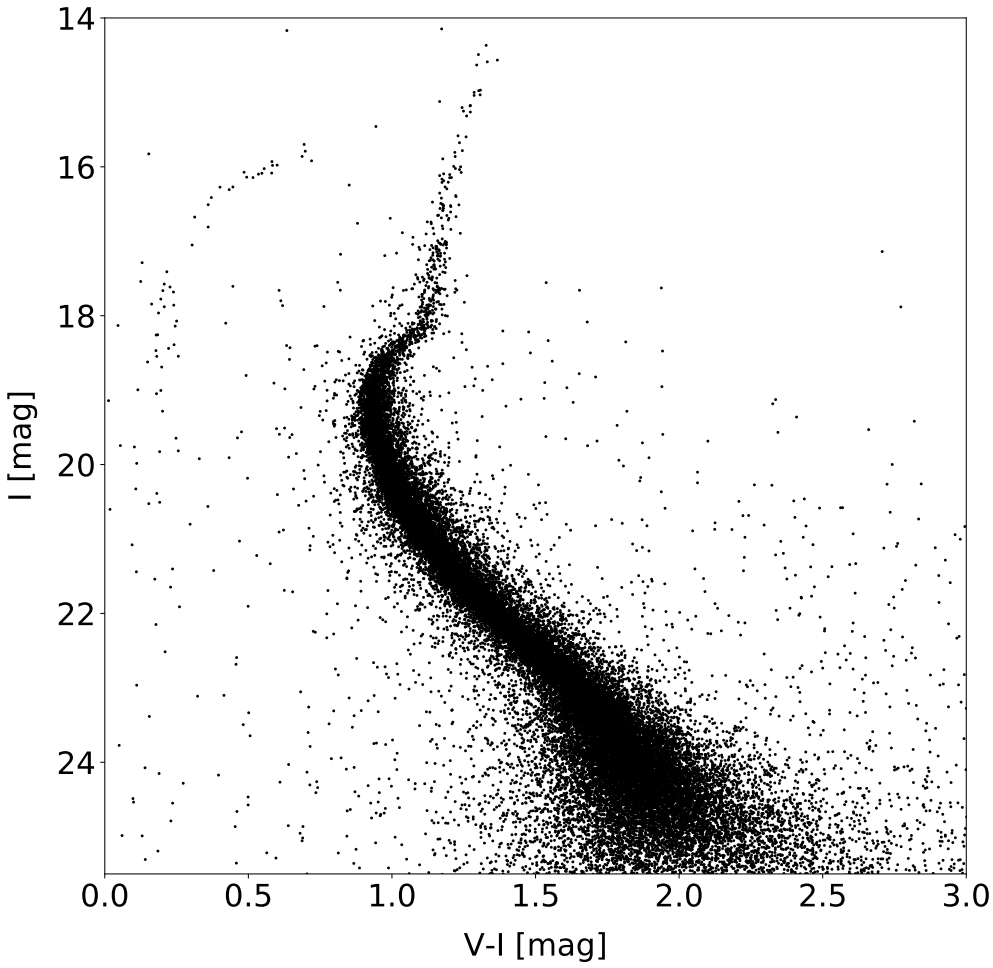

Figure 2.2: Cluster NGC 5286 *I*, *V–I* CMD based only on ACS-*HST* data.

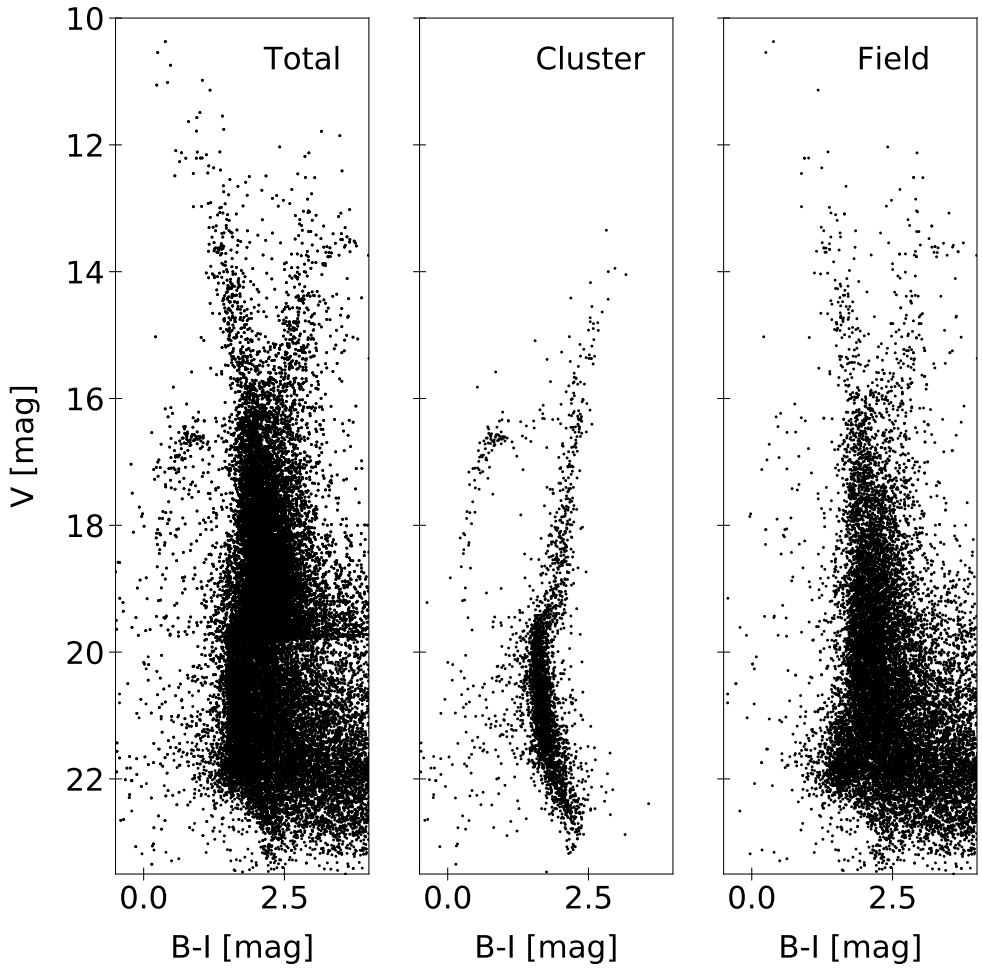

Figure 2.3: Cluster NGC 5286 V, B–I CMD. The left panel shows all stars. The central panel shows our candidate cluster stars. The right panel shows the candidate field stars. Candidate cluster and field stars have been selected following the method described in the main text.

RRL instability strip were neglected. To account for the number of variables we took advantage of the Clement catalogue of variable stars in GGCs. This catalogue was originally presented in Clement et al. (2001), but it is constantly updated[1]. For each cluster, it gives the number of variable stars together with their main pulsation parameters: pulsation period, mean magnitude and colour, and luminosity amplitude. For our analysis we took into account only confirmed cluster RRL stars, meaning that candidate cluster RRLs were not included.

Throughout our analysis, we adopted the homogeneous metallicity scale provided by Carretta et al. (2009). The authors estimated the iron abundances from high resolution spectra collected with the Fibre Large Srray Multi Element Spectrograph (FLAMES) at the Very Large Telescope (VLT), covering the entire metallicity range of GGCs. To increase the sample size they also re-calibrated the most common metallicity scales available in the literature (Zinn & West, 1984; Kraft & Ivans, 2003; Carretta & Gratton, 1997). For two clusters in our sample (NGC 6624 and Lynga 7) we adopted the metallicity estimate available in the 2010 version of the Harris (1996) catalogue[2].

To validate the current estimates of the HBR index with similar estimates available in the literature, Fig. 2.4 shows the comparison of our values with those provided by Harris in the 2003 version of his catalogue (Harris, 1996). Data plotted in this figure show that both sets agree well over the entire metallicity range. Indeed, the difference is on average smaller than 20%. There are a few outliers (NGC 1851 and NGC 4590) for which the difference is approximately 30%-40%, but they are affected by a higher field-star contamination than the others, despite our homogeneous cluster and field star separation. For each GGC in our sample, Table 2.2 gives its name (columns 1 and 2), the metallicity (column 3), and the number of blue (B) and red (R) stars (columns 4 and 5). In column 6 the values of the HBR' index, defined as $HBR' = HBR + 2$, are listed. The reason for this change is the following. From Fig. 2.4 we can see that the errors on the HBR index are small and not realistic. We define the uncertainty of the measured HBR as

$$\sigma(HBR) = \frac{B-R}{B+R+V} \cdot \left(\frac{1}{\sqrt{B-R}} + \frac{1}{\sqrt{B+R+V}} \right), \tag{2.2}$$

which takes into account the Poisson uncertainties in the star counts. The errors provided by this formula vanish as soon as B and R attain similar values, that is when HBR approaches zero. This is an intrinsic limitation affecting the definition of the HBR index. To overcome this problem we decided to use HBR'.

To investigate the dependence of the HB morphology on intrinsic cluster parameters, Fig. 2.5 shows the HBR' index as a function of iron content for the current sample. Data plotted in this figure display some well established correlations. The HB morphology becomes systematically redder when moving from metal-poor to

[1] http://www.astro.utoronto.ca/~cclement/cat/listngc.html
[2] http://physwww.mcmaster.ca/~harris/mwgc.dat

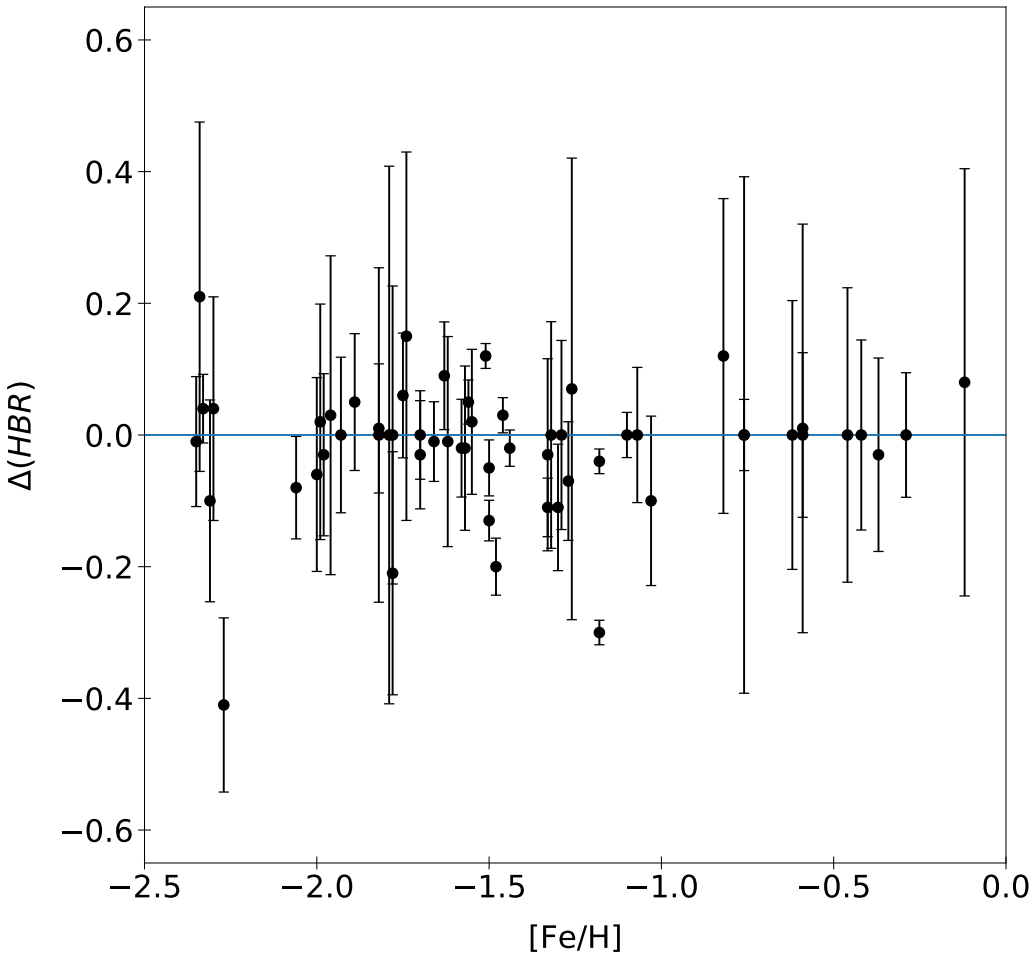

Figure 2.4: Difference between Harris (1996) values (2003 version) for *HBR* and our measurements as a function of [Fe/H].

Table 2.2: Parameters and observational HB morphology indices for the GGCs in the sample.

ID	Name	[Fe/H]	B	R	HBR'	L1[(a)]	L2[(a)]	∂Y[(b)]	V(HB)[(c)]	CND (V-I)	τ_{HB}
NGC 0104	47 Tuc	-0.76	0	1336	1.01 ± 0.04	0.078 ± 0.005	0.068 ± 0.006	0.049 ± 0.005	14.06	137.9 ± 11.7	1.58 ± 0.01
NGC 0288		-1.32	130	0	2.98 ± 0.12	0.534 ± 0.086	0.337 ± 0.086	0.016 ±0.012	15.44	47.8 ± 6.9	9.39 ± 0.37
NGC 0362		-1.30	12	282	1.24 ± 0.07	0.086 ± 0.005	0.608 ± 0.064	0.026 ±0.008	15.44	126.1 ± 11.2	3.24 ± 0.01
NGC 1261		-1.27	35	201	1.36 ± 0.06	0.088 ± 0.005	0.644 ± 0.038	0.019 ± 0.007	16.70	114.0 ± 10.7	2.42 ± 0.02
NGC 1851		-1.18	137	156	1.95 ± 0.01	0.098 ± 0.004	0.679 ± 0.010	0.025 ± 0.006	16.09	90.9 ± 9.5	3.51 ± 0.06
NGC 2298		-1.96	53	1	2.90 ± 0.17	0.486 ± 0.020	0.267 ± 0.023	0.011 ± 0.012	16.11	57.7 ± 7.6	5.97 ± 0.17
NGC 3201		-1.51	90	103	1.96 ± 0.01	0.106 ± 0.015	0.649 ± 0.022	0.028 ± 0.032	14.76	88.7 ± 9.4	2.80 ± 0.05
NGC 4147		-1.78	61	2	2.76 ± 0.13	0.271 ± 0.027	0.476 ± 0.029	-	17.02	61.7 ± 7.9	5.96 ± 0.12
NGC 4590	M 68	-2.27	61	1	2.58 ± 0.09	0.205 ± 0.029	0.524 ± 0.030	0.012 ± 0.009	15.68	74.8 ± 8.6	4.43 ±0.07
NGC 4833		-1.89	280	8	2.88 ± 0.07	0.287 ± 0.037	0.538 ± 0.037	0.051 ± 0.009	15.60	55.2 ± 7.4	6.21 ± 0.28
NGC 5024	M 53	-2.06	495	0	2.89 ± 0.06	0.158 ± 0.035	0.602 ± 0.036	0.04 ± 0.008	16.81	57.9 ± 7.6	6.67 ± 0.16
NGC 5053		-2.30	34	8	2.46 ± 0.12	0.223 ± 0.090	0.439 ± 0.090	0.004 ± 0.35	16.69	74.2 ± 8.6	4.35 ± 0.11
NGC 5272	M 3	-1.50	213	392	2.21 ± 0.02	0.150 ± 0.016	0.613 ± 0.018	0.041 ± 0.009	15.64	81.5 ± 9.0	4.13 ± 0.05
NGC 5286		-1.70	548	36	2.80 ± 0.05	0.213 ± 0.034	0.670 ± 0.035	0.044 ± 0.004	16.63	53.7 ± 7.3	6.17 ± 0.30
NGC 5466		-2.31	72	5	2.62 ± 0.11	0.225 ± 0.062	0.457 ± 0.063	0.007 ± 0.024	16.52	68.7 ± 8.3	5.02 ± 0.10
NGC 5904	M 5	-1.33	98	155	2.42 ± 0.03	0.150 ± 0.012	0.681 ± 0.014	0.037 ± 0.007	15.07	68.9 ± 8.3	5.04 ± 0.14
NGC 5927		-0.29	0	447	1.00 ± 0.07	0.043 ± 0.003	0.062 ± 0.004	0.055 ± 0.015	16.55	135.2 ± 11.6	0.97 ± 0.01
NGC 5986		-1.63	459	26	2.88 ± 0.06	0.460 ± 0.052	0.443 ± 0.053	0.031 ± 0.012	16.52	46.1 ± 6.8	7.85 ± 0.46
NGC 6093	M 80	-1.75	332	16	2.87 ± 0.07	0.464 ± 0.059	0.447 ± 0.062	0.027 ± 0.012	16.10	53.8 ± 7.3	7.86 ± 0.36
NGC 6101		-1.98	169	17	2.87 ± 0.09	0.485 ± 0.025	0.223 ± 0.025	0.017 ± 0.011	16.60	62.4 ± 7.9	5.43 ± 0.15
NGC 6121	M 4	-1.18	51	55	1.98 ± 0.01	0.120 ± 0.020	0.569 ± 0.020	0.014 ± 0.006	13.45	86.7 ± 9.3	1.96 ± 0.06
NGC 6144		-1.82	62	0	3.00 ± 0.18	0.533 ± 0.024	0.229 ± 0.023	0.017 ± 0.013	16.40	28.6 ± 5.3	4.98 ± 0.88
NGC 6171	M 107	-1.03	12	89	1.37 ± 0.09	0.100 ± 0.014	0.513 ± 0.074	0.024 ± 0.014	15.00	116.2 ± 10.8	0.28 ± 0.03
NGC 6205	M 13	-1.58	705	0	2.99 ± 0.05	0.527 ± 0.013	0.441 ± 0.012	0.052 ± 0.004	14.90	41.0 ± 6.4	13.37 ± 0.72
NGC 6218	M 12	-1.33	188	0	3.00 ± 0.10	0.561 ± 0.034	0.299 ± 0.035	0.011 ± 0.011	14.60	49.8 ± 7.1	9.05 ± 0.32
NGC 6254	M 10	-1.57	257	0	3.00 ± 0.09	0.588 ± 0.032	0.260 ± 0.033	0.029 ± 0.011	14.65	40.6 ± 6.4	11.03 ± 0.66
NGC 6304		-0.37	0	170	1.03 ± 0.10	0.062 ± 0.007	0.060 ± 0.004	0.025 ± 0.006	15.60	0	0
NGC 6341	M 92	-2.25	340	6	2.92 ± 0.07	0.261 ± 0.075	0.542 ± 0.075	0.039 ± 0.006	15.10	47.4 ± 6.9	8.95 ± 0.30
NGC 6352		-0.62	0	96	1.00 ± 0.14	0.072 ± 0.007	0.056 ± 0.003	0.027 ± 0.006	15.13	130.6 ± 11.4	1.44 ± 0.01
NGC 6362		-1.07	56	135	1.65 ± 0.07	0.122 ± 0.004	0.621 ± 0.039	0.004 ± 0.011	15.33	115.1 ± 10.7	2.24 ± 0.02
NGC 6366		-0.59	0	39	1.02 ± 0.22	0.076 ± 0.005	0.058 ± 0.018	0.011 ± 0.011	15.65	136.9 ± 11.7	0.23 ± 0.01
NGC 6388		-0.45	267	1549	1.30 ± 0.03	0.057 ± 0.004	0.836 ± 0.008	0.067 ± 0.009	16.85	119.5 ± 10.9	1.88 ± 0.03
NGC 6397		-1.99	120	0	2.98 ± 0.13	0.534 ± 0.023	0.232 ± 0.030	0.008 ± 0.011	12.87	51.3 ± 7.1	8.29 ± 0.17
NGC 6426		-2.15	46	11	2.49 ± 0.10	0.178 ± 0.018	0.519 ± 0.023	0.021 ± 0.006	18.16	75.8 ± 8.7	1.01 ± 0.16
NGC 6441		-0.44	243	1769	1.26 ± 0.02	0.048 ± 0.003	0.904 ± 0.024	0.081 ± 0.022	17.51	113.9 ± 10.7	1.55 ± 0.03
NGC 6496		-0.46	0	80	1.00 ± 0.16	0.074 ± 0.011	0.056 ± 0.005	0.021 ± 0.006	16.00	143.2 ± 12.0	0.11 ± 0.02
NGC 6535		-1.79	24	0	3.00 ± 0.29	0.510 ± 0.026	0.271 ± 0.031	0.003 ± 0.022	15.75	53.0 ± 7.2	3.01 ± 0.33
NGC 6541		-1.82	411	0	2.99 ± 0.07	0.563 ± 0.026	0.347 ± 0.033	0.045 ± 0.006	15.35	41.7 ± 6.4	10.26 ± 0.46
NGC 6584		-1.50	25	38	1.90 ± 0.03	0.102 ± 0.012	0.558 ± 0.026	0.015 ± 0.011	16.53	94.4 ± 9.7	2.81 ± 0.05
NGC 6624		-0.42	0	192	1.00 ± 0.10	0.077 ± 0.006	0.085 ± 0.006	0.022 ± 0.003	15.60	141.8 ± 11.9	0.11 ± 0.02
NGC 6637		-0.59	0	256	1.00 ± 0.09	0.078 ± 0.004	0.065 ± 0.005	0.011 ± 0.005	15.34	137.8 ± 11.7	0.54 ± 0.02
NGC 6652		-0.76	0	26	1.00 ± 0.28	0.073 ± 0.011	0.080 ± 0.012	0.017 ± 0.011	15.40	139.8 ± 11.8	0.64 ± 0.01
NGC 6656	M 22	-1.70	512	13	2.94 ± 0.06	0.336 ± 0.088	0.577 ± 0.087	0.041 ± 0.012	14.15	55.1 ± 7.4	6.53 ± 0.31
NGC 6681	M 70	-1.62	147	0	2.97 ± 0.11	0.558 ± 0.046	0.334 ± 0.045	0.029 ± 0.015	15.55	45.1 ± 6.7	10.21 ± 0.37
NGC 6717		-1.26	30	0	3.00 ± 0.25	0.495 ± 0.032	0.310 ± 0.033	0.003 ± 0.009	15.55	52.3 ± 7.2	4.46 ± 0.24
NGC 6723		-1.10	106	152	1.85 ± 0.02	0.127 ± 0.007	0.704 ± 0.010	0.024 ± 0.007	15.48	83.4 ± 9.1	3.38 ± 0.08
NGC 6752		-1.55	330	0	3.00 ± 0.08	0.378 ± 0.024	0.578 ± 0.025	0.042 ± 0.004	13.70	39.4 ± 6.3	13.94 ± 0.78
NGC 6779	M 56	-2.00	177	0	3.00 ± 0.10	0.508 ± 0.031	0.284 ± 0.030	0.031 ± 0.008	16.18	47.1 ± 6.9	7.38 ± 0.25
NGC 6809	M 55	-1.93	244	2	2.93 ± 0.08	0.476 ± 0.055	0.313 ± 0.053	0.026 ± 0.015	14.40	58.3 ± 7.6	6.59 ± 0.21
NGC 6838	M 71	-0.82	0	70	1.00 ± 0.17	0.084 ± 0.012	0.057 ± 0.010	0.024 ± 0.010	14.48	126.5 ± 11.2	1.40 ± 0.01
NGC 6934		-1.56	103	71	2.13 ± 0.02	0.097 ± 0.013	0.678 ± 0.016	0.018 ± 0.004	16.86	83.7 ± 9.1	3.41 ± 0.08
NGC 6981	M 72	-1.48	37	27	2.14 ± 0.03	0.142 ± 0.016	0.570 ± 0.019	0.017 ± 0.006	16.90	84.9 ± 9.2	3.61 ± 0.06
NGC 7006		-1.46	75	93	1.92 ± 0.02	0.123 ± 0.016	0.581 ± 0.018	-	18.80	92.5 ± 9.6	3.12 ± 0.05
NGC 7078	M 15	-2.33	554	56	2.64 ± 0.04	0.174 ± 0.011	0.713 ± 0.019	0.069 ± 0.006	15.83	58.3 ± 7.6	6.63 ± 0.24
NGC 7089	M 2	-1.66	896	14	2.92 ± 0.04	0.150 ± 0.035	0.790 ± 0.037	0.052 ± 0.009	16.05	50.8 ± 7.1	8.23 ± 0.47
NGC 7099	M 30	-2.33	175	6	2.90 ± 0.10	0.462 ± 0.103	0.261 ± 0.103	0.022 ± 0.010	15.10	57.7 ± 7.6	6.40 ± 0.20
ARP 2		-1.74	22	0	2.86 ± 0.10	0.491 ± 0.021	0.184 ± 0.021	-	18.13	64.7 ± 8.0	5.83 ± 0.05
IC 4499		-1.62	81	108	1.90 ± 0.02	0.113 ± 0.026	0.508 ± 0.041	0.017 ± 0.008	17.65	94.7 ± 9.7	2.65 ± 0.04
Lynga 7		-0.67	0	90	1.00 ± 0.15	0.055 ± 0.050	0.093 ± 0.009	-	16.70	0	0
Pal 2		-1.29	194	0	3.00 ± 0.10	-	-	-	20.85	88.2 ± 9.4	0.11 ± 0.08
Rup 106		-1.78	42	0	2.78 ± 0.16	0.135 ± 0.012	0.210 ± 0.032	-	17.80	119.2 ± 10.9	1.84 ± 0.02
Terzan 7		-0.12	0	38	1.00 ± 0.23	0.057 ± 0.007	0.032 ± 0.008	-	17.50	133.7 ± 11.6	0.53 ± 0.01
Terzan 8		-2.34	49	0	2.92 ± 0.19	0.500 ± 0.050	0.223 ± 0.050	-	17.95	55.9 ± 7.5	5.21 ± 0.17

Notes. Columns are: observational values of HBR', blue (B) and red (R) HB star counts. L1, L2 indices, the spread in helium content ∂Y. V(HB) and CND(V-I) we used to estimate the new parameter τ_{HB}.

References. (a) Harris (1996), (b)Milone et al. (2018), (c) Milone et al. (2014), (d) Estimated by the authors.

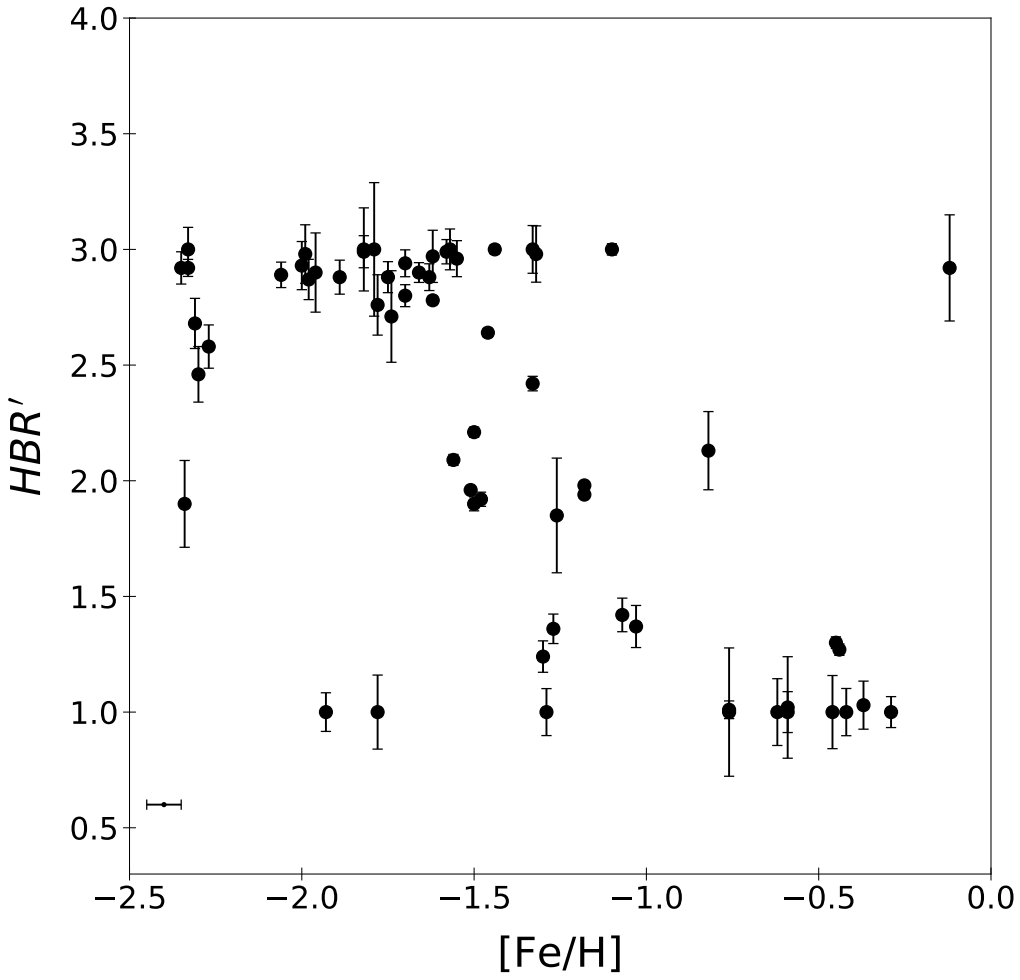

Figure 2.5: Observed *HBR′* values as a function of metal content. The metallicity scale is from Carretta et al. (2009) (see the Appendix for more details). The error bar in the lower left corner gives the uncertainty of the metal content (0.1 dex).

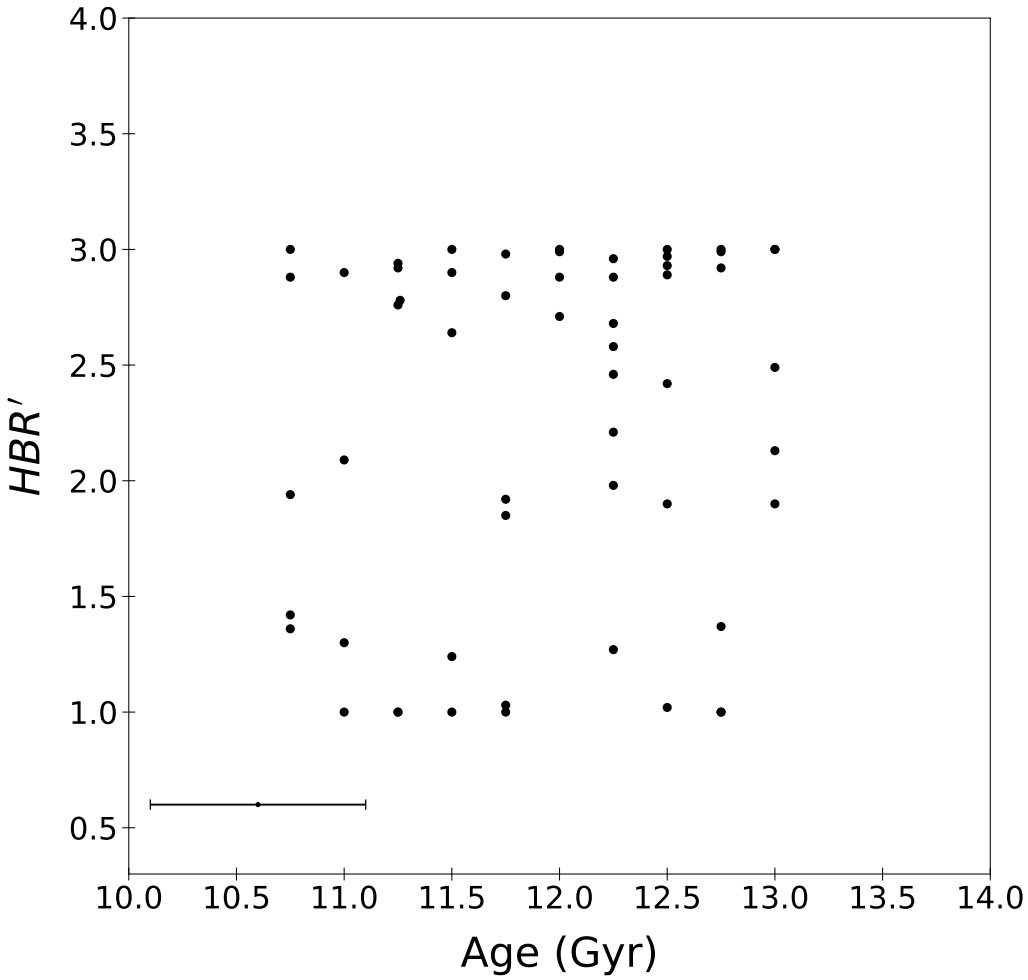

Figure 2.6: Observed *HBR′* values as a function of the cluster ages (gigayears (Gyr)) provided by VandenBerg et al. (2013); Leaman et al. (2013). The error bar in the lower left corner gives the uncertainty in the cluster ages (± 0.5 Gyr).

more metal-rich GGCs.

There is a well-defined degeneracy in the metal-intermediate regime (-1.6 ≤ [Fe/H] ≤ -1) in which GGCs with very similar metal abundances (the typical error on cluster metallicity being on the order of 0.1 dex – see horizontal error bar in the left bottom corner) cover a broad range in HBR' values. This means a variation from a very blue to a very red HB morphology, the well known second parameter problem. Figure 2.5 shows that HBR' is affected by degeneracy in its extreme values, $HBR' \sim -1$ (metal-rich regime) and $HBR' \sim +1$ (metal-poor regime). This means that HBR' has a low dynamical range attaining similar values for clusters with different metallicity.

Cluster age has been considered together with iron content as one of the main culprits affecting the HB morphology. We took advantage of the homogeneous cluster age estimates provided by VandenBerg et al. (2013); Leaman et al. (2013) for the same GGCs, to investigate the correlation with HBR' index. They estimated the cluster ages as follows. Firstly, they de-reddened the HB stars and then estimated the absolute visual magnitude by fitting a theoretical zero-age horizontal branch (ZAHB) to the lower bound of the HB star distributions. The absolute age of the globulars is estimated by the isochrone which, at fixed chemical composition, best matches the CMD from the main sequence turn off (MSTO) point to the beginning of the sub giant branch (SGB). Data plotted in Fig. 2.6 show that the HB morphology, at fixed cluster age, can move from very blue to very red. Indeed, the HBR' index, within the uncertainty on the cluster age (∼ 1 Gyr, displayed by the error bar in the left bottom corner), ranges from 1 to 3. This evidence shows that the HBR' index does not show any relevant correlation either with cluster age or with iron content.

In the figure a significant fraction of GGCs is located around the two extreme values attained by the HBR' index, namely 1 (eight globulars) and 3 (ten globulars). This means that the weak sensitivity of the HBR' index does not allow us to properly trace the variation of the HB morphology when moving from metal-poor to metal-rich globulars, while the HBR' index manages to trace the variation of the HB morphology in the metal-intermediate regime, where the relation appears to be almost linear. From the HBR'-age plane we can merely identify three different groups of clusters, with of $HBR' \sim +1$, $\sim +2$, and $\sim +3$, respectively.

2.4 L1 and L2 HB morphology indices

A new approach to parametrize the HB properties has been recently proposed by Milone et al. (2014). They introduced two indices, L1 and L2, and provided several possible correlations between the HB morphology and GGC global properties. The L1 index measures the distance in colour between the RGB at the same HB magnitude level and red HB stars; the L2 index is the colour extension of the HB. L1 and L2 are very easy to estimate, since their definition relies on the selection

of three different points on an optical (m_{F606W}, m_{F606W}-m_{F814W}) CMD. Since they are based on colour differences, they are independent of both cluster distance and reddening. Moreover, empirical evidence indicates that L1 and L2 correlate with intrinsic GGC properties.

Despite these advantages, the identification of the reddest HB point might be affected by the contamination of field stars since they attain similar colours. Moreover, the GGCs for which the reddest HB stars are RR Lyrae stars require additional information concerning their mean magnitudes. Furthermore, there is mounting evidence that the HB morphology changes when moving from the innermost to the outermost cluster regions (Castellani et al., 2003b; Iannicola et al., 2009; Milone et al., 2014). We also note that the perceived values of both L1 and L2 might be also affected by differential reddening.

Figure 2.7 (similar to Fig. 2 in Milone et al., 2014) shows the new indices as a function of GGC metallicity (from Carretta et al., 2009) for the 62 GGCs in common with our sample. The GGC data set adopted by Milone et al. (2014) is similar to the current one and relies on the same ACS@*HST* photometric catalogues we are using for the central cluster regions. This is the reason why we decided to use the L1 and L2 values given in Table 1 of Milone et al. (2014) and listed in columns 7 and 8 of Table 2.2 together with their errors.

The data plotted in the top panel of this figure show that GGCs belonging to the G1 and the G2 groups display a steady increase of the L1 index when moving from metal-rich to metal-poor clusters. The G3 clusters attain an almost constant L1 value over more than 1 dex in metallicity. Moreover, a glance at the data shows that the standard deviation is modest, but the correlation does not seem to be mono-parametric. Indeed, there is evidence of metal-intermediate GGCs, mainly the G2 clusters, with the same metal content but with the L1 index changing by almost a factor of two. The data plotted in the bottom panel show that the L2 index does not show a correlation with the metal content (first parameter) and indeed metal-rich clusters (G1) display a modest extent in colour, while metal-intermediate and metal-poor (G2+G3) clusters cover a broad colour range. There are only two exceptions: NGC 6388 and NGC 6441, the two peculiar metal-rich globulars that host red HB and blue, extreme HB stars, plus RR Lyrae stars with unusually long periods (Pritzl et al., 2003). However, the data plotted in the bottom panel do not display any relevant correlation with the metal content.

Figure 2.8 (similar to Fig. 5 in Milone et al., 2014) shows the correlation between the new L1 (top panel) and L2 (bottom panel) indices and the homogeneous cluster age estimates provided by VandenBerg et al. (2013); Leaman et al. (2013). The data plotted in the top panel seem to suggest a possible mild correlation between the G2 clusters and the absolute age. On the other hand, the G1 and the G3 clusters do not show any significant correlation with cluster age. The data plotted in this diagram clearly show that GGCs with the same age have L1 indices that change by a factor of two or three. The data plotted in the bottom panel display

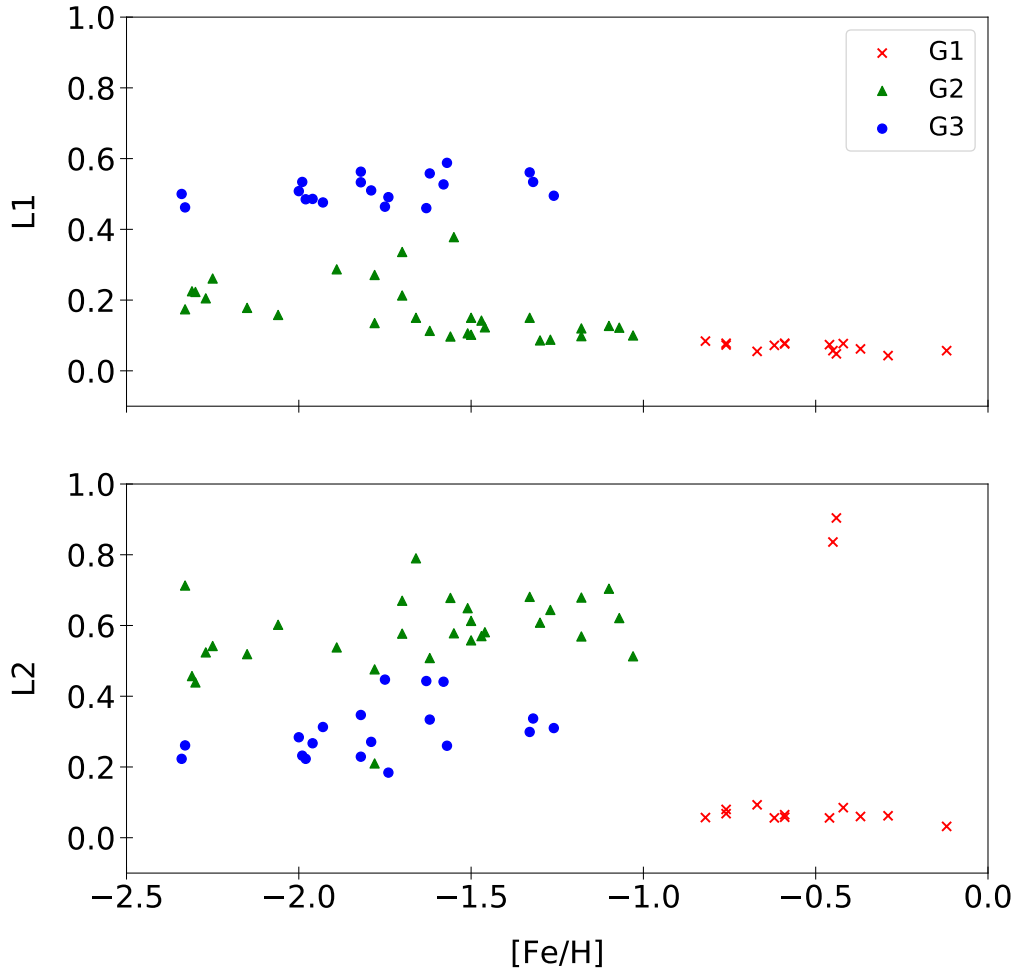

Figure 2.7: L1 and L2 indices as a function of the metal content (Carretta et al., 2009). The different symbols and colours identify the different cluster groups defined in Milone et al. (2014): G1 (red crosses) for metal-rich globulars ([Fe/H]>-1.0), G2 (green triangles) for clusters with [Fe/H]<-1.0 and L1 $\leq$ 0.4, G3 (blue circles) for globulars with L1 $\geq$ 0.4.

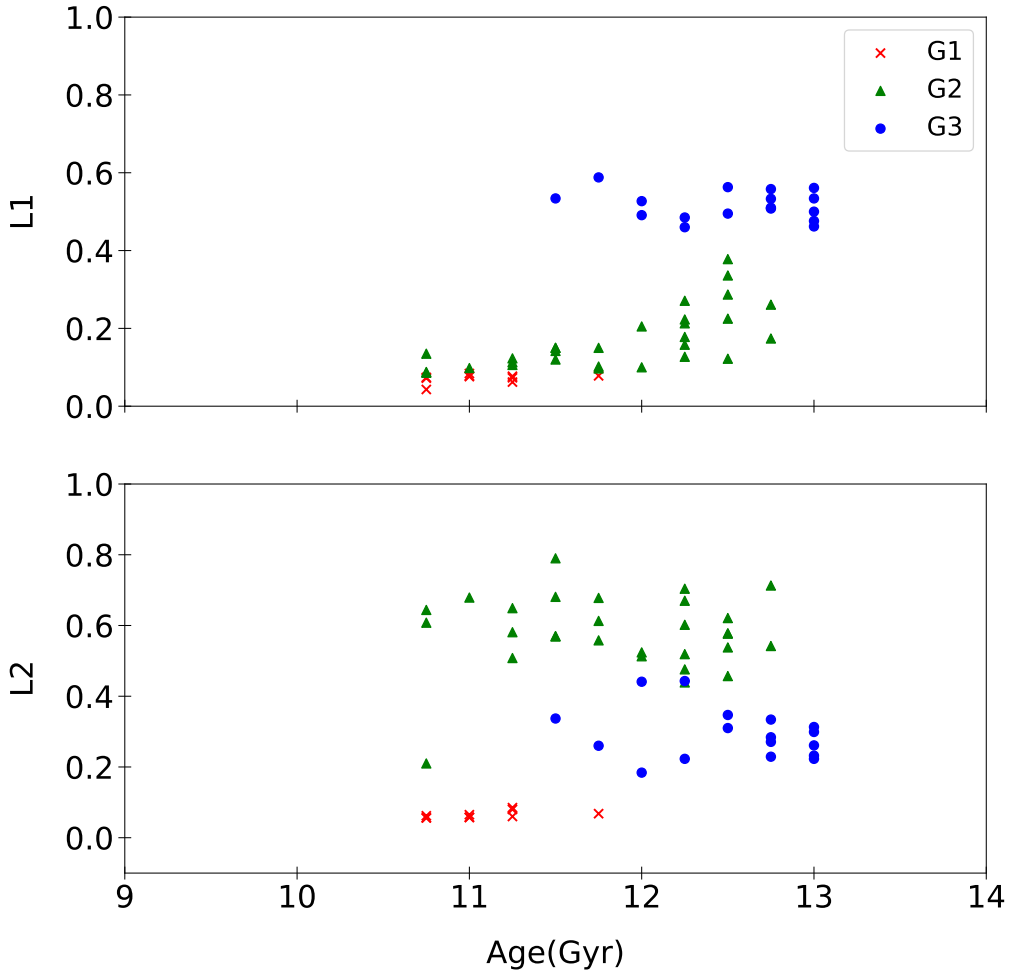

Figure 2.8: L1 and L2 indices as a function of the cluster age (Gyr) from VandenBerg et al. (2013); Leaman et al. (2013). The different symbols and colours identify the different cluster groups defined in Milone et al. (2014): G1 (red crosses) for metal-rich globulars ([Fe/H]>-1.0), G2 (green triangles) for clusters with [Fe/H]<-1.0 and L1 $\leq$ 0.4, G3 (blue circles) for globulars with L1 $\geq$ 0.4.

that the L2 index is independent of cluster age. L2 index hardly changes inside the range in age covered by G1, G2 and G3 globulars. We performed the same analysis using the GCC ages provided by Salaris & Weiss (2002) and found similar trends. The reader interested in a more detailed analysis of the correlation between the L1/L2 indices and the GGC parameters is referred to Milone et al. (2014).

2.5 A new HB morphology index: τ_{HB}

To provide a new perspective on the investigation of the HB morphology and to overcome some of the limitations affecting the current HB morphology indices, we have devised a new parameter, christened τ_{HB}, based on the ratio of the areas subtended by the CNDs as a function of magnitude (I-band) and colour (V–I) of HB stars. To estimate the new HB morphology index first we defined a box in the I, V–I CMD large enough to include all cluster HB stars, independently of the HB morphology. Then for each cluster we computed the CND in both magnitude and in colour. The reference luminosity level we selected from the Harris catalogue is the V(HB), which is the mean visual magnitude of HB stars inside the RR Lyrae instability strip. This V magnitude was transformed into an I-band magnitude assuming a mean V–I colour for the RR Lyrae stars equal to 0.45 (Braga et al., 2016). To perform homogeneous star counts ranging from EHB to RHB stars, we defined a box covering 1.7 mag in V–I colour and 6.5 mag in I-band, which is 4.5 magnitudes fainter and 2.0 magnitudes brighter than the I-band HB luminosity level. Finally, the selected HB stars are sorted as a function of the I-band apparent magnitude and we cumulated the star counts starting from the faintest and reddest stars in the box.

The top panels of Fig. 2.9 display HB stars in the I,V–I CMD for three GGCs covering a broad range of iron abundances and HB morphologies. They are NGC 6341 ([Fe/H]=-2.25), with an HB dominated by hot and extreme blue HB stars, NGC 5272 ([Fe/H]=-1.50) with a HB that includes blue and red HB stars, as well as RR Lyrae stars, and finally NGC 104 ([Fe/H]=-0.76) which is characterized by a red HB morphology. The bottom panels of the same figure display the normalized I-band CNDs of the HB stars plotted in the top panel. The data plotted in these panels show that the area subtended by the three CNDs (A_{CND}, shaded area) changes significantly when moving from an HB morphology dominated by hot and extreme HB stars, to a morphology dominated by red HB stars. We find a slightly constant decrease of the I-band A_{CND} by a factor of $\sim$ 1.4 when moving from NGC 6341 ($A_{CND}(I)$= 424.2) to NGC 5272 ($A_{CND}(I)$=336.6) to NGC 104 ($A_{CND}(I)$=217.9). A decrease on the order of approximately two when moving from an extreme blue HB morphology (NGC 6341) to a red one (NGC 104).

Then, we sorted the HB stars located inside the box as a function of the (V–I) colour. The apparent colours were de-reddened using the colour excesses (E(B–V)) listed in Table 2.1. In this case the HB stars were counted starting from the reddest

(coldest) HB stars. The top panels of Fig. 2.10 display HB stars in the I, V–I CMD for the same GGCs as in Fig. 2.9. The bottom panels display the normalized V–I CND of the HB stars plotted in the top panel. The shaded area shows a stronger sensitivity compared with the I-band A_{CND}; indeed, they increase by almost a factor of three when moving from NGC 6341 ($A_{CND}(V–I)$= 47.4) to NGC 5272 ($A_{CND}(V–I)$=81.5) and to NGC 104 ($A_{CND}(V–I)$=137.9).

To estimate the CNDs in magnitude and in colour we accounted for the entire sample of HB stars, meaning stars located inside the RRL instability strip were included. The spread in magnitude and in colour of these objects is larger compared with typical HB stars. The difference is intrinsic, since we are using the mean of the measurements in both the V and the I band. In other words, we did not perform an analytical fit of the phased measurements.

To investigate the difference between the classical (HBR') and the new (τ_{HB}) morphology index on a more quantitative basis, the left panel of Fig. 2.11 shows the comparison between the I-band A_{CND} and the HBR' index. The data plotted in this panel display a very well-defined linear correlation between I-band A_{CND} and HBR' index in the regime in which the latter attains intermediate values. The saturation for clusters dominated by blue HB morphologies ($HBR' \sim 3$) and red HB morphologies ($HBR' \sim 1$) is also quite clear at the top and the bottom of the panel. The right panel shows the same comparison as the left panel, but for the V–I A_{CND}. The data plotted in this panel show a linear anti-correlation over the entire range of values attained by the HBR' index.

We estimated the ratio between the area covered by the CND in magnitude and in colour, namely

$$\tau_{HB} = \frac{A_{CND}(I)}{A_{CND}(V–I)}. \tag{2.3}$$

The V magnitude levels of the HB, which we transformed to I(HB) using the mean V–I of 0.45 mag, $A_{CND}(V–I)$, τ_{HB}, and their errors for the GGCs in our sample are listed in columns 10, 11, and 12 of Table 2.2, respectively. We propagated the error on τ_{HB} considering Poissonian uncertainties in the A_{CND}. We note that considering a typical mean reddening uncertainty of $\sim$ 15%, we find a mean difference in τ_{HB} of a factor of $\sim$ 10%.

Although τ_{HB} estimate is slightly more complex than the other indices presented in the literature, the new HB morphology index presents several key advantages compared with the classical HBR' and L1/L2 indices:

Dynamical range — The current sample covers a range in τ_{HB} that is a factor of seven larger than the range covered by the HBR' index. The data plotted in Fig. 2.12 show that when moving from metal-rich to less metal-rich GGCs (-1.0 $<$ [Fe/H]$<$0.) the new index changes from zero to roughly three while the old one changes from one to roughly 1.5. The correlation between the old and new indices is linear in the metal intermediate regime, but it degenerates in the more metal-poor regime. Indeed, the τ_{HB} index increases by more than a factor of two

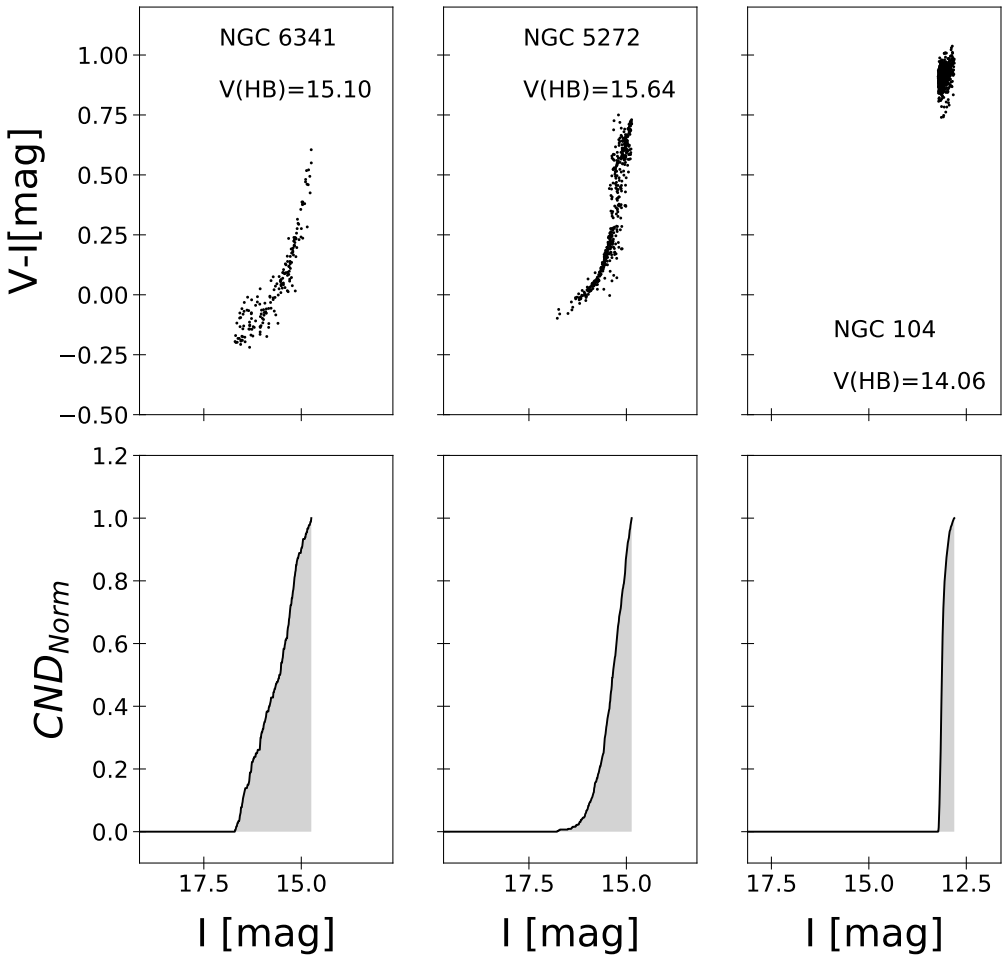

Figure 2.9: Run of the normalized CND with respect to the I magnitude for three globular clusters (lower panels), chosen as representative of three different metallicity regimes (NGC 6341, NGC 5272, and NGC 104). Upper panels show the horizontal branch of the three chosen globulars in I,V–I CMDs.

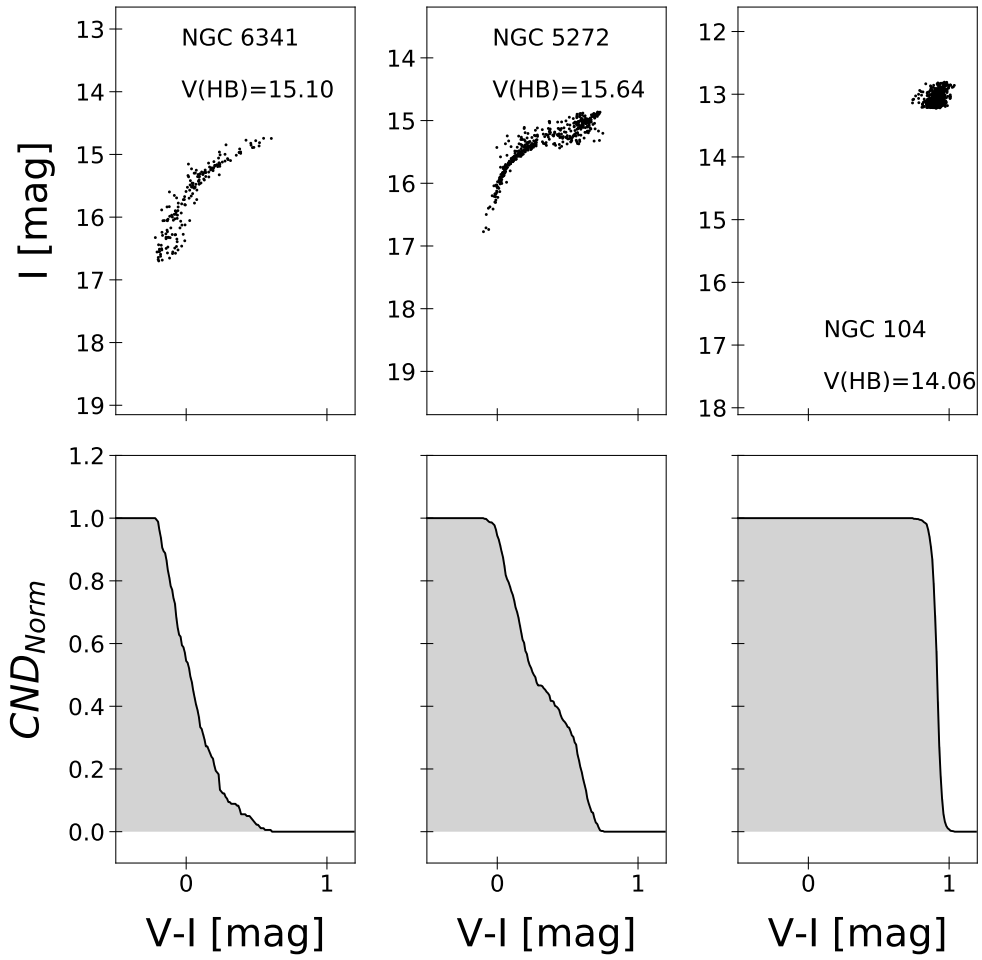

Figure 2.10: Run of the normalized CND with respect to *V–I* for the same three globular clusters (lower panels) of Fig. 2.9. Upper panels show the horizontal branch of the three chosen globulars in *I*, *V–I* CMDs.

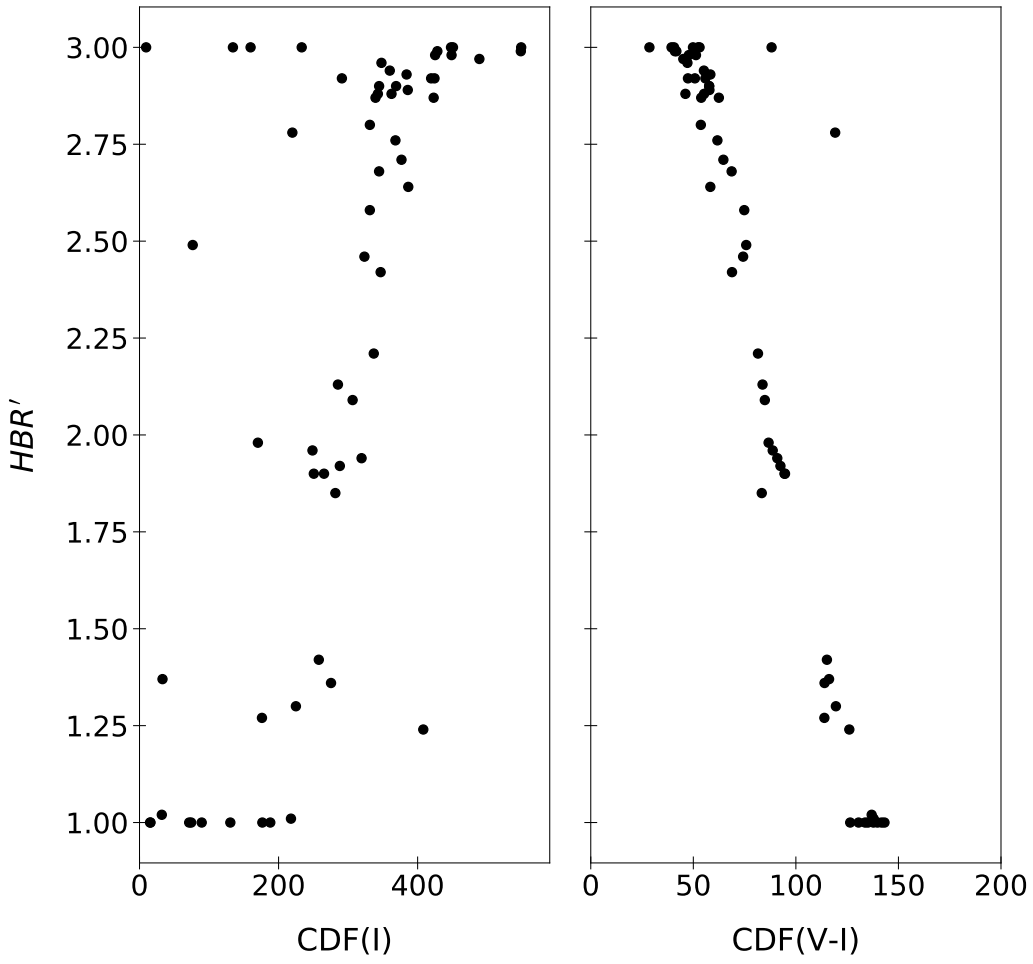

Figure 2.11: The indices $A_{CND}(I)$ and $A_{CND}(V–I)$ vs. the HBR' morphology index.

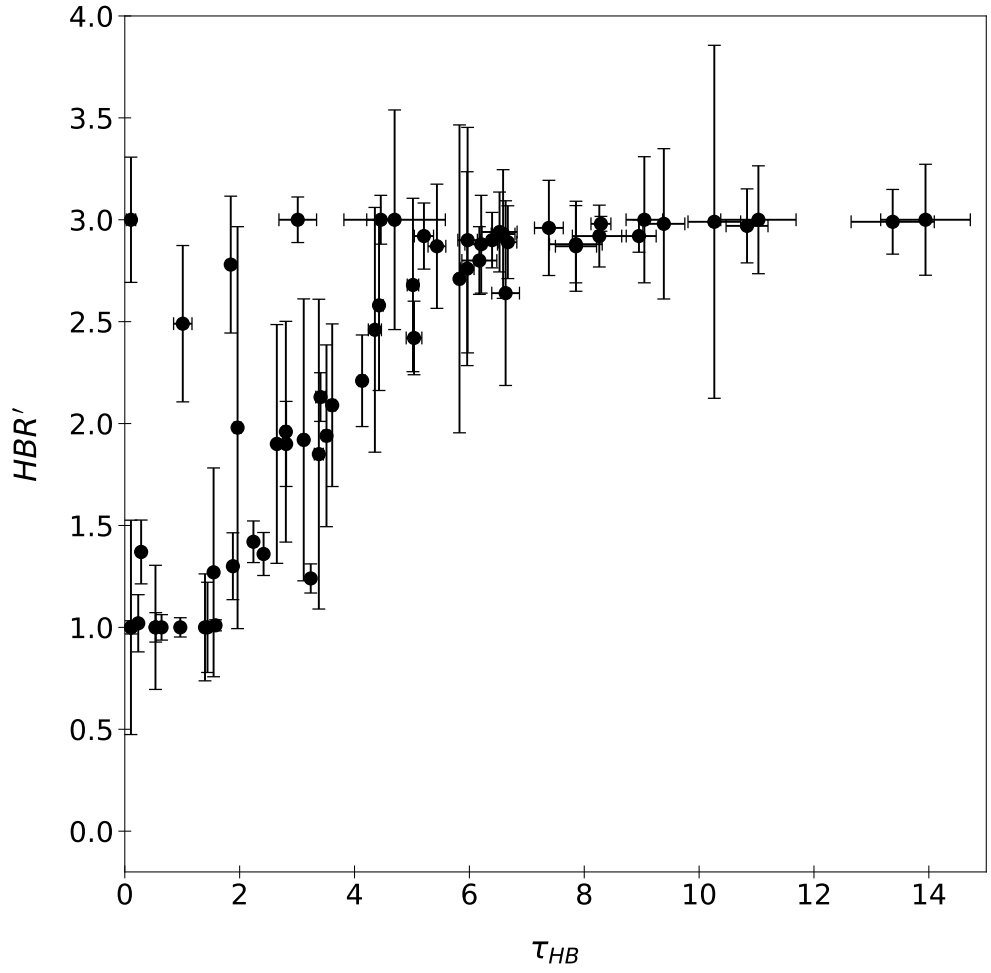

Figure 2.12: Our new HB morphology index τ_{HB} vs. HBR'.

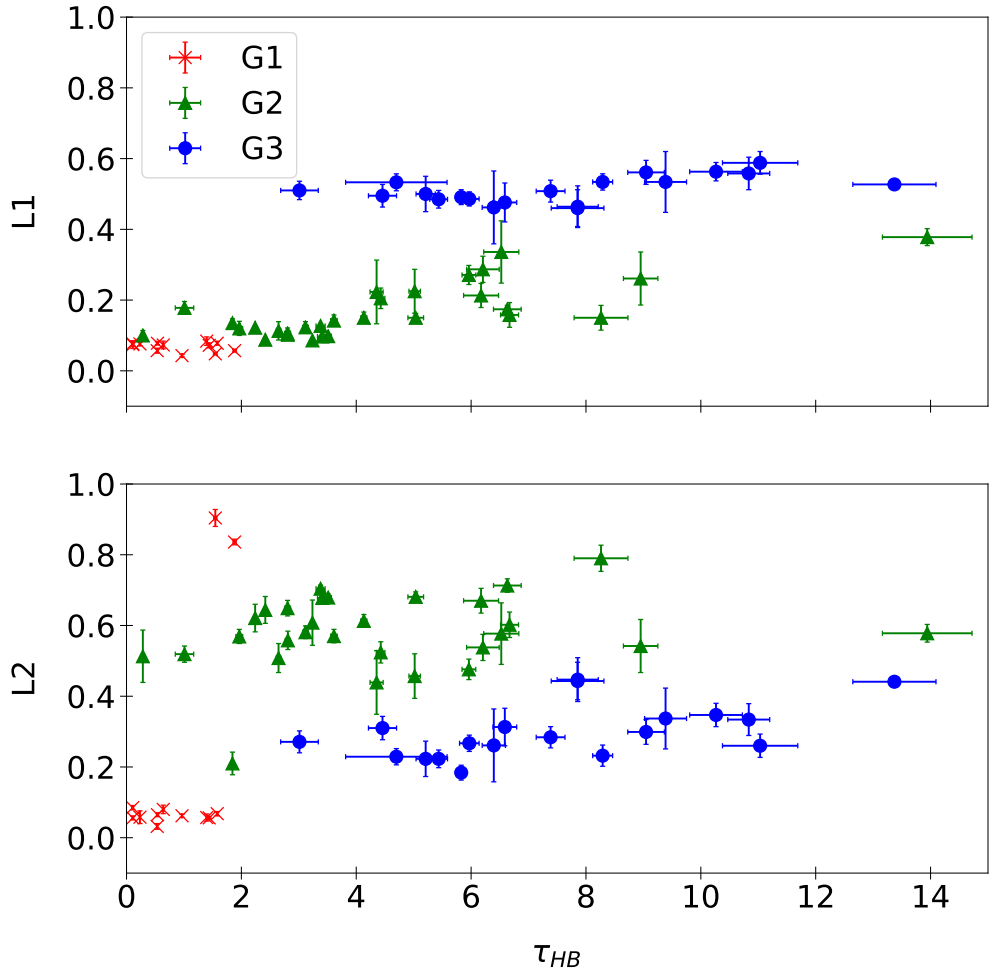

Figure 2.13: L1 (top) and L2 (bottom) indices as a function of τ_{HB} for the globulars in our sample. The different symbols and colours identify the different cluster groups defined in Milone et al. (2014): G1 (red crosses) for metal-rich globulars ([Fe/H]>-1.0), G2 (green triangles) for clusters with [Fe/H]<-1.0 and L1 $\leq$ 0.4, G3 (blue circles) for globulars with L1 $\geq$ 0.4.

Table 2.3: Examples of globular pairs of similar metallicity and HBR', but different values in τ_{HB}.

ID	[Fe/H]	HBR'	L1	τ_{HB}
NGC 0104	-0.76 ± 0.02	1.01 ± 0.04	0.078 ± 0.005	1.58 ±0.01
NGC 6652	-0.76 ± 0.14	1.00 ± 0.28	0.073 ± 0.011	0.64 ± 0.01
NGC 6121	-1.18 ± 0.02	1.98 ± 0.01	0.120 ± 0.020	1.96 ± 0.06
NGC 1851	-1.18 ± 0.08	1.95 ± 0.01	0.098 ± 0.004	3.51 ± 0.06
NGC 6752	-1.55 ± 0.01	3.00 ± 0.08	0.378 ± 0.024	13.94 ± 0.78
NGC 6934	-1.56 ± 0.09	2.13 ± 0.02	0.097 ± 0.0013	3.41 ± 0.08
NGC 6144	-1.82 ± 0.05	3.00 ± 0.18	0.533 ± 0.024	4.98 ± 0.88
NGC 6541	-1.82 ± 0.08	2.99 ± 0.07	0.563 ± 0.026	10.26 ± 0.46

(from six to fourteen), whereas the HBR' takes on an almost constant value of three.

The variation in τ_{HB} is a factor of twenty larger than the range covered by the L1 and L2 indices. The data plotted in Fig. 2.13 show that the G3 group is characterized by L1 values that are almost constant (L1 $\sim$ 0.5), while τ_{HB} changes from three to thirteen. The G1 and G2 groups display a mild linear correlation between L1 and τ_{HB}, but once again the variation in the L1 index is modest when compared with τ_{HB} index (0.3 vs. 7). The correlation between L2 and τ_{HB} is more noisy with a large spread at fixed τ_{HB} value.

Detailed sampling of the HB morphology – The CND in both magnitude and colour is sensitive to the star distribution along the HB. Data listed in Table 2.2 show that two metal-poor clusters, NGC 4833 and NGC 6341, with similar HBR' (2.88±0.07 vs. 2.92±0.07) and L1 (0.287 ± 0.037 vs. 0.261 ± 0.075) indices, attain τ_{HB} values that differ at the 50% level (6.21±0.21 vs. 8.95±0.30). The same applies to metal-rich clusters, and indeed, two clusters like NGC 104 and NGC 6637 have the same HBR' (1.01±0.04 vs. 1.00±0.09) and L1 (0.078 ± 0.005 vs. 0.078 ± 0.004) values, but the τ_{HB} value of the former cluster is a factor of three larger than the latter one (1.58±0.01 vs. 0.54±0.02). Data listed in Table 2.3 highlight several other pairs of GGCs characterized by a very similar iron content (column 2), HBR' (column 3), and L1[1] (column 4) value, but quite different τ_{HB} values (column 5). The various pairs are separated in the table with horizontal lines.

Global star count of HB stars – The τ_{HB} does not require any identification of specific subgroups (blue, red, variables).

2.6 Comparison between space- and ground-based data

As described in Sect. 2.2, when available we preferred the space-based observations for our analysis, while we used the ground-based data for the outer regions of the globulars in our sample. In this section, we analyse the HBR' and τ_{HB} index evaluations using either ACS or ground-based observations, comparing them to the 'global' index, which is the index estimated from both space- and ground-based data (see Sects. 2.3 and 2.5), giving higher priority to the first ones when

[1] *We did not consider L2 since it does not correlate with age, metallicity, and* τ_{HB}.

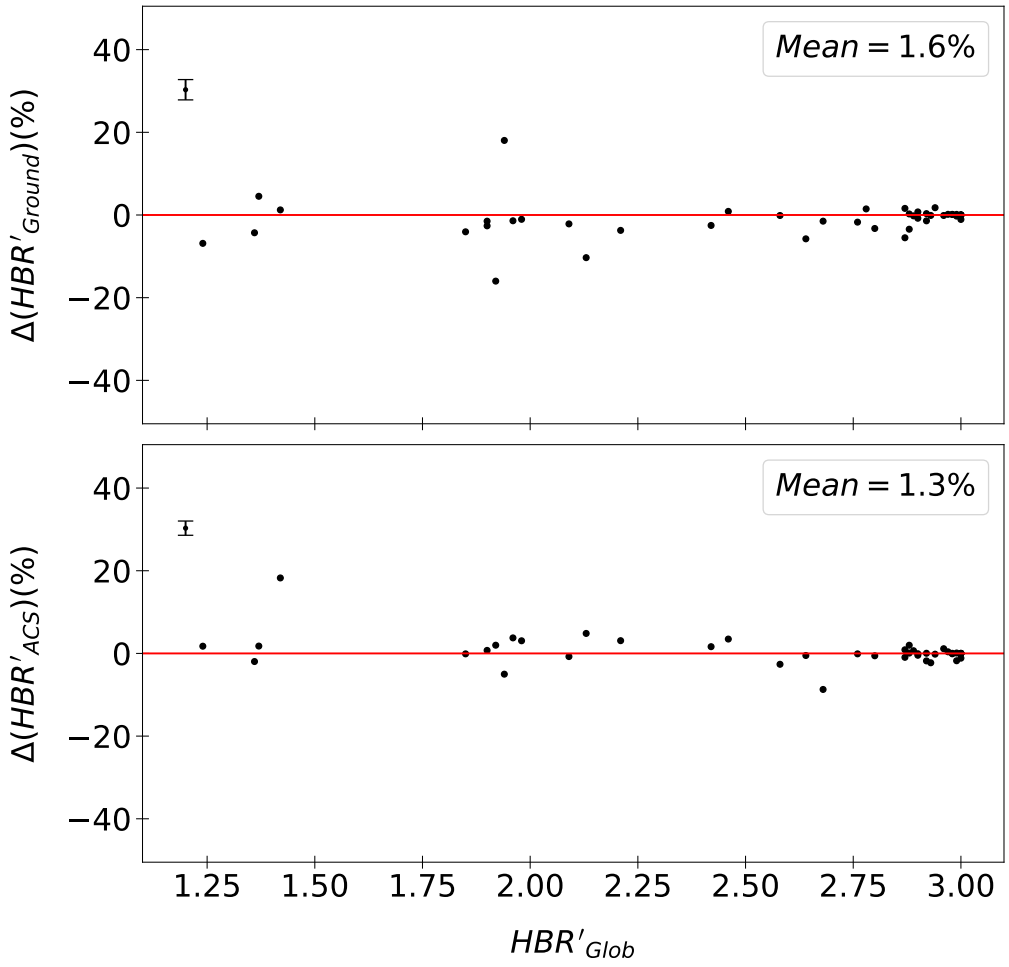

Figure 2.14: Top: relative difference between the global HBR' and the HBR' values only based on ground-based data versus the global index. Note that in the estimate of the global index the priority in selecting the photometry was given to space-based (ACS at *HST*) data. Bottom: as the top panel, but the relative difference is between the global index and the HBR' index only based on space-based data. The standard deviation of the estimates is represented by the error bar at the top left corner of the panels. At the top right corners we display the mean relative difference.

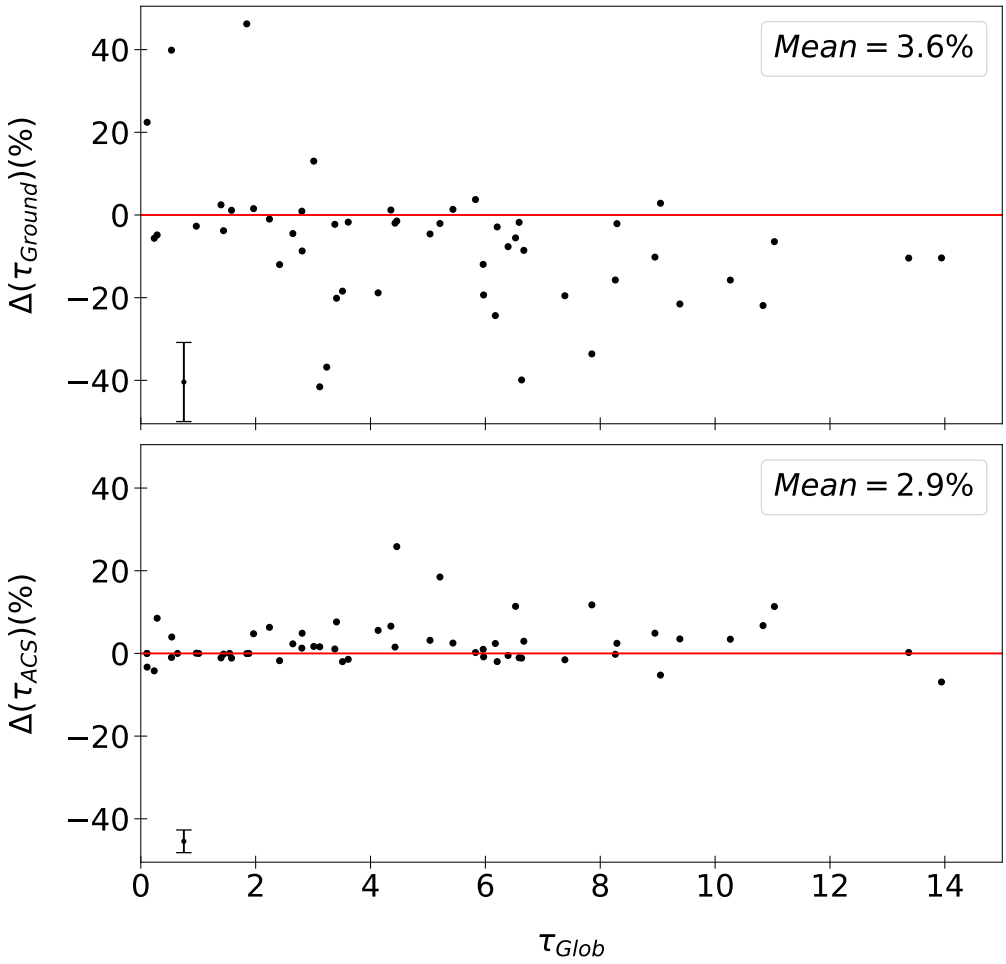

Figure 2.15: Top: relative difference between the global τ_{HB} and the τ_{HB} index only based on ground-based data versus the global index. Note that in the estimate of the global index the priority in selecting stars was given to space-based (ACS at *HST*) data. Bottom: as the top panel, but the relative difference is between the global index and the τ_{HB} index only based on space-based data. The standard deviation of the estimates is represented by the error bar at the bottom left corner of the panels. At the top right corners we display the mean relative difference.

both measures where available.

Figure 2.14 shows the relative difference between the HBR' index estimated by using either ground-based (top panel) or ACS (bottom panel) data as a function of the global value listed in column 6 of Table 2.2. Data plotted in this figure show the following results. The top panel of Fig. 2.14 shows that the relative difference in HBR' index from ground-based data is on average approximately 1.6%. The major exceptions are represented by the globulars NGC 1851 ($|\Delta(HBR'_{Ground})| \sim 18\%$) and NGC 7006 ($|\Delta(\mathrm{HBR'}_{Ground})| \sim 16\%$). The difference is mainly caused by the star counts of red HB stars (R) from ground-based observations. They provide a lower contribution when compared with space-based data ($HBR'_{Ground} \sim 2.28$ vs. $HBR'_{Global} \sim 1.94$ for the former cluster, $HBR'_{Ground} \sim 1.61$ vs. $HBR'_{Global} \sim 1.92$ for the latter one).

The bottom panel shows that the difference in HBR' index between HBR'_{ACS} and HBR'_{Global} is on average ~1.3 %. It is marginally lower than the difference based on ground-based data. The single exception is NGC 6362, which is characterized by $|\Delta(HBR'_{ACS})| \sim 18\%$. Its global HBR' index turns out to be redder than the ACS one ($HBR'_{ACS} \sim 1.42$ vs. $HBR'_{Global} \sim 1.68$) since in the global HBR' estimate the contribution of red HB stars is mainly given by red HB stars from ground-based observations.

Figure 2.15 shows the global τ_{HB} index, evaluated in Sect. 2.5, versus the relative difference between the τ_{HB} index based either on ground-based (top panel) or on ACS (bottom panel) observations and the global one. A glance at the data plotted in this figure discloses a couple of interesting findings. The top panel shows that the relative difference in τ_{HB} index based on ground-based data shows a larger dispersion compared to that from space-based (bottom panel) data. The mean relative difference between $\tau_{HB,Global}$ and $\tau_{HB,Ground}$ is $\sim 3.6\%$. Moreover, thirteen globulars have a difference of $|\Delta(\tau_{HB,Ground})|$ greater than 20%. In this context it is worth mentioning that amongst them eleven are small, concentrated globulars. Indeed, their half-mass radius r_h (Harris, 1996) is entirely located inside the ACS FoV, namely NGC 1851 (23%, $r_h = 0.51 arcmin$), NGC 2298 (24%, $r_h = 0.98 arcmin$), NGC 5286 (32%, $r_h = 0.73 arcmin$), NGC 5986 (51%, $r_h = 0.98 arcmin$), NGC 6681 (28%, $r_h = 0.71 arcmin$), NGC 6779 (24%, $r_h = 1.1 arcmin$), NGC 6934 (25%, $r_h = 0.69 arcmin$), NGC 7006 (71%, $r_h = 0.44 arcmin$), NGC 7078 (66%, $r_h = 1.0 arcmin$), Rup 106 (32%, $r_h = 1.05 arcmin$), and Terzan 7 (29%, $r_h = 0.77 arcmin$). This means that the main contribution in the τ index comes from space-based data, while ground-based data mainly contribute for HB stars located in the cluster outskirts. Two out of the thirteen globulars are larger, but located at large distances (true distance modulus $DM \sim 15$ mag), namely NGC 288 (27%, $r_h = 2.23 arcmin$) and NGC 5272 (27%, $r_h = 2.31 arcmin$). This means that, even in these cases, most of the cluster stars are located inside the ACS FoV, giving a major contribution to the $\tau_{HB,Global}$ when compared to the ground-based observations.

The bottom panel shows that the relative variation between $\tau_{HB,Global}$ and $\tau_{HB,ACS}$

is, as expected low, on average 2.9%. The only exception is NGC 6717 (26%), in which ACS data do not populate the brighter region of the HB, giving a different estimate of $\tau_{HB,ACS}$ compared to the global one (5.61 vs. 4.46).

These findings support the fact that both ground-based and space observations of our sample of GGCs are statistically consistent and reliable. Moreover, our estimates of HBR' and τ_{HB} are valid and well grounded: independently of the choice about the origin of the data they give the same results within a difference of at most 20% for τ_{HB} estimates.

The evidence of a larger relative difference in the τ_{HB} index shows that potentially our new index could quantify the different possible contribution to the HB morphology given by inner and outer populations within the globulars. This difference between star counts based on ground-based and on space-based data will be addressed in a future paper focused on the spectral energy distribution of Galactic globulars.

2.7 Correlation of τ_{HB} with cluster metallicity, age, and helium content

To investigate the correlation between τ_{HB} and fundamental cluster parameters, we study its relationship to cluster metallicity, absolute age, and internal spread in Helium abundance. Figure 2.16 shows τ_{HB} as a function of the iron content. The bulk of metal-poor GGCs ([Fe/H] $\leq$ -1.5) attains τ_{HB} values ranging from $\sim$ 9 to $\sim$ 4. In the metal-intermediate regime (-1.5 $\leq$ [Fe/H] $\leq$ -1.0) the bulk of the GGCs are characterized by τ_{HB} ranging from $\sim$ 5 to $\sim$ 2, while metal-rich clusters ([Fe/H]$\geq$ -1.0) attain τ_{HB} values smaller than 2 on average. There is a small sample of GGCs that attains τ_{HB} values that are, at fixed metal content, either systematically larger or systematically smaller than the typical ranges. To investigate on a more quantitative basis the identification of these GGCs, we performed a quadratic fit of the bulk of the GGCs. We found the best-fit function

$$\tau_{HB} = 0.06 - 0.83 \cdot [Fe/H] + 1.03 \cdot [Fe/H]^2 \quad (2.4)$$

,

with a σ = 3.08 dispersion (see the red line in Fig. 2.16). We have defined as 'outliers' the GGCs that attain, at fixed metal content, τ_{HB} values that are more than 1.5σ away from the best quadratic fit. We ended up with a subsample of seven metal-poor and metal-intermediate ($-1.82 \leq$ [Fe/H] ≤ -1.32) GGCs with τ_{HB} values larger than 9 (see red squares in Fig. 2.16). This subsample includes the GGCs that attain the largest τ_{HB} values, namely NGC 6205 (τ_{HB}= 13.37 $\pm$ 0.72) and NGC 6752 (τ_{HB}= 13.94 $\pm$ 0.78). This means that they are characterized by very blue HB morphologies. Data plotted in Fig. 2.16 also show a metal-poor

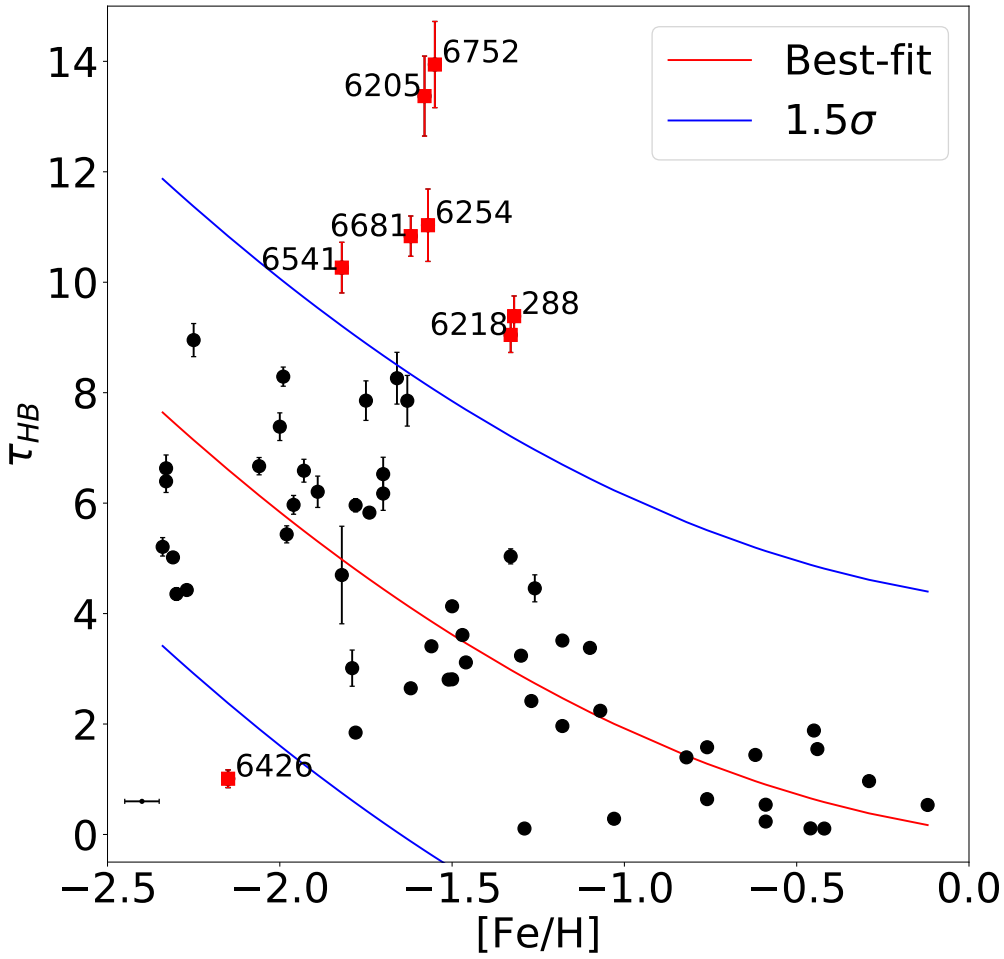

Figure 2.16: Variation of τ_{HB} as a function of cluster metallicity (Carretta et al., 2009). The red line shows the quadratic best fit, the blue lines show 1.5 σ levels. Red squares display the outliers, which are those objects located at more than 1.5 σ from the quadratic fit. In the left corner the error bar shows the 0.1 dex error on the metal content.

GGC (NGC 6426) with τ_{HB}=1.01 ± 0.16 that is a factor of four to ten smaller than the bulk of GGCs with similar metal abundances.

The above empirical evidence indicates that the new HB morphology index appears to be a solid diagnostic to select GGCs that are strongly affected by the second parameter problem. To further investigate the nature of these clusters we decided to perform a more detailed analysis of the GGCs in the metallicity range covered by the second parameter clusters. We selected three out of the eight outliers, namely NGC 6218 ([Fe/H]=-1.33, Age= 13 Gyr), NGC 6254 ([Fe/H]=-1.57, Age= 11.75 Gyr), and NGC 6541 ([Fe/H]=-1.82, Age= 12.50 Gyr), covering roughly 0.5 dex in metal content. The left panels of Fig. 2.17 show the *I*,*V*–*I* CMDs of these clusters. Assuming that the HB morphology is mainly driven by a difference in metal content, we selected three GGCs with iron abundances very similar to the selected outliers, but with τ_{HB} values close to the best-fit line plotted in Fig. 2.16, namely NGC 362 ([Fe/H]=-1.30, Age= 10.75 Gyr), NGC 6934 ([Fe/H]=-1.56, Age= 11.75 Gyr), and NGC 6144 ([Fe/H]=-1.82, Age=12.75 Gyr). The right panels of Fig. 2.17 display their *I*,*V*–*I* CMDs. The CMDs display several interesting features worth discussing.

The top panels of Fig. 2.17 compare the CMDs of two metal-intermediate GGCs: an outlier cluster characterized by a very blue HB morphology, and a typical one (in terms of τ_{HB}, 9.05 vs. 3.24) , mainly dominated by red HB stars. It is worth mentioning that the HB morphology of this pair of clusters could also be traced on the basis of the ***HBR′*** index. Indeed, the ***HBR′*** value of NGC 6218 is a factor of 2.5 larger than the ***HBR′*** value of NGC 362.

The middle panels of Fig. 2.17 also display the CMDs of two metal-intermediate GGCs. The outlier GGC is characterized by a very blue HB morphology, while the typical one shows an HB that hosts variable stars, blue and red HB stars. For these GGCs the ***HBR′*** index decreases by only the 30% when moving from NGC 6254 (3.00) to NGC 6934 (2.13). Interestingly enough, the τ_{HB} index differs by more than a factor of three.

The bottom panels of Fig. 2.17 display the CMDs of two metal-poor GGCs. The outlier GGC shows, as expected, a very blue HB morphology, while the 'typical' one also shows a blue HB morphology. The ***HBR′*** index for these two GGCs is identical within the errors: 2.99 for NGC 6541 and 3.00 for NGC 6144. On the other hand, the τ_{HB} index differs by more than a factor of two (10.26 vs 4.98).

The current findings further support the strong sensitivity of the τ_{HB} index to variations in HB morphology when moving from the metal-intermediate to the metal-poor regime. We note that we did not find in the literature an indication of an extreme multi-population or some peculiar dynamical characteristics for the second parameter clusters in our sample. The anti-correlation found between the τ_{HB} index and the cluster metallicity does not include information about the cluster age. We have then investigated whether the new HB morphology index is correlated with the cluster ages.

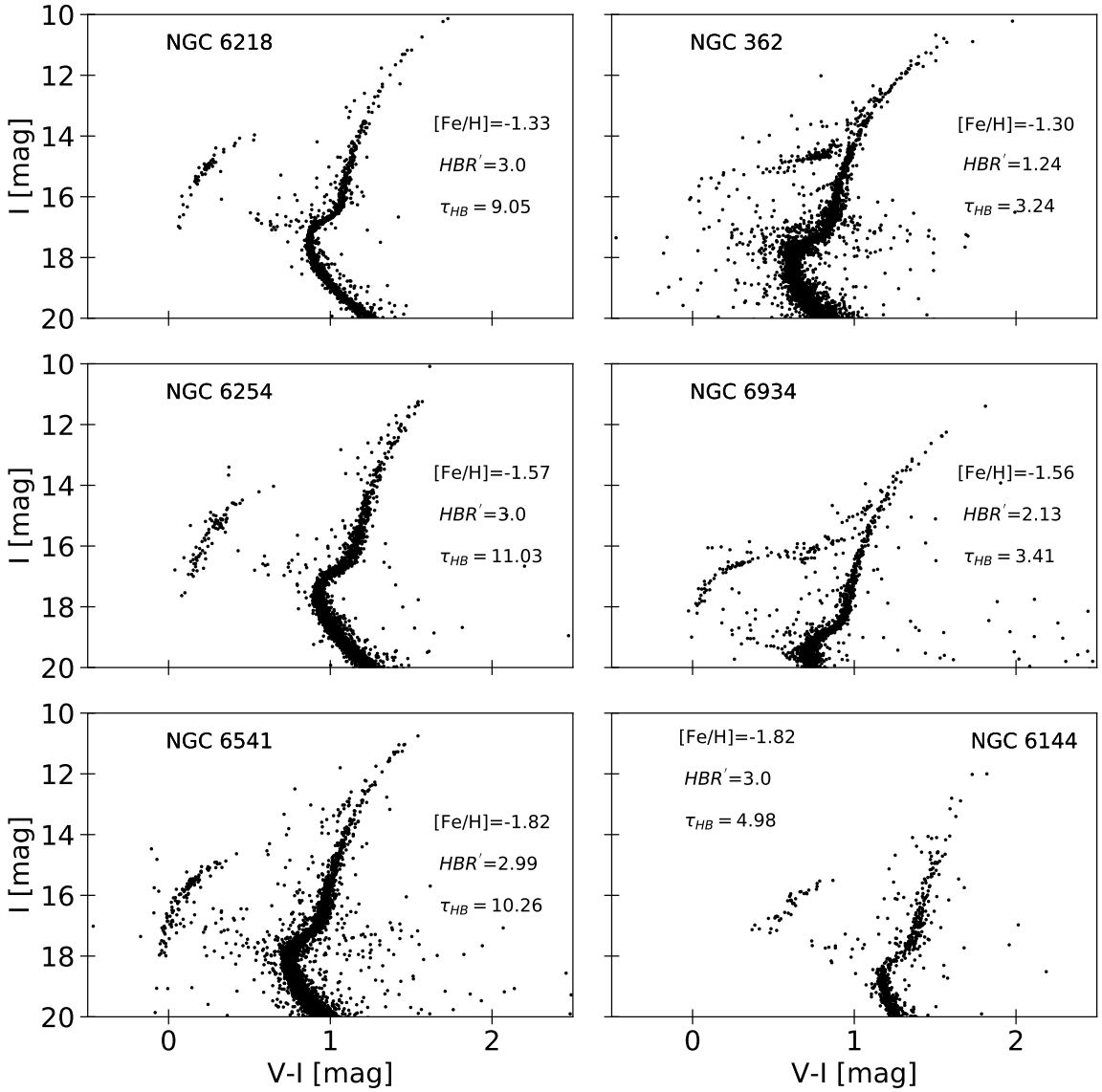

Figure 2.17: CMDs (*I*, *V–I*) for three pairs of GGCs in the sample. Left panels: Clusters belonging to the outlier group. Right panels: CMDs of clusters with similar [Fe/H] as the outlier ones, but following the main τ_{HB}-[Fe/H] relation.

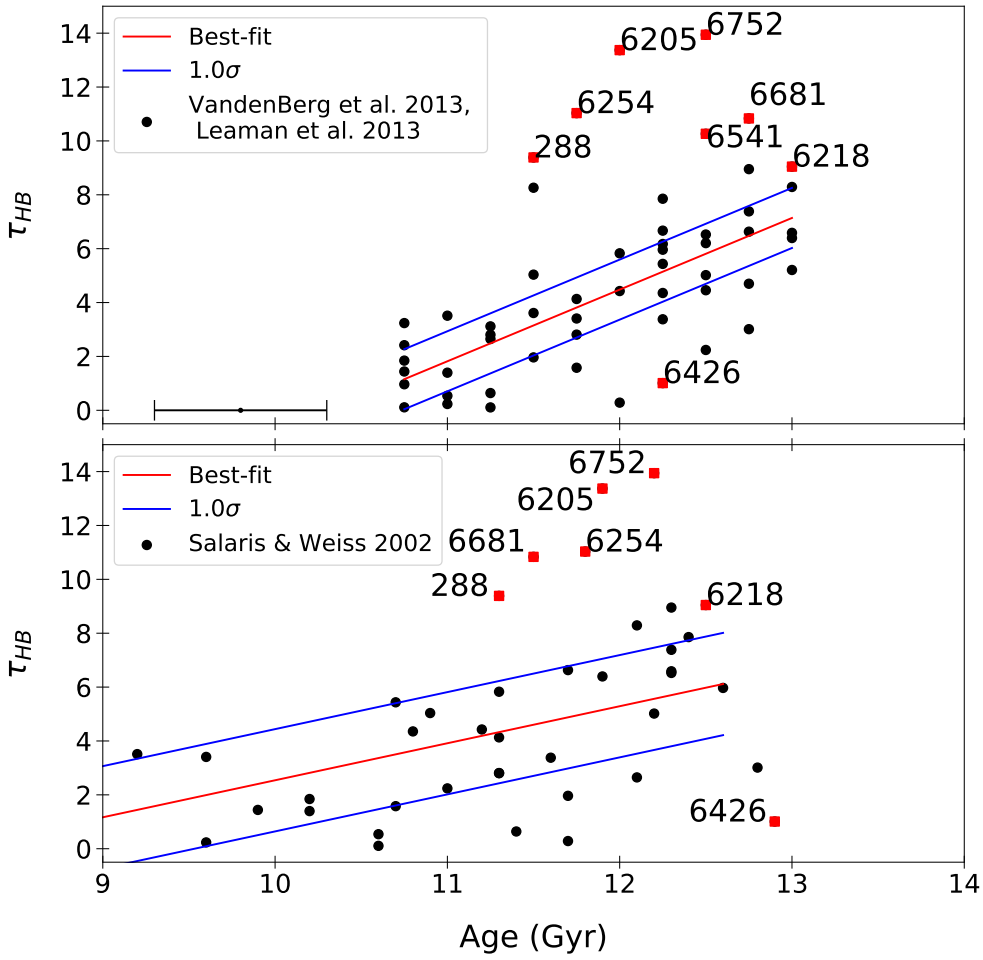

Figure 2.18: Our index τ_{HB} as a function of cluster ages obtained from different authors. Top: cluster ages from VandenBerg et al. (2013); Leaman et al. (2013). The error bar in the lower left corner shows the conservative ±0.5 Gyr error on the GGC ages. Bottom: ages from Salaris & Weiss (2002) based on the metallicity scale provided by Carretta & Gratton (1997). In both panels red squares are the same second parameter clusters shown in Fig. 2.16 and discussed in this section. Red lines determine the best-fit to each data sample, blue lines the $\pm 1\sigma$ levels.

Table 2.4: Best fit parameters for the linear functions fitting the τ_{HB}-Age relations used in this work

	a	b	σ
VandenBerg + Leaman et al.	-27.23 ± 6.34	2.69 ± 0.53	1.21
Salaris and Weiss	-11.20 ± 3.55	1.37 ± 0.32	1.89

To establish the age dependence we took advantage of the recent homogeneous age estimates provided by VandenBerg et al. (2013); Leaman et al. (2013). The data plotted in the top panel of Fig. 2.18 display a well-defined linear correlation between age and τ_{HB}. In particular, there is evidence that, when moving from a red to a blue HB morphology, GGCs become on average older. We performed a linear fit ($\tau_{HB} = a + b \cdot Age$, red line) whose coefficients are listed in Table 2.4, together with the standard deviation (σ). The dispersion around the linear fit is modest, equal to 1.21. However, the second parameter globulars identified in the τ_{HB}-[Fe/H] plane do not follow the same trend. They are on average more than 1.5σ away from the main relation, that is, at fixed cluster age their τ_{HB} values are systematically larger than typical GGCs. This further supports the evidence that the τ_{HB} index is a robust diagnostic to identify second parameter GGCs. It is worth mentioning the presence of four GGCs (NGC 6171, NGC 6362, NGC 6535, and NGC 7089) that are $\sim 2.5\sigma$ away from the linear fit, but their position might also be affected by uncertainties in the absolute cluster age (see the horizontal error bar plotted in the bottom right corner).

To further investigate the impact of possible systematics on the cluster ages, we used the results by Salaris & Weiss (2002) employing the Carretta & Gratton (1997) metallicity scale, for their 43 GGCs in common with our sample. They divided the sample into four different metallicity bins and for each of them selected a calibrating cluster. They then estimated the absolute age of the calibrating cluster by using the vertical method, that is, the difference in visual magnitude (ΔV) between the HB luminosity level and the MSTO. For all the other clusters in a specific metallicity bin, they estimated the relative age with respect to the calibrating cluster by using the horizontal method, that is, the difference in colour ($\Delta(V–I)$ or $\Delta(B–V)$) between the main sequence TO and the base of the RGB.

Data are shown in the bottom panel of Fig. 2.18. Once again, we found that the τ_{HB} index correlates with the cluster age. We performed the same linear fit as for the age estimates by VandenBerg et al. (2013); Leaman et al. (2013), and the coefficients are listed in Table 2.4 together with the standard deviation, which is equal to 1.89. The red and the blue lines display the linear fit and the 1σ limits, respectively. The difference between the second parameter clusters and the linear fit is larger than 2σ. This means that their peculiarity is independent of the adopted absolute age. Moreover, this plot also shows a few GGCs, roughly 2σ away from the linear fit, already identified in the top panels: NGC 6171 and NGC 6535, plus a new one, NGC 6652.

We analysed the age and the metallicity dependencies of τ_{HB}, since they are

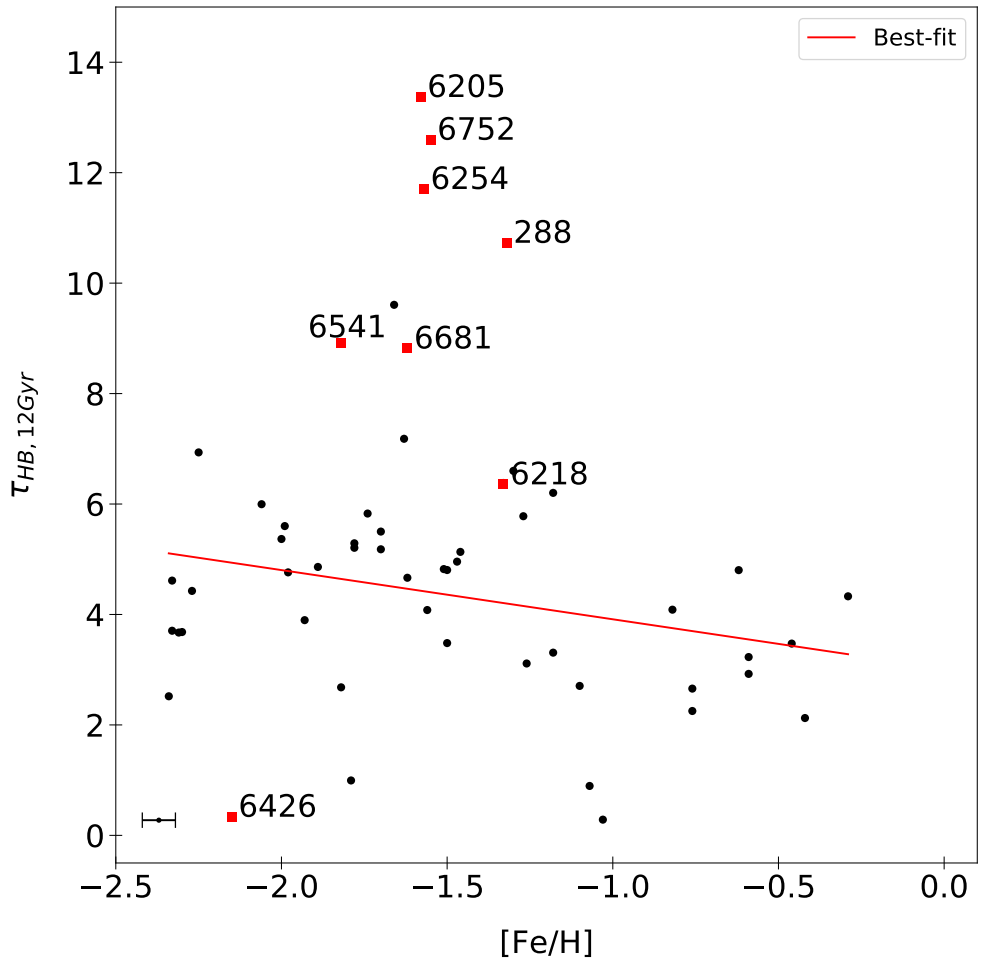

Figure 2.19: [Fe/H] vs. $\tau_{HB,12\ Gyr}$. The red line identifies the linear best-fit function of the plane, and red squares mark the eight second parameter clusters (see text for details).

considered as the main culprits affecting the HB morphology. However, the current findings further support the need for at least one more parameter to explain the observed variation in HB morphology. We assumed as a working hypothesis that the dispersion in the τ_{HB}-age diagram was caused by both age and helium variations (D'Antona et al., 2002; Caloi & D'Antona, 2005). Therefore, we decided to empirically remove the age dependence of τ_{HB}, and check whether the residuals in the reduced τ_{HB}-[Fe/H] diagram correlate with the spread in helium of the cluster. This empirical 'reduction' of τ_{HB} to a single age accounts automatically for possible age-metallicity relations in the cluster sample, as well as for the dependence of τ_{HB} on age at fixed metallicity. To perform this experiment we reduced the individual τ_{HB} measurements (Table 2.2) to the values they would have for an age of 12 Gyr ($\tau_{HB,12\ Gyr}$, using the ages by VandenBerg et al., 2013), as detailed below.

We first calculated the index value at an age of 12 Gyr as provided by the best-fit relation in the upper panel of Fig. 2.18 (value equal to 4.63); then, for each cluster, we calculated the values determined from the same best-fit relation but for the individual cluster ages. For each GGC we then calculated the difference $d\tau$ between the value expected at the cluster age and the value expected at 12 Gyr, and finally determined $\tau_{HB,12\ Gyr} = \tau_{HB} - d\tau$.

Figure 2.19 shows the $\tau_{HB,12\ Gyr}$ values as a function of [Fe/H]. In contrast to what we found in Fig. 2.16, after eliminating on average the effect of age, we now have a linear best-fit relation between $\tau_{HB,12\ Gyr}$ and the metal content (the red line in Fig. 2.19):

$$\tau_{HB,12\ Gyr} = 3.02 - 0.89 \cdot [Fe/H], \tag{2.5}$$

with dispersion $\sigma = 1.64$. The red squares identify the second parameter clusters: they still attain $\tau_{HB,12\ Gyr}$ values far from the best-fit relation.

In a very recent paper, Milone et al. (2018) estimated the spread in initial helium content ($0.245 \leq Y \leq 0.4$) for a sizeable sample of GGCs (57). They used data from the *HST* UV survey of Galactic GCs (*F275W*, *F336W*, and *F438W* filters of the ultraviolet and visual channel of *HST*/WFC3 (UVIS/WFC3), Piotto et al., 2015a; Milone et al., 2017) and from the Wide Field Channel of the Advanced Camera for Surveys (WFC/ACS) (*F606W* and *F814W* photometry, Sarajedini et al., 2007; Dotter et al., 2011) programmes. The He spread values, ∂Y_{max}, for each of the 56 GGCs in common with Milone et al. (2018) are listed in column 9 of Table 2.2.

The spread in helium content ranges from almost zero for NGC 6362, NGC 6535, and NGC 6717, up to ~0.08 for NGC 6388, NGC 6441, and NGC 7078. To further constrain the sensitivity of the new HB morphology index, we correlated the residuals of $\tau_{HB,12\ Gyr}$ of the best-fit function in Fig. 2.19 as a function of the metallicity, shown in Fig. 2.20.

The figure shows that the $\tau_{HB,12\ Gyr}$ index does not seem to be correlated with the spread in helium content. This means that, despite our attempt to limit the age and metallicity effects, the spread in helium content is not able to justify

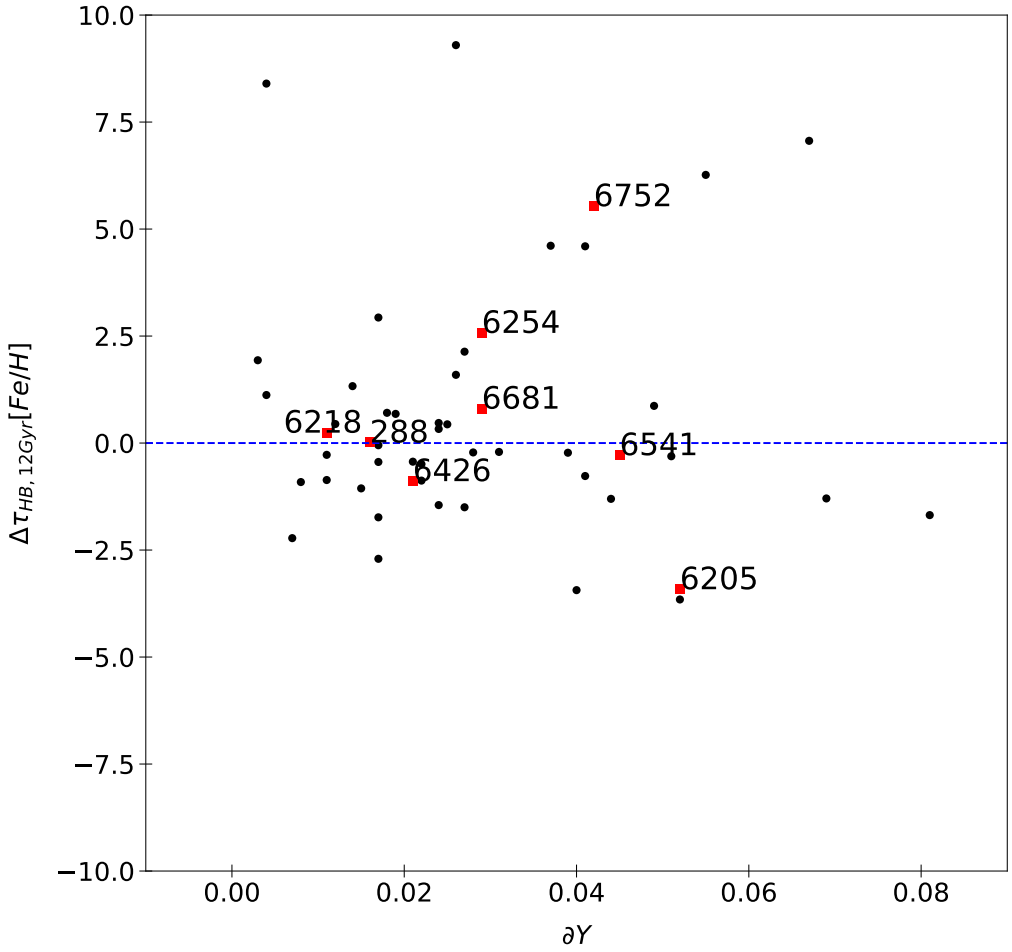

Figure 2.20: Residuals of the corrected $\tau_{HB,12\ Gyr}$ as a function of the metal content (Carretta et al., 2009) versus the spread in helium content ∂Y estimated by Milone et al. (2018). Red squares identify the second parameter globulars.

the observed spread in τ_{HB}. We note that we also estimated the residuals of the $\tau_{HB,12\ Gyr}$ using just space data (see Sect. 2.6) and related them to ∂Y values, since the latter quantities are evaluated from the same ***HST*** data. Once again, despite the data homogeneity, we did not find any clear correlation with ∂Y values.

2.8 Comparison with synthetic horizontal branch models

To constrain on a more quantitative basis the impact that both cluster age and spread in helium content have on the observed spread of the new HB morphology index, we decided to use a novel set of synthetic horizontal branch (SHB) models. The synthetic HB models have been computed employing HB tracks and progenitor isochrones from the α-enhanced a Bag of Stellar Tracks and Isochrones (BaSTI) stellar model library (Pietrinferni et al., 2006) [1] and a code fully described in Dalessandro et al. (2013). We considered three different metallicities, namely [Fe/H]=−0.7, [Fe/H]=−1.62, and [Fe/H]=−2.14 (all with [α/Fe]=0.4). The initial He abundances of the HB progenitors at these three metallicities are equal to Y=0.245, 0.246, and 0.256, respectively.

For each [Fe/H] we calculated first a set of synthetic HBs for an age equal to 12 Gyr (keeping Y constant for each [Fe/H]), assuming the RGB progenitor loses an amount of mass $\Delta M = 0.28\,M_\odot$, $\Delta M = 0.21\,M_\odot$, and $\Delta M = 0.16\,M_\odot$ for Fe/H]=−0.7, [Fe/H]=−1.62, and [Fe/H]=−2.14, respectively. The mass loss is estimated with a 1σ Gaussian spread equal to $0.01\,M_\odot$, irrespective of the chemical composition. In addition, assuming the same age and RGB mass loss, we calculated SHBs for each metallicity with an uniform distribution of initial Y for the progenitors, with a range ∂Y=0.03.

In brief, the synthetic HB code first draws randomly a value of Y with a uniform probability distribution between Y and $Y+\partial Y$ (∂Y=0 for the models at constant He) and determines the initial mass of the star at the RGB tip ($M_{\rm TRGB}$) from interpolation amongst the BaSTI isochrones of the chosen age. The mass of the corresponding object evolving along the HB ($M_{\rm HB}$) is then calculated as $M_{\rm HB} = M_{\rm TRGB} - \Delta M$, where ΔM is drawn randomly according to a Gaussian distribution with the specified mean values and σ. The magnitudes of the synthetic star are then determined according to its position along the HB track with appropriate mass and Y obtained by interpolation among the available set of HB tracks, after an evolutionary time t has been randomly extracted. The value of t is determined assuming that stars reach the ZAHB at a constant rate, employing a flat probability distribution ranging from zero to $t_{\rm HB}$, where $t_{\rm HB}$ is the time spent from the ZAHB to the He-burning shell ignition along the early asymptotic giant branch. The value of $t_{\rm HB}$ is set by the HB mass with the longest lifetime (the lowest masses for a given chemical composition). This implies that for some objects the randomly

[1] *http://www.oa-teramo.inaf.it/BASTI*

selected value of t will be longer than its $t_{\rm HB}$, meaning that they have already evolved to the next evolutionary stages.

Figure 2.21 shows the comparison between the $\tau_{HB,12\ Gyr}$ morphology index as a function of cluster iron abundance, and synthetic horizontal branch models. The blue line shows the SHB model at constant helium content ($\partial Y = 0$), while the black one is the synthetic model constructed assuming an internal spread in He content of $\partial Y = 0.03$. This value was adopted according to the recent estimates provided by Milone et al. (2018).

In the metal-rich regime ([Fe/H]≥-0.7) the predicted τ_{HB} weakly changes with the spread in helium content. This is a consequence of the fact that SHB models predict an extreme red HB morphology, minimally affected by the intrinsic parameters we are taking into account. In the metal-intermediate regime ([Fe/H]=-1.62) the τ_{HB} value predicted assuming an internal spread ∂Y is characterized by a spike. This is due to the fact that at this metallicity values, a small mass variation causes significant changes in the SHB colour.

To explain the existence of our second parameter clusters, the triangles in Fig. 2.21 identify a further three different synthetic models for [Fe/H]=-1.6, the mean metallicity value of our second parameter clusters, at the fixed age of 12 Gyr. The yellow triangle shows the synthetic τ_{HB} considering a higher spread in He compared to the one estimated by Milone et al. (2018) ($\partial Y = 0.05$) at the mass loss value we used for the blue and black models ($\Delta M = 0.21$); the magenta triangle identifies the model for $\partial Y = 0$ and a mass loss of $\Delta M = 0.29$ (higher of 0.08 $\mathrm{M}_{\odot}$ than the standard one); finally the green triangle identifies the synthetic τ_{HB} value for the case with $\partial Y = 0.05$ and $\Delta M = 0.25$.

Therefore, Fig. 2.21 shows that if we want to model the estimated values of $\tau_{HB,12Gyr}$ we have three different possibilities. If we adopt the spread in He content estimated by Milone et al. (2018) (e.g. $\partial Y = 0.05$ for NGC 6205, $\partial Y = 0.04$ for NGC 6752, $\partial Y = 0.03$ for NGC 6254, $\partial Y = 0.03$ for NGC 6681, considering the second parameter cluster with $[Fe/H] \sim -1.6$), we need to increase the mass loss value to 0.29, which is a value greater by 0.08 $\mathrm{M}_{\odot}$ than the one able to fit the bulk of the clusters. If we fix the mass loss to the one needed to model the bulk of the clusters ($\Delta M = 0.21$), then we need to increase the spread in He content (from $\partial Y = 0.03$ to, at least, $\partial Y = 0.05$). Finally, we can explain the existence of the second parameter cluster also considering a higher mass loss together with a higher spread in He. We note that the adoption of a higher mass loss cannot be attributed to systematic errors in age estimations, since they should be on the order of 2-3 Gyr.

2.9 Conclusions

We took advantage of a sample of 64 GGCs for which we have homogeneous and accurate *UBVRI* ground photometry and V ($F606W$), I ($F814W$) ACS/*HST* data

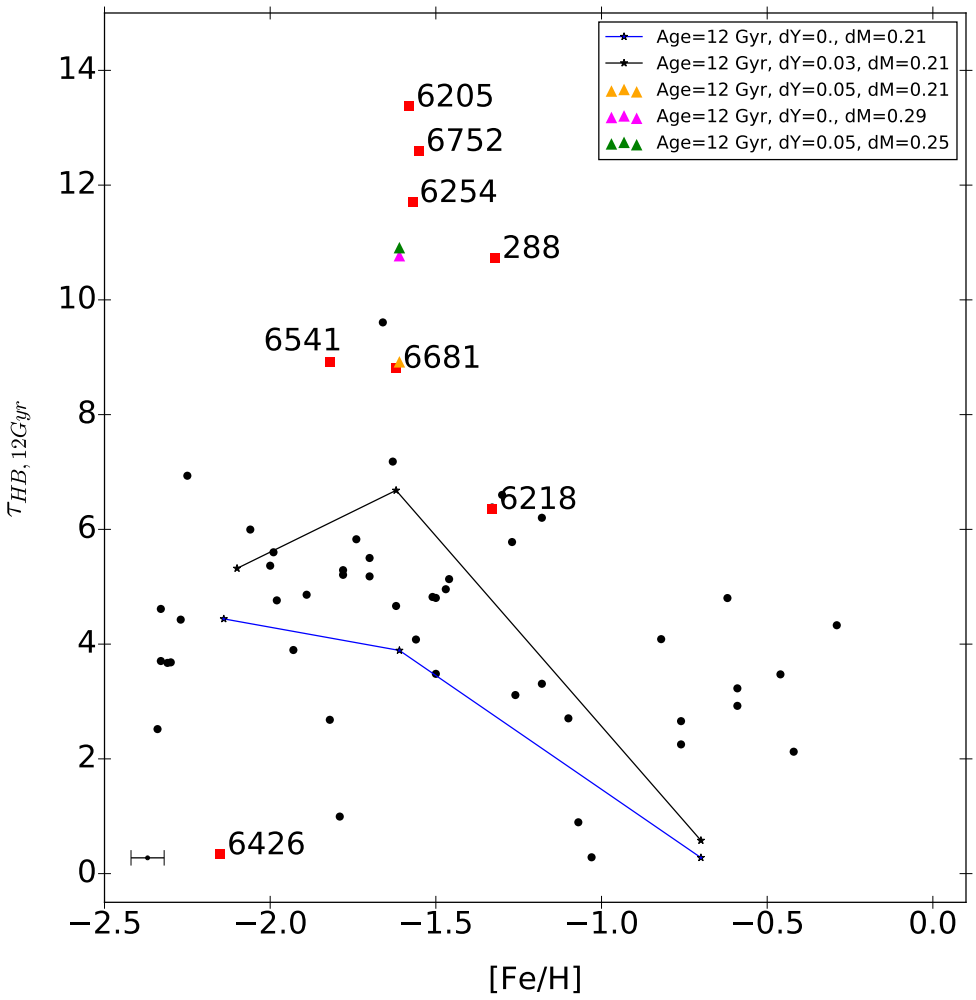

Figure 2.21: The new HB morphology index, $\tau_{HB,12\ Gyr}$, as a function of cluster iron abundance (Carretta et al., 2009). The two lines display synthetic HB models at fixed cluster age (12 Gyr), but either with a canonical helium content (∂Y = 0, blue line) or with an internal spread in He of ∂Y = 0.03 (black line). The coloured triangles identify three models for [Fe/H]=-1.6 for three different combinations of ∂Y and ΔM (see legend). Red squares mark the eight second parameter clusters. The error bar on the left corner gives the 0.1 dex error on the metal content.

(Sarajedini et al., 2007; Dotter et al., 2011), to introduce a new HB morphology index, named τ_{HB}, to investigate on a more quantitative basis the variation of the HB morphology when moving from the metal-poor to the metal-rich regime. We define τ_{HB} as the ratio of the area below the cumulative number distribution in apparent magnitude ($A_{CND}(I)$) and in colour ($A_{CND}(V–I)$) of the entire HB region.

Even though the estimate of the τ_{HB} index appears to be more complicated compared with HB morphology indices based either on star counts (***HBR′***, Lee et al. (1990)) or on specific evolutionary features (L1, L2, Milone et al. (2014)), it offers several advantages. Indeed, we found that τ_{HB} is a factor of seven more sensitive than the classical ***HBR′*** index and more than one order of magnitude more sensitive compared to L1 or L2 indices. Moreover, and even more importantly, the τ_{HB} 4index shows a linear trend over the entire metallicity range (-2.35≤[Fe/H]≤-0.12) covered by GGCs. Furthermore, the τ_{HB} index traces the HB luminosity function and it is independent of uncertainties affecting either the definition of different sub-groups (blue, red, variables) or the position of specific evolutionary features (L1, L2).

Moreover, to analyse the possible sensitivity of the HB morphology indices to the different contribution of inner and outer populations in GGCs, we estimated ***HBR′*** and τ_{HB} considering just space-based and just ground-based data. Comparing them to the results obtained using the combined ***HST*** and ground-based observations, we found that ***HBR′*** has on average lower differences (∼ 1.6%, just ground-based, and ∼ 1.3%, just space-based) than the ones attained by τ_{HB} (∼ 3.6%, just ground-based, and ∼ 2.9%, just space-based). For ***HBR′*** we observed major differences for the globulars in which the contribution of the red HB stars is mainly driven by ***HST*** observations. In τ_{HB} analysis we found higher differences for small and concentrated clusters, or for those clusters which are larger but located at higher distances. In all these cases most of the cluster stars are located inside the ACS FoV and so the space-based data give the higher contribution to the global τ_{HB}. In general our data are self-consistent and reliable and τ_{HB} higher relative differences could mean that it is sensitive to the different contribution given by inner and outer populations observed in GGCs.

To quantify the sensitivity of the τ_{HB} index on intrinsic stellar parameters, we investigated its dependence on cluster global properties (metallicity, absolute age, spread in He content). The main results of our analysis are the following:

Anti-correlation with cluster metallicity – We found a quadratic anti-correlation between τ_{HB} and [Fe/H]. The majority of the metal-poor globulars ([Fe/H]≤-1.5) have τ_{HB} between ∼ 4 and ∼ 9, while the metal-intermediate ones (-1.5≤ [Fe/H] ≤-1.0) have values between ∼ 2 and ∼ 5. On the other hand, the metal-rich clusters, with [Fe/H] ≥-1.0, attain τ_{HB} values smaller than two.

Identification of second parameter clusters – We found a subsample of eight GGCs in the metal-poor and metal-intermediate regime (-1.82≤ [Fe/H] ≤-1.32) which, at fixed metallicity, are characterized by τ_{HB} values that are, on average,

at least a factor of two larger than canonical clusters. The outlier clusters do not display any peculiarity in the HBR' metallicity plane. To investigate their HB morphology, we selected three of them that sample the metal-rich ([Fe/H]=-1.33, NGC 6218), metal-intermediate ([Fe/H]=-1.57, NGC 6254), and metal-poor ([Fe/H]=-1.82, NGC 6541) regimes. We compared their $I, V–I$ CMDs to those of three 'regular' clusters with similar metallicities within the errors (NGC 362, NGC 6934, and NGC 6144). For each cluster pair, we find similar HBR' values but different τ_{HB} values, with differences even on the order of three. For these reasons we can associate these clusters in our sample with the so-called second parameter clusters.

Correlation with cluster age – We investigate the relation between our HB morphology index τ_{HB} and the absolute cluster age. To exclude possible dependence on the particular age estimation, we used the different homogeneous evaluations from VandenBerg et al. (2013); Leaman et al. (2013); Salaris & Weiss (2002), finding a linear correlation betweenτ_{HB} and the absolute age. We found that, in general, when moving from red to blue HB morphology, the GGCs become older. The second parameter clusters selected according to the τ_{HB}-metallicity plane appear to be peculiar also in the τ_{HB}-absolute age plane. In particular they attain cluster ages ranging from $\sim$ 11.5 to $\sim$ 13 Gyr. Moreover, they seem to be characterized by bluer HB morphologies than the typical clusters.

Reductio ad unum – We limited the age impact on our analysis by reducing the τ_{HB} values to the ones they would attain for an age of 12 Gyr. In contrast to what we originally found, we found a linear correlation between the corrected $\tau_{HB,12\ Gyr}$ values and [Fe/H]. However, the second parameter clusters are still located far from the best-fit linear relation of the plane.

Comparison with spread in helium content – We investigated our new HB morphology index in the context of internal helium content variation, supposed to be one of the main drivers of the HB morphology. We compared the residuals of the corrected $\tau_{HB,12Gyr}$ as a function of cluster metallicity with the internal spread in helium content, ∂Y, estimated by Milone et al. (2018), but we did not find a solid correlation.

Comparison with theory – We calculated a novel set of synthetic horizontal branch models to investigate the impact on τ_{HB} of the spread in Helium content and mass loss along the branch, at the fixed age of 12 Gyr. We found that we can fit the second parameter clusters in our sample if: we fix the spread in He content to the one estimated by Milone et al. (2018) and we increase the mass loss value from $\Delta M = 0.21$ (the one able to fit the bulk of the clusters) to $\Delta M = 0.29$; we fix the mass loss to $\Delta M = 0.21$ and we increase the spread in He content from $\partial Y = 0.03$ (Milone et al., 2018) to, at least, $\partial Y = 0.05$; we consider a higher mass loss together with an higher spread in He content.

Nature versus nurture – It is not clear whether the outlier clusters display a bluer HB morphology because they are intrinsically different (nature) or because

the HB morphology is tracing a specific dynamical status of the cluster (nurture).

Chapter 3

Horizontal Branch photometric parametrization on nearby dwarf spheroidal galaxies

Dwarf galaxies represent a fundamental tool to investigate a number of important problems currently affecting different astrophysical fields.

One of the most interesting for the scientific community is their role in the so-called "missing satellite problem" (Klypin et al., 1999; Moore et al., 1999), which could compromise the validity of the current cosmological model: the Λ-Cold Dark Matter (ΛCDM) scenario. Indeed, cosmological simulations predict an over-abundance of CDM sub-halos compared to satellite galaxies known to exist in the Local Group.

Possible solutions have been proposed through the years, both from the theoretical and observational point of views. For example, the inclusion in simulations of some physical processes able to suppress star-formation in sub-halos allows to make these systems starless and consequently difficult to observe. Another solution is considering our current catalogues of dwarfs incomplete due to limited survey areas and depths, causing bias at the faint end of the galaxy luminosity and mass functions (see also Chapter 5). However, the advent of large and deep surveys, like the Sloan Digital Sky Survey (SDSS) and PAN-STARRS, allowed to detect an increasing number of dwarf galaxies and to discover the ultra faint dwarf (UFD) galaxies. Therefore, current observations seem to be close to solve of the missing satellite problem.

In particular, dwarf spheroidal (dSph) galaxies are faint objects of low surface brightness, they have a typical size of $10 - 100pc$ and they appear to not contain gas. They are observed to be characterized by large velocity dispersions, hence they represent a fundamental tool to trace and test the distribution of dark matter (see for example Mateo, 1997). Moreover, they are, at fixed stellar mass, metal-rich than dwarf irregulars (see for example Mateo, 1998) and they show a complex

SFH, characterized by an old ($12-13Gyr$) star-formation episode with a number of following episodes.

This leads to the presence of visible multiple populations in their observed CMDs. In general, the presence of the old stellar population is signalled by the HB stars: an high populated blue region in the HB morphology is observed for example in Carina and Ursa Minor dSphs. Moreover, all dSph galaxies are also characterized by a red region of the HB, but in many cases it is difficult to distinguish it from the RC, which is located at the base of the RGB of populations with an age between 1 and 10 Gyr and consists of stars burning He in their core (Mateo, 1998).

Conversely, the presence of one or more well-populated SGBs below the RC gives the hint of the existence of several intermediate-age populations (2-6 Gyr) in the dSph galaxies. Moreover, the observed RGB is affected by the age-metallicity degeneracy in the sense that increasing age or metallicity have the same effect on the RGB colour, which becomes redder. This means that we have the overlap of populations of different age or metallicity on the RGB. With the current deep surveys, we are able to eliminate the age-metallicity degeneracy only for Local Group dwarf galaxies, for which we can resolve the MSTO for the age-dating of the stellar population. Therefore, studying the SGB, RC and HB phases allows to determine the SFH of these resolved CSPs, and hence, to understand the physical processes behind galaxy formation.

Actually, the HB phase is usually neglected in the SFH estimate of dSph galaxies, since, as we have shown in Chapter 2, the HB morphology of GGCs, much simpler stellar populations than the ones characterizing the dSphs, is affected by the 2ndP problem. Moreover, in the literature there are findings on the 2ndP effect observed in the HB morphology of dSphs and GCs belonging to them (e.g., Buonanno et al., 1985; Majewski et al., 1999; Harbeck et al., 2001; Sarajedini et al., 2002). These observations together with the similar spatial distribution between GGCs in the halo and the dSph galaxies, can be the evidence of a possible connection between the origin of old GGCs and a tidal disruption of the ancient numerous dSph systems around the Galaxy. Therefore, despite the stressed difficulties, it is important to take advantage of HB morphology in determining the SFH of dSph galaxies (see e.g., Salaris et al., 2013; Savino et al., 2015).

For this reason, we decided to more deeply investigate the HB morphology of a sample of 19 nearby dSph isolated and satellite galaxies of Milky Way and Andromeda taking advantage of our new photometric index τ_{HB} presented in Chapter 2. In this way, we conduct the very first systematic study about the HB morphology of a large sample of nearby dSph galaxies within the Local Group.

The Chapter is organized as follows. In Sect. 3.1 we present our sample of dSph galaxies and the available photometry. In Sect. 3.3, we investigate the validity of τ_{HB} index estimated taking advantage of $I, B-I$ diagram instead of the $I, V-I$ one analysed in Chapter 2. This is essential to analyse the HB morphology of

the majority of Andromeda dSphs, for which we data in $F475W$ (~ B) and in $F814W$ (~ I) from HST/ACS. In Sect. 3.4, we show our results on the estimate of τ_{HB} index for dSph galaxies and its correlation with the absolute age and the metallicity of these objects.

We note that throughout the Chapter, we consider the age of the oldest population (first SFH episode), as the absolute age of the dSphs, since we are interested in the HB stellar evolutionary phase, in which the oldest stars are burning He in their core and Hydrogen in a shell. We note that we used the old dSph stellar population age values available in the literature and that their uncertainty is undoubtedly conservative.

3.1 Dwarf spheroidal galaxy sample

We take advantage of a sample of 19 nearby dSph galaxies: eight are Milky Way [MW] satellites, nine are Andromeda [M31] satellites and two are isolated dSph galaxies in the Local Group [LG].

For the eight MW dSph galaxies, we have secure and homogeneous ground-based optical $UBVRI$ data (provided by P. B. Stetson), while for the rest of the sample we have space-based HST/ACS data in different photometric bands. We have data in $F606W$ and in $F814W$ photometric bands for two dSphs, namely NGC 147 and NGC 185 (Monelli et al., 2017), while for the other eight galaxies we have data in $F475W$ and in $F814W$ (Monelli et al., 2010a,b, 2017; Skillman et al., 2017; Hidalgo et al., 2011). We note that we used the relations by Sirianni et al. (2005) to transform $F475W$, $F606W$ and $F814W$ data into B, V, I Johnson-Cousins bands, respectively.

In Table 3.1 we list the sample of dSphs with their main parameters together with the available photometric data.

We performed a candidate galaxy/field star separation for the MW dSph galaxies based on stellar SEDs following the same procedure we adopted in Chapter 2 for our sample of GGCs and fully described in Calamida et al. (2017). We show two examples of our selection (see Appendix E for more CMDs) in Figure 3.1 and Figure 3.2 representing the V, B–I CMD of Sculptor and Carina dSph galaxies, respectively, for total (left panels), candidate galaxy (central panel) and candidate field (right panel) stars.

A glance to the Figures reveals that Sculptor seems to be characterized by a much simpler SFH if compared to Carina. Indeed, in its CMD (Figure 3.1) we can observe a well populated HB, much less colour-extended than the one characterizing Carina (Figure 3.2) and a rich RC, while we cannot observe the two distinct MSTOs and the two distinct SGBs revealing the existence of a second stellar population of intermediate age we can observe in Carina CMD (Figure 3.2). These findings seem to confirm that Carina has experienced two or more episodes of SFHs, separated by several Gyr. Moreover, the presence of a blue plume above

Table 3.1: Dwarf spheroidal galaxies in the sample with parameters used in this work.

ID	Association	Ra (J2000)	Dec (J2000)	*U*	*B*	*V*	*R*	*I*	*F475W*	*F606W*	*F814W*	Age(Gyr)	E(B-V)	[Fe/H]	μ	M_* ($10^6 M_\odot$)	Ref.
Carina	MW	06:41:36.7	-50:57:58	✓	✓	✓	✓	✓				12.0 ± 0.5	0.061	-2.15 ± 0.06	20.11	0.38	[1],[2],[3],[4]
Draco	MW	17:20:12.4	-50:57:58	✓	✓	✓	✓	✓				12.5 ± 0.5	0.027	-1.93 ± 0.01	19.40	0.29	[2],[5],[6],[7],[8]
Sculptor	MW	01:00:09.4	-33:42:33	✓	✓	✓	✓	✓				13.0 ± 0.5	0.018	-1.90 ± 0.35	19.67	2.3	[2],[9],[10],[11],[12]
Ursa Minor	MW	15:09:08.5	+67:13:21	✓	✓	✓	✓	✓				13.0 ± 1.0	0.030	-2.13 ± 0.01	19.40	0.29	[2],[5],[8],[13],[14]
Fornax	MW	02:39:59.3	-34:26:57	✓	✓	✓	✓	✓				12.0 ± 0.5	0.021	-0.99 ± 0.01	20.84	20	[2],[3],[8],[9]
Leo I	MW	10:08:28.1	+12:18:23	✓	✓	✓	✓	✓				12.0 ± 0.5	0.036	-1.43 ± 0.01	22.02	5.5	[2],[8],[15],[16]
Leo II	MW	11:13:28.8	+22:09:06	✓	✓	✓	✓	✓				12.0 ± 0.5	0.017	-1.62 ± 0.01	21.84	0.74	[2],[8],[15],[16]
Sextans (I)	MW	10:13:03	-01:36:53	✓	✓	✓	✓	✓				12.0 ± 0.5	0.047	-1.93 ± 0.01	19.67	0.44	[2],[8],[17],[18]
Andromeda I	M31	00:45:39.8	+38:02:28						✓		✓	12.5 ± 0.5	0.047	-1.45 ± 0.04	24.36	3.9	[2],[19],[20],[21],[22]
Andromeda II	M31	01:16:29.8	+33:25:09						✓		✓	12.5 ± 0.5	0.054	-1.64 ± 0.04	24.07	7.6	[2],[19],[20],[21],[22]
Andromeda III	M31	00:35:33.8	+36:29:52						✓		✓	12.5 ± 0.5	0.050	-1.78 ± 0.04	24.37	0.83	[2],[19],[20],[21],[22]
Andromeda XV	M31	01:14:18.7	+38:07:03						✓		✓	12.5 ± 0.5	0.041	-1.80 ± 0.20	24.00	0.49	[2],[21],[23],[24]
Andromeda XVI	M31	00:59:29.8	+32:22:36						✓		✓	12.5 ± 0.5	0.059	-2.00 ± 0.20	23.60	0.41	[2],[21],[23],[24]
Andromeda XXVIII	M31	22:32:41.2	+31:12:58						✓		✓	12.5 ± 0.5	0.080	-1.84 ± 0.10	24.10	0.21	[2],[21],[23],[25],[26]
LGS 3	M31	01:03:55.0	+21:53:06						✓		✓	11.7 ± 0.5	0.04	-1.50 ± 0.30	24.43	0.96	[2],[20],[27],[28]
NGC 147	M31	00:33:12.1	+48:30:32							✓	✓	12.0 ± 0.5	0.184	-1.10 ± 0.01	24.15	62	[2],[20],[29],[30]
NGC 185	M31	00:38:58.0	+48:20:15							✓	✓	12.0 ± 0.5	0.172	-1.30 ± 0.10	23.95	68	[2],[20],[30],[31]
Cetus	LG	00:26:11.0	-11:02:40						✓		✓	12.0 ± 0.5	0.03	-1.70 ± 0.10	24.39	2.6	[2],[20],[32],[33]
Tucana	LG	22:41:49.6	-64:25:10						✓		✓	13.0 ± 0.5	0.031	-1.95 ± 0.15	24.74	0.56	[2],[34],[35],[36],[37]

Notes: List of the Dwarf spheroidal galaxies in the sample with parameters used in this work: J 2000 coordinates, data availability, age in Gyr, colour excess E(B-V), [Fe/H], distance modulus μ and references.

References: [1] Cannon et al. (1977), [2] McConnachie (2012), [3] Pietrzyński et al. (2009), [4] Fabrizio et al. (2015), [5] Wilson (1955), [6] Bonanos et al. (2004), [7] Girardi et al. (2004), [8] Kirby et al. (2011), [9] Shapley (1938), [10] Pietrzyński et al. (2008), [11] de Boer et al. (2012), [12] Martínez-Vázquez et al. (2016), [13] Carrera et al. (2002), [14] Cohen & Huang (2010), [15] Harrington & Wilson (1950), [16] Bellazzini et al. (2004), [17] Irwin et al. (1990), [18] Lee et al. (2009b), [19] van den Bergh (1972), [20] McConnachie et al. (2005) [21] Skillman et al. (2017), [22] Kalirai et al. (2010), [23] Ibata et al. (2007), [24] Letarte et al. (2010), [25] Slater et al. (2011), [26] Collins et al. (2015), [27] Karachentseva (1976), [28] Hidalgo et al. (2011), [29] Herschel (1833), [30] Geha et al. (2010), [31] Herschel (1789), [32] Whiting et al. (1999), [33] Monelli et al. (2010a), [34] Lavery (1990), [35] Bernard et al. (2009), [36] Monelli et al. (2010b), [37] Fraternali et al. (2009)

the MS could suggest the existence of a very young stellar population (Savino et al., 2015).

In contrast to what we did for ground-based photometry, we did not make any candidate galaxy/field star separation on space-based data, because we expect negligible contamination by field stars in the ACS FoV ($\sim 4 arcmin$). In Figure 3.3 we show, as an example, the *I*, *B–I* CMD of Andromeda III dSph, which appears to be very similar to a GGC CMD, implying that the SFH of this galaxy is much simpler than the one undergone by Sculptor or Carina dSphs.

3.2 The *HBR* morphology index for dwarf spheroidal galaxies

We firstly investigated the HB morphology in our sample of dSph galaxies estimating the classical *HBR′* index using the same formulae defined in Sect. 2.3. For each galaxy, we defined two boxes to identify the candidate blue (B) and red (R) HB stars. Moreover, we took advantage of the most updated variable star catalogues found in the literature to estimate the number of variables (V). The counts for B, R, V (with references) are listed in Table 3.2 together with the estimated values for *HBR′* and the references for V counts.

Data plotted in Figure 3.4 show that dwarf galaxies in the Local Group (LG) cover a limited range in HB morphologies. Indeed nearby gas-poor dwarfs when

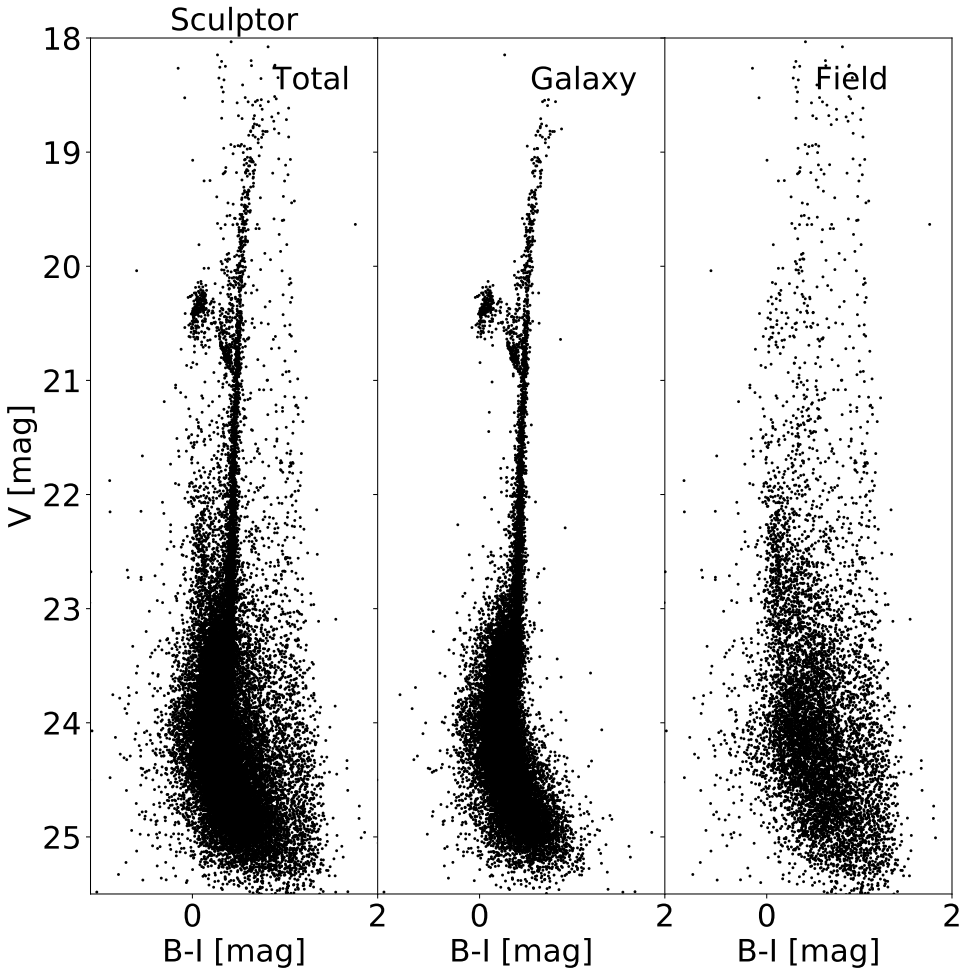

Figure 3.1: Sculptor V, B–I CMD of the entire catalogue (left panel), candidate galaxy (central panel) and candidate field (right panel) stars.

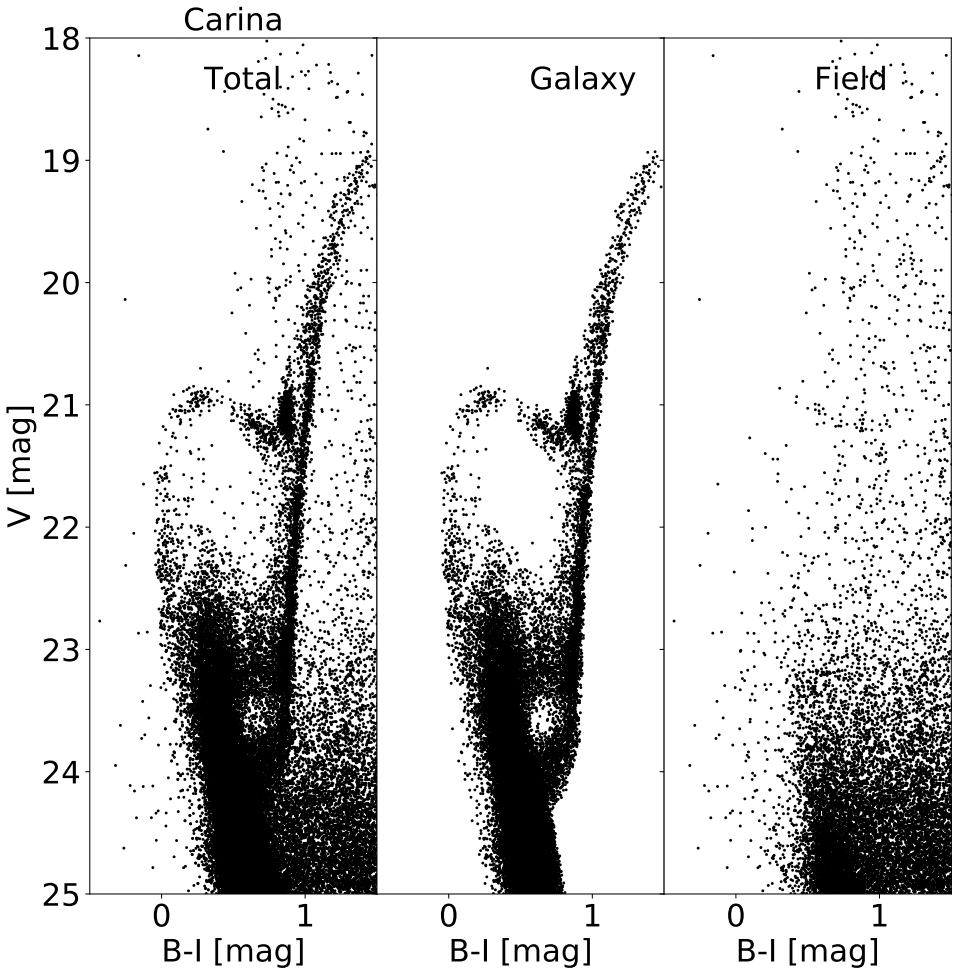

Figure 3.2: Carina *V*, *B–I* CMD of the entire catalogue (left panel), candidate galaxy (central panel) and candidate field (right panel) stars.

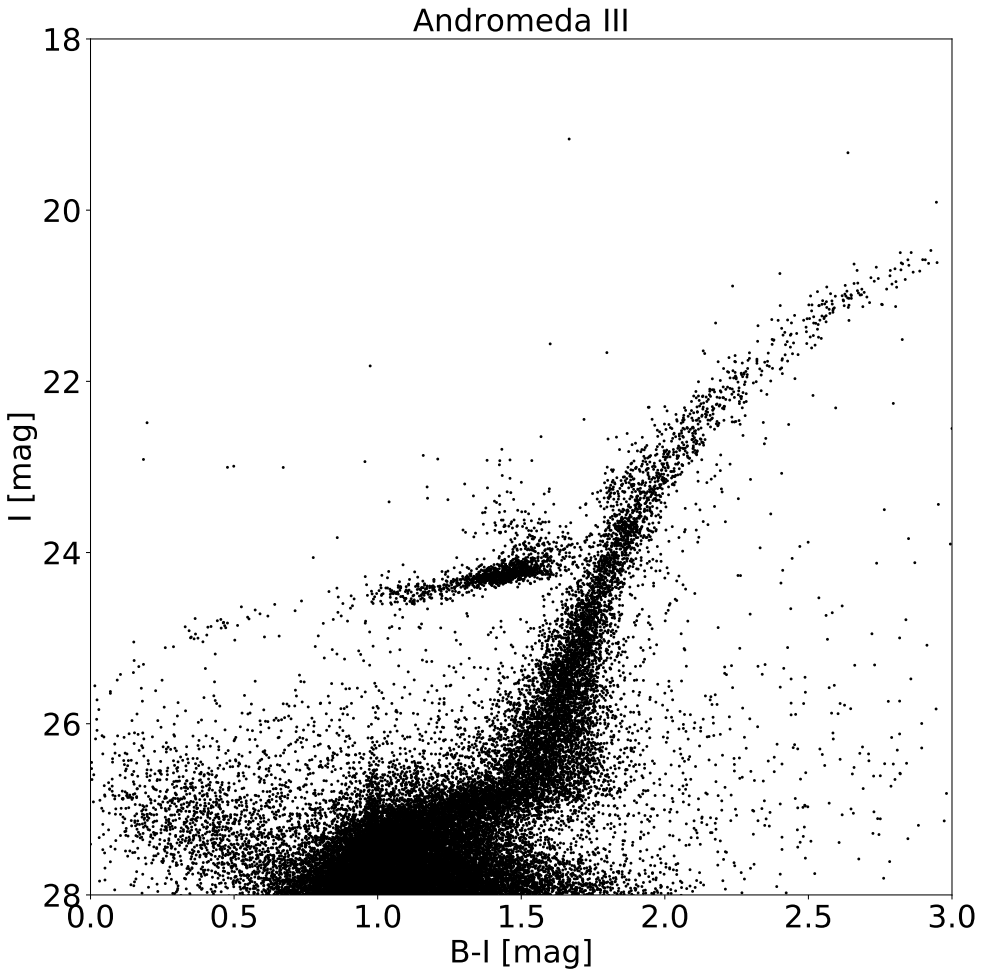

Figure 3.3: Andromeda III *I*, *B–I* CMD.

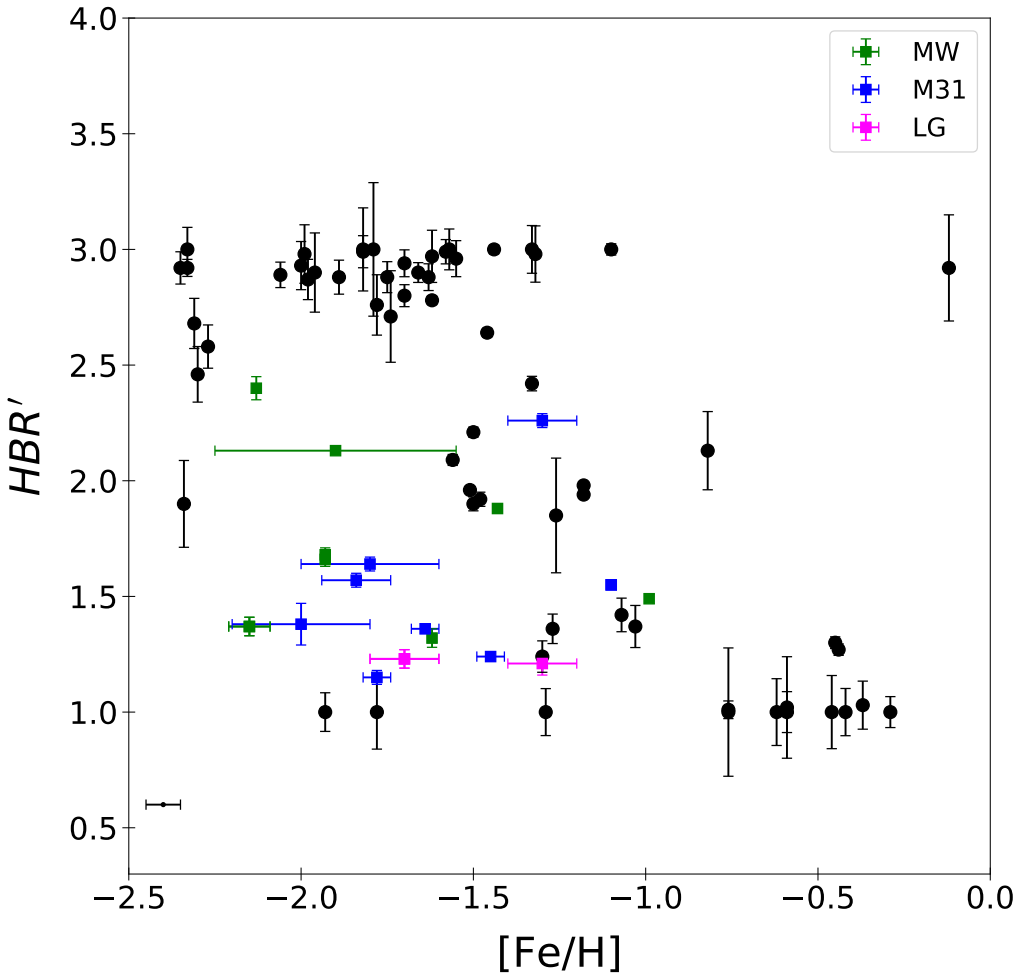

Figure 3.4: Observed HBR' values as a function of metal content for GGCs (black dots) and our sample of dSph galaxies (coloured squares, see legend in the upper right corner). The error bars on dSph [Fe/H] values show the dispersion of metallicity distributions.

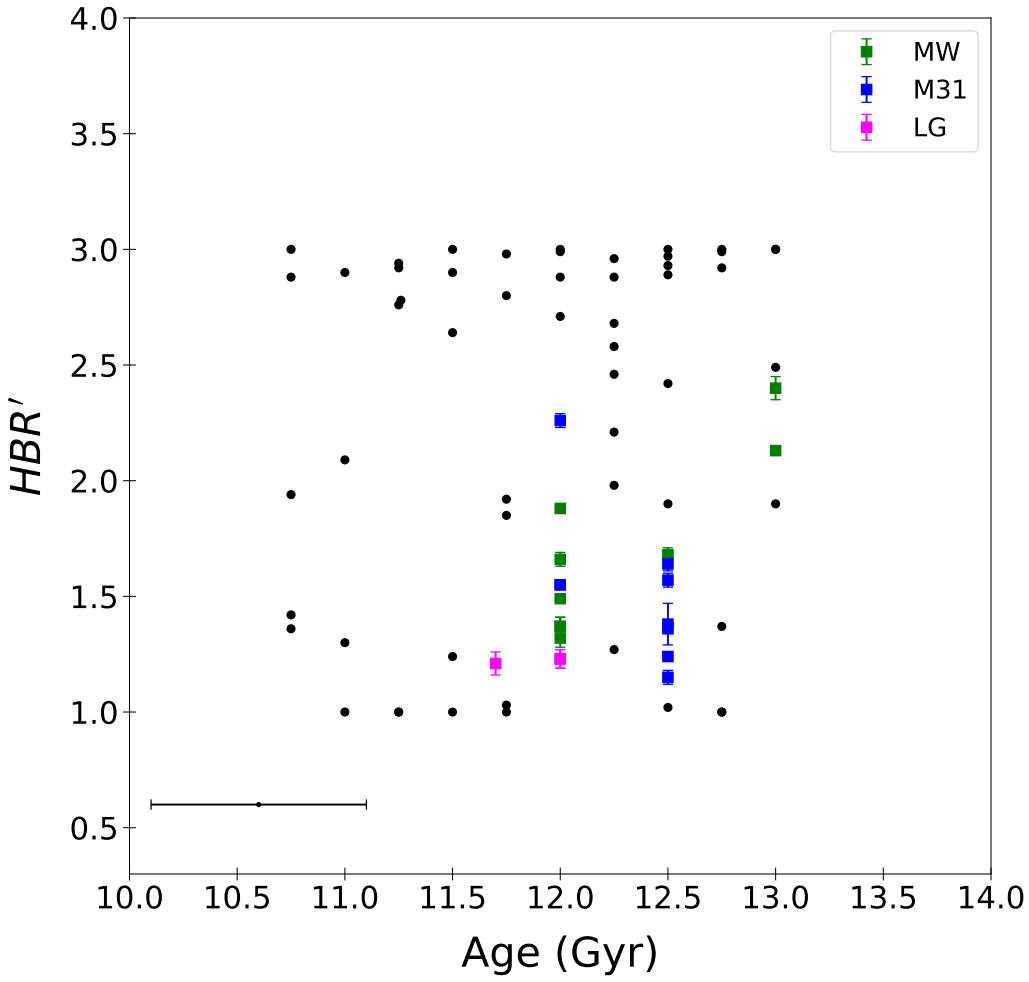

Figure 3.5: Observed HBR' values as a function of the absolute age for GGCs (black dots) and our sample of dSph galaxies (coloured squares, see legend in the upper right corner).

Table 3.2: Parameters and observational HBR' values for the dSph galaxies in the sample.

ID	Association	B	R	V	HBR'	Age (Gyr)	[Fe/H]	References
Carina	MW	69	458	95	1.37±0.04	12.0 ± 0.5	-2.15 ± 0.06	[1]
Draco	MW	40	197	267	1.68 ±0.03	12.5 ± 0.5	-1.93 ± 0.01	[2]
Sculptor	MW	1031	725	536	2.13±0.01	13.0 ± 0.5	-1.90 ± 0.35	[3]
Ursa Minor	MW	325	30	83	2.40±0.05	13.0 ± 1.0	-2.13 ± 0.01	[4]
Fornax	MW	391	2666	1426	1.49 ± 0.01	12.0 ± 0.5	-0.99 ± 0.01	[5]
Leo I	MW	219	289	100	1.88± 0.01	12.0 ± 0.5	-1.43 ± 0.01	[6]
Leo II	MW	53	591	148	1.32 ±0.04	12.0 ± 0.5	-1.62 ± 0.01	[7]
Sextans (I)	MW	71	248	199	1.66±0.03	12.0 ± 0.5	-1.93 ± 0.01	[8]
Andromeda I	M31	221	2528	302	1.24±0.02	12.5 ± 0.5	-1.45 ± 0.04	[9]
Andromeda II	M31	281	1730	257	1.36±0.02	12.5 ± 0.5	-1.64 ± 0.04	[9]
Andromeda III	M31	38	1149	116	1.15± 0.03	12.5 ± 0.5	-1.78 ± 0.04	[9]
Andromeda XV	M31	94	270	121	1.64±0.03	12.5 ± 0.5	-1.80 ± 0.20	[9]
Andromeda XVI	M31	18	90	9	1.38±0.09	12.5 ± 0.5	-2.00 ± 0.20	[9]
Andromeda XXVIII	M31	160	469	90	1.57±0.03	12.5 ± 0.5	-1.84 ± 0.10	[9]
LGS 3	M31	43	476	28	1.21±0.05	11.7 ± 0.5	-1.50 ± 0.30	[10]
NGC 147	M31	214	90	177	2.26±0.03	12.0 ± 0.5	-1.10 ± 0.01	[11]
NGC 185	M31	1080	3533	818	1.55±0.01	12.0 ± 0.5	-1.30 ± 0.10	[11]
Cetus	LG	28	844	187	1.23±0.04	12.0 ± 0.5	-1.70 ± 0.10	[12]
Tucana	LG	387	596	345	1.84±0.01	13.0 ± 0.5	-1.95 ± 0.15	[12]

Notes: Columns are: B, R,V, HBR', Age in Gyr, [Fe/H] and references for V counts.

References: [1] Coppola et al. (2015), [2] Kinemuchi et al. (2008), [3] Martínez-Vázquez et al. (2016), [4] Nemec et al. (1988), [5] Fiorentino et al. (2017) , [6]Stetson et al. (2014b), [7]Siegel & Majewski (2000) , [8] Vivas et al. (2019), [9] Martínez-Vázquez et al. (2017), [10]Bernard & Lcid Team (2007), [11] Monelli et al. (2017) , [12] Bernard et al. (2009).

compared with GGCs lack of both extremely blue and extremely red HB morphologies. This outcome applies not only to MW and M31 satellites, but also to isolate dwarf galaxies like Cetus and Tucana. There are a few galaxies (namely, Sculptor, Ursa Minor and NGC 147) that have bluer HB morphologies, but their HBR' values on average are, at fixed iron content, systematically redder than GGCs.

The comparison between the HBR' of nearby dwarfs and GGCs (see Figure 3.5) brings forward the evidence that the oldest stellar populations in the former stellar systems only cover absolute ages older than 12 Gyr. This means that they appear to be coeval with the old tail of GGCs. However, we cannot reach firm conclusions concerning possible systematic differences, because the absolute ages of nearby dwarfs were estimated using different approaches (see Tables 3.1 and 3.2).

We note that our estimates on B and R counts can be affected by our galaxy/-field star separation. Calamida et al. (2017) already tested our technique on ω Cen, whose SFH is similar to the complex SFHs characterizing the dSph galaxies. The method is conservative, in the sense that we prefer to lose a few candidate galaxy stars rather than taking into account possible candidate field stars. Indeed, we estimated the HBR' values for GGCs presented in Chapter 2 for which we can separate the cluster from field stars using Gaia proper motions. We found a mean difference of $\sim$ 1% between the HBR' values estimated using the candidate HB cluster stars from our selection and the ones calculated using the cluster stars from proper motion selection.

3.3 τ_{HB} estimate in $I, B–I$ diagram

To analyse the HB morphology in dSph galaxies, we also used our new τ_{HB} index. Since for dSph galaxies associated to Andromeda, we have only IBI photometry, we need to verify the validity of our τ_{HB} HB morphology index also in $I, B–I$ diagram:

$$\tau_{HB}(IBI) = \frac{A_{CND}(I)}{A_{CND}(B–I)} \tag{3.1}$$

To do this, for each cluster of the sample described in Chapter 2 we estimated the τ_{HB} through the areas subtended by the CNDs as a function of magnitude (I-band) and colour ($B–I$) of HB stars. Therefore, in this analysis we defined a box in the I, $B–I$ CMD large enough to include all the HB stars and then we computed the CND in I and in $B–I$ colour.

In this case, to perform homogeneous star counts, we defined a box covering 4 mag in $B–I$ colour, while we left unvaried the range in I-band (6.5 mag). Also in this analysis, the selected HB stars are sorted as a function of the I-band apparent magnitude and we cumulated the star counts starting from the faintest and reddest stars in the box.

Since for the GGC sample the B-band is available only for ground-based photometry, we decided to estimate $\tau_{HB}(IBI)$ considering just ground-based B, I data

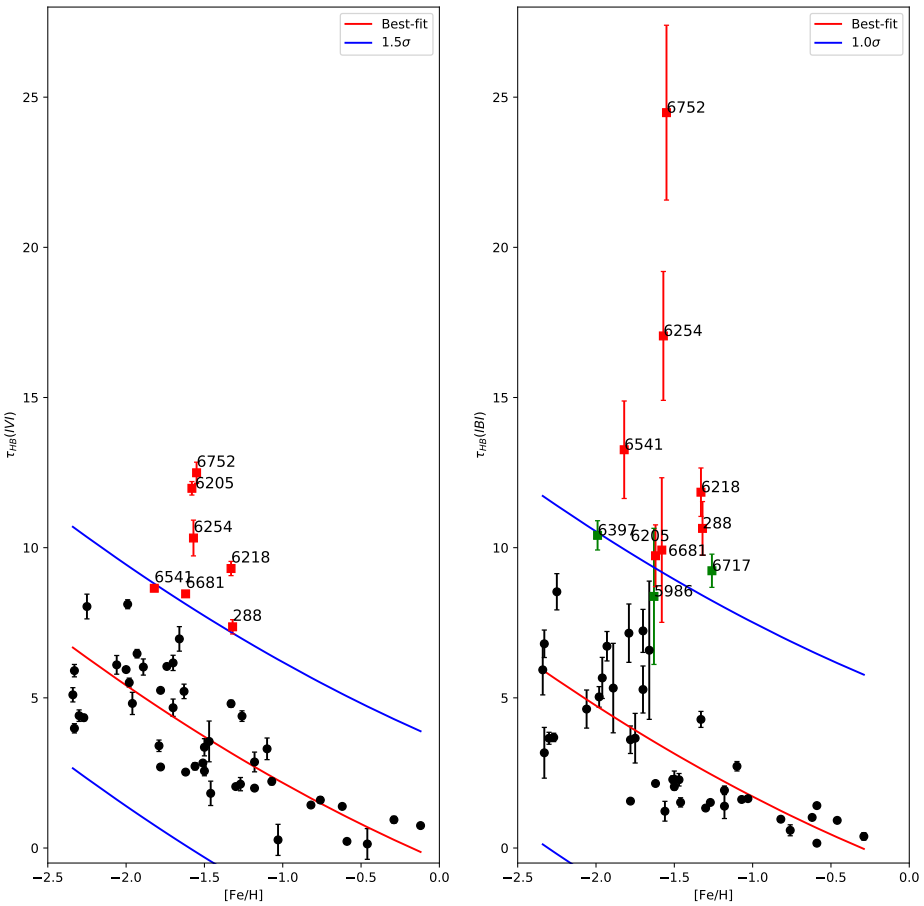

Figure 3.6: [Fe/H] vs $\tau_{HB}(IVI)$ (left panel) and $\tau_{HB}(IBI)$ (right panel). Red lines show the best-fit relations in both panels, red squares mark the 2ndP clusters already identified in Chapter 2, while green squares show other three possible clusters in $\tau_{HB}(IBI) - [Fe/H]$ diagram, peculiar for their $\tau_{HB}(IBI)$ values.

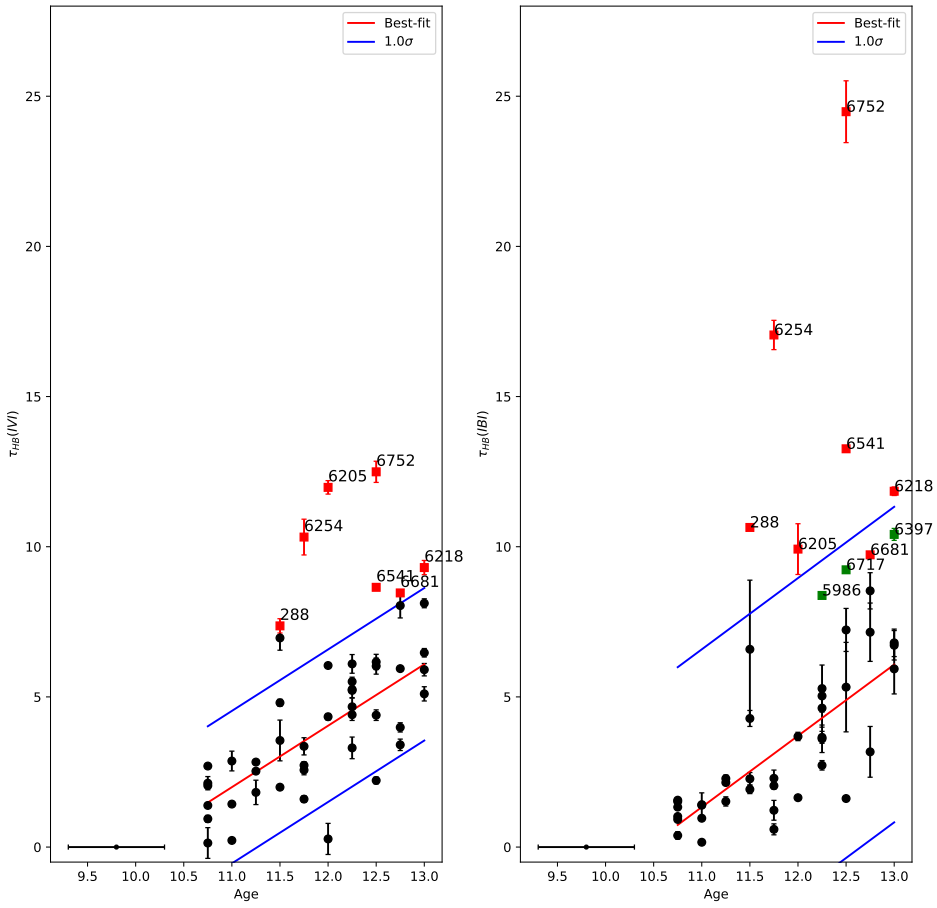

Figure 3.7: Age vs $\tau_{HB}(IVI)$ (left panel) and $\tau_{HB}(IBI)$ (right panel). Red lines show the best-fit relations in both panels, red squares identifies the 2ndP clusters already defined in Chapter 2, while green squares show the three possible outliers identified in $\tau_{HB}(IBI) - [Fe/H]$ diagram. The error bar in the lower left corner shows the conservative ± 0.5 Gyr error on the GGC ages.

and to compare these values to the ones in $I, V–I$ diagram ($\tau_{HB}(IVI)$) estimated using just ground-based observations (see Sect. 2.2).

Figure 3.6 shows $\tau_{HB}(IVI)$ (left panel) and $\tau_{HB}(IBI)$ as a function of [Fe/H] values. As already found out in Sect. 2.7, a quadratic anti-correlation ($\tau_{HB}(IBI) = 0.34 \cdot [Fe/H]^2 - 2.02 \cdot [Fe/H] - 0.64$, with $\sigma = 5.8$) still exists for $\tau_{HB}(IBI) - [Fe/H]$, even more linear if we compare it to the one found in Eq. 2.4. We find an higher dispersion in $\tau_{HB}(IBI)$ values if compared to $\tau_{HB}(IVI) - [Fe/H]$ diagram, which seems to be even more significant for $[Fe/H] < -1.5$. Finally, the 2ndP clusters (red squares) defined in Chapter 2 are located above the 1σ levels in the diagram and we are also able to identify other three clusters (green squares), namely NGC 5986, NGC 6397 and NGC 6717, peculiar for their $\tau_{HB}(IBI)$ values ($\sim 8, 10, 9$, respectively) and located above the 1σ levels. As the 2ndP clusters previously identified, NGC 5986, NGC 6397 and NGC 6717 are characterized by a bluer HB morphology if compared to the GGCs with similar metallicity.

Figure 3.7 shows $\tau_{HB}(IVI)$ (left panel) and $\tau_{HB}(IBI)$ as a function of the absolute ages of the clusters. As expected, we find a linear correlation also between $\tau_{HB}(IBI)$ and the age ($\tau_{HB}(IBI) = 2.4 \cdot Age - 24.8$, with $\sigma = 5.3$). The 2ndP clusters (red squares) are still located above the 1σ levels, except for NGC 6681, while the three outliers identified in the left panel of Figure 3.6 (green squares) are located just below the 1σ levels.

Interestingly enough, τ_{HB} values are characterized by an even higher dynamical range (a factor of ~ 2) in $I, B–I$ diagram, reaching the maximum value $\tau_{HB}(IBI) \sim 26$, compared to the one found in $I, V–I$ diagram. This was somehow expected since $B–I$ colour is characterized by an increased sensitivity to the effective temperature variation of the HB stars (see for example Cassisi & Salaris, 2013; Natali et al., 1994). These findings confirm that our τ_{HB} is a valid photometric index also in the $I, B–I$ diagram.

3.4 Photometric parametrization of the HB morphology in dwarf spheroidal galaxies

Thanks to the analysis done in the previous section, we are confident to investigate the HB morphology of our sample of dSph galaxies using both the IVI and IBI photometry.

As done for the globular clusters, we estimate $\tau_{HB}(IVI)$ and $\tau_{HB}(IBI)$ for each galaxy in our sample. For the MW dwarfs we are able to evaluate both of them, since we have a complete $UBVRI$ photometry, while for Andromeda and isolated galaxies we estimate τ_{HB} depending on the data availability. Our results are contained in Table 3.3 in which we list $V(HB)$, which we transformed to $I(HB)$ through the $V–I$ colour fixed to the 0.45 value (Braga et al., 2016, see Chapter 2), $CND(V-I)$ and/or $CND(B-I)$, $\tau_{HB}(IVI)$ and/or $\tau_{HB}(IBI)$.

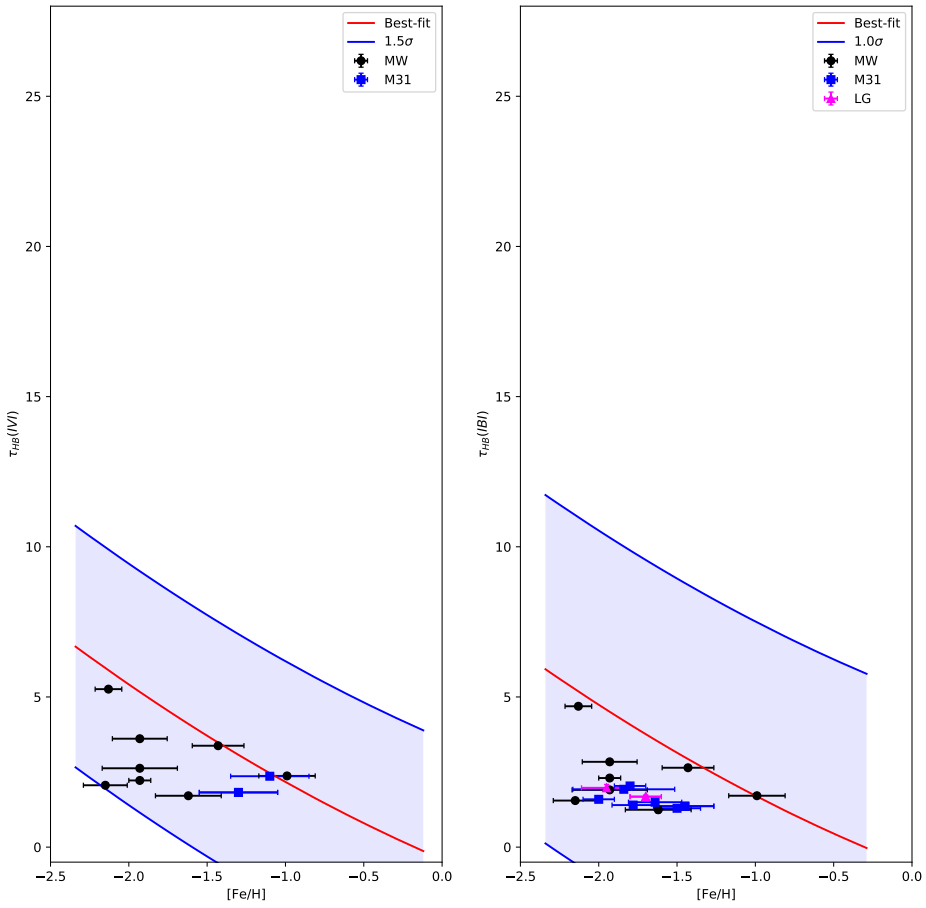

Figure 3.8: [Fe/H] vs $\tau_{HB}(IVI)$ (left panel) and $\tau_{HB}(IBI)$ (right panel) estimated for dwarf spheroidal galaxies. Blue shaded regions show the 1.5σ (left panel) and 1.0σ (right panel) areas from GGCs. Red lines are the best-fit relations from GGC analysis. Black dots identifies MW satellites, blue squares show the Andromeda satellites [M31], while the magenta triangles represent isolated galaxies in the Local Group [LG].

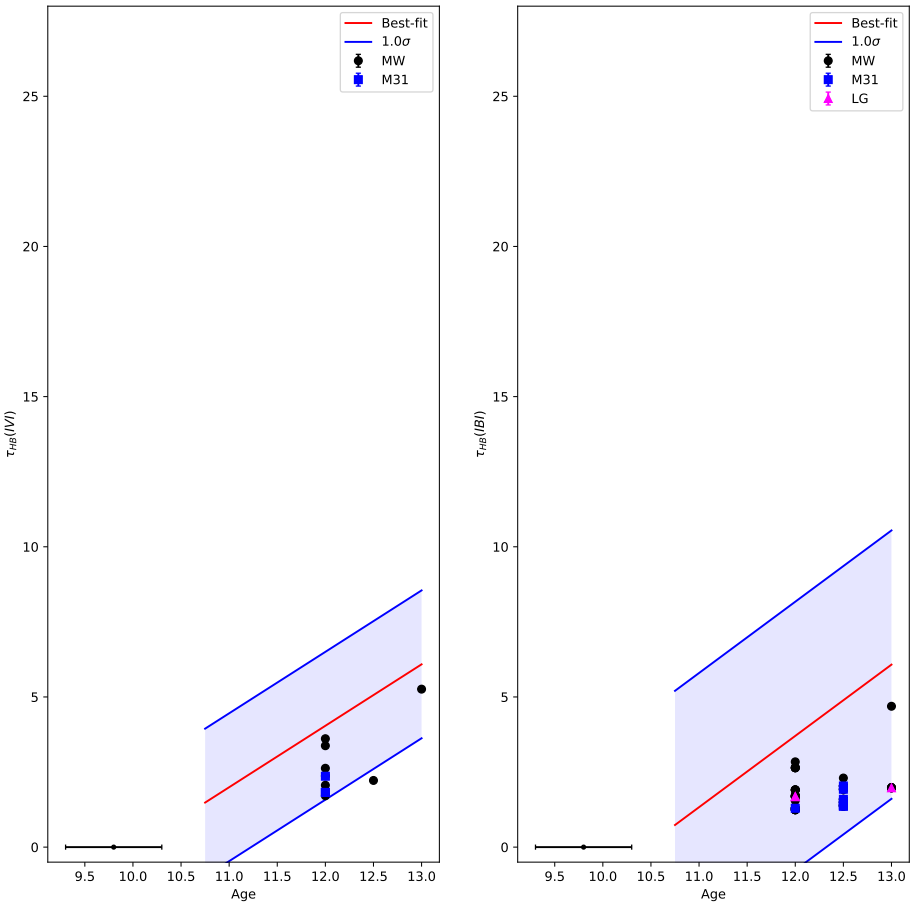

Figure 3.9: Age vs $\tau_{HB}(IVI)$ (left panel) and $\tau_{HB}(IBI)$ (right panel) estimated for dwarf spheroidal galaxies. Blue shaded areas show the 1.0σ levels from GGCs. Red lines are the best-fit relations from GGC analysis. Black dots identifies MW satellites, blue squares show the Andromeda satellites [M31], while the magenta triangles represent isolated galaxies in the Local Group [LG]. The error bar in the lower left corner shows the conservative ± 0.5 Gyr error on the dSph galaxy ages.

Figure 3.8 shows our results on $\tau_{HB}(IVI)$ (left panel) and $\tau_{HB}(IBI)$ (right panel) as a function of [Fe/H] for the dSph galaxies in our sample. As we can appreciate from the figure, the dSph galaxies arrange in the $IVI1.5\sigma$ (left panel) and $IBI1.0\sigma$ areas (blue shaded regions) defined by the best-fit functions (red lines) estimated for GGCs in Figure 3.6. In particular, all the galaxies are located below the red best-fit lines.

Figure 3.9 shows our values of $\tau_{HB}(IVI)$ (left panel) and $\tau_{HB}(IBI)$ (right panel) as a function of the age for the dSph galaxies in our sample. Also in these diagrams, the dSph galaxies arrange in the 1.0σ areas (blue shaded regions) defined by the best-fit functions (red lines) estimated for GGCs in Figure 3.7 and again, all the galaxies are located below the red best-fit lines.

Firstly, we note that in contrast to what we found for GGCs (Figures 3.6 and 3.7), for dSph galaxies we do not find an higher dynamical range of τ_{HB} in $I, B-I$ diagram compared to the one estimated in $I, V-I$ diagram. Indeed, dSph galaxies are in general characterized by a more horizontal HB morphology compared to the one observed in GGCs, this means that *B–I* sensitivity to T_{eff} variation of the HB stars is comparable to *V–I* one, hence we do not have the same effect on τ_{HB} as found for GGCs.

The limited (τ_{HB} ranging from ~ 1 for Leo II to ~ 5 for Ursa Minor) location below the GGC best-fit functions of dSph galaxies in $\tau_{HB} - [Fe/H]$ and $\tau_{HB} - Age$ diagrams, seems to confirm the fact that in dSph galaxies the HB morphology lacks of the presence of an extreme blue and hot region. Indeed, for same age and metallicity values, the dSph galaxy HB morphology is redder than the one observed for the GGCs, as already found in Sect. 3.2 analysing the HBR' index.

We observe that the MW satellite galaxies (black dots) are characterized by an higher variation both in $\tau_{HB}(IVI)$ (from ~ 1.7 to ~ 5.3) and $\tau_{HB}(IBI)$ (from ~ 1.6 to ~ 4.7), with Ursa Minor attaining the maximum values. On the contrary, Andromeda and isolated dSph galaxies are characterized by a lower variation in τ_{HB}, from ~ 1.3 to ~ 2.0, i.e., a factor five lower than the one shown by the MW galaxies. However, despite the modest variation both in age and in metallicity, the observed limited range in HB morphologies of nearby dSphs seems to suggest a significant environmental effect in old stellar populations when moving from GGCs ($10^4 - 10^6 M_\odot$) to dSph galaxies ($10^7 - 10^9 M_\odot$).

3.5 Conclusions

We conducted the very first systematic study on the HB morphology of a sample of 19 nearby dSph galaxies through the estimate of both HBR' and our new HB morphology index τ_{HB}.

We took advantage of homogeneous *UBVRI* ground-based photometry for nine MW dSph satellites, and *F*475*W*, *F*606*W*, *F*814*W* space-based data from ACS/HST for seven Andromeda satellites and two isolated dSphs in the Local Group.

Table 3.3: Parameters and observational HB morphology indices for the dSph galaxies in the sample.

ID	Association	$V(HB)$	CND $(V-I)$	$\tau_{HB}(IVI)$	CND $(B-I)$	$\tau_{HB}(IBI)$	Age (Gyr)	[Fe/H]
Carina	MW	20.8	105.4	2.06 ± 0.05	106.5	1.55 ± 0.05	12.0 ± 0.5	-2.15 ± 0.06
Draco	MW	20.1	110.1	2.22 ±0.07	140.3	2.30 ± 0.07	12.5 ± 0.5	-1.93 ± 0.01
Sculptor	MW	20.2	84.5	3.61 ± 0.07	107.3	2.84 ± 0.07	13.0 ± 0.5	-1.90 ± 0.35
Ursa Minor	MW	19.7	72.8	5.26±0.06	81.6	4.69 ± 0.06	13.0 ± 1.0	-2.13 ± 0.01
Fornax	MW	21.5	111.3	2.37±0.01	154.3	1.71 ± 0.04	12.0 ± 0.5	-0.99 ± 0.01
Leo I	MW	22.5	96.9	3.38 ± 0.02	124.6	2.64 ± 0.01	12.0 ± 0.5	-1.43 ± 0.01
Leo II	MW	22.1	118.1	1.71± 0.02	162.3	1.24± 0.09	12.0 ± 0.5	-1.62 ± 0.01
Sextans (I)	MW	20.3	105.8	2.63 ± 0.02	143.3	1.91±0.21	12.0 ± 0.5	-1.93 ± 0.01
Andromeda I	M31	25.1	-	-	182.4	1.36±0.09	12.5 ± 0.5	-1.45 ± 0.04
Andromeda II	M31	24.7	-	-	173.6	1.50±0.43	12.5 ± 0.5	-1.64 ± 0.04
Andromeda III	M31	25.0	-	-	174.5	1.40± 0.24	12.5 ± 0.5	-1.78 ± 0.04
Andromeda XV	M31	25.0	-	-	138.7	2.04± 0.03	12.5 ± 0.5	-1.80 ± 0.20
Andromeda XVI	M31	24.3	-	-	157.9	1.59± 0.45	12.5 ± 0.5	-2.00 ± 0.20
Andromeda XXVIII	M31	25.0	-	-	148.7	1.93± 0.43	12.5 ± 0.5	-1.84 ± 0.10
LGS 3	M31	24.6	-	-	175.0	1.29±0.04	11.7 ± 0.5	-1.50 ± 0.30
NGC 147	M31	25.5	112.4	2.36± 0.01	-	-	12.0 ± 0.5	-1.10 ± 0.01
NGC 185	M31	25.3	115.9	1.82± 0.01	-	-	12.0 ± 0.5	-1.30 ± 0.10
Cetus	LG	24.9	-	-	166.7	1.68± 0.05	12.0 ± 0.5	-1.70 ± 0.10
Tucana	LG	25.2	-	-	138.8	1.97± 0.36	13.0 ± 0.5	-1.95 ± 0.15

Notes: Columns are: $V(HB)$, CND$(V-I)$, $\tau_{HB}(IVI)$, CND$(B-I)$, $\tau_{HB}(IBI)$,Age in Gyr, [Fe/H].

We transformed $F475W$, $F606W$, $F814W$ magnitudes into B, V, I Johnson-Cousins photometry and we firstly estimated the classical HBR' index for each dSph galaxy in our sample. We found that Milky Way and Andromeda satellites, and isolated dwarfs, are characterized by systematically redder HB morphologies when compared to the sample of GGCs. This means that they lack of the blue and extremely blue components of the HB.

Then, we investigated the validity of our τ_{HB} index, already proved in I, V–I, also in the I, B–I diagram. We found that, as expected, $\tau_{HB}(IBI)$ is characterized by an higher dynamical range (a factor of ~ 2) compared to the one found for $\tau_{HB}(IVI)$, thanks to the higher sensitivity of B–I colour to the T_{eff} variation of the HB stars. Moreover, we still find a quadratic anti-correlation with cluster metallicity, even though it appears to be more linear in the $\tau_{HB}(IBI) - [Fe/H]$ diagram and a linear correlation with absolute cluster ages. Moreover, the 2ndP clusters are still located above the 1.0σ levels. We also find three other clusters (NGC 5986, NGC 6397 and NGC 6717), characterized by blue morphology, attaining peculiar $\tau_{HB}(IBI)$ values. This allowed us to confirm the validity of our HB morphology index independently of the photometric bands used to estimate it.

Therefore, we estimated $\tau_{HB}(IVI)$ and/or $\tau_{HB}(IBI)$, depending on the photometric availability, for our sample of 19 dSphs. Firstly, we found that in contrast to the GGC case, the dynamical range of $\tau_{HB}(IBI)$ for dSphs is not higher than the one of $\tau_{HB}(IVI)$, since the dSph HB morphology is already quite horizontal, and so, the IVI and IBI colours have similar sensitivities.

We found that in all diagrams ($\tau_{HB}(IVI)$-[Fe/H], $\tau_{HB}(IVI)$-Age, $\tau_{HB}(IBI)$-[Fe/H], $\tau_{HB}(IBI)$-Age), the galaxies are located in the same region below the best-fit rela-

tions obtained for GGCs. Moreover, dSph τ_{HB} values suggest that these galaxies are characterized by redder HB morphologies, lacking of an extreme blue and hot region, than the ones observed in GGCs, as already found analysing the HBR' index. Our findings confirm that we have a significant difference in HB morphologies in old stellar populations when moving from GGCs ($M \sim 10^4 - 10^6 M_\odot$) to dSph galaxies ($M \sim 10^7 - 10^8 M_\odot$), suggesting a significant environmental effect.

Chapter 4

Calibration of stellar population synthesis models on Galactic Globular Clusters

In Section 1.3.2, we described the stellar populations synthesis techniques used to analyse the stellar content of unresolved systems through integrated light. As already stated, the integrated SED of a galaxy gives us clues about the physical mechanisms controlling the formation and the evolution of galaxies from the epoch of re-ionization to present time. For this reason, it is important to have reliable methods and models to extract parameters like age, mass, SFR, from the galaxy SED.

In Section 1.3.2, we give an overview concerning the most used codes (Bruzual & Charlot, 2003; Fioc & Rocca-Volmerange, 1999, 2019; Maraston, 1998, 2005; Kotulla et al., 2009; Conroy & Gunn, 2010a) for stellar populations synthesis. Each code has a different prescription for isochrones, stellar spectra, IMF, the effect of dust and metallicity (for a number of SPSM comparisons, see Maraston, 2005; Maraston et al., 2006; Conroy & Gunn, 2010a) and the accuracy of the inferred parameters of unresolved stellar populations from SED fitting depends on the reliability of the adopted models. Indeed, different combinations of stellar parameters (T_{eff}, luminosity, g), IMF and spectral libraries provide different results on the derived ages and chemical compositions. As described in Chapter 1, major uncertainties come from our knowledge about stellar evolution, for example the description of the overshooting in MS stars, the mass loss along the RGB affecting both the HB morphology and the AGB phase, the treatment of TP-AGB stars, blue straggles, binary stars.

In this context, GGCs play a key role to explore the formation and the evolution of stellar populations in the Universe. Indeed, thanks to the current facilities, we are able to resolve their entire stellar content obtaining independent information about their age and composition. This means that we can use their integrated

measures to test and calibrate the SPSMs. In this way, we can verify the validity of theoretical models for both galaxy and stellar evolution.

Obviously, we have to deal with a number of issues. Firstly, we need to take into account that very bright stars could dominate the integrated light, giving a misleading measure in a specific band of the cluster SED. Then, we can calibrate models only in the age-metallicity range spanned by the clusters ($[Fe/H] < 0$). Moreover, we have to consider that the metal-rich GGCs are mostly located in the Milky Way bulge, and so, they could be affected by contamination of field stars in spite of a well calibrated cluster/field star separation.

Finally, throughout this work, we consider globular clusters as SSPs, even though many observations have revealed the existence of multiple populations. Since our current understandings are not able to quantify the effect of multiple populations on the final integrated SEDs of globular clusters, we still retain the SSP as a good approximation for the globular cluster SFHs.

The work is organised as follows. In Sect. 4.1 we present unprecedented multi-wavelength (FUV-IR) integrated SEDs for a sample of 69 GGCs, specific notes on individual clusters are listed in Sect. 4.5. In Sect. 4.3 we describe the library built to model the observed SEDs of our cluster sample, and we show our results from the model calibration. Finally, in Sect. 4.4 we summarize and discuss the future perspectives of our work.

4.1 Globular cluster integrated magnitudes

We estimated the integrated magnitudes in each available band for each GGC combining the single cluster star magnitudes, using:

$$m_{int} = -2.5 \cdot Log\left(\sum_{i=1}^{n} 10^{-0.4 \cdot m_i}\right) \tag{4.1}$$

where m_i is the magnitude of the single stars in the catalogue and n is the total number of candidate cluster stars. We consider a systematic error of about 0.5 mag on the estimate of the integrated magnitudes, which takes into account the depth and completeness of our photometry.

4.1.1 Optical bands

In this analysis we added to the sample of 64 GGCs described in the previous Chapter nine more globulars, namely NGC 1904, NGC 2808, NGC 4372, NGC 5139, NGC 5634, NGC 5694, NGC 6712, NGC 7492 and Palomar 14 for which we have *UBVRI* photometry from ground-based observations. For these clusters, we used the same technique described in Chapter 2 to separate cluster stars from the field ones.

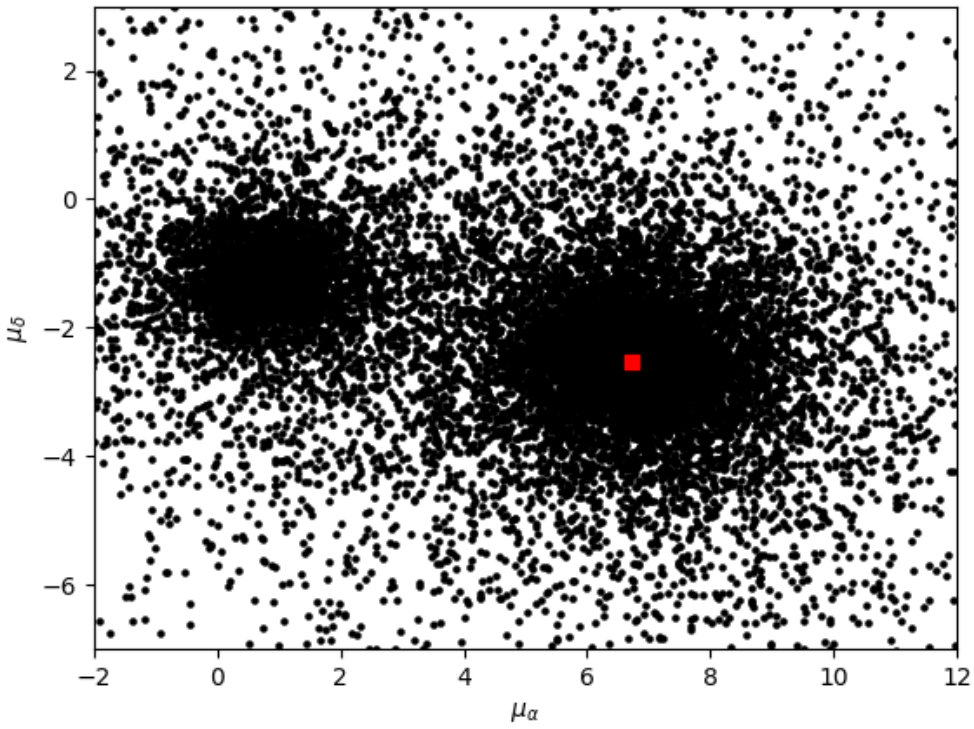

Figure 4.1: Proper motion distribution for NGC 362. Red square identifies the centre of the cluster.

We decided to exclude from the sample described in Chapter 2 NGC 6388, NGC 6441, Palomar 2 and Lynga 7: NGC 6388 and NGC 6441 photometry along the MS up to the AGB-tip is characterized by a severe contamination of the field stars, despite our efforts in cluster/field star separation, being projected on the Bulge. On the contrary, Palomar 2 and Lynga 7 are very small clusters and so we have not a complete photometry. Therefore, we have a sample of 69 GGCs. Moreover, taking advantage of the Gaia Data Release 2 (DR2), firstly, we cross-matched each GGC Gaia DR2 positions to the first data release from The Panoramic Survey Telescope and Rapid Response System (Pan-STARRS), then we cross-correlated our catalogues to the Pan-STARRS ones. We separated the field stars from the cluster ones taking advantage of Gaia proper motions, when possible, i.e., when we were able to clearly recognize cluster and field star groups in the $\mu_\alpha - \mu_\delta$ diagram, (see Figure 4.1). In this way, we obtain a secure cluster/field star separation based on their dynamics. When the proper motion distributions did not allow us to easily identify the two groups, we used our candidate cluster/field star separation technique described in Sect. 2.2.

In this way we have data in g (486.6nm), r (754.5nm), i (621.5nm), y (867.9nm),

z ($963.3nm$) for 39 clusters in our sample. We compared data in r and i bands from Pan-STARRS to our R and I photometry and found that Pan-STARRS observed magnitudes are always fainter than the ones in R and I-bands. This could be due to Pan-STARRS high spatial resolution ($0.6''$) which does not allow to fully resolve stars in the central crowded regions of globular clusters. In particular, we found a mean difference of $\sim 0.5mag$. We applied this difference in each Pan-STARRS photometric band to have consistent photometry in all optical filters.

4.1.2 Ultraviolet bands

In the Ultraviolet (UV) wavelengths, we used the estimates from Dalessandro et al. (2012). They have observations for 44 GGCs (30 in common with our sample) both in far-UV (FUV) and near-UV (NUV) bands obtained with three observing cycles of the Galaxy Evolution Explorer (GALEX). The integrated magnitudes are estimated using the surface brightness profile fitting (SBPF) technique. The authors used concentric annuli centred on the cluster centres in order to have almost the same light fraction for each globular. In each annulus, the calculated flux was normalized adopting a pixel size of $1.5''$. We estimated the integrated magnitudes from their published UV colours, using: $FUV_0 = (FUV-V)_0 + V_{t,0} - A_V$ and $NUV_0 = (NUV - V)_0 + V_{t,0} - A_V$ where $A_V = 3.1 \cdot E(B-V)$, $(FUV - V)_0$ and $NUV - V)_0$ are the integrated reddening corrected colours, $V_{t,0}$ is the integrated V-magnitude. For these parameters, we used the values listed in Dalessandro et al. (2012).

Moreover, in the NUV wavelengths we also used the observations for 56 GGCs in $F275W$ ($\lambda_c = 2697.05$Å) filter within The Large Legacy Treasury Program "The HST Legacy Survey of Galactic Globular Clusters: Shedding UV Light on Their Populations and Formation" (HUGS) (Piotto et al., 2015b; Nardiello et al., 2018), a UV-initiative proposal to complement the $F606W$ and $F814W$ database of "An ACS Survey of Galactic Globular Cluster" we presented in Chapter 2.

Inside the HUGS database[1] a photometric catalogue, containing UV data for the single stars, is available for each cluster. Therefore, we used Eq. 4.1 to estimate the integrated magnitudes in the $F275W$-band.

In any case, we compared GALEX and HUGS integrated magnitudes in the NUV wavelengths obtaining a mean difference of 0.3 in magnitude, which is a good and acceptable result, considering that both filters and methods are different.

For those clusters for which we do not have measures for magnitudes from GALEX and/or HUGS, we calculated them synthetically using the code fully described in Salaris et al. (2013) allowing to produce synthetic CMDs taking account for an user-defined SFH and total mass loss along the RGB to model the HB morphology.

The code uses the models and tracks from BaSTI database (Hidalgo et al.,

[1] https://archive.stsci.edu/prepds/hugs/

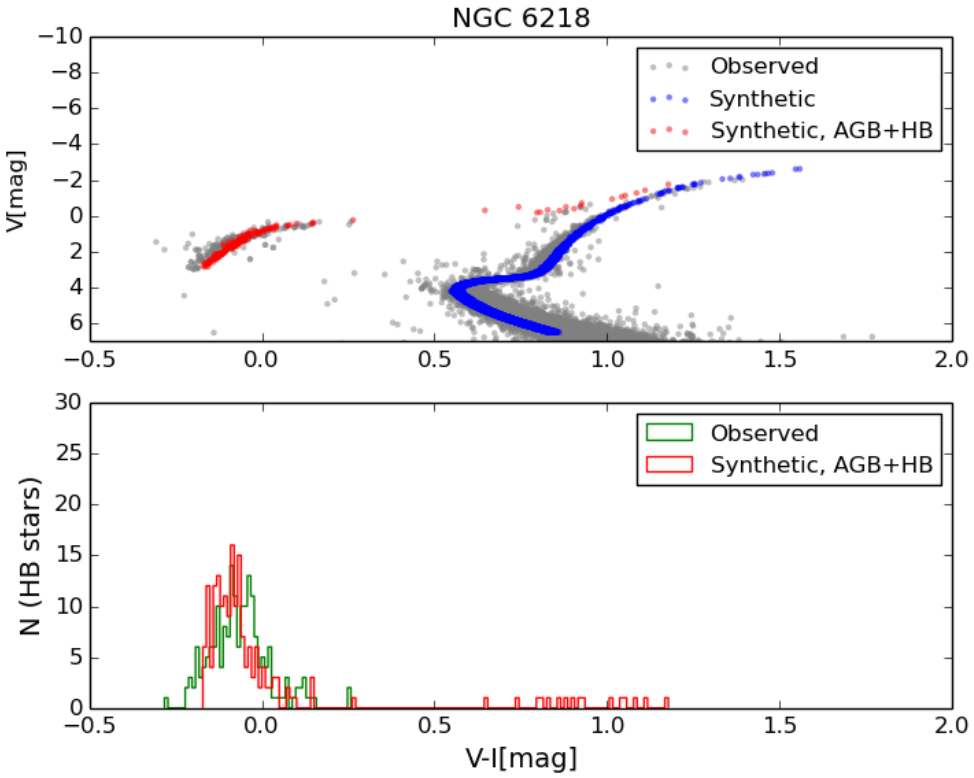

Figure 4.2: Upper panel: *VVI* CMD of the observed (grey dots) and synthetic (blue from MS to RGB-tip, red for AGB+HB phases) for NGC 6218 stars. Bottom panel: number distribution of the observed (green) and synthetic (red) HB stars.

2018) for a wide grid of scaled-solar metallicities. We chose a single burst SFH to model a SSP with a Salpeter IMF. Briefly, the code calculates the number of stars inside the age and metallicity bin defined by the input SFH. Then, for each star the stellar evolutionary track is computed interpolating with BaSTI tracks in metallicity and in mass. At this point the position of the star on the *VVI* CMD is determined.

Then, we compared the synthetic *VVI* CMD to the observed one. Firstly, we checked that TO point, RGB inclination and HB morphology are recovered to fix the age, the metallicity and the reddening of the synthetic CMD (see Table 4.1). Then we normalized the input total number of stars to the one of the observed HB stars, comparing the star counts and their distribution along the branch. The normalization of the total number of the stars allows the unique opportunity to have a complete synthetic CMD in all the stellar evolutionary phases.

To reproduce the observed optical CMDs we implemented the synthetic models using uniform and/or Gaussian distributions to reproduce the mass-loss along

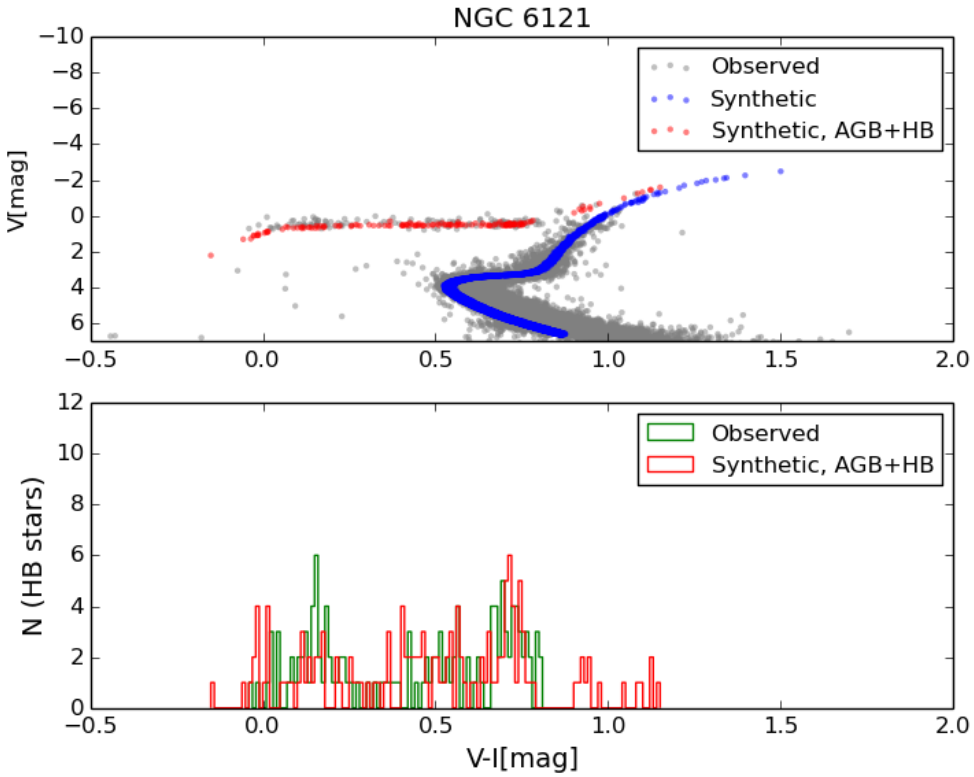

Figure 4.3: Upper panel: *VVI* CMD of the observed (grey dots) and synthetic (blue from MS to RGB-tip, red for AGB+HB phases) for NGC 6121 stars. Bottom panel: number distribution of the observed (green) and synthetic (red) HB stars.

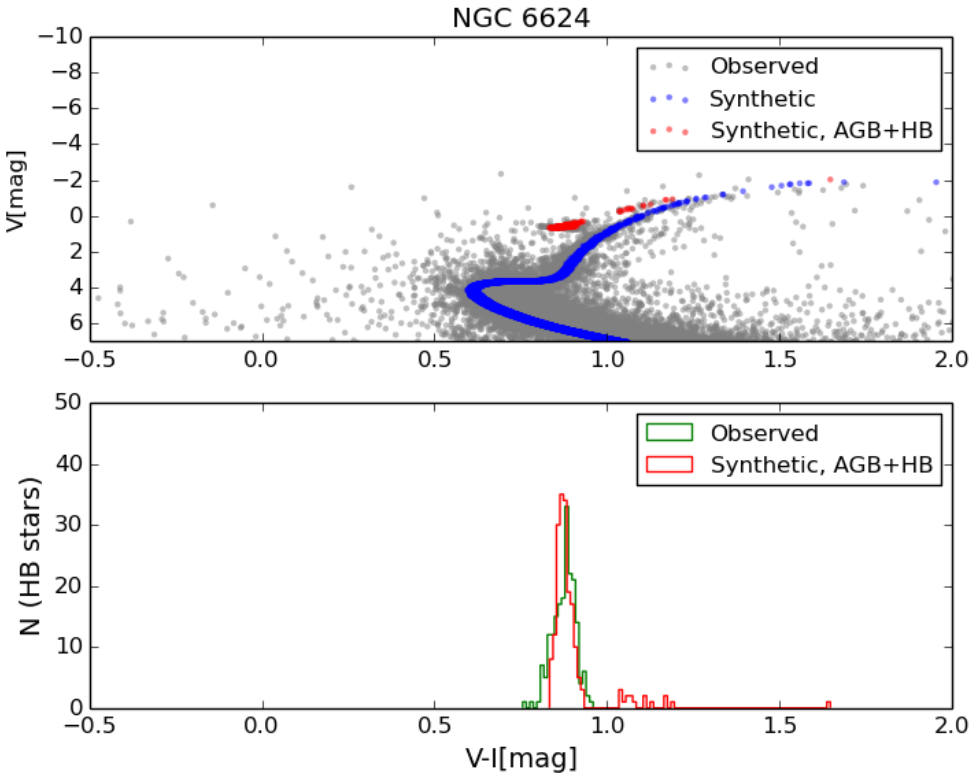

Figure 4.4: Upper panel: *VVI* CMD of the observed (grey dots) and synthetic (blue from MS to RGB-tip, red for AGB+HB phases) for NGC 6624 stars. Bottom panel: number distribution of the observed (green) and synthetic (red) HB stars.

the RGB, choosing the progenitor mass (M) and the variation around this mean value (ΔM). M and ΔM are free input parameters (see Table 4.1) in the synthetic simulations and in general, decreasing M means having a bluer synthetic HB morphology, while decreasing ΔM means obtaining a redder HB and a more peaked HB stellar distribution.

For some GGCs we used a combination of two or more uniform/Gaussian distributions to fit a bluer extended HB morphology or multi-modal colour distribution (see Table 4.1).

Upper panels in Figures 4.2, 4.3, 4.4 display the observed (grey dots) and synthetic (red and blue) VVI CMDs for NGC 6218, NGC 6121 and NGC 6624 characterized by three different HB morphologies: blue, horizontal, red, respectively. The synthetic stars from MS to RGB-tip are shown in blue, while those in the HB and AGB phases are shown in red.

Bottom panels of the Figures show the number distribution of the observed (green) and synthetic (red) HB stars as a function of the $V-I$ colour.

In general, we are able to well reproduce both the observed CMD and HB star distribution for the clusters in our sample. In Sect. 4.4, we give notes on globular clusters peculiar for their synthetic CMDs.

Then, we estimated the magnitudes in GALEX/FUV-NUV and $F275W$ bands using the PARSEC database of bolometric corrections[2]. We employed Kurucz & Phoenix (COMARCS for TP-AGB) library for low-intermediate T_{eff} (5500-6000 K) stars, the Kurucz & WMbasic & PoWR libraries for high T_{eff} stars, and COMARCS library to model AGB stars.

For consistency, we compared the synthetic and the observed magnitudes for both GALEX bands and $F275W$ filter: we obtained a difference of $0.5mag$ for NUV-band, $0.6mag$ for FUV-band and $0.2mag$ for $F275W$ filter. Therefore, as expected, major differences arise for GALEX, probably due to the possible contamination of field stars affecting the observed integrated magnitudes estimated through the SBPF technique by Dalessandro et al. (2012). Moreover, as already stated, we also compared the integrated magnitudes in GALEX/NUV and in $F275W$ filters, obtaining a mean difference of $0.3mag$, i.e., NUV integrated magnitudes are less bright than the ones measured in $F275W$-band. This could be due to the different spatial resolutions of GALEX and WFC3-UVIS ($\sim 8''$ vs $\sim 0.08''$): GALEX is not able to resolve the single stars in the central brighter region of the globular clusters. In general, we consider these results acceptable, and so, we consider reliable our synthetic UV integrated magnitudes, in spite of the many uncertainties in this field (e.g., blue stragglers, post AGB stars, hot flashers).

Therefore, in the NUV wavelengths, we decided to take advantage of both GALEX/NUV ($\lambda_c = 2326.2$Å) and WFC3/$F275W$ ($\lambda_c = 2697.05$Å) to take advantage of both the larger GALEX FoV ($1.2°$ vs $0.05°$ of WFC3-UVIS) and the higher spatial resolution of WFC3-UVIS.

[2] http://stev.oapd.inaf.it/YBC/

Table 4.1: Parameters used to calculate synthetic bands.

ID	Name	[Fe/H]	E(B-V)	μ_V	Age	M	ΔM	Distribution
					Gyr	$M_\odot$	$M_\odot$	
NGC 0104	47 Tuc	-0.46	0.02	13.25	11.75	0.125	0.035	Gaussian
NGC 0288		-1.10	0.01	14.87	11.5	0.2	0.06	Uniform
NGC 0362		-1.1	0.03	14.80	10.75	0.115 / 0.15	0.02 / 0.005	Gaussian+Gaussian
NGC 1261		-1.1	0.02	16.02	10.75	0.17	0.09	Uniform
NGC 1851		-1.0	0.04	15.31	11.0	0.18	0.09	Uniform
NGC 2298		-1.96	0.18	15.2	13.2	0.13	0.02	Uniform
NGC 3201		-1.51	0.22	13.7	10.5	0.11 / 0.2	0.02 / 0.03	Uniform+Gaussian
NGC 4147		-1.78	0.03	16.33	12.25	0.13	0.04	Uniform
NGC 4590	M 68	-1.9	0.06	15.0	12.0	0.1	0.03	Gaussian
NGC 4833		-1.89	0.28	14.3	12.5	0.11 / 0.22	0.02 / 0.03	Gaussian+Gaussian
NGC 5024	M 53	-1.95	0.02	16.31	12.25	0.125 / 0.09	0.025 / 0.01	Gaussian+Gaussian
NGC 5053		-2.0	0.02	16.19	12.25	0.10	0.02	Uniform
NGC 5272	M 3	-1.3	0.01	14.99	11.75	0.12	0.1	Uniform
NGC 5286		-1.70	0.21	15.5	12.25	0.11 / 0.13 / 0.15 / 0.25	0.01 / 0.01 / 0.025 / 0.02	Gaussian+Gaussian+Gaussian+Gaussian
NGC 5466		-2.0	0.02	16.09	12.5	0.08	0.03	Gaussian
NGC 5904	M 5	-1.0	0.03	14.26	11.5	0.19	0.09	Uniform
NGC 5927		-00.4	0.35	15.0	10.75	0.09	0.04	Uniform
NGC 5986		-1.63	0.26	15.2	12.25	0.18	0.08	Gaussian
NGC 6093	M 80	-1.75	0.18	15.2	13.0	0.145 / 0.16	0.09 / 0.02	Uniform+Gaussian
NGC 6101		-1.98	0.10	15.9	12.25	0.11	0.02	Uniform
NGC 6121	M 4	-1.18	0.35	11.9	11.5	0.17	0.04	Gaussian
NGC 6144		-1.82	0.36	15.0	12.75	0.13	0.06	Uniform
NGC 6171	M 107	-1.03	0.35	14.0	12.0	0.12	0.04	Gaussian
NGC 6205	M 13	-1.5	0.02	14.39	12.0	0.1	0.3	Gaussian
NGC 6218	M 12	-1.2	0.17	13.65	14.0	0.185	0.06	Uniform
NGC 6254	M 10	-1.57	0.2	14.08	11.75	0.2	0.06	Gaussian
NGC 6304		-0.47	0.42	14.4	11.25	0.06	0.08	Uniform
NGC 6341	M 92	-2.0	0.02	14.66	12.75	0.13	0.04	Uniform
NGC 6352		-0.62	0.25	13.8	10.75	0.15	0.06	Uniform
NGC 6362		-0.9	0.07	14.5	12.5	0.11	0.09	Uniform
NGC 6366		-0.59	0.6	13.1	11.0	0.1	0.08	Uniform
NGC 6388		-	-	-	-	-	-	-
NGC 6397		-2.0	0.16	12.0	13.0	0.12	0.02	Gaussian
NGC 6426		-2.0	0.32	17.0	11.25	0.11	0.08	Uniform
NGC 6441		-	-	-	-	-	-	-
NGC 6496		-0.46	0.2	15.2	10.75	0.10	0.08	Uniform
NGC 6535		-1.79	0.38	14.2	14.0	0.11	0.06	Uniform
NGC 6541		-1.9	0.1	14.5	12.5	0.13 / 0.25	0.015 / 0.02	Gaussian+Gaussian
NGC 6584		-2.0	0.09	15.9	12.75	0.08	0.01	Uniform
NGC 6624		-0.5	0.23	14.7	11.25	0.11	0.08	Uniform
NGC 6637		-0.45	0.13	14.90	11.0	0.125	0.08	Uniform
NGC 6652		-0.7	0.11	15.0	13.0	0.08	0.06	Uniform
NGC 6656	M 22	-1.65	0.25	13.2	12.5	0.14	0.03	Gaussian
NGC 6681	M 70	-1.62	0.10	14.78	12.75	0.2	0.04	Gaussian
NGC 6717		-1.26	0.2	14.25	12.5	0.19	0.03	Gaussian
NGC 6723		-1.0	0.065	14.7	12.25	0.15 / 0.25	0.02 / 0.015	Gaussian+Gaussian
NGC 6752		-1.55	0.06	13.13	12.5	0.2	0.04	Gaussian
NGC 6779	M 56	-1.9	0.18	15.5	12.75	0.12 / 0.21	0.01 /0.01	Gaussian+Gaussian
NGC 6809	M 55	-1.63	0.1	13.62	13.0	0.15	0.025	Gaussian
NGC 6838	M 71	-0.82	0.22	13.3	11.0	0.10	0.035	Uniform
NGC 6934		-1.45	0.1	16.05	11.75	0.12	0.06	Gaussian
NGC 6981	M 72	-1.55	0.06	16.1	11.5	0.14	0.03	Gaussian
NGC 7006		-1.36	0.07	18.0	10.5	0.16	0.06	Uniform
NGC 7078	M 15	-1.8	0.05	15.3	12.75	0.09 / 0.2	0.01 / 0.02	Gaussian+Gaussian
NGC 7089	M 2	-1.66	0.04	15.41	11.50	0.17 / 0.25	0.02 / 0.04	Gaussian+Gaussian
NGC 7099	M 30	-2.0	0.04	14.60	13.0	0.12	0.02	Uniform
ARP 2		-1.74	0.11	17.25	12.0	0.11	0.03	Uniform
E 3		-0.83	0.25	14.5	13.0	0.12	0.02	Uniform
IC 4499		-1.5	0.19	16.5	12.0	0.10	0.07	Uniform
Lynga 7		-0.65	0.6	15.0	11.75	0.08	0.08	Uniform
Pal 2		-	-	-	-	-	-	-
Rup 106		-1.78	0.15	16.8	13.0	0.02	0.01	Uniform
Terzan 7		-	-	-	-	-	-	-
Terzan 8		-2.0	0.12	17.14	13.0	0.125	0.02	Gaussian
NGC 1904	M 79	-1.4	0.01	15.59	12.0	0.19	0.08	Uniform
NGC 2808		-1.0	0.13	15.4	10.9	0.12 / 0.19 / 0.25	0.04 / 0.005 / 0.02	Gaussian+Gaussian+Gaussian
NGC 4372		-2.0	0.38	14.3	12.0	0.09	0.04	Uniform
NGC 5139	ω Cen	-1.3	0.02	14.5	12.0	0.16	0.008	Gaussian
NGC 5634		-1.93	0.06	17.0	12.0	0.13	0.015	Gaussian
NGC 5694	C 66	-2.0	0.08	18.0	12.0	0.15	0.03	Gaussian
NGC 7492		-1.69	0.01	17.2	14.0	0.11	0.02	Uniform
Pal 14		-1.53	0.04	19.54	10.0	0.06	0.03	Gaussian

4.1.3 Infrared bands

To recover the IR bands for our GGC sample, we took advantage of the Two Micron All-Sky Survey (2MASS) catalogues, using the Gaia DR2 positions as already described in Sect. 4.1.1 for the Pan-STARRS optical data.

2MASS is a ground-based, near-infrared (*NIR*) survey of the whole sky: the Data Release contains images and catalogues covering 99.998% of the sky, derived from all northern and southern Survey observations. This means that we have data in J ($\sim 1.235\mu m$), H ($\sim 1.662\mu m$) and K_s ($\sim 2.159\mu m$) filters for each cluster in our sample. The integrated magnitudes in these photometric bands are listed in Table 4.2. We note that we decided to ignore 2MASS data for NGC 6352 since they are characterized by an incomplete photometry.

Furthermore, we used the same synthetic bands described in the previous section to evaluate the mid-infrared (*MIR*) photometric bands. Indeed, we used the PARSEC database to estimate the bolometric corrections for four IRAC channels filter system on board of SPITZER ($CH1 \sim 3.55\mu m$, $CH2 \sim 4.49\mu m$, $CH3 \sim 5.73\mu m$, $CH4 \sim 7.87\mu m$).

In this case we tested and calibrated the reliability of our synthetic measures in the *MIR* wavelengths comparing the synthetic integrated J, H and K_s magnitudes with the observed ones, obtaining a mean difference of $\sim 0.1 mag$. Also in this case, these results show an acceptable accuracy of our synthetic magnitudes.

4.2 Globular cluster spectral energy distributions

Once we obtain the integrated magnitudes, listed in Table 4.2, we are able to build the observed photometric SED from FUV to MIR wavelengths for each cluster of our sample. The integrated magnitudes are corrected for Galactic extinction using the reddening $E(B-V)$ values listed in Table 2.1 and following the Cardelli et al. (1989) extinction curve (see Figure 1.9).

It is worth noting that this is the first time that photometric SEDs for a complete and extended GGC sample as the one presented in this work with such wavelength coverage are analysed .

Figure 4.5 shows the GGC SEDs in six different metallicity bins, accurately chosen to have an homogeneous sample of the clusters in each of them. On the y-axis we display the flux normalized to the V-band in the Vega photometric system:

$$F_{norm} = -2.5 Log\left(\frac{F_\lambda}{F_V}\right) \tag{4.2}$$

so, in practice, the quantity F_{norm} is a colour giving us the opportunity to better analyse the UV and IR emissions from our globulars. Indeed, as expected, the 2ndP clusters we identified in Chapter 2 (red lines) show higher UV-emission

Table 4.2: Integrated magnitudes corrected for reddening for each cluster in our sample in different photometric bands.

ID	Name	*FUV*	*NUV*	*F275W*	*U*	*B*	*V*	*R*	*I*	*g* (ABmag)	*r* (ABmag)	*i* (ABmag)	*z* (ABmag)	*y* (ABmag)	*J*	*H*	K_s	[3.6]	[4.5]	[5.7]	[8.0]
NGC 0104	47 Tuc	10.50	7.50	7.56	5.11	4.99	4.03	3.65	3.11	99.00	99.00	99.00	99.00	99.00	2.68	1.98	1.81	1.38	1.48	1.43	1.36
NGC 0288		10.27	9.88	10.54	8.57	8.57	7.93	7.68	7.22	8.09	7.66	7.47	7.39	7.30	6.49	5.94	5.82	5.89	5.96	5.93	5.86
NGC 0362		11.41	9.21	8.56	7.64	7.60	6.50	6.38	5.60	99.00	99.00	99.00	99.00	99.00	5.35	4.69	4.55	5.65	5.72	5.69	5.63
NGC 1261		12.35	10.18	10.12	9.37	9.29	8.41	8.17	7.55	99.00	99.00	99.00	99.00	99.00	7.22	6.65	6.50	6.31	6.39	6.36	6.29
NGC 1851		11.56	10.08	8.97	8.50	8.33	7.33	7.26	6.54	99.00	99.00	99.00	99.00	99.00	5.86	5.27	5.25	5.28	5.36	5.33	5.26
NGC 2298		12.01	10.90	11.19	9.35	9.49	8.80	8.54	8.01	99.00	99.00	99.00	99.00	99.00	7.42	6.99	6.80	7.49	7.56	7.53	7.47
NGC 3201		9.57	7.93	9.76	6.63	6.44	5.83	6.59	5.15	99.00	99.00	99.00	99.00	99.00	4.70	4.20	4.10	3.35	3.42	3.39	3.33
NGC 4147		12.99	11.81	11.75	10.86	10.94	10.29	10.04	9.54	10.29	10.00	9.80	9.69	9.70	9.18	8.68	8.49	8.01	8.09	8.06	7.99
NGC 4590	M 68	12.10	9.70	9.93	8.50	8.61	7.95	7.66	7.07	7.85	7.61	7.52	7.40	7.37	6.80	6.29	6.17	7.34	7.40	7.38	7.32
NGC 4833		9.56	9.14	9.29	6.68	6.62	5.93	5.76	5.22	99.00	99.00	99.00	99.00	99.00	4.77	4.27	4.12	5.28	5.33	5.31	5.25
NGC 5024	M 53	10.68	9.30	9.38	8.42	8.35	7.57	7.14	6.73	7.85	7.37	7.17	7.06	6.93	6.44	5.86	5.73	5.48	5.54	5.52	5.46
NGC 5053		13.68	11.98	12.21	10.45	10.52	9.92	9.57	9.12	9.89	9.49	9.33	9.26	9.21	8.98	8.51	8.38	8.15	8.22	8.19	8.12
NGC 5272	M 3	10.12	8.45	8.45	7.34	7.34	6.48	6.09	5.63	6.66	6.21	6.06	5.90	5.76	5.35	4.75	4.61	4.71	4.78	4.75	4.68
NGC 5286		9.16	8.34	7.80	7.84	7.68	6.58	6.72	5.90	99.00	99.00	99.00	99.00	99.00	5.54	4.90	4.71	3.91	3.98	3.96	3.89
NGC 5466		13.08	11.12	11.98	10.06	10.18	9.57	9.25	8.80	9.55	9.19	9.00	8.95	8.94	8.71	8.22	8.09	7.50	7.56	7.54	7.47
NGC 5904	M 5	8.65	8.05	8.16	6.78	6.70	6.24	5.59	5.34	6.22	5.86	5.65	5.54	5.40	4.69	4.03	3.90	3.99	4.06	4.03	3.96
NGC 5927		17.20	10.19	10.90	6.89	6.19	5.33	5.46	4.66	99.00	99.00	99.00	99.00	99.00	4.06	3.49	3.36	2.45	2.57	2.50	2.42
NGC 5986		10.02	8.98	9.12	7.79	7.53	6.64	7.03	5.91	99.00	99.00	99.00	99.00	99.00	5.53	4.99	4.86	5.64	5.71	5.69	5.62
NGC 6093	M 80	9.35	9.27	8.80	8.01	7.93	6.77	6.70	5.93	7.17	6.79	6.56	6.38	6.29	5.54	5.00	4.80	5.54	5.60	5.58	5.51
NGC 6101		12.57	11.56	10.79	8.98	8.98	8.31	8.12	7.52	99.00	99.00	99.00	99.00	99.00	7.13	6.61	6.50	6.77	6.83	6.81	6.75
NGC 6121	M 4	8.76	6.95	8.67	5.23	5.27	4.82	4.75	4.34	5.10	5.02	5.02	4.98	4.93	3.79	3.35	3.25	2.02	2.09	2.06	2.00
NGC 6144		12.16	11.69	10.01	99.00	7.53	7.14	7.25	6.90	6.91	6.71	6.69	6.76	6.80	6.44	6.00	5.92	7.73	7.79	7.77	7.70
NGC 6171	M 107	15.16	10.16	11.32	7.87	7.78	7.05	6.78	6.33	6.93	6.63	6.45	6.39	6.33	5.74	5.19	5.03	4.45	4.53	4.50	4.43
NGC 6205	M 13	8.10	7.76	7.80	6.34	6.76	6.10	5.25	5.24	6.01	5.71	5.51	5.51	5.45	4.80	4.26	4.10	3.43	3.49	3.47	3.40
NGC 6218	M 12	9.27	8.72	9.44	7.34	7.33	6.70	6.34	5.91	6.69	6.42	6.26	6.14	6.04	5.41	4.82	4.65	4.03	4.11	4.08	4.00
NGC 6254	M 10	8.15	7.62	8.60	6.65	6.79	6.23	6.01	5.65	5.85	5.74	5.65	5.61	5.54	5.06	4.56	4.41	4.35	4.42	4.39	4.33
NGC 6304		99.00	99.00	10.99	99.00	99.00	6.65	99.00	5.76	7.16	6.63	6.37	6.10	5.69	5.10	4.30	4.10	99.00	99.00	99.00	99.00
NGC 6341	M 92	8.82	8.24	8.07	7.16	7.19	6.56	6.18	5.70	6.72	6.40	6.21	6.19	6.07	5.38	4.85	4.75	4.56	4.62	4.60	4.53
NGC 6352		17.48	10.76	10.98	99.00	6.90	6.09	99.00	5.38	99.00	99.00	99.00	99.00	99.00	99.00	99.00	99.00	4.33	4.42	4.38	4.31
NGC 6362		17.18	10.95	10.56	99.00	8.25	7.50	7.22	6.65	99.00	99.00	99.00	99.00	99.00	6.19	5.60	5.45	5.04	5.12	5.09	5.02
NGC 6366		17.58	10.78	12.50	7.55	7.37	6.63	6.65	6.01	6.50	6.11	5.92	5.90	5.84	5.35	4.89	4.79	4.50	4.58	4.55	4.48
NGC 6397		7.89	6.82	8.14	5.72	5.78	5.26	99.00	4.65	99.00	99.00	99.00	99.00	99.00	4.19	3.78	3.67	3.00	3.06	3.04	2.97
NGC 6426		14.56	13.67	13.19	99.00	99.00	9.79	99.00	9.01	10.09	9.55	9.32	9.23	9.15	8.66	8.15	8.06	9.47	9.53	9.50	9.44
NGC 6496		19.90	12.94	12.03	10.02	9.34	8.41	8.03	7.51	99.00	99.00	99.00	99.00	99.00	6.79	6.13	5.94	6.53	6.60	6.57	6.51
NGC 6535		13.46	11.86	11.85	9.65	9.78	9.16	99.00	8.51	9.06	8.68	8.52	8.49	8.45	8.23	7.79	7.67	6.82	6.89	6.86	6.79
NGC 6541		9.13	8.76	8.27	6.76	6.75	5.97	99.00	5.28	99.00	99.00	99.00	99.00	99.00	5.02	4.49	4.32	4.84	4.90	4.88	4.82
NGC 6584		13.55	10.79	10.53	99.00	9.20	8.40	99.00	7.58	99.00	99.00	99.00	99.00	99.00	6.91	6.36	6.25	6.94	7.01	6.98	6.91
NGC 6624		18.32	11.36	10.82	99.00	99.00	7.28	99.00	6.26	7.82	7.52	7.05	6.84	6.71	5.63	4.97	4.69	4.78	4.88	4.83	4.76
NGC 6637		18.42	11.42	10.41	99.00	7.64	6.64	99.00	5.73	99.00	99.00	99.00	99.00	99.00	6.33	5.68	5.50	4.84	4.93	4.89	4.82
NGC 6656	M 22	7.99	7.28	7.85	5.01	4.44	3.80	5.48	3.11	3.99	3.70	3.55	3.47	3.43	2.87	2.37	2.25	3.06	3.12	3.10	3.03
NGC 6681	M 70	9.84	9.69	9.42	8.51	8.52	7.74	99.00	6.97	99.00	99.00	99.00	99.00	99.00	6.29	5.83	5.84	5.77	5.83	5.81	5.74
NGC 6717		11.88	11.36	10.99	99.00	7.76	7.08	7.17	6.40	7.18	6.79	6.59	6.54	6.53	5.91	5.30	5.16	6.59	6.68	6.65	6.57
NGC 6723		10.35	9.44	9.19	99.00	7.42	6.71	99.00	5.99	99.00	99.00	99.00	99.00	99.00	5.65	5.10	4.98	4.11	4.20	4.16	4.09
NGC 6752		7.71	7.48	7.67	6.06	6.02	5.31	99.00	4.59	99.00	99.00	99.00	99.00	99.00	3.95	3.37	3.23	3.35	3.42	3.39	3.32
NGC 6779	M 56	10.92	10.34	9.91	8.37	8.40	7.59	99.00	6.86	7.46	7.11	6.93	6.91	6.87	6.41	5.91	5.83	6.35	6.40	6.38	6.33
NGC 6809	M 55	9.21	8.17	9.11	6.81	6.78	6.18	6.06	5.39	6.39	6.14	5.93	5.97	5.97	5.05	4.53	4.42	4.96	5.03	5.00	4.94
NGC 6838	M 71	16.67	10.27	10.63	7.40	7.34	6.58	6.63	5.93	6.19	5.93	5.87	5.85	5.82	5.53	5.01	4.93	4.31	4.39	4.36	4.29
NGC 6934		13.09	11.38	10.48	9.38	9.27	8.36	8.14	7.51	8.51	8.05	7.83	7.73	7.70	7.20	6.63	6.46	6.41	6.49	6.46	6.39
NGC 6981	M 72	13.37	10.87	11.04	10.20	10.16	9.31	9.08	8.48	9.46	9.02	8.75	8.62	8.54	8.13	7.52	7.36	7.56	7.62	7.60	7.54
NGC 7006		15.17	12.77	12.67	10.97	11.14	10.27	9.69	9.37	10.85	10.20	9.94	9.85	9.61	8.98	8.32	8.23	8.56	8.64	8.61	8.54
NGC 7078	M 15	9.11	8.49	7.91	6.90	6.96	6.23	5.97	5.44	6.41	6.16	6.01	5.93	5.84	5.22	4.74	4.64	4.35	4.41	4.39	4.33
NGC 7089	M 2	8.75	8.14	8.11	7.55	7.52	6.56	6.44	5.73	6.96	6.66	6.35	6.25	6.08	5.53	4.91	4.74	4.21	4.28	4.25	4.18
NGC 7099	M 30	9.51	8.82	8.99	8.06	8.13	7.56	7.21	6.80	7.49	7.42	7.24	7.19	7.15	6.30	5.91	5.66	5.16	5.22	5.20	5.13
Terzan 7		99.00	99.00	99.00	99.00	11.66	10.85	10.49	9.98	99.00	99.00	99.00	99.00	99.00	10.57	9.99	9.76	99.00	99.00	99.00	99.00
Terzan 8		15.37	13.42	13.08	11.50	11.51	10.92	10.67	10.25	99.00	99.00	99.00	99.00	99.00	9.85	9.36	9.26	9.39	9.45	9.43	9.36
ARP 2		16.22	13.49	13.97	99.00	11.25	10.48	99.00	9.61	10.60	10.05	9.81	9.72	9.65	9.18	8.62	8.48	10.11	10.18	10.15	10.09
E 3		20.59	13.90	12.67	11.24	11.26	10.51	10.36	9.86	99.00	99.00	99.00	99.00	99.00	9.53	9.08	8.98	7.65	7.73	7.70	7.63
IC 4499		13.85	11.35	11.35	9.97	10.03	8.91	9.05	8.13	99.00	99.00	99.00	99.00	99.00	8.24	7.69	7.58	7.42	7.48	7.46	7.39
Rup 106		19.08	13.84	12.95	99.00	10.66	9.88	99.00	9.02	99.00	99.00	99.00	99.00	99.00	8.45	7.94	7.84	9.07	9.12	9.10	9.04
NGC 1904	M 79	9.85	9.48	9.91	8.71	8.75	8.09	7.61	7.19	8.34	7.96	7.76	7.69	7.64	6.54	4.99	5.96	6.12	6.20	6.17	6.09
NGC 2808		8.81	8.23	8.35	6.37	6.33	5.60	5.11	4.77	99.00	99.00	99.00	99.00	99.00	4.49	3.87	3.74	3.93	4.01	3.98	3.91
NGC 4372		11.75	10.47	9.90	6.43	6.43	5.86	5.69	5.25	99.00	99.00	99.00	99.00	99.00	4.78	4.30	4.22	6.16	6.22	6.20	6.13
NGC 5139	ωCen	10.15	7.17	6.42	4.21	4.14	3.55	3.31	2.84	99.00	99.00	99.00	99.00	99.00	2.87	2.38	2.27	2.25	2.33	2.30	2.23
NGC 5634		13.65	12.67	12.17	10.50	10.43	9.78	9.38	8.91	9.78	9.43	9.16	9.05	9.02	8.44	7.91	7.81	8.73	8.79	8.76	8.71
NGC 5694	C 66	13.55	12.96	12.53	11.05	10.94	10.33	9.98	9.47	10.33	10.05	9.89	9.79	9.79	9.13	8.52	8.30	8.98	9.04	9.02	8.95
NGC 6712		114.60	114.60	114.60	6.70	6.33	5.60	5.82	4.84	6.13	5.80	5.68	5.63	5.57	5.28	4.74	4.61	99.00	99.00	99.00	99.00
NGC 7492		14.04	13.18	13.42	11.78	12.01	11.45	11.09	10.68	11.55	11.12	10.93	10.85	10.81	10.63	10.09	9.98	9.57	9.64	9.61	9.54
Palomar 14		21.12	16.01	15.14	13.42	13.43	12.84	12.91	12.12	13.21	12.81	12.69	12.60	12.55	12.52	12.12	12.01	10.99	11.07	11.04	10.97

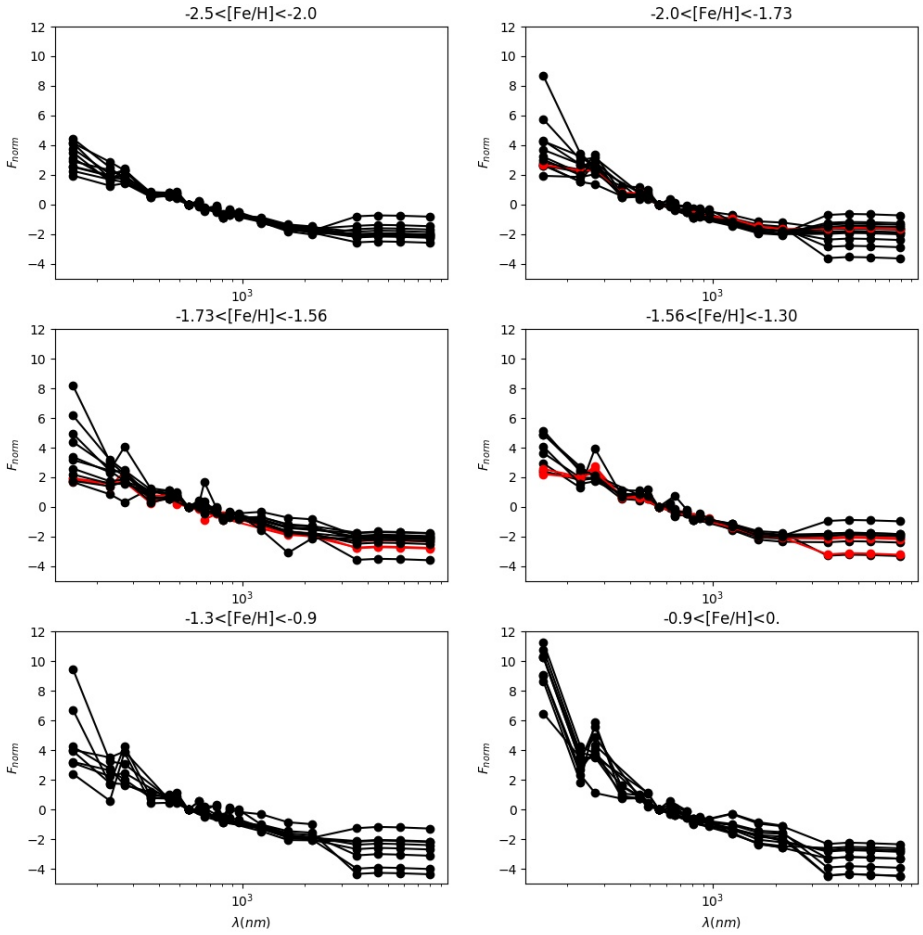

Figure 4.5: SEDs for each cluster in our sample for six different bins in metallicity. Red lines show the photometric SEDs for the 2ndP clusters identified in Chapter 2, while the black ones define the SEDs for the "typical" GGCs. Each SED is normalized to the V-band.

Table 4.3: Integrated magnitudes corrected for reddening for seven 2ndP clusters in our sample in different photometric bands with and without considering the EHB stars.

ID	Name	*FUV*	*NUV*	*F275W*	*U*	*B*	*V*	*R*	*I*	*J*	*H*	K_s	[3.6]	[4.5]	[5.7]	[8.0]
NGC 0288		10.27	9.88	10.54	8.57	8.57	7.93	7.68	7.22	6.49	5.94	5.82	5.89	5.96	5.93	5.86
NGC 0288 no EHB		13.86	11.01	10.98	8.95	8.91	8.17	7.76	7.28	6.64	6.05	5.93	5.78	5.78	5.72	5.65
NGC 0288 no BHB		16.75	11.19	11.07	8.98	8.95	8.19	7.78	7.29	6.63	6.04	5.92	5.79	5.78	5.72	5.65
NGC 6205	M 13	8.10	7.76	7.80	6.34	6.76	6.10	5.25	5.24	4.80	4.26	4.10	3.43	3.49	3.47	3.40
NGC 6205 no EHB	M 13	10.39	8.37	8.20	6.44	6.87	6.17	4.45	5.27	4.82	4.27	4.12	3.32	3.31	3.26	3.19
NGC 6205 no BHB	M 13	17.05	10.87	8.28	6.47	6.92	6.19	4.45	5.28	4.83	4.28	4.12	3.41	3.45	3.42	3.35
NGC 6218	M 12	9.27	8.72	9.44	7.34	7.33	6.70	6.34	5.91	5.41	4.82	4.65	4.03	4.11	4.08	4.00
NGC 6218 no EHB	M 12	11.14	9.57	9.92	7.65	7.59	6.85	6.46	5.97	5.50	4.93	4.76	4.08	4.09	4.03	3.94
NGC 6218 no BHB	M 12	16.31	10.13	9.96	7.66	7.60	6.86	6.46	5.98	5.50	4.93	4.76	4.08	4.09	4.03	3.95
NGC 6254	M 10	8.15	7.62	8.60	6.65	6.79	6.23	6.01	5.65	5.06	4.56	4.41	4.35	4.42	4.39	4.33
NGC 6254 no EHB	M 10	10.27	8.95	9.01	6.82	6.94	6.32	6.09	5.70	5.09	4.59	4.44	4.24	4.22	4.17	4.10
NGC 6254 no BHB	M 10	14.81	9.44	9.03	6.92	7.04	6.39	6.15	5.74	5.12	4.61	4.46	4.24	4.23	4.18	4.11
NGC 6541		9.13	8.76	8.27	6.76	6.75	5.97	99.00	5.28	5.02	4.49	4.32	4.84	4.90	4.88	4.82
NGC 6541 no EHB		10.23	8.91	8.65	6.87	6.85	6.02	99.00	5.30	5.02	4.50	4.32	4.40	4.38	4.33	4.27
NGC 6541 no BHB		14.76	9.52	8.73	6.92	6.90	6.05	99.00	5.32	5.03	4.50	4.32	4.41	4.39	4.34	4.27
NGC 6681	M 70	9.84	9.69	9.42	8.51	8.52	7.74	99.00	6.97	6.29	5.83	5.84	5.77	5.83	5.81	5.74
NGC 6681 no EHB	M 70	12.37	10.61	10.05	8.65	8.64	7.81	99.00	7.00	6.30	5.84	5.85	5.66	5.64	5.59	5.52
NGC 6681 no BHB	M 70	16.50	10.97	10.10	8.68	8.68	7.83	99.00	7.01	6.30	5.84	5.85	5.66	5.65	5.60	5.53
NGC 6752		7.71	7.48	7.67	6.06	6.02	5.31	99.00	4.59	3.95	3.37	3.23	3.35	3.42	3.39	3.32
NGC 6752 no EHB		10.10	8.30	8.20	6.21	6.17	5.47	99.00	4.62	4.16	3.61	3.48	3.25	3.24	3.19	3.11
NGC 6752 no BHB		14.26	8.72	8.21	6.25	6.21	5.49	99.00	4.63	4.16	3.61	3.48	3.25	3.25	3.19	3.12

when compared to the "typical" ones (black lines). This is due to the fact that they have bluer HB morphologies than the other clusters of similar metallicity.

Furthermore, Figure 4.6 shows our fits obtained combining the SEDs in three different metallicity bins, namely $-2.5 < [Fe/H] < -2.0$ (metal-poor, red line), $-1.56 < [Fe/H] < -1.3$ (metal-intermediate, blue line) and $-0.9 < [Fe/H] < 0.$ (metal-rich, black line). We find that, as expected, the metal-poor clusters, which in general are characterized by bluer HB morphologies, have an UV stronger emission than the metal-rich clusters ($\sim 6mag$- difference, more than 1000 in flux). On the contrary, the metal-rich clusters, characterized by redder CMDs, have an higher emission in NIR-MIR bands ($\sim 2mag$-difference).

Finally, we investigated the dependence of the total integrated magnitude on the blue HB (BHB) stars as a function of the wavelength using seven out of the eight 2ndP clusters in our sample. We excluded NGC 6426 since it does not show an extremely blue HB morphology.

We estimated the integrated magnitudes in the UV, optical, NIR and MIR wavelengths firstly eliminating the HB stars bluer (BHB) than the instability strip from the 2ndP cluster catalogues, then eliminating just the extremely blue HB stars (EHB). We list in Table 4.3 the magnitudes with and without considering the EHB and BHB regions. We find that: excluding all the BHB stars, the FUV-magnitude becomes fainter of a mean factor of ~ 7 mag (more than 1000 in flux) compared to the ones estimated including the entire HB region; excluding just the EHB stars, the FUV-magnitude becomes fainter of a mean factor of ~ 2 mag. Therefore, as expected, we find that the HB stars give an important contribution

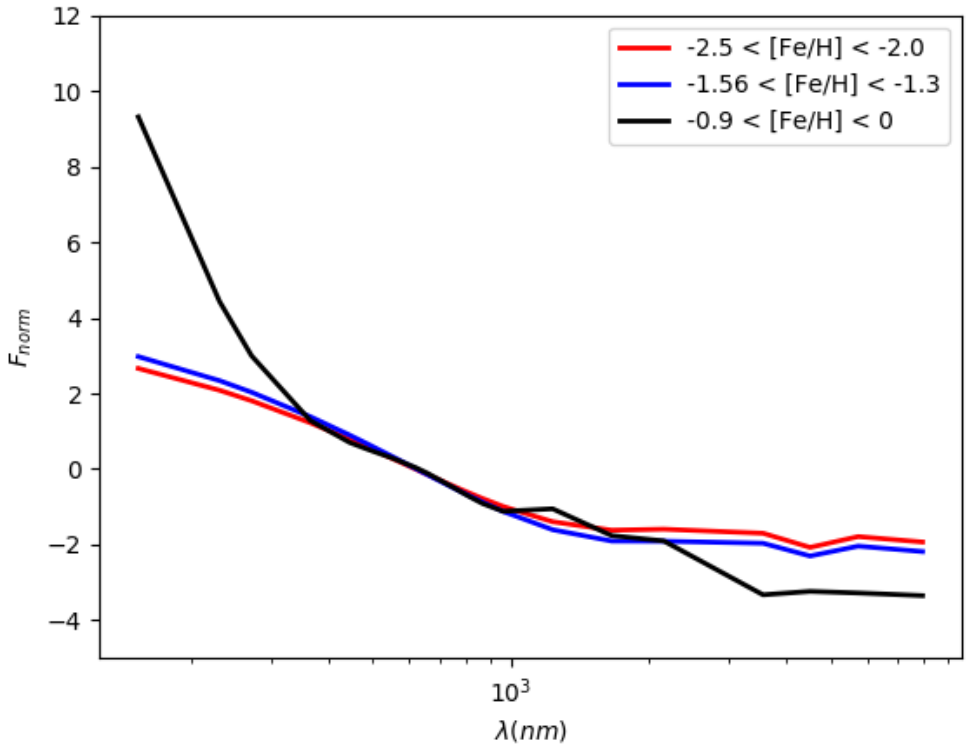

Figure 4.6: Fits of the normalized SEDs shown in Figure 4.5 for three different bins in metallicity (see legend).

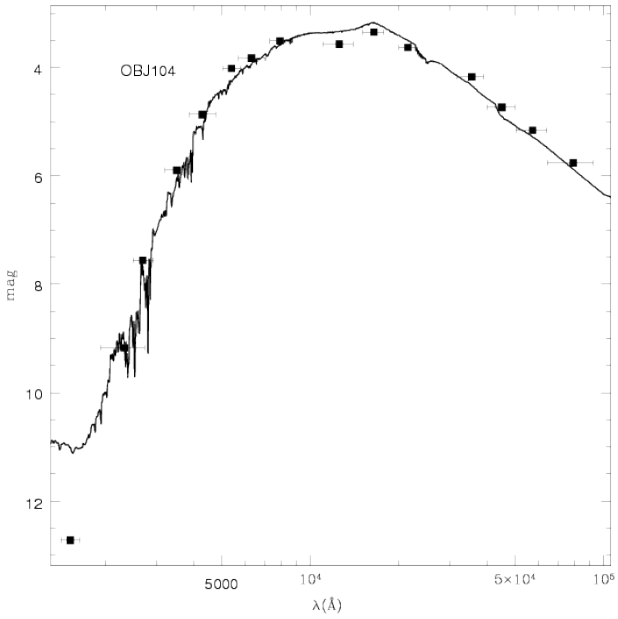

Figure 4.7: Multi-wavelength SED fitting of NGC 104.

to the *FUV*-flux, in particular, the effect appears to be more measurable cutting the entire blue region of the HB morphology. On the contrary, EHB and BHB regions do not affect the optical emission and mildly affect the *MIR* wavelengths. Indeed, in the latter case, if we exclude the EHB or the BHB region, we find *MIR*-magnitudes brighter of a mean factor of $\sim 5\%$ in both cases. Therefore, as expected, the HB stars have a poor emission in the IR-bands.

4.3 Model calibration

We built our library using the BC03 models (see Sect. 1.3.2) with Padova 1994 isochrones. Considering the [Fe/H] range covered by our sample of GGCs, we fixed the metallicity of the models to the values $Z/Z_{\odot}$= 0.005, 0.02, 0.2, 0.4, available in BC03. We used the Salpeter IMF and a τ-model SFH with $\tau = 0.01$ to simulate a simple stellar population. For the age we adopted a fine grid from 1.0 Gyr to the age of the Universe.

Since we decided to compare the inferred ages to the ones estimated by Vanden-Berg et al. (2013); Leaman et al. (2013) through the vertical method, we divided our clusters, according to their [Fe/H] values listed in Table 2.1, in four different metallicity bins centred in $Z/Z_{\odot} = 0.005, 0.02, 0.2, 0.4$ to minimize the effects of the age-metallicity degeneracy.

Therefore, using *zphot* (Sect. 1.3.5), we implemented a SED fitting procedure

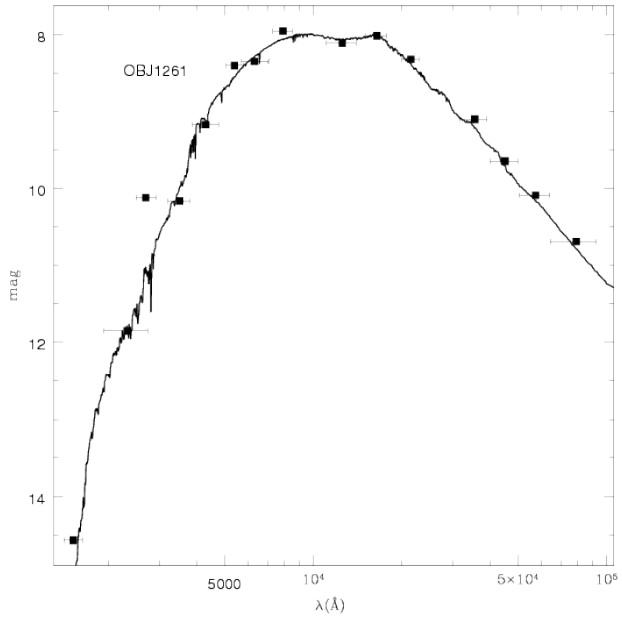

Figure 4.8: Multi-wavelength SED fitting of NGC 1261.

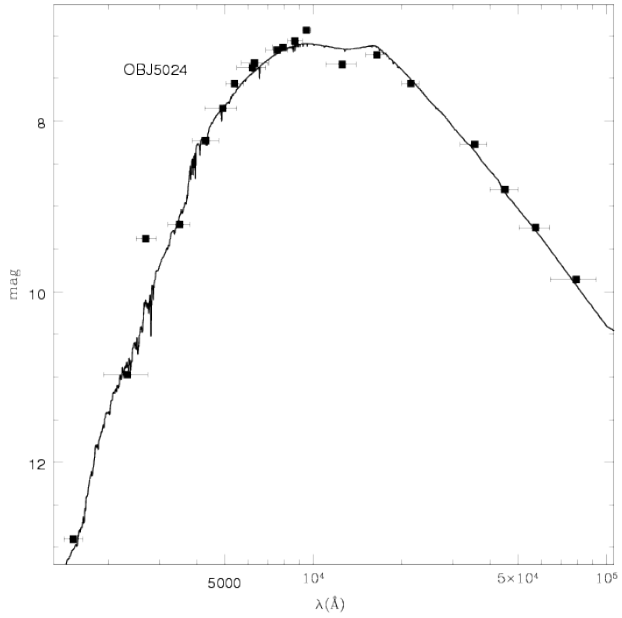

Figure 4.9: Multi-wavelength SED fitting of NGC 5024.

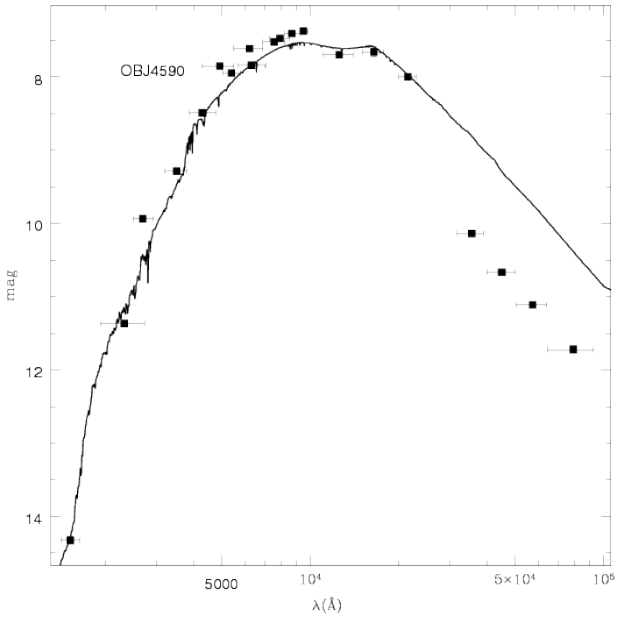

Figure 4.10: Multi-wavelength SED fitting of NGC 4590.

on each observed SED of our clusters, considering their specific metallicity and eventually ignoring bad photometric measures from the fitting procedure. In Figure 4.7, 4.8, 4.9, 4.10, we show results from our SED fitting for four clusters in our sample, NGC 104, NGC 1261, NGC 5024 and NGC 4590, respectively. In general we have good agreement between the observed magnitudes (black squares) and the fit (black line). However, we note that the *FUV*-band for NGC 104 is not fitted at all by the model predicting a brighter *FUV*-magnitude than the observed one. Indeed, we recall that in the *FUV*-band major emission come from the HB and the post-AGB stars: NGC 104 is characterized by an extremely red HB morphology (see Table 2.2), so the observed *FUV* emission is quite low.

Moreover, the *MIR*-bands for NGC 4590 are over-fitted: the model predicts brighter *MIR*-magnitudes than the observed one, which could be due to a number of AGB stars in the observed data of NGC 4590 lower than the one expected for its metallicity.

In cases like NGC 104 and NGC 4590, we decided to ignore the cited "bad" photometric bands from the χ^2-minimization.

Firstly, we decided to investigate the GGC ages inferred from SED fitting since the literature offers the opportunity to compare them to the ones obtained through independent measures using the observed GGC CMDs (vertical method, see Chapter 1).

Figure 4.11 shows the difference in age between the estimates by VandenBerg

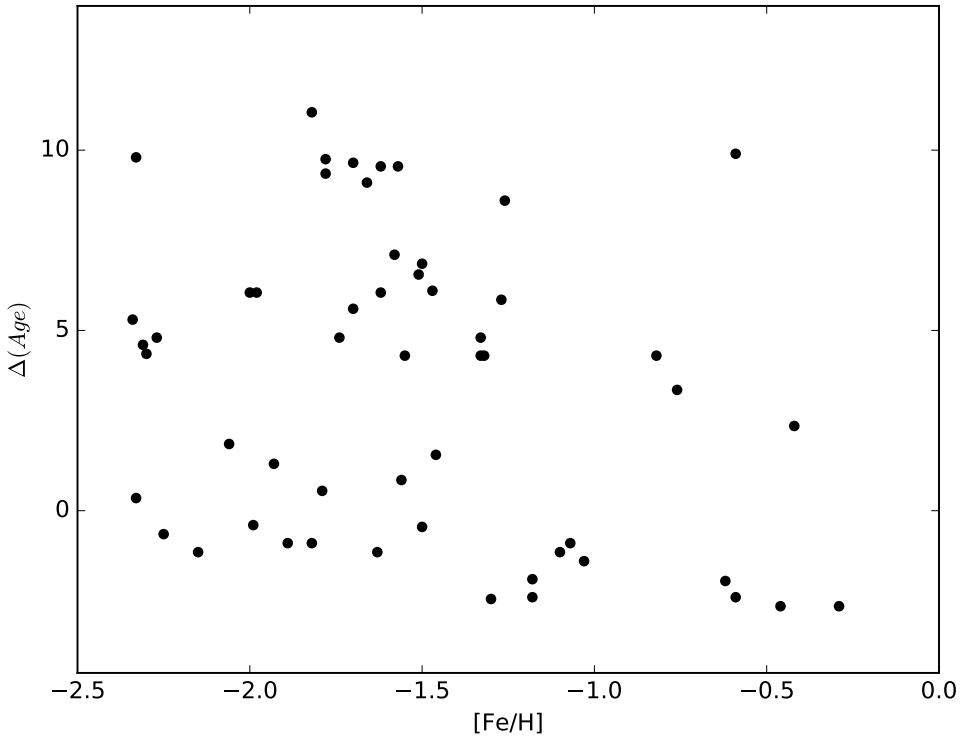

Figure 4.11: Difference between the age estimated by VandenBerg et al. (2013); Leaman et al. (2013) and the inferred values from SED fitting by *zphot* as a function of [Fe/H].

et al. (2013); Leaman et al. (2013) and the inferred values by *zphot* through SED fitting as a function of [Fe/H]. It is evident that the spread in ΔAge is higher than expected, spanning from -2.5 to 11. Taking into account the uncertainties both in VandenBerg et al. (2013); Leaman et al. (2013) and in the SED fitting procedure, we expected a maximum difference of $\sim \pm 2 Gyr$, well below the results shown in Figure 4.11.

Moreover, we observe that the clusters arrange in three groups: a group of clusters with $\Delta Age < 3 Gyr$, a second sample with $3 Gyr < \Delta Age < 7 Gyr$ and a third one characterized by $\Delta Age > 7 Gyr$, mostly located in the metal-poor regime ($[Fe/H] < -1.5$).

Interestingly enough, we find a mild relation between ΔAge and $[Fe/H]$, in which ΔAge seems to decrease as metallicity increases. This trend seems to be mostly evident observing the two groups with $\Delta Age < 3 Gyr$ and $3 Gyr < \Delta Age < 7 Gyr$, thanks to their higher statistics compared to clusters located at $\Delta Age > 7 Gyr$.

We examined the globulars inside the three groups but unfortunately we did not find a relation between their ΔAge values and parameters like age, metallicity or photometry.

To exclude possible uncertainties due to both SPS models and to observational errors (poor angular resolution, potential flux excesses from circumstellar dust). we decided to analyse our results excluding the MIR photometry. We show in Figure 4.12 the difference between the age estimated by VandenBerg et al. (2013); Leaman et al. (2013) and the inferred values from SED fitting by *zphot* as a function of [Fe/H] excluding the MIR photometry. We note that we still observe an high discrepancy between the two age estimates and we can still distinguish the three group arrangement, even though the second sample with $3 Gyr < \Delta Age < 7 Gyr$ is now poorly populated. The difference between age estimates based on SEDs including/neglecting the MIR is of the order of $\sim 20\%$.

For this reason, we analysed the rest-frame colours in several bands, since they are independent from distance and can give us further information on the stellar populations of our clusters (see Chapter 1).

Then, we calculated the models fixing the metallicity and leaving the age free during the simulation.

Figures 4.13, 4.14, 4.15 show six rest-frame colours in optical and *NIR* bands as a function of the age for [Fe/H]=-0.7, -1.7, -2.3, respectively. Our BC03 models are represented by red lines, while our observed available colours and ages are identified by the dots. In each figure we show our GGCs which we divided in different metallicity bins according to their [Fe/H] values from Carretta et al. (2009). We note that these bins do not contain an homogeneous number of clusters (17 GGCs for [Fe/H]=-2.3, 38 GGCs for [Fe/H]=-1.7, 8 for [Fe/H]=-0.7, 6 for [Fe/H]=-0.4, not shown in the Figure), because of the large meshes defined by the four sub-solar metallicities available in BC03. Moreover, we plot as blue dots the globulars located in the region with $\Delta Age < 3.0$ in Figure 4.11. We note that in general, the

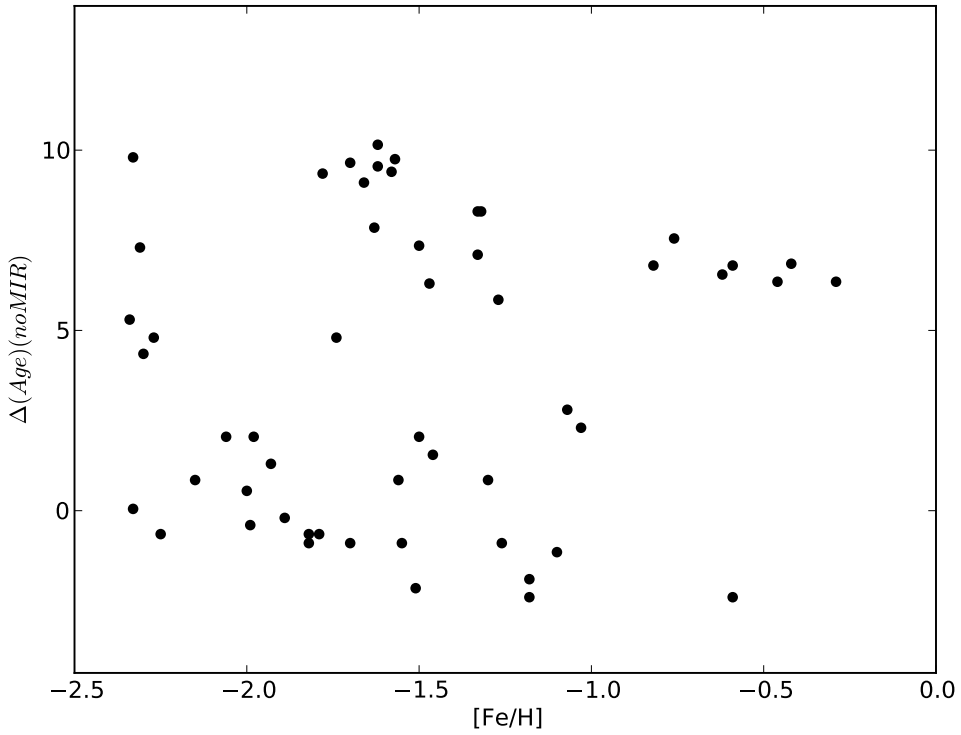

Figure 4.12: Difference between the age estimated by VandenBerg et al. (2013); Leaman et al. (2013) and the inferred values from SED fitting by *zphot* as a function of [Fe/H] excluding the MIR photometry.

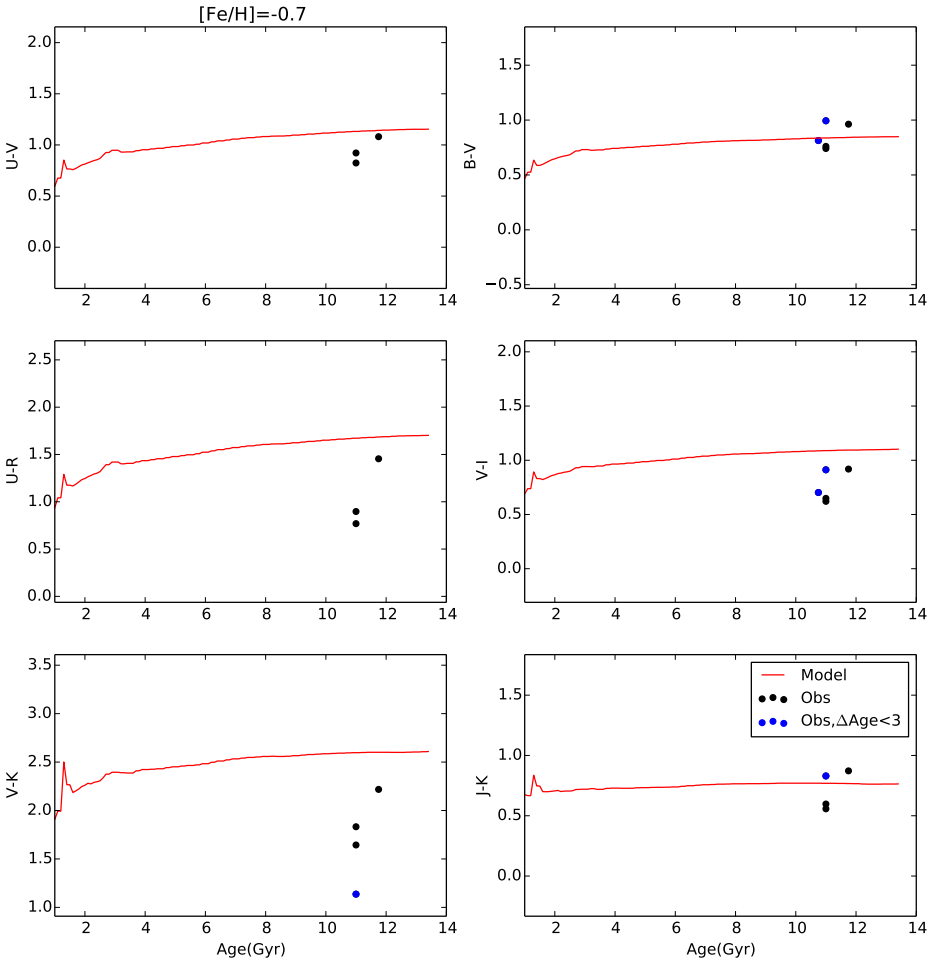

Figure 4.13: Rest-frame colours as a function of the age in Gyr. Red lines identifies our BC03 models for [Fe/H] value fixed to -0.7. Dots represent the observed points for globular clusters with [Fe/H] similar to -0.7. Blue dots identify the globulars in this metallicity bin located in the region with $\Delta Age < 3.0$ in Figure 4.11.

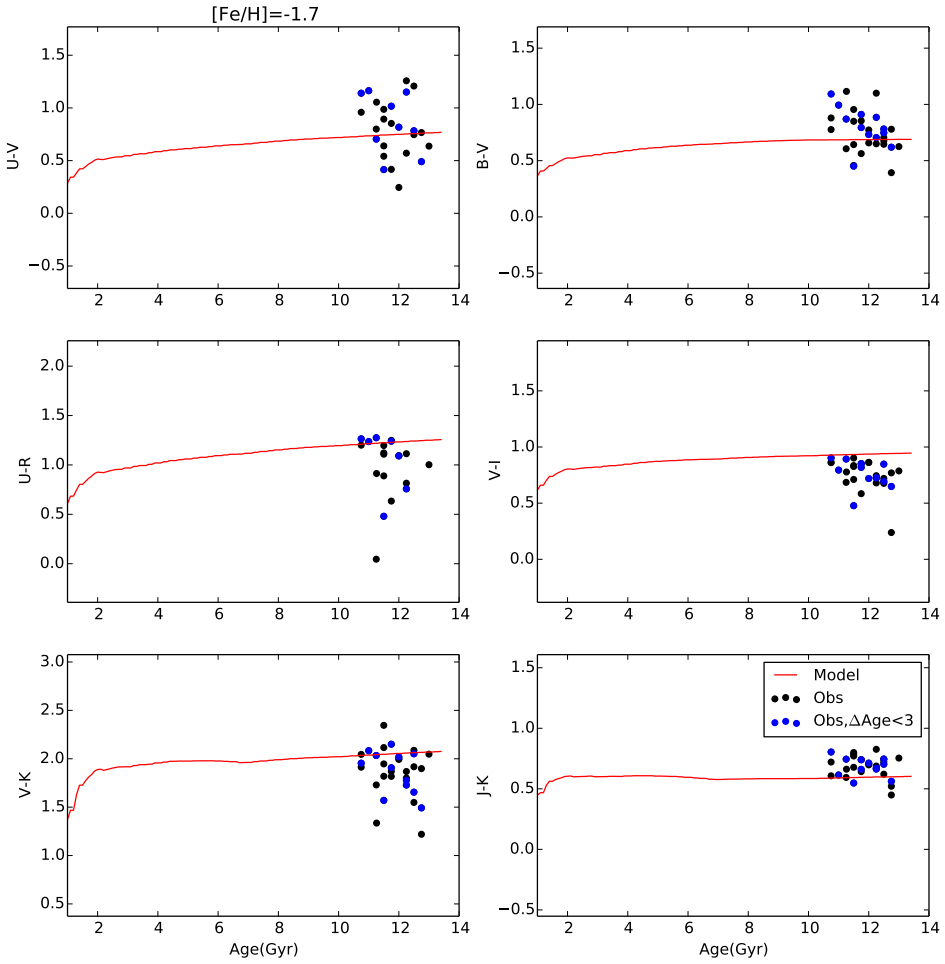

Figure 4.14: Rest-frame colours as a function of the age in Gyr. Red lines identifies our BC03 models for [Fe/H] value fixed to -1.7. Dots represent the observed points for globular clusters with [Fe/H] similar to -1.7. Blue dots identify the globulars in this metallicity bin located in the region with $\Delta Age < 3.0$ in Figure 4.11.

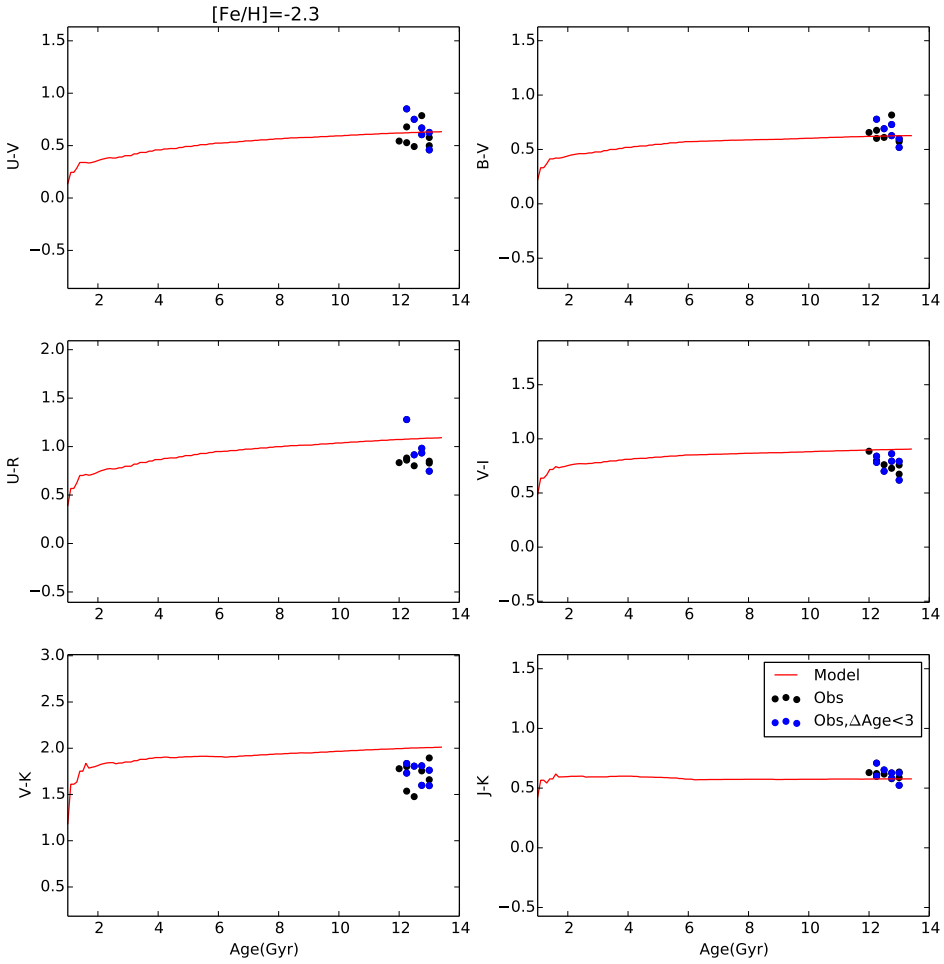

Figure 4.15: Rest-frame colours as a function of the age in Gyr. Red lines identifies our BC03 models for [Fe/H] value fixed to -2.3. Dots represent the observed points for globular clusters with [Fe/H] similar to -2.3. Blue dots identify the globulars in this metallicity bin located in the region with $\Delta Age < 3.0$ in Figure 4.11.

models attain an almost constant colour value after $t > 1Gyr$, while the clusters are placed in a cloud centred at $t \sim 12Gyr$ around this constant value. In the metallicity bins centred at [Fe/H]=-0.7 and [Fe/H]=-2.3 we have low statistics in our observations because of the already cited large [Fe/H] grid in BC03, while in [Fe/H]=-1.7 major differences ($< 0.5mag$) between models and observations arise in $U-R$ and $V-I$ for which the models are always redder than the observed points. In all cases, the observed colours are compatible with the younger theoretical regions. Finally, we do not find any trend characterizing the clusters with $\Delta Age < 3$, they arrange randomly inside the cloud of points, and so, their smaller ΔAge compared to the ones estimated for the other clusters cannot be explained with an better agreement to the theoretical rest-frame colours.

Then, we performed the models fixing the age to $13Gyr$ allowing the metallicity to attain the values: $Z/Z_{\odot} = 0.005, 0.02, 0.2, 0.4$. We extracted the rest-frame colours and compared them to the ones published in Conroy & Gunn (2010b), who used data of MW, Magellanic Clouds, M87 and Andromeda star clusters to perform a calibration of their FSPS models and a comparison between FSPS, BC03 and Ma05 (see Chapter 1).

Firstly, to check whether our models are valid, we compared them to the BC03 ones estimated by Conroy & Gunn (2010b) investigating the theoretical rest-frame colours, which are useful parameters since they are independent from distance effect. In general, we find good agreement with Conroy & Gunn (2010b) theoretical models. Major discrepancies arise in $U-V$ and in $B-V$ colours, where we find a difference of ~ 0.2 mag of ~ 0.1 mag between our and Conroy & Gunn (2010b) models, respectively. The highest difference is observed in the *NIR* $J-K$ colour (~ 0.3 mag), where, in any case, our model well-fits the observed points. These differences can be easily explained considering that they use the Kroupa (2001) IMF while we use the Salpeter (1955) one and we surely make use of different filter transmission curves. Considering these uncertainties, we can confirm the accuracy of our models.

Then, we compared our BC03 models to the ones by Conroy & Gunn (2010b) estimated through their FSPS code (see Chapter 1). Figure 4.16 shows the rest-frame optical and *NIR* colours as a function of [Fe/H]. The black dots identify the observed colours of our GGCs, we show our models, evaluated using BC03 and fixing the age to 13 Gyr, with red lines, while the green lines show the FSPS models published in Conroy & Gunn (2010b). From the Figure we can appreciate that in these wavelengths, the models are in good agreement. Indeed, we find higher differences in $U-V$ and $J-K$ colours both of a factor < 0.2 mag. Moreover, we find that they generally fit well the observed colours. The exceptions are in $V-I$-[Fe/H] and $V-K$-[Fe/H] diagrams, in which both models predict bluer colours than the observed ones. Interestingly, our model predict $J-K$ colours more consistent with data than the ones estimated through FSPS.

Furthermore, Figure 4.17 shows the rest-frame ultraviolet colours as a function

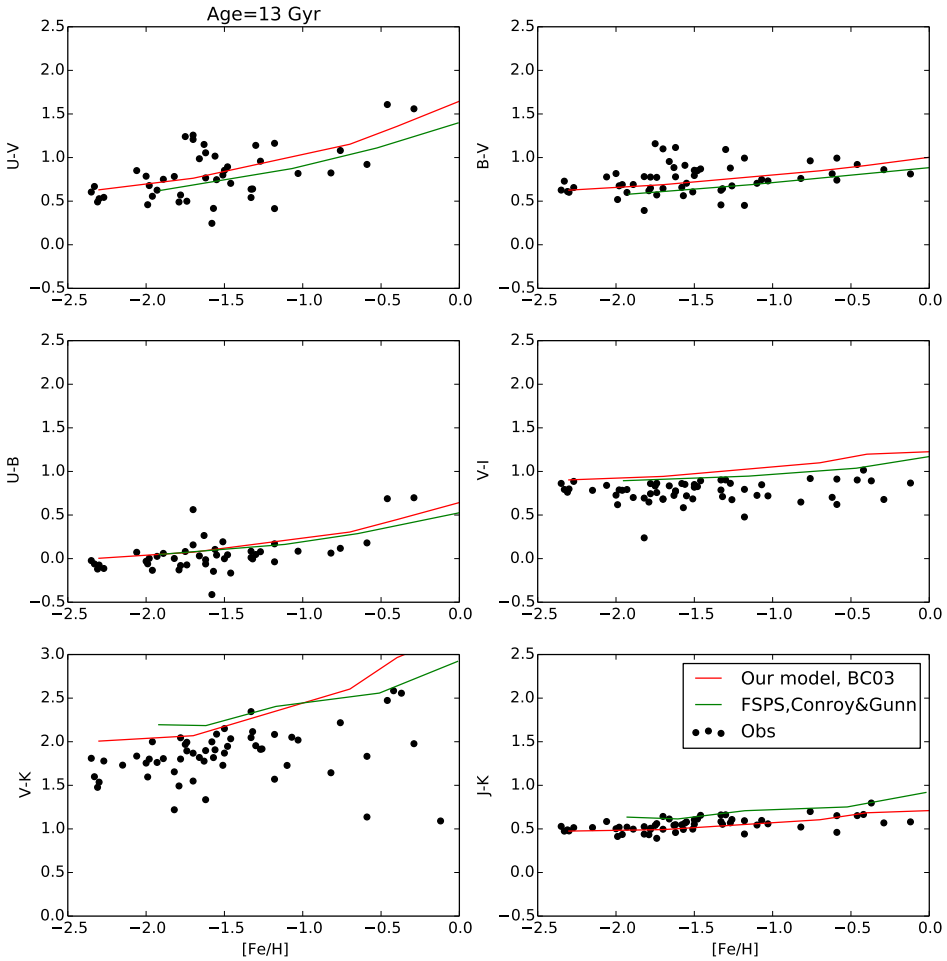

Figure 4.16: Comparison between our BC03 (red) and Conroy & Gunn (2010b) FSPS (green) models in optical and *NIR* wavelengths. Black dots show the observed colours of our sample of GGCs.

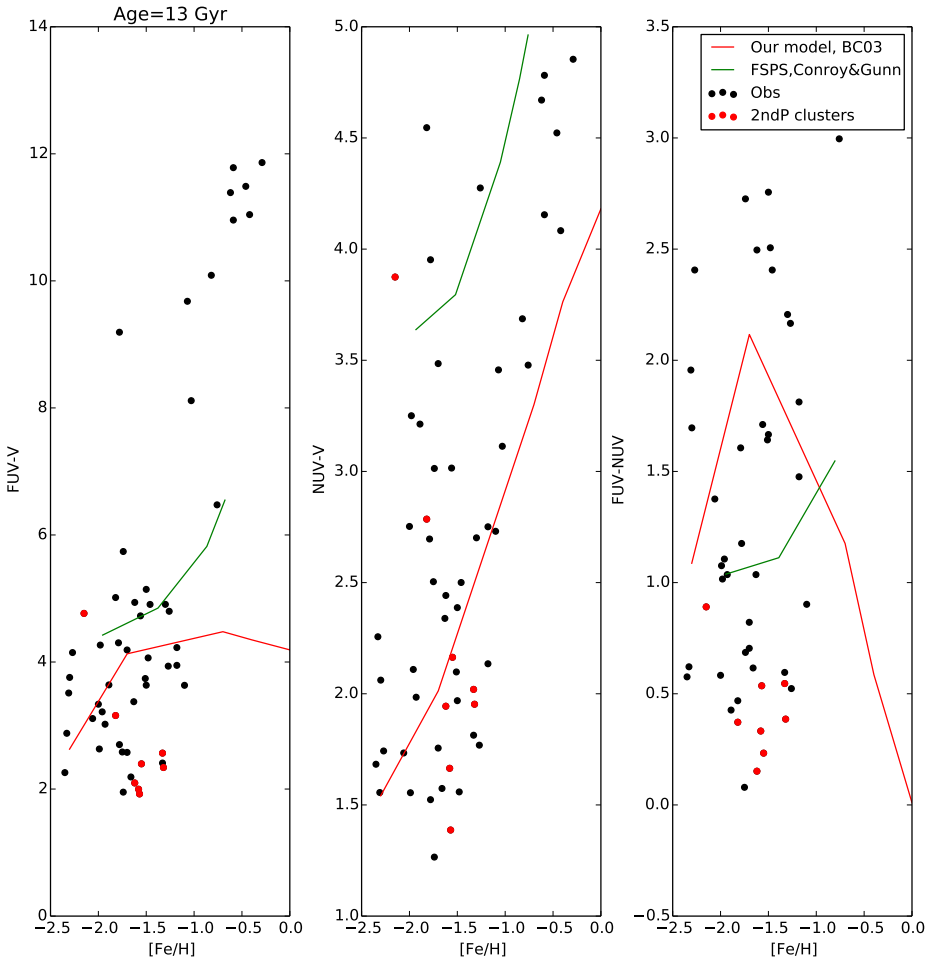

Figure 4.17: Comparison between our BC03 (red) and Conroy & Gunn (2010b) FSPS (green) models in *UV* wavelengths. Black dots show the observed colours of our sample of GGCs.

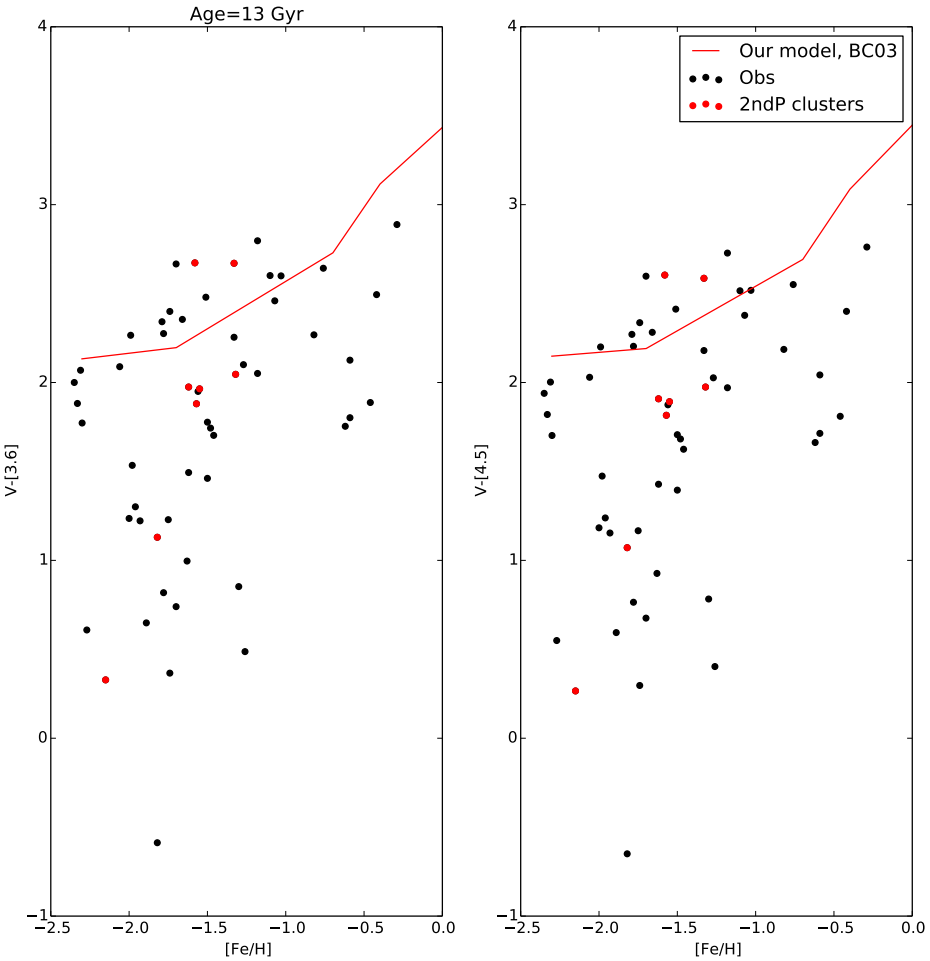

Figure 4.18: *MIR* colours as a function of metallicity. Red lines identify our BC03 models, black dots show the observed colours of our sample of GGCs. We show with red dots the 2ndP cluster colours.

of [Fe/H], also in this case black dots represent the observed colours of our GGCs, red lines show our BC03 models while we show with green lines the FSPS models by Conroy & Gunn (2010b). In these wavelengths, major differences between the two models and between models and observations arise. This can be explained through the different treatment of post-AGB and blue HB stars which are the main contributors in the UV colours. We recall that BC03 models includes post-AGB but lack of a specific treatment for hot and blue HB stars. On the contrary evolutionary tracks in FSPS models are supplied by the post-AGB treatment by Vassiliadis & Wood (1994), while the blue/ extended HB morphology is uniformly populated from RC to $Log(T_{eff}/K) = 4.2$ (Conroy & Gunn, 2010b). The FSPS models shown in this Figure are estimated including post-AGB stars and varying the fraction of blue HB stars as $f_{HB} = -0.75Log(Z/Z_{\odot}) - 0.5$ for $Log(Z/Z_{\odot}) < -0.7$ and zero otherwise. Firstly, we observe that the effect of the 2ndP problem is well observed in UV colours. Indeed, at fixed metallicity, $FUV - V$ colour varies of a factor of 5 mags, while $NUV - V$ colour varies at most of 3 mags. This is also confirmed by our 2ndP clusters identified in Chapter 2 (red dots) which, as expected, are characterized by an higher emission in UV wavelengths. We find that, in the FUV-band, both models are not able to cover the entire observed colour range spanned by the clusters, especially for the metal-rich regime ($[Fe/H] > -1.0$). On the contrary, the theoretical NUV-band seems to work better at least for our BC03 models. Indeed, FSPS models over-estimate NUV colours of metal-poor clusters. In fact, we note that FSPS models do not trace the extreme metal-rich and the extreme metal-poor regimes.

Moreover, we show in Figure 4.18 the rest-frame $V - [3.6]$ and $V - [4.5]$ colours, not investigated in Conroy & Gunn (2010b), as a function of[Fe/H]. Our BC03 models (red lines) seem to be systematically bluer than the observed ones (black dots), especially in the metal-poor regime.

We are still investigating about the possible reasons behind the high differences observed comparing the GGC ages from the literature and the ones inferred from SED fitting. However, we can suppose that the younger ages we infer for most of the globulars could be due to the fact the observed colours seem to be more compatible with the younger regions predicted by BC03 models. Moreover, the meshes defined by the four sub-solar metallicities available in BC03 are too large to properly divide the sample of GGCs in metallicity bins. This means that the age-metallicity relation cannot be properly identified and this certainly could be a source of uncertainty when inferring the cluster ages from SED fitting. Finally, we note that we used just one SED fitting code (*zphot*) combined with just one stellar library (Padova 1994) and SPSM (BC03) model since this combination was the simplest one to employ with our SED fitting code. Therefore, in the future, we aim to perform this investigation also for other SPSMs and to include other, and more updated, stellar libraries (see Sect. 1.3.2 for a list of the state-of-the art models in this field). We note that Conroy & Gunn (2010b) performed a more

extended comparison of BC03, FSPS and Ma05 models finding that: (1) all models predict similar optical and NIR colours for old metal-poor systems, while they all fail predicting the integrated J-K and V-K colours of observed MW and M31 star clusters; (2) they find a mismatch in the predicted FUV and NUV colours due to the different treatment of post-AGB and HB evolutionary phases; (3) FSPS and BC03 can reproduce the optical and NIR colours of post-starburst galaxies, while M05 cannot, probably due to different treatment of the TP-AGB stars.

Finally, to exclude a possible bias in inferred ages due to our SED fitting technique (χ^2-minimization), we are planning to take advantage of other codes, like EAZY or BEAGLE (see Sect. 1.3.5).

4.4 Conclusions

We performed an empirical calibration of BC03 SPSMs (Bruzual & Charlot, 2003), widely used in SED fitting codes to infer and investigate important physical parameters, like age, mass, SFR, of high-redshift galaxies. We calibrated the models against the observed GGC SEDs in an unprecedented wide coverage in wavelength (from FUV to MIR). In particular, we took advantage of GALEX/FUV-NUV (Dalessandro et al., 2012) and ACS/$F275W$ (Piotto et al., 2015b; Nardiello et al., 2018) integrated magnitudes for UV wavelengths. For those clusters for which we did not have data from the literature in FUV and/or NUV, we synthetically estimated the integrated magnitudes in these filters, performing a detailed and complete synthetic CMD using the code described in Salaris et al. (2013) and the bolometric corrections from PARSEC database.

In the optical range we took advantage of the $UBVRI$ ground-based data and $F606W$ ($\sim V$), $F814W$ ($\sim I$) space-based photometry already described in Chapter 2. Moreover, we also used the *grizy* data from the first data release of Pan-STARRS.

In the IR wavelengths, we employed the JHK_s photometry from the all-sky survey 2MASS, while for MIR bands we calculated the integrated magnitudes from bolometric corrections of the IRAC four channels filter system on board of SPITZER using the same synthetic CMDs estimated for the UV integrated magnitudes.

In this way, we have $FUV - MIR$ SEDs for each GGC in our sample. We found that, as expected, the 2ndP clusters identified in Chapter 2 have bluer UV colours if compared to the other globulars in the sample, considered as "standard" GGCs.

At this point, we performed the empirical calibration using the BC03 models with Padova 1994 isochrones. Firstly, we fixed the metallicity of the models to the values $Z/Z_\odot$= 0.005, 0.02, 0.2, 0.4, available in BC03. We used the Salpeter IMF and a τ-model SFH with τ = 0.01 to simulate a simple stellar population. We left the age as a free parameter in a fine grid from 1.0 Gyr to the age of the Universe. We divided the GGCs in four, not homogeneous, metallicity bins,

according to their [Fe/H] values and we performed for each of them the SED fitting using *zphot*. At this point, we were able to compare the cluster ages inferred from SED fitting to the ones independently estimated by VandenBerg et al. (2013); Leaman et al. (2013).

Surprisingly, we found a spread ΔAge which is higher than expected, spanning from -2.5 to 11. Indeed, considering the possible uncertainties both from SED fitting and from the photometric vertical method, we expected a difference of at most $\sim \pm 2 Gyr$.

Moreover, the clusters seem to arrange in three groups: a group of clusters with $\Delta Age < 3 Gyr$, a second sample with $3 Gyr < \Delta Age < 7 Gyr$ and a third one characterized by $\Delta Age > 7 Gyr$, mostly located in the metal-poor regime ($[Fe/H] < -1.5$). We also observed, thanks to their higher statistics, that the first two cited groups seem to be characterized by a mild relation between ΔAge and $[Fe/H]$, in which ΔAge seems to decrease as metallicity increases. So far, we did not find a correlation between their ΔAge values and parameters like age, metallicity or photometry, able to explain this behaviour.

To better investigate the possible causes, we decided to analyse the rest-frame colours since they are independent from distance and can give us further information on the stellar content of our clusters. Firstly, we calculated the theoretical models fixing the metallicity and leaving the age as a free parameter. Comparing the theoretical colours to the observed ones, we found that major differences ($< 0.5 mag$) arise in $U - R$ and $V - I$ colours and the observed colours are compatible with the younger theoretical regions. Moreover, we did not find any trend characterizing the clusters with $\Delta Age < 3$, since they are located randomly inside the other observed GGCs.

We also compared the rest-frame colours predicted by our BC03 models and the FSPS code by Conroy & Gunn (2010b). We found that, while in the optical and *NIR* wavelengths we have a fair good agreement both between the two models and between models and observations, we did not find the same results for *UV* and *MIR* colours. Indeed, we found high discrepancies (> 1 mag) between the models. Moreover, we found that both model fail to predict the observed $FUV - V$ colour, especially in the metal-rich regime, while in *NUV* band we find that BC03 model works better. We also found that in *MIR* colours, BC03 models over-estimate the observed colours, especially in the metal-poor regime.

We are still investigating about the possible reasons behind the high differences observed comparing the GGC ages from the literature and the ones inferred from SED fitting. A possible source of uncertainty is represented by the very large meshes defining the metallicity grid in BC03. In this way, we are not able to properly associate each GGC to its right [Fe/H] value, hence the age-metallicity relation cannot be properly estimated.

4.5 Notes on individual clusters

In the following we give notes about the clusters characterized by a peculiar synthetic CMD.

NGC 5986: the synthetic HB is not able to reproduce the extreme blue region of the observed one.

NGC 6752: the synthetic HB is not able to reproduce the extreme blue region of the observed one. The globular is a 2ndP cluster.

NGC 5904: the synthetic HB is not able to reproduce the redder region of the observed one.

NGC 5927: the synthetic HB is not able to reproduce the redder region of the observed one.

NGC 6712: the synthetic HB is not able to reproduce the observed one, which seems to be redder than expected at the cluster metallicity.

Terzan 7: the code does not reach extreme metal-poor [Fe/H] values. For this reason we do not list synthetic integrated magnitudes.

Chapter 5

The galaxy stellar mass function

After having analysed the resolved simple (Chapter 2) and composite (Chapter 3) stellar populations, now we are going to investigate the unresolved stellar populations in high redshift galaxies. To perform this analysis we have to take into account physical parameters inferred from SED fitting, also considering the results we obtained in our empirical calibration of BC03 SPSM against our sample of GGCs. In particular, we decided to investigate the high redshift Universe through the galaxy stellar mass function (GSMF).

GSMF is a fundamental tool to understand the formation and the evolution of galaxies in the Universe. It is nothing but a mass distribution, i.e., galaxy counts with a certain mass in a comoving volume. This statistical tool can provide information about the physics of galaxy growth across cosmic time: thanks to the fact that the integral of the Universe SFH is equal to the stellar mass density (SMD), it is a crucial observable to test and calibrate the modern galaxy formation and evolution simulations.

GSMF is more difficult to estimate if compared to the galaxy luminosity function. In fact, the GSMF estimation is affected not only by observational uncertainties but also by the significant model uncertainties due to the inferring of stellar masses (and redshifts, if spectroscopy is not available) from SED fitting techniques (see Chapter 1). Moreover, the presence of active galactic nuclei (AGNs) has an impact especially on the massive tail (Marchesini et al., 2009; Santini et al., 2012). Finally, different methods (e.g., Lyman Break galaxies (LBGs, Steidel et al., 1996) or photo-z) are often used to select galaxies at high redshift and each of them need corrections to provide a consistent sampling of the GSMF (see e.g., Duncan et al., 2014).

The improvement of observational technologies (both ground and space-based) allowed to analyse spectroscopic and photometric data from recent time to the early Universe epoch. In the literature, we can find GSMF measures in the local Universe ($z < 0.5$, Cole et al., 2001; Bell et al., 2003; Li & White, 2009; Baldry et al., 2012; Weigel et al., 2016) and evolutionary studies both in the low-z regime

($z < 2$, Fontana et al., 2004; Arnouts et al., 2007; Ilbert et al., 2010; Pozzetti et al., 2010; Brammer et al., 2011; Beare et al., 2019) and in the highest one ($2 < z < 7$, Fontana et al., 2006; Mortlock et al., 2011; Santini et al., 2012; Muzzin et al., 2013; Grazian et al., 2015; Tomczak et al., 2014; Stefanon et al., 2015; Davidzon et al., 2017).

Surveys covering large areas of the sky (e.g., UltraVISTA/COSMOS $\sim 2 deg^2$) give the opportunity to reach the highest mass-end of the GSMF thanks to the large-number statistics, while those reaching fainter magnitudes (e.g. the CANDELS or Frontier Fields programs) allow to cover the low mass-end. Therefore, combining the power of deep space-based and ground-based data is crucial to probe the entire description of stellar mass assembly and the physical processing driving it, from the re-ionization age to more recent epochs.

The Chapter is organized as follows. In Sect. 5.1, we describe the datasets (Ultravista/COSMOS, CANDELS and Frontier Fields Parallels) we used to estimate the GSMF. In Sect. 5.2, we describe our SED fitting recipe to estimate the stellar masses and our method to estimate the GSMF. Particular attention is given to our correction for incompleteness effects. In the same section we present our results on the GSMF estimated combining the three different data samples. We also show the Schechter fit and the comparison with previous measures in the literature. In Sect. 5.3 we show our results on the GSMF of the quiescent and star-forming galaxy populations selected through the UVJ diagram. In Sect. 5.4 we present the effects of our empirical calibration against our sample of GGCs on the GSMF of the galaxy quiescent population. We give a summary of the results and a brief discussion concerning future developments of the analysis in Sect. 5.5.

Throughout the work we assume a flat ΛCDM cosmology with $\Omega_m = 0.3$, $\Omega_\Lambda = 0.3$ and $H_0 = 70 kms^{-1}Mpc^{-1}$. In particular, we note that we chose a H_0 value which is a mean value between the estimates provided by Planck collaboration ($66.93 \pm 0.62 kms^{-1}Mpc^{-1}$, see for example Planck Collaboration et al., 2016) and the ones provided by stellar astrophysics ($73.24 \pm 1.7 kms^{-1}Mpc^{-1}$, see for example Riess et al., 2018)

5.1 Dataset

5.1.1 CANDELS

The Cosmic Assembly Near-IR Deep Extra-galactic Legacy Survey (CANDELS, Grogin et al., 2011; Koekemoer et al., 2011) is an extragalactic survey investigating the evolution of galaxies up to redshift ~ 8 through a deep imaging of $\sim 250,000$ objects with WFC3/IR and ACS on board of *HST*. It consists of five different fields (Fig. 5.1, ~ 800 $arcmin^2$) widely separated to mitigate the cosmic variance effects.

The analysed catalogues cover from UV to mid/far-IR wavelengths thanks to

the employment of different facilities in addition to *HST* data.

GOODS-S catalogue contains 34930 sources within an area of $\sim 170 arcmin^2$. We used 17 bands inside the photometric catalogue published and described in Guo et al. (2013).

We used 18 of the 25 photometric bands included in GOODS-N catalogue (Barro et al., 2019) containing 35445 sources ($\sim 176 arcmin^2$), while UDS catalogue (19 photometric bands) (Galametz et al., 2013) contains 35932 sources within an area of $\sim 202 arcmin^2$.

The 43-bands COSMOS photometric catalogue (Nayyeri et al., 2017) has 38671 sources within an area of $\sim 200 arcmin^2$, while the EGS catalogue (Stefanon et al., 2017) has photometric data for 41457 sources in 23 bands, within an area of $\sim 206 arcmin^2$.

The survey detection filter, $F160W$, reaches a 5σ limiting AB-magnitude of 27.56, 27.6, 27.8, 27.36, 27.45 for COSMOS, EGS, GOODS-N, GOODS-S, UDS, respectively (Merlin et al., 2019).

We took advantage of the latest CANDELS estimates for photometric redshifts obtained combining four independent estimations using different tools inside the CANDELS collaboration (Kodra, 2019).

5.1.2 Frontier Fields parallels

The Frontier Fields (FF) survey (Lotz et al., 2014; Koekemoer et al., 2014) collects data for six deep fields inside clusters of galaxies and six nearby deep parallel fields. It consists of observations from both space (*HST* and Spitzer) and ground-based (VLT) telescopes.

We took advantage of the multi-wavelength photometric and photo-z catalogues for four Frontier Fields parallels (Fig. 5.2): Abell-2744 (A2744), MACS-J0416 (M0416) (Merlin et al., 2016; Castellano et al., 2016), MACS-J0717 (M0717) and MACS-J1149 (M1149) (Di Criscienzo et al., 2017).

They offer an unprecedented opportunity to have high quality and extremely deep observations ($\sim 29th$ ABmag) thanks to the magnification provided by the foreground galaxy clusters. Moreover, as in the CANDELS case, the high number of fields reduces the cosmic variance effects.

5.1.3 UltraVista

UltraVista (McCracken et al., 2012) is the deepest component of the survey performed by the VISTA telescope of the European Southern Observatory (ESO), through the wide-field near-IR VIRCAM survey camera.

The survey covers an area of $2.0 deg^2$ and it is centred on the COSMOS field, the largest ACS/HST optical mosaic (Fig. 5.3a).

It consists of three separate components: the wide and deep Y, J, H, Ks survey, covering the entire area (orange area in Fig. 5.3a, the deep region is the difference

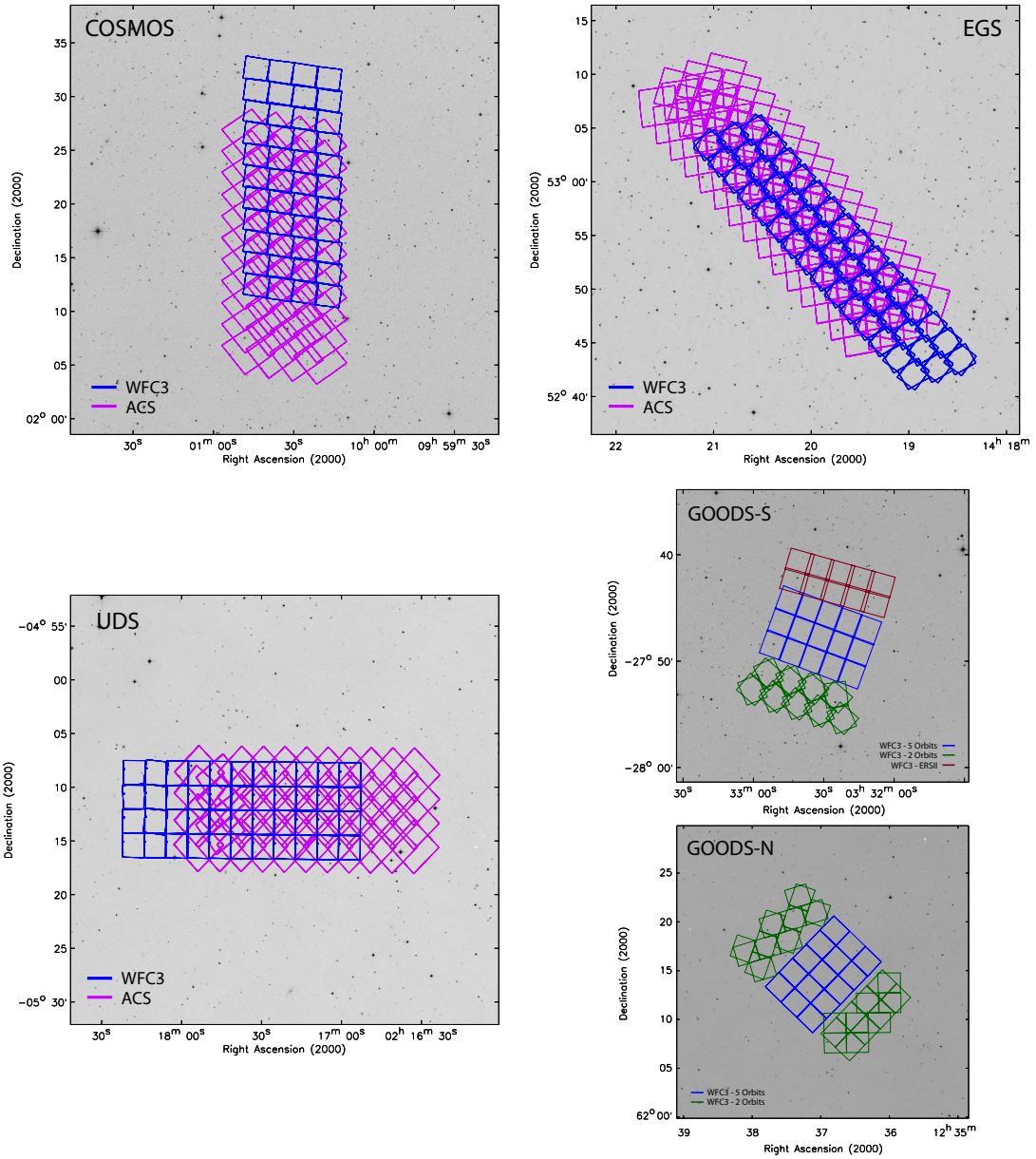

Figure 5.1: CANDELS fields.

between the orange and the light green areas); the ultra-deep Y, J, H, Ks survey which is composed by strips covering $0.7 deg^2$ (light green areas in Fig. 5.3a); an ultra-deep narrow-band ($1.18 \mu m$) survey to observe emission-line galaxies up to redshift ~ 9.

We took advantage of the latest COSMOS2015 UltraVista catalogue by Laigle

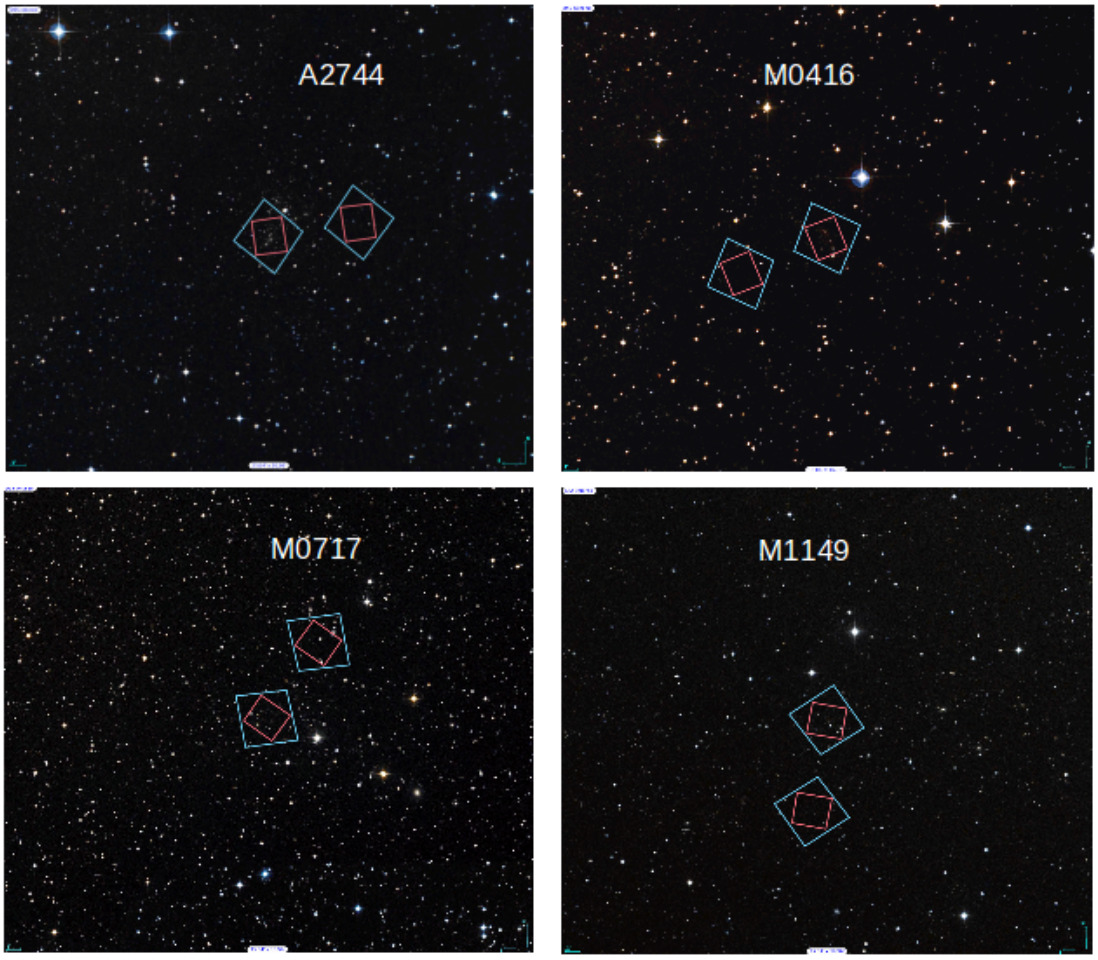

Figure 5.2: Frontier Fields areas. Top left: A2744 cluster (on the left) and parallel (on the right). Top right: M0416 cluster (on the right) and parallel (on the left). Bottom left: M0717 cluster (on the left) and parallel (on the right). Bottom right: M1149 cluster (top) and parallel (bottom).

et al. (2016). It includes new YJHKs data from the UltraVISTA-DR2 survey, Y-band data from Subaru/Hyper-Suprime-Cam, and infrared data from the Spitzer Large Area Survey inside the Hyper-Suprime-Cam Spitzer legacy program.

We made use of the $1.38 deg^2$ UltraVista area inside the COSMOS $2 deg^2$ field, for a total of 536077 sources, after removing flagged regions in the optical bands (Fig. 5.3b). The area corresponds to the intersection of the good region in the background image of Fig. 5.3a and the COSMOS $2 deg^2$ field for not masked sources in the optical bands.

When available we used the spectroscopic redshifts accessible within the COSMOS collaboration (Salvato et al., *in prep*), otherwise we used the Laigle et al. (2016) photo-z, obtained using ***LePhare*** as described in Ilbert et al. (2009).

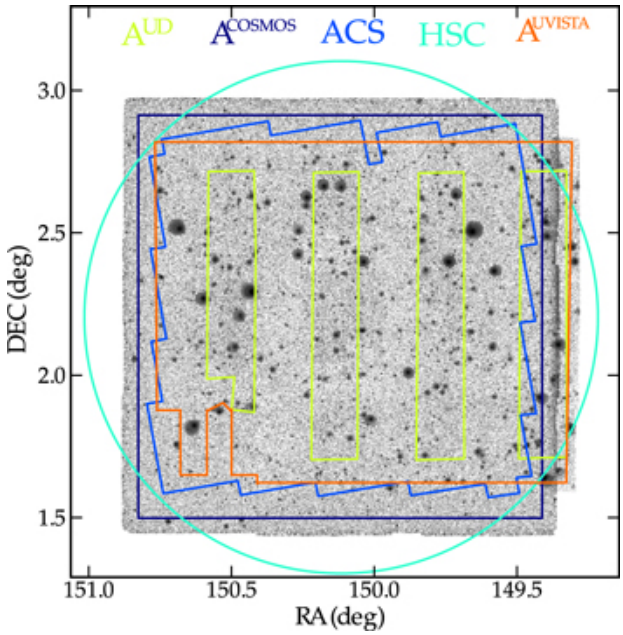

(a) $2deg^2$ UltraVista field (Laigle et al., 2016) from optical (dark blue and turquoise areas) and NIR (green and orange areas) observations. The cyan region is the one covered by the COSMOS-ACS/HST data, the dark blue and the orange regions identify the COSMOS $2deg^2$ and the UltraVISTA-DR2 observations, respectively. The light green area specifies the ultra-deep stripes in UltraVISTA.

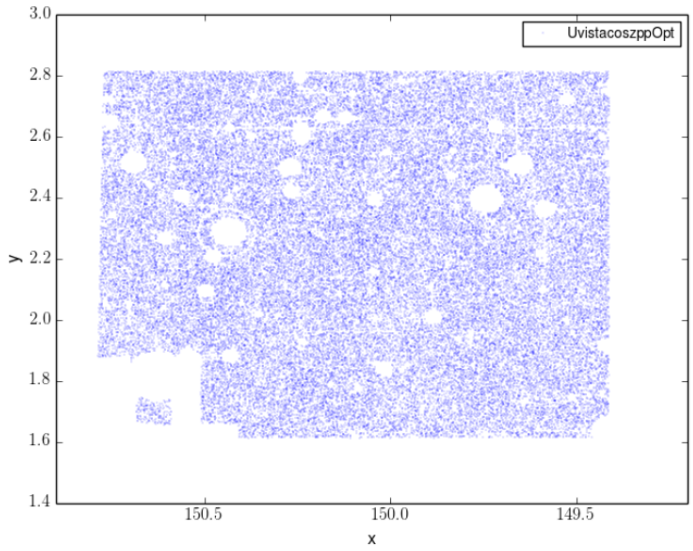

(b) UltraVista effective area ($1.38deg^2$) investigated in this work (Laigle et al., 2016).

Finally, we note that since the UltraVISTA/COSMOS field contains the CANDELS/COSMOS field, we made a cross-correlation within $0.4''$ and eliminated from the UltraVISTA catalogue the objects in common.

Therefore, we have ten fields for a total area of $1.65 deg^2$ reaching $z \sim 7$ (see Figure 5.4, showing the redshift distribution obtained from each field, in black the total distribution).

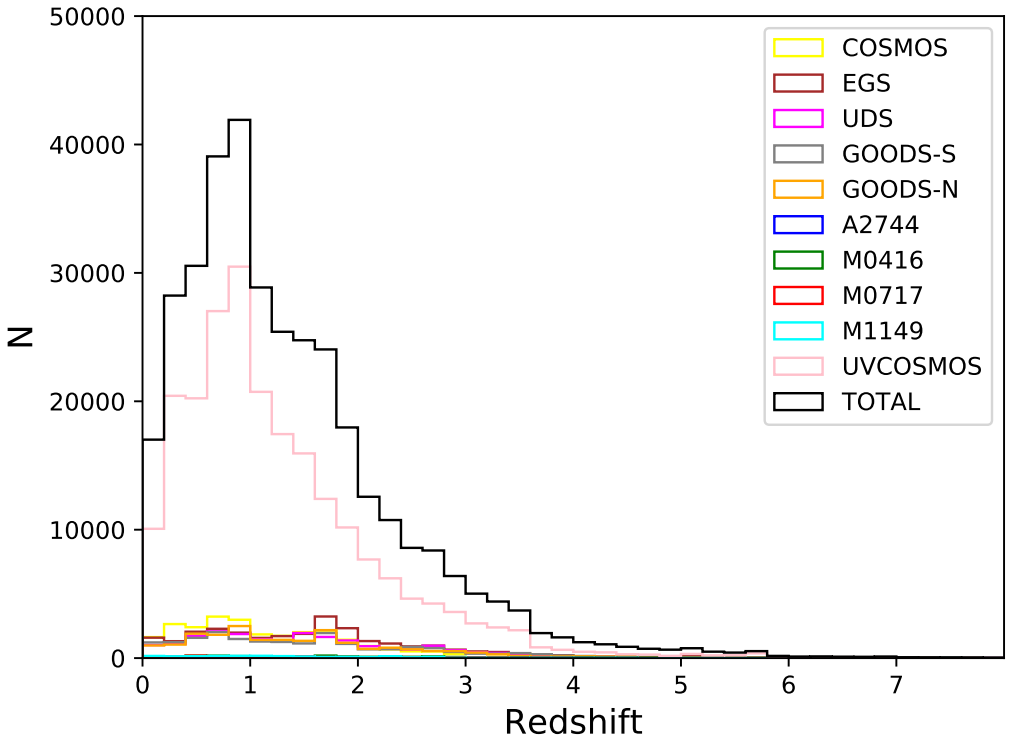

Figure 5.4: Redshift distribution of the galaxies in the different fields. In black the total distribution of the entire sample.

5.2 The galaxy stellar mass function derivation

5.2.1 Stellar masses

We derived the stellar masses using *zphot* code (see Sect. 3.1, Giallongo et al., 1998; Fontana et al., 2000). For each field we implemented the SED fitting procedure fixing the redshifts to the estimates described in the previous section.

We computed the stellar masses using the BC03 SPSMs and the Chabrier IMF. We fixed the metallicity values to Z= 0.02, 0.2 ,1, 2.5, while the colour excess E(B-V) varies from 0.1 to 1.1. We used the Calzetti et al. (2000) or the Small Magellanic Cloud (SMC, Hutchings, 1982) extinction curves. We adopted the "delayed" SFH ($SFH \propto t^2/\tau \cdot e^{-t/\tau}$, see Sect. 2.4), which increases up to the maximum value for $t = 2\tau$ and then decreases. τ values range from 0.1 to 2.0, while for the age we adopted a fine grid from 7 Gyr to the age of the Universe.

Finally, we adopted the Schaerer & de Barros (2009) prescription for nebular emission lines, as described in Castellano et al. (2014).

Fig. 5.5 shows the best-fit stellar mass distribution of the galaxies in the different fields as a function of redshift. This sample offers the unique opportunity to cover a large stellar mass range: thanks to FF deep photometry we cover very low masses ($10^5 - 10^6 M/M_\odot$), while the wide UltraVista area allows to reach the very high mass range ($M > 10^9 M/M_\odot$) also at $z \sim 6$. The red lines identify the mean stellar mass for each field: the decreasing to lower masses is compatible with the increasing of the limiting magnitude (i.e., fainter sources are detected).

Covering this large range in the stellar mass at different redshifts means improving our knowledge about the stellar mass assembly process in the Universe.

5.2.2 The galaxy stellar mass function estimate

We computed the GSMF adopting the standard procedure described in Fontana et al. (2004, 2006); Santini et al. (2012); Grazian et al. (2015) based on the non-parametric $1/V_{max}$ method defined by Schmidt (1968) for the luminosity function estimate. Following this technique, we firstly divide the galaxy sample in redshift bins, then we weight each galaxy in the comoving volume in which it can be observed according to the survey photometric limits. We estimate the maximum volume V_{max} at the maximum redshift over which the survey is complete for the object of mass M. Finally, in each redshift bin, the GSMF can be estimated as $1/V_{max}$.

In formulas:

$$\Phi(M,z) = \frac{1}{dM} \sum_{i=1}^{n} \left[\sum_{j} \omega(j) \int_{z_1}^{z_{up}(i,j)} \frac{dV}{dz} dz \right]^{-1} \tag{5.1}$$

where dM is the stellar mass bin, $\omega(j)$ is the area in units of steradians for each field j, while i is the object. $\frac{dV}{dz}$ is the comoving volume element per steradian.

Therefore, each field consists of sub-regions characterized by different depth and areas $\omega(j)$, which we need to take into account in the GSMF computation. Table 5.1 provides the depth and the area covered by different sub-regions for each analysed field.

Since the sample is magnitude-limited, we have not a well defined limit in stellar mass. This is due to the fact that there is not a univocal conversion from

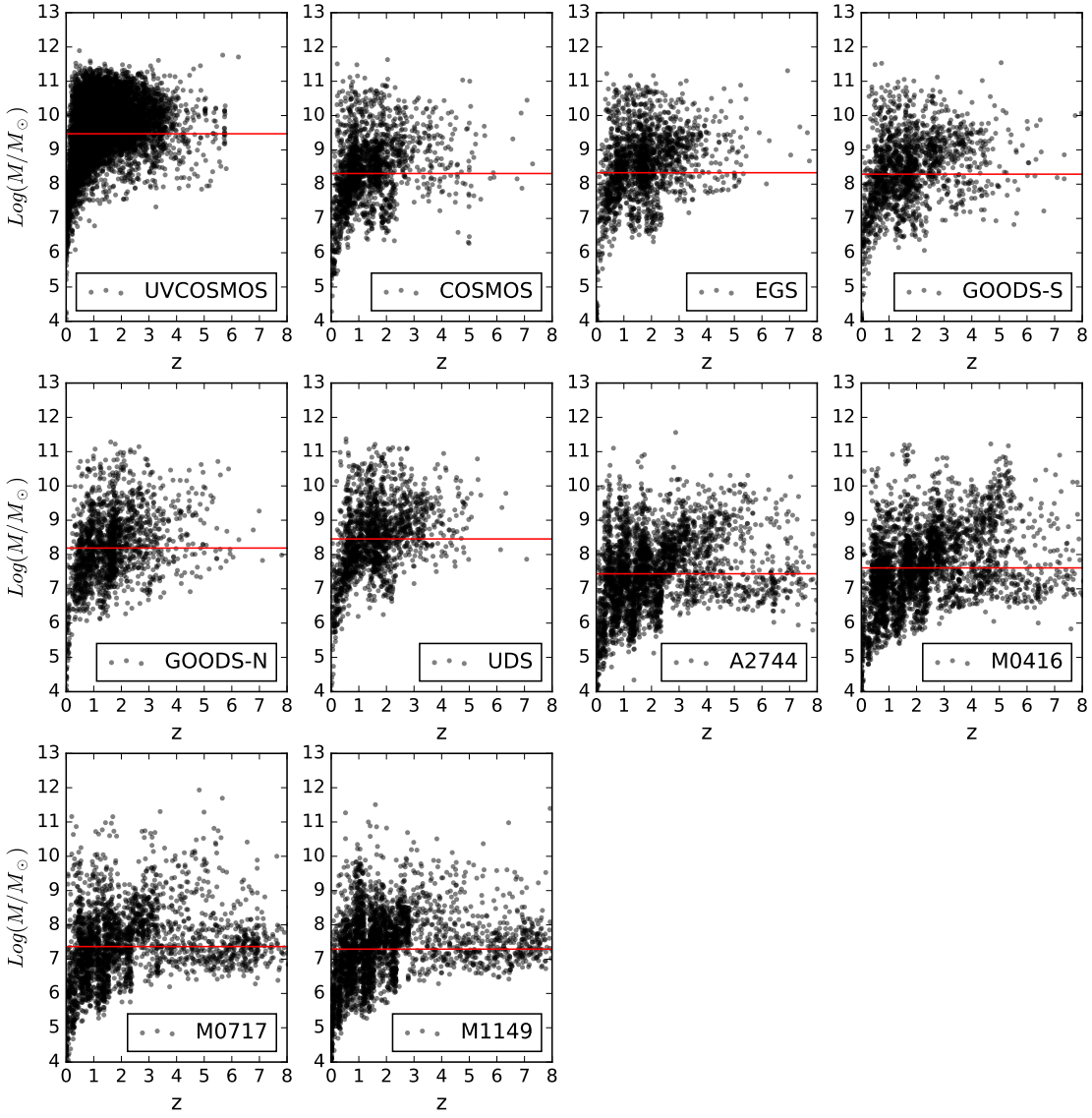

Figure 5.5: Mass distribution of the galaxies in the different fields as a function of redshift. The red line identifies the mean stellar mass in each field.

the observed magnitude to the stellar mass. This means that each galaxy of a

Table 5.1: Area and magnitude limits of the investigated fields.

Field	Area ($arcmin^2$)	Magnitude compl. limit (90 %)
EGS #1	48.90	26.5
EGS #2	138.22	26.7
EGS #3	19.27	26.8
COSMOS #1	63.30	26.3
COSMOS #2	136.7 5	26.5
GOODS-N #1	25.01	26.3
GOODS-N #2	71.27	26.4
GOODS-N #3	79.90	27.1
GOODS-S #1	9.26	26.0
GOODS-S #2	48.15	26.25
GOODS-S #3	105.76	27.2
GOODS-S #4	0.23	27.4
GOODS-S #5	5.05	28.7
UDS #1	58.9	26.2
UDS #2	132.5	26.45
UDS #3	10.3	26.7
A2744 #1	0.12	27.2
A2744 #2	0.52	27.4
A2744 #3	4.33	27.8
M0416 #1	0.097	27.8
M0416 #2	0.49	28.0
M0416 #3	4.39	28.4
M0717 #1	0.13	27.2
M0717 #2	0.65	27.8
M0717 #3	4.17	28.1
M1149 #1	0.18	27.2
M1149 #2	0.53	27.7
M1149 #3	4.32	28.1
UVCOSMOS #1	1.38	23.9

certain magnitude in our sample has a range of possible M/L values. Therefore, we need to correct for this incompleteness effect which mostly arises at the faintest levels of the GSMF. The effect is well shown in Fig. 5.6 (Fontana et al., 2004) which displays, considering a K-limited sample, the best-fit stellar mass for objects with $z > 0.7$ (filled red points) as a function of the K-flux (bottom x-axis) and K-mag (top x-axis). The natural scatter in the M/L_K ratios causes a scatter in stellar mass of about $\sim 0.6dex$, specified by the diagonal lines. Fig. 5.6 shows that if we consider a limiting magnitude of $K = 20$, the galaxy stellar mass can vary from $Log(M_*/M_\odot) \sim 9.5$ to $Log(M_*/M_\odot) \sim 10.3$. For each M_* value, we can estimate the fraction of galaxies we miss in the sample due to incompleteness (e.g., the dashed region in the figure).

To correct for this effect, we used the procedure described in Fontana et al. (2004).

At any redshift we estimate the completeness curve $M_{compl}(z)$, i.e., the observed M/L distributions of galaxies with a magnitude value close to the limiting magnitude of the sample.

Then, using an analytical functional form (linear or quadratic), we recover the fraction $1 - f_{obs}$ of galaxies that we are losing, and so the effective number of observed galaxies, f_{obs}. In general, as shown in Fig. 5.6, fixing the redshift value, only the sources with $M \geq M_{compl}(z)$ provide the complete sample.

Fig. 5.7 shows the galaxy stellar masses as a function of the redshift for the

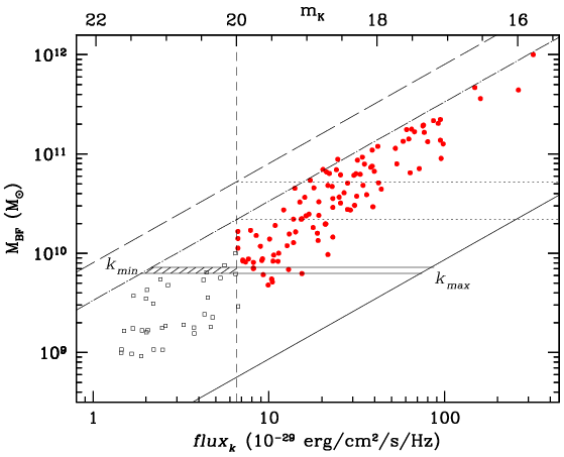

Figure 5.6: Observed K_s flux (lower scale) and K_s magnitudes (upper scale) as a function of the best-fit stellar masses estimated by Fontana et al. (2004) The diagonal lines identify the stellar mass the galaxies can attain according to their K_s magnitude. The solid line shows the minimum mass, the dashed line shows the maximum mass for dusty sources, while the dashed-dotted line is the maximum mass for dust-free objects. The dotted line is the completeness limit on stellar masses, while the shaded area identifies the fraction of galaxies lost due to incompleteness effect.

GOODS-S sample. The red solid line identifies the completeness curve and displays that for GOODS-S, only sources with $M > 10^{9.8} M_\odot$ can be detected at all redshifts, while the detection of less massive objects depends on the redshift value.

In general, thanks to the incompleteness correction, we can extend the GSMF to stellar masses smaller of a factor ~ 0.5 dex when compared to the ones estimated without the correction.

For each field, we computed the GSMF in seven redshift bins in the range $0.2 \leq z \leq 4.0$. We show the results in Fig. 5.8 with different coloured dots for each field, while the black square symbols identifies the *total* GSMF estimated considering the 10 fields as a whole. As expected, thanks to deeper IR photometry of the FF parallels ($H \sim 29$) we reach the very low mass end ($Log(M_*/M_\odot) \leq 7$ for $z \leq 1.5$, dwarf galaxies mass range), while thanks to the wide area of the UltraVista/COSMOS field we are able to cover the highest mass-end reaching the $Log(M_*/M_\odot) \sim 12$ also at $z \sim 4$. Fig. 5.8 shows an overall agreement between the functions of each single field. Major differences arise at low redshifts ($z < 0.5$) especially for the FF GSMFs, due to the fact that they contain a lower number of sources which causes a worse statistics. Moreover, the discrepancies in this redshift bin could be also due to the cosmic variance which especially affects the fainter objects.

We note that the error bars in the GSMF points are the Poissonian uncertainties due to the galaxy counts.

In Fig. 5.9, we compare our results (black dots) with the ones published in the literature using the same cosmology, IMF and stellar library. In general, we note

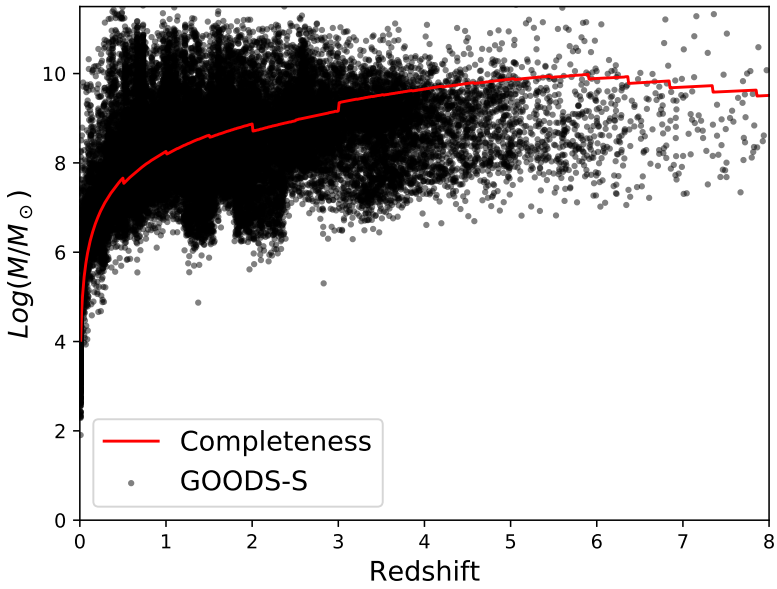

Figure 5.7: Mass distribution as a function of redshift for galaxies in the GOODS-S field (black dots). The red solid line identifies the completeness curve for the sample.

Table 5.2: Best-fit parameters for the Single and Double Schechter functions.

z_1	z_2	ϕ ($10^{-3}Mpc^{-3}$)	α	M^* ($M_\odot$)	ϕ_1 ($10^{-3}Mpc^{-3}$)	α_1	ϕ_2 ($10^{-3}Mpc^{-3}$)	α_2	M_2^* ($M_\odot$)
0.2	0.5	0.63 ± 0.13	-1.43 ± 0.01	11.28 ± 0.14	1.47 ± 0.48	-0.71 ± 0.31	0.67 ± 0.21	-1.48 ± 0.03	10.85 ± 0.11
0.5	1.0	0.73 ± 0.17	-1.39 ± 0.02	11.23 ± 0.15	2.38 ± 0.31	-0.65 ± 0.17	0.49 ± 0.16	-1.55 ± 0.04	10.73 ± 0.06
1.0	1.5	0.68 ± 0.11	-1.33 ± 0.03	11.01 ± 0.07	1.27 ± 0.19	-0.30 ± 0.32	0.61 ± 0.18	-1.42 ± 0.05	10.64 ± 0.07
1.5	2.0	0.28 ± 0.08	-1.51 ± 0.03	11.19 ± 0.14	0.85 ± 0.14	-0.86 ± 0.24	0.11 ± 0.09	-1.80 ± 0.14	10.78 ± 0.08
2.0	2.5	0.17 ± 0.04	-1.50 ± 0.03	11.11 ± 0.10	0.38 ± 0.07	-0.84 ± 0.32	0.08 ± 0.07	-1.74 ± 0.15	10.79 ± 0.09
2.5	3.0	0.11 ± 0.02	-1.65 ± 0.02	11.06 ± 0.05	0.15 ± 0.05	-1.37 ± 0.42	0.04 ± 0.09	-1.88 ± 0.32	10.93 ± 0.09
3.0	4.0	0.04 ± 0.01	-1.86 ± 0.02	11.04 ± 0.05	0.01 ± 0.004	1.13 ± 0.59	0.06 ± 0.01	-1.81 ± 0.03	10.85 ± 0.07

that there is good agreement between our $1/V_{max}$ points and the ones collected from the literature. At all redshift bins, we reach, as expected, lower masses than the ones attained by the other authors ($M \sim 10^7 M_\odot$ for $z < 2.0$, $M \sim 10^8 M_\odot$ otherwise, on average $1.5 - 2.0 dex$ lower than previous studies), while in the high-mass end (reaching the $M \sim 10^{12} M_\odot$) our results are consistent with the UltraVista GFMFs estimated by Muzzin et al. (2013); Ilbert et al. (2013); Davidzon et al. (2017), yellow pentagons, green diamonds and cyan triangles, respectively.

Up to $z = 3$, we display the GSMF from Tomczak et al. (2014) (red squares), measured using observations from the FourStar Galaxy Evolution Survey (ZFOURGE) and CANDELS: also in this case we find an excellent agreement. In $1.0 < z < 2.5$, Santini et al. (2012) (brown hexagons) measure an higher density of galaxies, i.e, they find a steeper GSMF because of the presence of a cluster of galaxies.

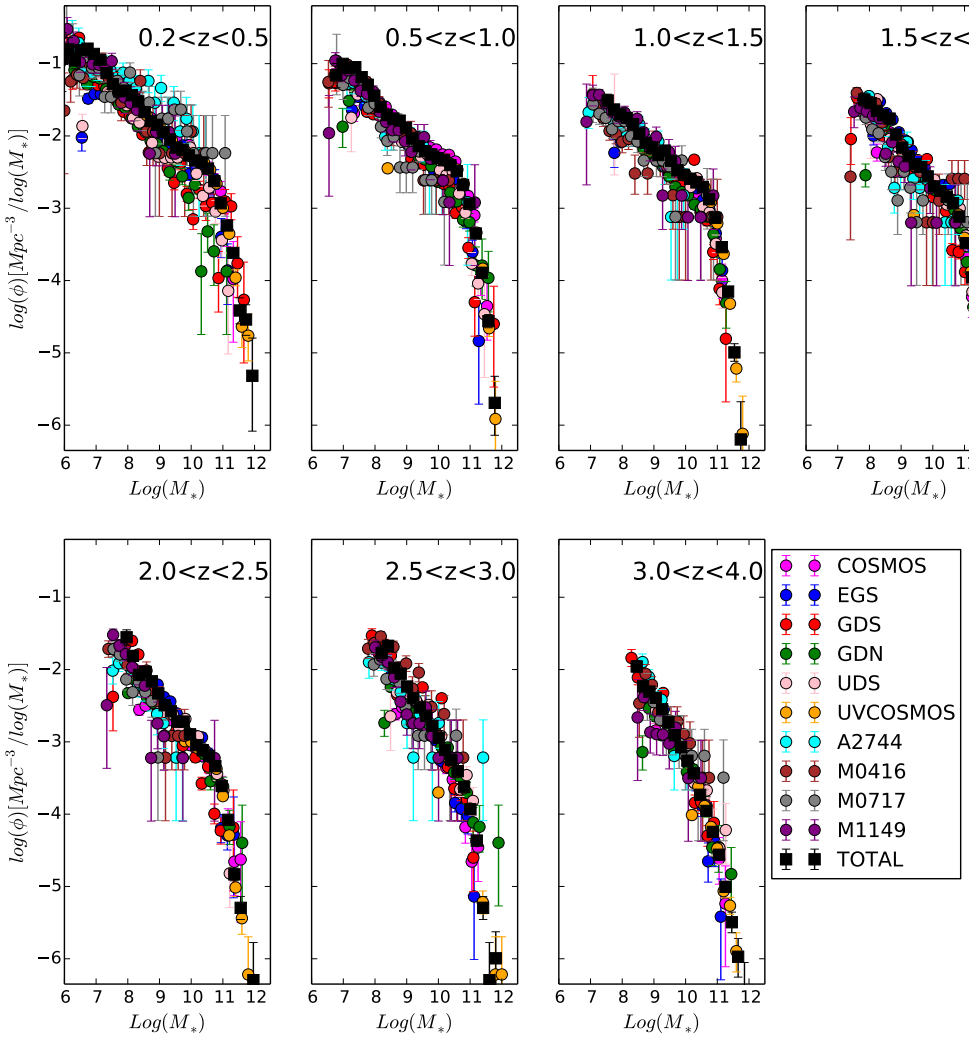

Figure 5.8: Individual and total GSMF in each redshift bin. Dot coloured symbols identify the GSMF for each field of the sample (see legend), black stars show the *total* GSMF of the joined fields.

GSMF can be described with the same functional form defined by Schechter (1976) for the luminosity function. In the logarithmic space, the number density

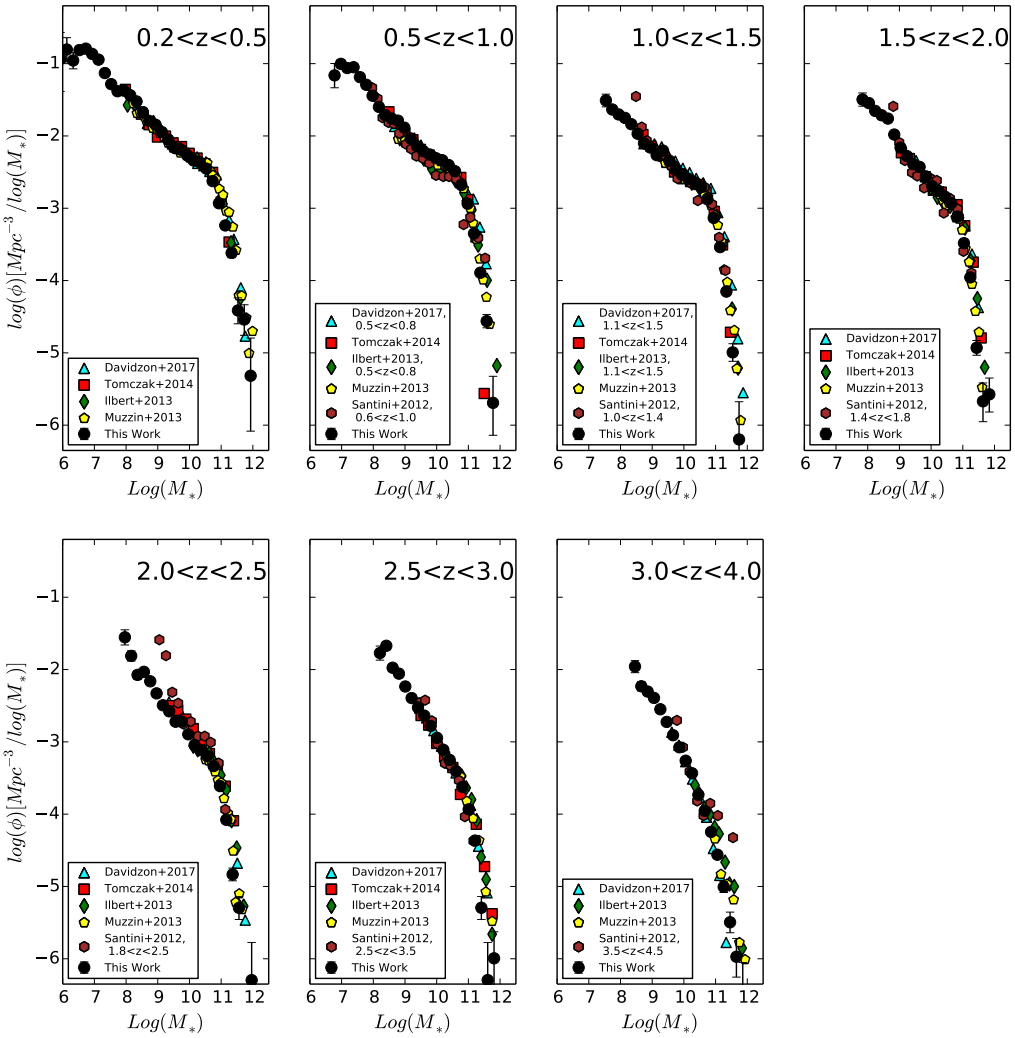

Figure 5.9: Total GSMF estimated in this work (black dots) compared to some of the results published in the literature: Santini et al. (2012) (brown hexagons), Ilbert et al. (2013) (green diamonds), Muzzin et al. (2013) (yellow pentagons), Tomczak et al. (2014) (red squares), Davidzon et al. (2017) (cyan triangles). In the legend we also display the redshift intervals in which the GSMF was computed if different from this work.

of galaxies of with mass M can be fitted as:

$$\phi(logM)d(logM) = ln(10)\phi^*\left(\frac{M}{M^*}\right)^{1+\alpha} exp\left(-\frac{M}{M^*}\right)dlogM \tag{5.2}$$

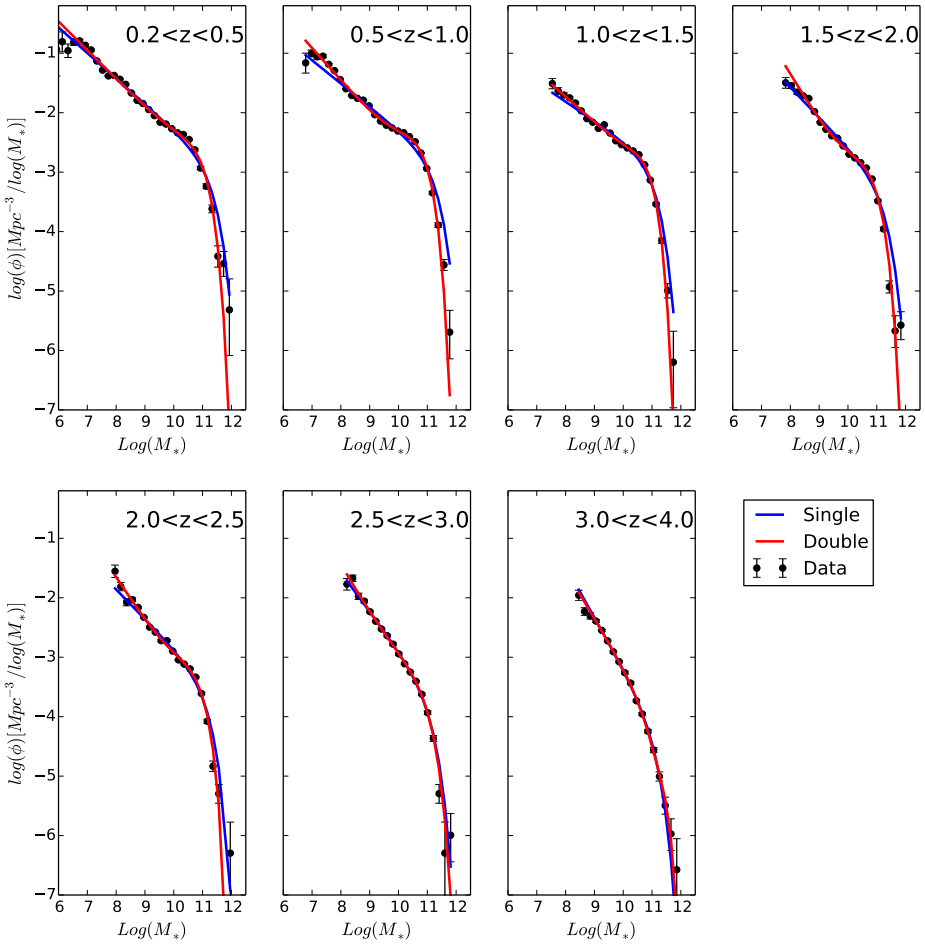

Figure 5.10: GSMF single Schechter (blue line) and Double Schechter (red line) best-fit functions.

where ϕ^* is the normalization, α is the low-mass end slope and M^* is the "knee" where the GFMF changes functional form: from a simple power law at lower masses to an exponential function at higher masses.

Recent studies (Li & White, 2009; Peng et al., 2010; Pozzetti et al., 2010; Baldry et al., 2012; Ilbert et al., 2013; Muzzin et al., 2013) have shown that at high redshift the GFMF is better described by a single Schechter function (Eq. 5.2) while at lower redshifts by the Double Schechter function, i.e., the sum of two single

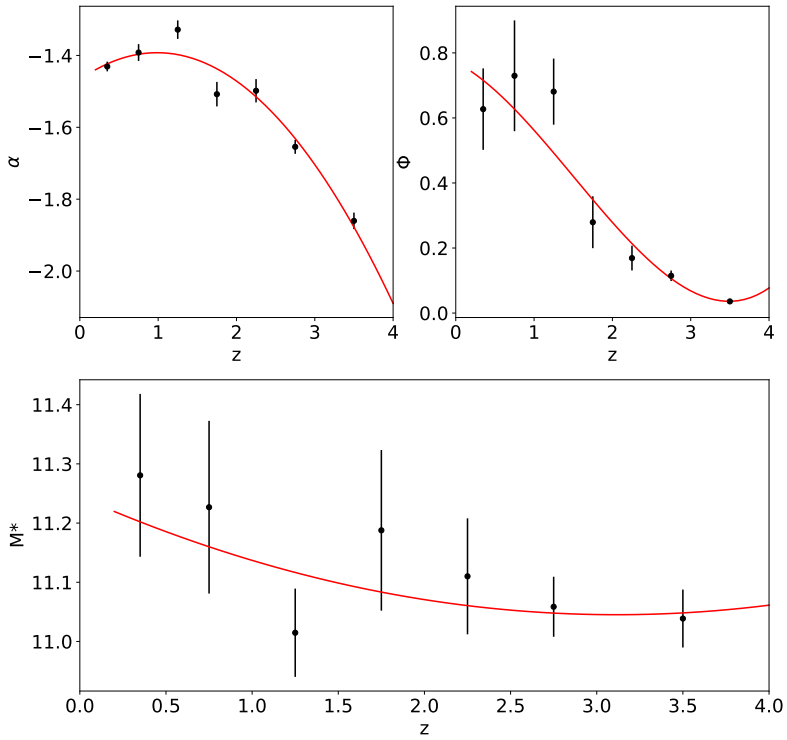

Figure 5.11: Single Schechter function best-fit parameters as a function of the redshift.

Schechter functions with the same M^*:

$$\phi(logM)dlogM = ln(10)exp\left(-\frac{M}{M^*}\right)\left[\phi_1^*\left(\frac{M}{M^*}\right)^{1+\alpha_1}\phi_2^*\left(\frac{M}{M^*}\right)^{1+\alpha_2}\right]d(logM) \tag{5.3}$$

where ϕ_1 and ϕ_2 are the normalization factors, while α_1 and α_2 are the low-mass end slopes of the two components.

Figure 5.10 shows the Schechter fit to our total GSMF in each redshift bin. The blue solid line identifies the single Schechter function, while the red line identifies the double Schechter one. The best-fit parameters, together with their errors and standard deviation are listed in Table 5.2, while the evolution with redshift of single Schechter function is shown in Figure 5.11.

Figure 5.10 and Figure 5.11 show that at $z > 1$ we have a progressive steepening of the faintest region (α reaches its maximum value in the third redshift bin, $1.0 < z < 1.5$). Moreover, the turn-over mass M^*, the GSMF "knee", at which the MF has an exponential decay, shows a slight decreasing with the redshift

increasing. This could suggest that the physics behind the appearance of the "knee" in the MF does not depend on the redshift. Finally, the normalization ϕ^*, i.e., the number density at M^*, decreases with the increasing of z, reaching the 0-value in the highest redshift bin ($3.0 < z < 4.0$). This means that while the overall shape of the GSMF does not change with redshift the normalization does. Moreover, we note that at $z < 2.5$ the GSMF seems to be better constrained by the double Schechter function, while at $z > 2.5$ we have not great discrepancies between the single and the double fits.

As already stated in Chapter 1, the galaxy stellar masses, and so the GSMF estimate, are affected by systematic uncertainties due to the chosen SED fitting ingredients. For example, Santini et al. (2012) found that stellar masses calculated using CB07 models (see Sect. 1.3.2), which contain an improved treatment of TP-AGB stars, are 0.12 dex lower that the galaxy stellar masses estimated employing the BC03 library. The observed shift has an effect also on the GSMF. Indeed, the authors found that, while at lowest and highest redshfits the GSMFs obtained using BC03 and CB07 models are quite in agreement, they show a more severe disagreement at intermediate redshifts. This is somewhat expected, since the TP-AGB phase gives an important contribution in the intermediate age range of 0.2-2 Gyr, i.e., 2<z<3. Moreover, Santini et al. (2012) investigated also the impact of the choice of different IMFs on the GSMF. As already stated by Salimbeni et al. (2009), they found that the galaxy stellar masses estimated employing a Chabrier IMF, are on average 0.24 dex lower that the ones calculated assuming a Salpeter IMF. This leads to a systematic shift of 0.24 dex on the GSMF at all redshifts.

Furthermore, Grazian et al. (2015) investigated the effects of the assumption of different SFH parametrizations on the GSMF and they found that the galaxy stellar masses are on average stable against the SFH parametrization, which mildly affects only the GSMF highest mass-end in 3.5<z<4.5. We show in Figure 5.12 the GOODS-S GSMF estimated assuming the delayed SFH (green squares) and the exponential declining SFH (red dots). As expected, we do not find a strong difference between the two GSMFs in this redshift range. Moreover, Grazian et al. (2015) also found that the stellar masses estimated employing or not the nebular emission is less than 0.1-0.2 dex, this means that the nebular contribution does not dramatically affect the GSMF estimate.

Therefore, our GSMF is certainly affected by the quoted systematic uncertainties due to SED fitting technique, but the GSMF estimate presented in this work is relevant thanks to the data combination which, for the first time, allowed us to explore the GSMF from its lowest mass-end to the highest one.

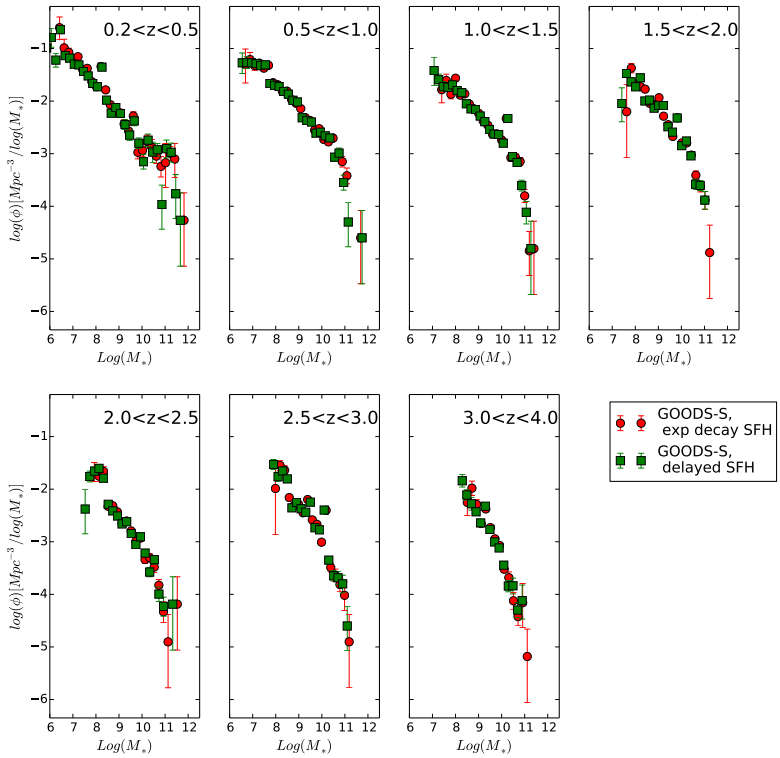

Figure 5.12: GSMF of CANDELS/GOODS-S field assuming an exponential declining (red dots) and a delayed (green squares) SFH.

5.3 The galaxy stellar mass function of star-forming and quiescent populations

Observations have shown that in the local Universe galaxies display a bimodal distribution in colour, mass and SFR (Kauffmann et al., 2003; Baldry et al., 2004; Blanton & Moustakas, 2009). Indeed, "quiescent" galaxies tend to be massive early-type galaxies showing little star-formation, redder colours and lower luminosity and mass functions if compared to other galaxies. Therefore, they form the so-called "red sequence" in the galaxy colour-mass diagram.

Moreover, recent works proved the existence of red quiescent galaxies also at $z > 3$ (e.g., Chen & Marzke, 2004; Fontana et al., 2009; Straatman et al., 2014; Merlin et al., 2018; Santini et al., 2019; Merlin et al., 2019), challenging our current models of galaxy formation and evolution. On the contrary, "star-forming" galaxies are active galaxies showing bluer colours and higher SFRs than the quiescent ones.

Analysing the GSMF of these two populations could allow to better understand the evolution and the stellar mass assembly in galaxies.

We decided to employ the rest-frame UVJ ($U-V$ vs $V-J$) diagram (Whitaker et al., 2011) to separate and select quiescent and star-forming galaxies. Indeed, the $V-J$ colour is a useful tool to distinguish quiescent galaxies from the dusty star-forming ones, which are characterized by red $U-V$ colours, and hence, they represent a source of contamination in the "red sequence" identified by the first ones. On the contrary, at fixed $U-V$, quiescent galaxies have red $V-J$ colours, while the dusty ones have bluer $V-J$ colours. Therefore, the UVJ diagram allows to easily identify the red clump associated to quiescent galaxies. In Figure 5.13, we show the UVJ diagram for the sources in all the ten fields we are considering in this analysis for each redshift bin. We can see that a clear bi-modality is visible up to $z \sim 2$ in the two regions selected by the red lines. We used the following criterion (red lines) to identify quiescent galaxies in our sample:

$$\begin{aligned}
&(U-V) > 0.88 \cdot (V-J) + 0.69, (U-V) > 1.3, (V-J) < 1.6 \quad [z < 0.5];\\
&(U-V) > 0.88 \cdot (V-J) + 0.59, (U-V) > 1.3, (V-J) < 1.6 \quad [0.5 < z < 1.5];\\
&(U-V) > 0.88 \cdot (V-J) + 0.59, (U-V) > 1.3, (V-J) < 1.5 \quad [1.5 < z < 2.0];\\
&(U-V) > 0.88 \cdot (V-J) + 0.59, (U-V) > 1.2, (V-J) < 1.4 \quad [2.0 < z < 4.0]
\end{aligned} \tag{5.4}$$

Once selected the two samples, we estimated the GSMF for star-forming and quiescent galaxies in $0.2 < z < 4.0$ applying the same method described in Sect. 5.2.2 and correcting for incompleteness effect.

In Figure 5.14 we show the total $1/V_{max}$ GSMF points of star-forming (blue) and quiescent (red) populations in the same redshift bins of Figure 5.8, while in Figure 5.15 we display GSMF Schechter fits for total (left), star-forming (middle) and quiescent (right) populations as a function of redshift (we list the best-fit parameters in Table 5.3). From both Figures, we have evidence that the GSMF for star-forming sample has a shape similar to the one attained by the total GSMF. On the contrary, we observe an upturn in the GSMF of quiescent population for $M < 10^9 M_\odot$. Indeed, as shown in Figure 5.15, while we can model the total and star-forming GSMFs through a single Schechter function at any redshift, we are able to fit the quiescent GSMF through a double Schechter function, such as we are facing to the arising of a double population in the red and passive galaxy sample. Left panel of Figure 5.15 shows that in general the GSMF evolution of the full sample is different if we consider the low-mass end and high-mass end. Indeed, for example, if we analyse galaxies with $M \sim 10^{8.5} M_\odot$, the MF increases of $\sim 0.3 dex$ from $1.0 < z < 1.5$ to $0.2 < z < 0.5$, while a galaxy of $M \sim 10^{11.5} M_\odot$ of $\sim 0.1 dex$ in the same redshift interval. This means that the evolution is mass-dependent. Moreover, we find an increasing of the number of galaxies with $10^{10} M_\odot < M < 10^{12} M_\odot$ up to $z \sim 2$, where we have the arising of the "knee" of the MF. Middle panel of Figure 5.15 shows that the GSMF of the star-forming population has

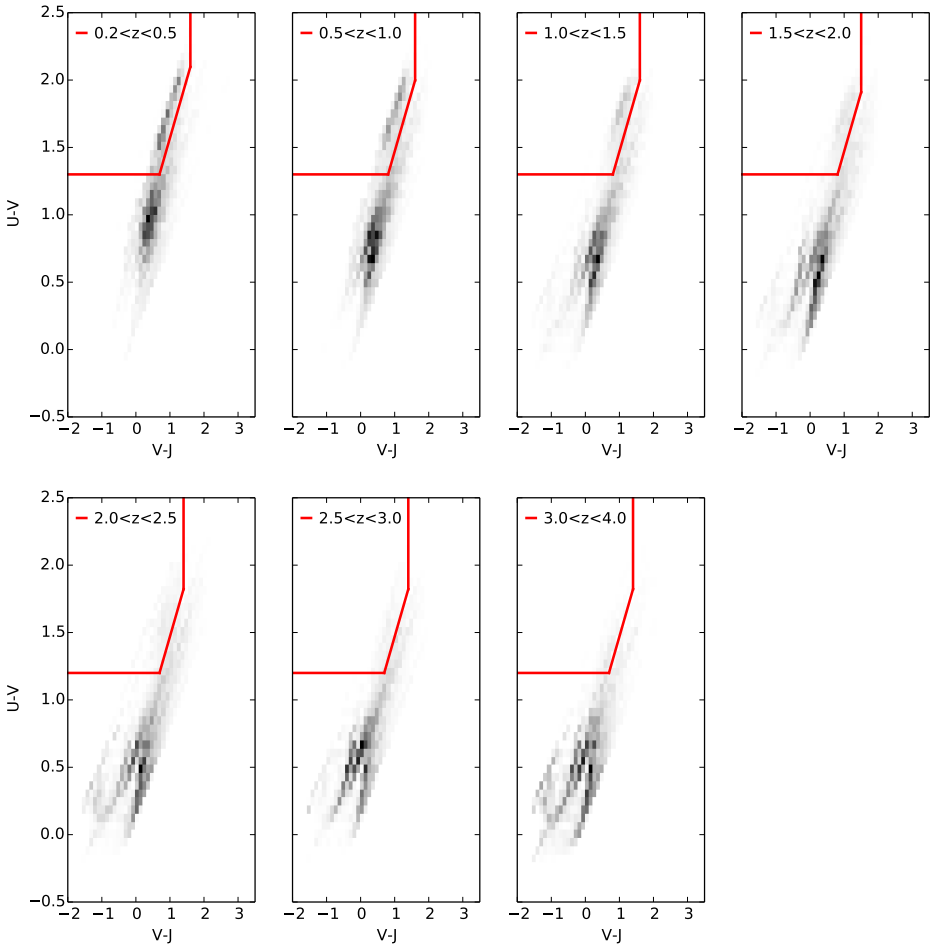

Figure 5.13: UVJ selection for sources in all ten fields in the seven different redshift bins. Darker areas identify higher densities of galaxies. Red lines show the separation between star-forming and quiescent populations.

an evolution similar to the total one. The low-mass end is in general steep in the entire redshift range. Moreover, we do not observe a strong evolution of the highest mass galaxies. Right panel of Figure 5.15 shows a clear bi-modality in the GSMF evolution of the quiescent galaxy population, for this reason we decide to fit it through a double Schechter function. In the $10^9 M_\odot < M < 10^{10.5} M_\odot$ range the GSMF is flatter, while the highest mass end does not seems to have a strong evolution. We observe a clear peak at $M \sim 10^{10.5} M_\odot$ up to $z \sim 0.5$, which turns

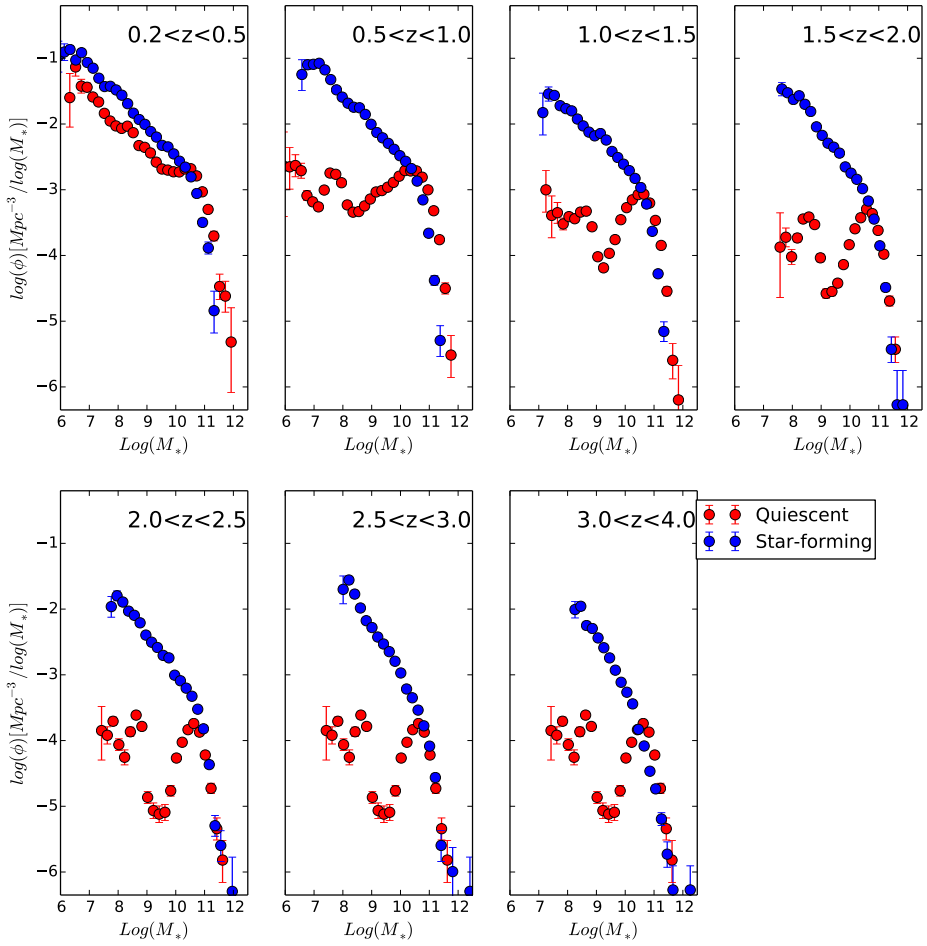

Figure 5.14: Total GSMF of star-forming (blue) and quiescent (red) populations in seven different redshift bins.

into the "knee" of the Schechter function at $z < 0.5$.

The arising of the upturn in the GSMF of the quiescent galaxy population at low masses ($M < 10^9 M_\odot$) has already been observed (see e.g., Tomczak et al., 2014) but it could not be explored because of incompleteness effects. On the contrary, thanks to our deep photometry we are now able to observe the steeper low-mass component of the quiescent GSMF up to $M \sim 10^7 M_\odot$. The bi-modality detected in the GSMF of quiescent galaxy population can be directly linked to the bi-modality

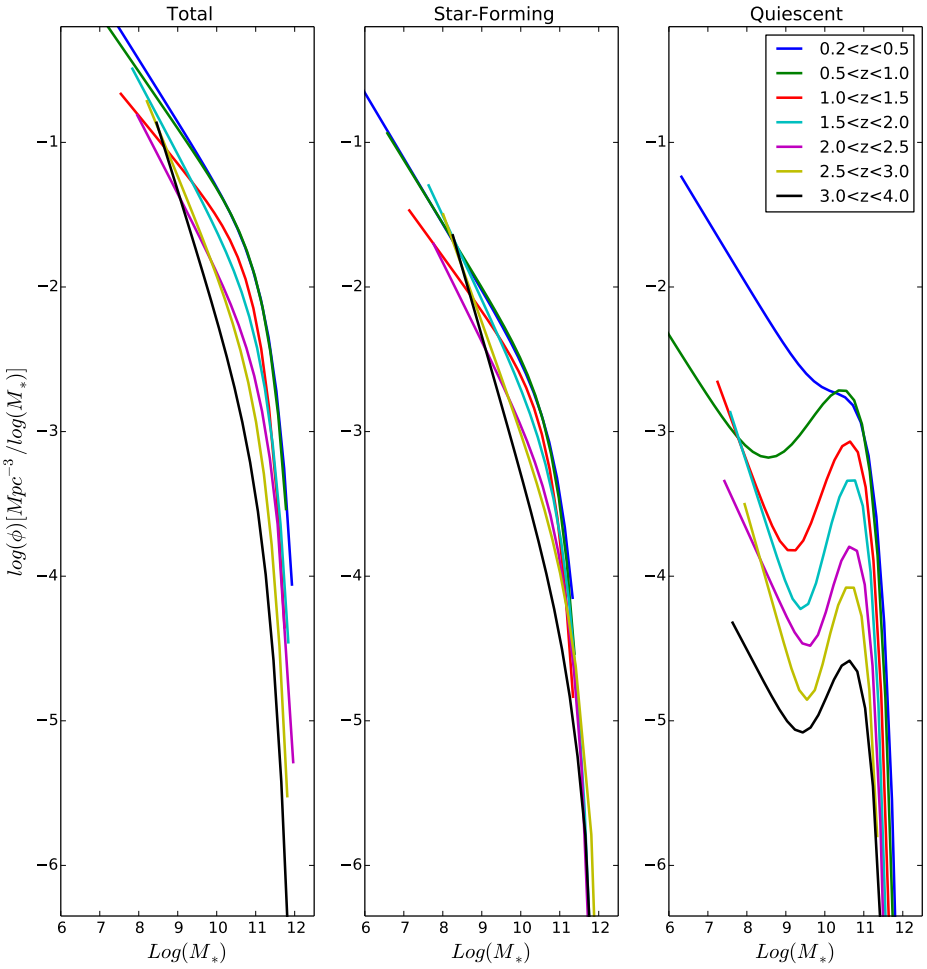

Figure 5.15: GSMF Schechter fits for total (left), star-forming (middle) and quiescent (right) populations as a function of the redshift.

observed in the Local GSMF (see e.g., Baldry et al., 2008, 2012; Peng et al., 2010, 2012; Taylor et al., 2015) shown in Figure 5.16 and which can be described by a double Schechter function (as well, we find that the double Schechter function well constrain the GSMF at z $<$ 2.5, see Sect.5.2.2).

According to the empirical approach described in Peng et al. (2010, 2012), the different evolution observed in the star-forming and in the quiescent GSMFs could be due to a combination of two different processes of quenching (i.e., a

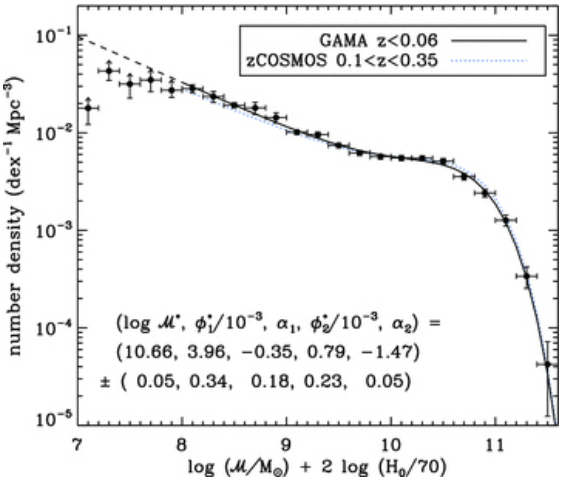

Figure 5.16: Local GSMF from Baldry et al. (2012) described through a double Schechter function

physical mechanism able to cease the star formation in a galaxy). Indeed, the single Schechter function able to describe the MF of the star-forming population could arise from a "mass" quenching, a dynamical process depending on a quenching rate which is proportional to the instantaneous SFR of the galaxy. According to this scenario, the mass quenching rate is the parameter determining the roughly constant M^* observed in the star-forming GSMF (see Figure 5.15 and the Schechter parameters listed in Table 5.3).

On the contrary, the arising of a second component in the GSMF of the quiescent population could be due to an "environment quenching", independent of stellar mass. The environmental mechanism causes a Schechter function with α and M^* similar to the ones attained by the star-forming function, but lower ϕ. From Table 5.3 it is evident that we find this behaviour at $z < 1.0$, while at higher redshifts the quiescent low-mass component attains α values more negative than the star- forming ones. On the contrary, the dominant component at high masses is due to the mass quenching. According to Peng et al. (2012), the environment quenching is entirely due to satellite galaxies and it does not depend on the mass of the satellite galaxy, but on the mass of the halo and satellite position in the halo itself.

In general, we find a more significant growth at $z < 2$, which is compatible with the scenario in which local early-type galaxies become quiescent in $0.8 < z < 2.5$ (Thomas et al., 2010).

Since we find a progressive decreasing of the number of quiescent galaxies, we can suppose that the GSMF at $z > 4$ is essentially driven by star-forming population, while the evolution of the highest mass-end is mainly due to passive galaxies.

Table 5.3: Best-fit parameters for star-forming, quiescent and total populations.

z_1	z_2	Sample	ϕ ($10^{-3}Mpc^{-3}$)	α	M^* ($M_\odot$)	ϕ_1 ($10^{-3}Mpc^{-3}$)	α_1	ϕ_2 ($10^{-3}Mpc^{-3}$)	α_2	M^*_d ($M_\odot$)
0.2	0.5	Total	0.63 ± 0.13	-1.43 ± 0.01	11.28 ± 0.14	1.47 ± 0.48	-0.71 ± 0.31	0.67 ± 0.21	-1.48 ± 0.03	10.85 ± 0.11
0.2	0.5	Quiescent	0.28 ± 0.11	-1.33 ± 0.03	11.55 ± 0.33	1.40 ± 0.24	-0.36 ± 0.24	0.25 ± 0.07	-1.45 ± 0.04	10.80 ± 0.08
0.2	0.5	Star-forming	0.55 ± 0.09	-1.45 ± 0.01	10.94 ± 0.10	–	–	–	–	–
0.5	1.0	Total	0.73 ± 0.17	-1.39 ± 0.02	11.23 ± 0.15	2.38 ± 0.31	-0.65 ± 0.17	0.49 ± 0.16	-1.55 ± 0.04	10.73 ± 0.06
0.5	1.0	Quiescent	1.21 ± 0.16	-0.80 ± 0.04	10.94 ± 0.09	2.00 ± 0.19	-0.45 ± 0.09	0.018 ± 0.02	-1.43 ± 0.16	10.72 ± 0.05
0.5	1.0	Star-forming	0.68 ± 0.10	-1.44 ± 0.02	10.84 ± 0.08	–	–	–	–	–
1.0	1.5	Total	0.68 ± 0.11	-1.33 ± 0.03	11.01 ± 0.07	1.27 ± 0.19	-0.30 ± 0.32	0.61 ± 0.18	-1.42 ± 0.05	10.64 ± 0.07
1.0	1.5	Quiescent	0.63 ± 0.11	-0.62 ± 0.09	10.88 ± 0.11	1.00 ± 0.07	0.07 ± 0.13	0.0033 ±0.0045	-1.73 ± 0.26	10.59 ± 0.04
1.0	1.5	Star-forming	0.69 ± 0.08	-1.37 ± 0.02	10.72 ± 0.05	–	–	–	–	–
1.5	2.0	Total	0.28 ± 0.08	-1.51 ± 0.03	11.19 ± 0.14	0.85 ± 0.14	-0.86 ± 0.24	0.11 ± 0.09	-1.80 ± 0.14	10.78 ± 0.08
1.5	2.0	Quiescent	0.30 ± 0.08	-0.70 ± 0.13	10.96 ± 0.20	0.50 ± 0.04	0.54 ± 0.23	0.002 ± 0.003	-1.84 ± 0.28	10.49 ± 0.06
1.5	2.0	Star-forming	0.26 ± 0.05	-1.58 ± 0.02	10.97 ± 0.09	–	–	–	–	–
2.0	2.5	Total	0.17 ± 0.04	-1.50 ± 0.03	11.11 ± 0.10	0.38 ± 0.07	-0.84 ± 0.32	0.08 ± 0.07	-1.74 ± 0.15	10.79 ± 0.09
2.0	2.5	Quiescent	0.08 ± 0.03	-0.90 ± 0.11	11.07 ± 0.29	0.16 ± 0.03	0.64 ± 0.44	0.003 ± 0.004	-1.59 ± 0.26	10.48 ± 0.10
2.0	2.5	Star-forming	0.15 ± 0.03	-1.54 ± 0.03	11.00 ± 0.08	–	–	–	–	–
2.5	3.0	Total	0.11 ± 0.02	-1.65 ± 0.02	11.06 ± 0.05	0.15 ± 0.05	-1.37 ± 0.42	0.04 ± 0.09	-1.88 ± 0.32	10.93 ± 0.09
2.5	3.0	Quiescent	0.05 ± 0.02	-0.80 ± 0.16	10.98 ± 0.30	0.08 ± 0.02	0.69 ± 0.43	0.00061 ± 0.0010	-1.95 ± 0.42	10.42 ± 0.10
2.5	3.0	Star-forming	0.05 ± 0.01	-1.75 ± 0.03	11.29 ± 0.12	–	–	–	–	–
3.0	4.0	Total	0.04 ± 0.01	-1.86 ± 0.02	11.04 ± 0.05	0.01 ± 0.004	1.13 ± 0.59	0.06 ± 0.01	-1.81 ± 0.03	10.85 ± 0.07
3.0	4.0	Quiescent	0.024 ± 0.004	-0.46 ± 0.12	10.75 ± 0.10	0.030 ± 0.003	0.19 ± 0.30	0.00066 ± 0.00110	-1.51 ± 0.43	10.55 ± 0.07
3.0	4.0	Star-forming	0.014 ± 0.007	-1.94 ± 0.048	11.31 ± 0.17	–	–	–	–	–

5.4 GGC calibration effects on quiescent GSMF

In Sect. 4.3, we present our results about our BC03 calibration on our sample of GGCs, obtaining that the ages inferred from SED fitting are on average younger than the ones estimated by VandenBerg et al. (2013); Leaman et al. (2013) through the vertical method. We plan to extend this calibration to high redshift galaxies, but first, we decided to investigate the effects of SPSM calibration on the GSMF of quiescent galaxies. Indeed, red quiescent galaxies similarly to the GGC sample, are considered to be composed primarily of old ($t > 10Gyr$) stellar populations.

Therefore, we decided to re-calibrate our galaxy stellar masses using a SED fitting prescription that prevents young ages from being assigned to quiescent galaxies at low and intermediate redshifts. In practice, following an approach already experimented in Fontana et al. (2004), we have achieved this by removing all the models where the formation redshift (that is a result of the model age and corresponds to the redshift at which the given model started producing stars) is lower than $1/\sqrt{\tau}$. This means that our prescription eliminates the non-physical low τ values at low redshifts, hence it "forces" galaxies for which we infer too young, non-physical ages for their observed redshift, to be older.

Therefore, firstly we performed our SED fitting procedure using the new prescription, obtaining new and re-calibrated physical parameters. Then, we re-selected the quiescent galaxies through UVJ diagram as we described in Sect. 5.3. We show the impact of our prescription on the age of quiescent galaxies in our sample in Figure 5.17. In this plot, we show the new re-calibrated ages as a function of the ages inferred without employing the prescription. As expected, the non-physical too young ages (especially if $Age < 8Gyr$) are forced to be older, while we do not significantly modify the ages of the already old galaxies.

We also compared the galaxy stellar masses inferred using the new prescription

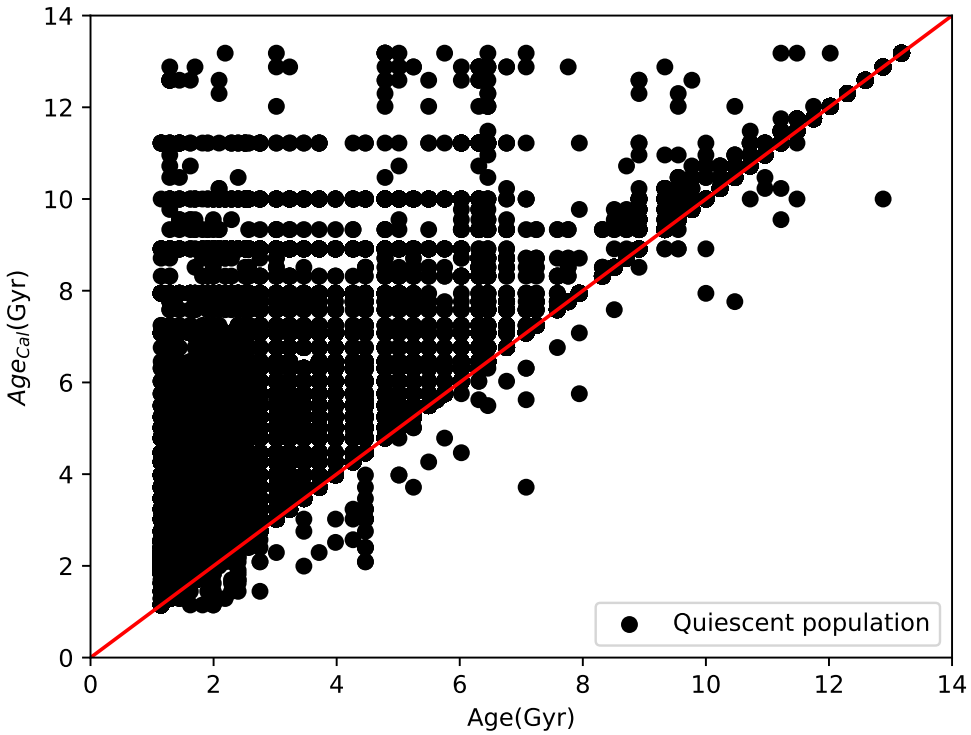

Figure 5.17: Quiescent galaxy calibrated ages using the prescription described in the main text as a function of the ages inferred not using the prescription. Red line shows the bisector of the diagram.

to the ones estimated with the old SED fitting procedure. We show our results in Figure 5.18 finding that the galaxy stellar masses are mildly affected by the new calibration, we estimate a maximum mean shift of $\sim 0.45 dex$.

Finally, we estimated the calibrated quiescent GSMF and compared it to the one obtained in Sect. 5.4 without employing our prescription. We show this comparison in Figure 5.19, red dots represent the quiescent GSMF estimated in Sect. 5.4, while the green squares identify the quiescent GSMF after calibration. We find that, at $z < 1.5$, a mild difference (< 0.1 dex) between the GSMFs arises at low masses ($M < 10^8 M_\odot$), while the calibration does not have impact on the GSMF in $1.5 < z < 2.5$. Conversely, we find major differences in the GSMFs at higher redshift. However, the observed discrepancies are not due to an age effect, but it is due to the lower statistics in the number of quiescent galaxies estimated after the employment of our prescription. Indeed, at high redshift, our calibration procedure eliminates models with $\tau = 0.1$, causing the decreasing of the number of selected quiescent galaxies.

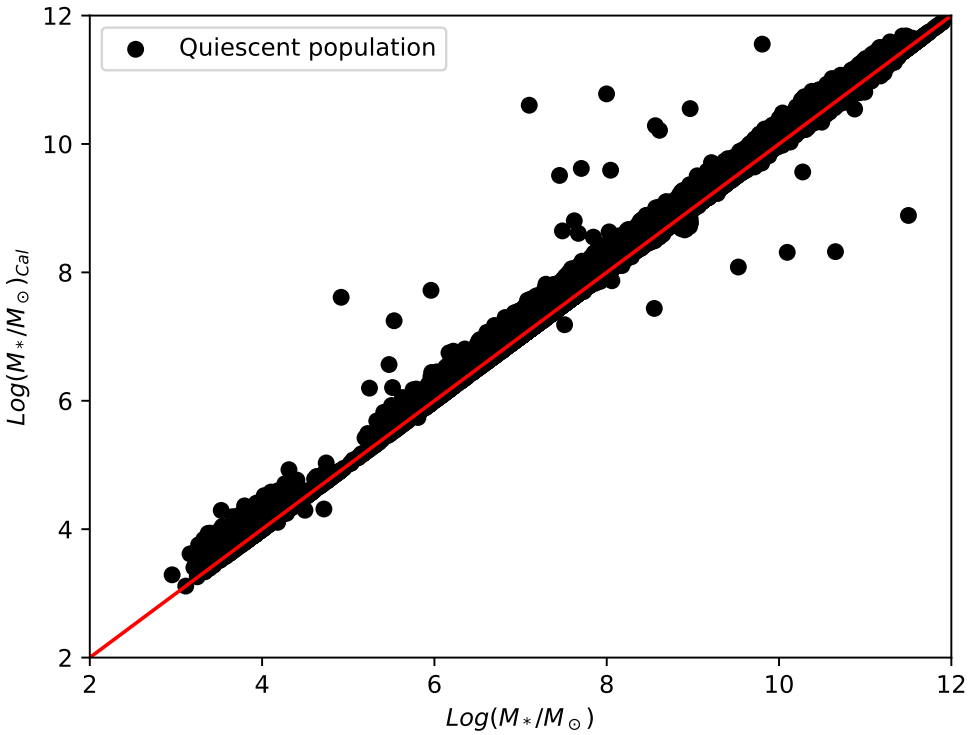

Figure 5.18: Quiescent galaxy calibrated stellar masses using the prescription described in the main text as a function of the masses inferred not using the prescription. Red line shows the bisector of the diagram.

5.5 Conclusions

We estimated the GSMF in the redshift range $0.2 < z < 4.0$ in a total area of $1.65 deg^2$. Indeed, we took advantage of the deep multi-wavelength (optical to *MIR*) photometry of the Frontier Fields Parallels ($H \sim 29$) and of the five CANDELS fields ($H \sim 27$). Moreover, we used the large area ($1.38 deg^2$) of the UltraVista/COSMOS field. This allows us to explore the GSMF in an unprecedented mass range, from very low masses ($\sim 10^7 - 10^8 M_\odot$, dwarf galaxy stellar mass limit) to the very high-mass end ($\sim 10^{12} M_\odot$) also at $z \sim 4$.

We infer the stellar masses of the galaxies in our sample from *zphot* SED fitting code using the BC03 SPSMs, the Chabrier IMF and a "delayed" SFH. We adopted the "delayed" SFH with $\tau = 0.1 - 2.0$. Then, for each field, we estimated in seven different redshift bins in $0.2 < z < 4.0$, the GSMF through the $1/V_{max}$ method correcting for incompleteness effects. In general, we found a good agreement between the MFs of the ten different fields, with major differences arising

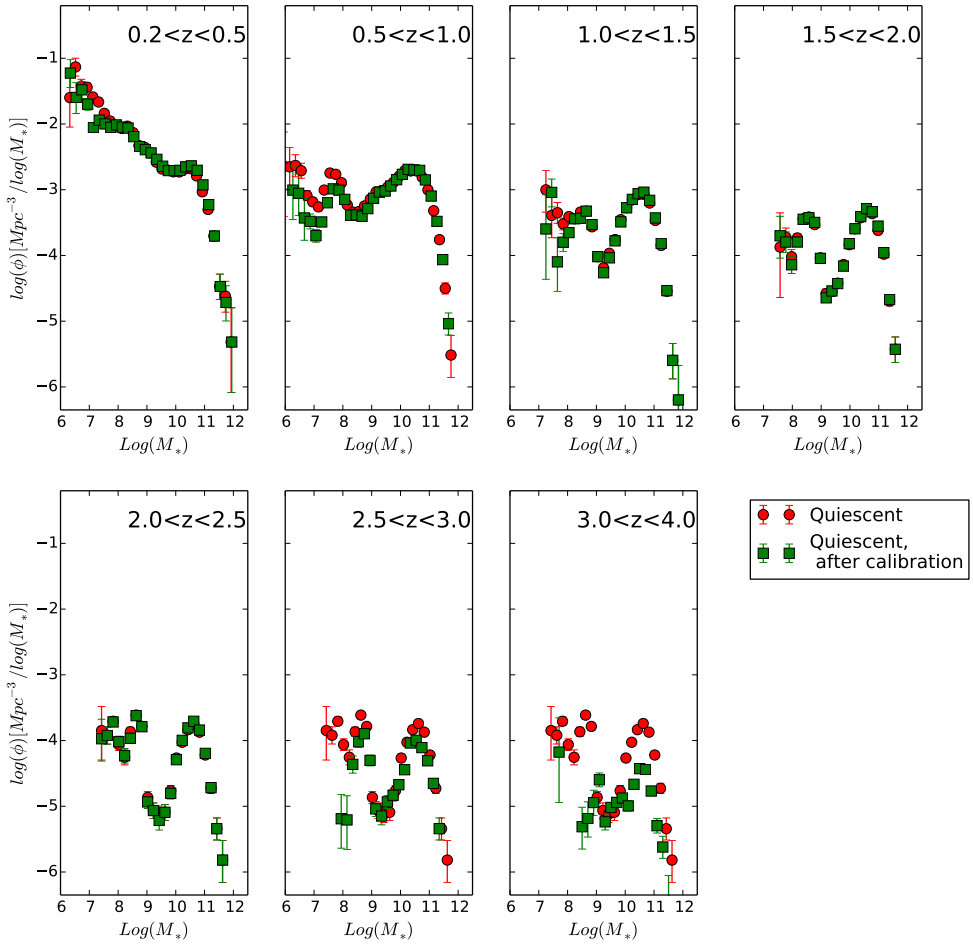

Figure 5.19: Comparison between the total GSMF quiescent (red dots) population investigated in the previous section and the one obtained after the application of the correction prescription for young ages (green squares).

just at $z < 0.5$ probably because of the worse statistics of the FF parallels and the effect of the cosmic variance. Then, we calculated the total GSMF obtained considering the ten fields as a whole, and compared them to several MF available in the literature. We found an overall agreement, but, as expected thanks to the FF deep NIR photometry, we reach masses lower of a factor of 1.5-2.0 dex than the ones observed in previous works, while in the high mass end we obtain consistent results with the most recent GSMF from UltraVista collaboration, meaning that

we can reach very high masses ($\sim 10^{12} M_{\odot}$) thanks to the huge area covered by the UltraVista/COSMOS field.

Moreover, we fit the total GSMF with a single and a double Schechter functions. We found a progressive steepening of the faintest region of the GSMF, while the "knee" of the Schechter function shows a slight decrease with redshift, suggesting that, probably, the exponential decay observed in the GSMF shape does not depend on redshift. On the contrary, the overall normalization parameter of the Schechter function decreases as redshift increases. Additionally, as already found in previous studies, we confirm that at $z < 2.5$ the GSMF seems to be better constrained by a double Schechter function, while at higher redshift both single and double functions well fit the observed GSMF.

Finally, we decided to investigate the GSMF of star-forming and quiescent populations. Firstly, we selected and separated the two populations according to their position in the rest-frame UVJ diagram. Then, we estimated the $1/V_{max}$ GSMF for both galaxy populations. We found that, in general, the GSMF of the star-forming population has a similar shape of the one observed for the total GSMF and it can be fit through a single Schechter function. The low-mass end of the star-forming GSMF is in general steep all the redshift bins and we do not observe a strong evolution of the highest mass galaxies. On the contrary, we found an upturn in the quiescent GSMF for $M < 10^{9} M_{\odot}$, better constrained by a double Schechter function. In the $10^{9} M_{\odot} < M < 10^{10.5} M_{\odot}$ range the quiescent GSMF is quite flat and the high-mass end does not show a strong evolution.

As expected, thanks to our deep photometry, we are now able to observe a bi-modality in the quiescent GSMF for which we had barely an hint from previous works. Moreover, it can be connected to the bi-modality observed also in the Local Universe GSMF and it is consistent with a combination of two different (mass and environment) quenching mechanisms.

Finally, we investigated the effects of our calibration on the GGC sample of the BC03 models on the GSMF of the galaxy quiescent populations, which, as the GGCs, contain old stellar populations. Therefore, we expect that their age could be affected by the same problem we found for GGCs in Chapter 4, especially at lower redshifts. At this purpose, we re-calibrated our SED fitting procedure on quiescent populations employing a new prescription able to eliminate too young, non-physical ages inferred for quiescent galaxies. In this way, we obtain new stellar masses and we re-estimated the GSMF. From the comparison with the previous non-calibrated GSMF, we found a mild difference for the low-mass end ($M < 10^{8} M_{\odot}$) at low redshift ($z < 1.5$).

Chapter 6

Conclusions

We took advantage of homogeneous *UBVRI* ground-based photometry and *V* (*F*606*W*), *I* (*F*814*W*) ACS/*HST* data (Sarajedini et al., 2007; Dotter et al., 2011) of a sample of 64 GGCs to introduce a new HB morphology index, τ_{HB}, to investigate the HB morphology variation over the entire metallicity range of GGCs. We note that when available we preferred the space-based observations *V* and *I*-bands within the ACS FoV ($\sim 4'$), while we used the ground-based data for the outer regions of the globulars in our sample. τ_{HB} is defined as the ratio between the areas below cumulative number distribution in apparent magnitude ($A_{CND}(I)$) and in colour ($A_{CND}(V–I)$) of the entire box containing the HB. We compared our new photometric index to other indices available in the literature, namely *HBR′*, the HB ratio defined by Lee (1989); Lee et al. (1994), and L1, L2 indices introduced by Milone et al. (2014). We found that τ_{HB} offers several advantages: it is characterized by a wider dynamical range, which is a factor of seven if compared to *HBR′* and a factor of twenty if compared to L1 and L2 indices. Moreover, τ_{HB} shows a linear trend over the entire GGC metallicity range (-2.3≤[Fe/H]≤-0.1), meaning that, in contrast to the well-known degeneracy of *HBR′*, our index traces the HB morphology variation from the most metal-poor to the most- metal-rich regimes. Furthermore, we investigated the possible sensitivity of *HBR′* and τ_{HB} to the different contribution to the HB morphology variation by inner and outer populations in GGCs. Indeed, we compared the estimates of the HB morphology indices to the ones obtained using just space-based (inner GGC regions) and just ground-based (outer GGC regions) data. We found a remarkable agreement between the two different catalogues. The difference is slightly larger in *HBR′* for those clusters dominated by red HB morphologies and in τ_{HB} for those clusters with a significant fraction of their light falling inside the ACS FoV (they are either small and concentrated or large but observed at higher distances). The difference in τ_{HB} is of the order of $\sim 3\%$.

We investigated the sensitivity of the τ_{HB} index on those physical parameters, considered as the main contributors to the observed variation of HB morphology,

namely metallicity, age and spread in He content. We found a quadratic anti-correlation with cluster metallicity, i.e., in general, τ_{HB} quadratically decreases moving from metal-poor ([Fe/H]≤-1.5) to metal-rich ([Fe/H] ≥-1.0) regime. In the metal-intermediate regime (-1.5≤ [Fe/H] ≤-1.0), we were able to identify a sub-sample of eight clusters appearing peculiar according to their τ_{HB} values. They attain τ_{HB} values greater of a factor $\sim$ 2 than the ones found for the clusters. Interestingly, these clusters do not have a peculiar HBR' value. Comparing their $I, V–I$ CMDs with the ones of the "standard" (i.e., located near the best-fit relation) clusters of similar metallicity (and age), we found that they are characterized by a bluer HB morphology. This means that we can define them as the 2ndP clusters in our sample. Moreover, we found a linear correlation with absolute cluster age: τ_{HB} increases as age increases. Therefore, when moving from red to blue HB morphology, the GGCs become older. The previously identified 2ndP clusters remain peculiar also in this diagram and have an age ranging from $\sim$ 11.5 to $\sim$ 13 Gyr. Moreover, we decided to limit the impact of the age estimate by reducing τ_{HB} values to the ones they would attain if the had an age of 12 Gyr, the mean age of the total sample. After the reduction, we found a linear correlation with cluster metallicity. However, the 2ndP clusters are located in a well-separated region far from the region of the diagram covered by the other clusters. On the contrary, we did not find a solid correlation between the residuals of the corrected $\tau_{HB,12Gyr}$ as a function of cluster metallicity and the internal spread in helium content estimated by Milone et al. (2018). Finally, we calculated new synthetic HB models and compared them to the observed $\tau_{HB,12Gyr}$ as a function of [Fe/H]. We found that the theoretical models are able to fit the 2ndP clusters only if: we fix the spread in He content to the one estimated by Milone et al. (2018) and we increase the mass loss value from $\Delta M = 0.21$ (i.e., the value we need to fit the bulk of the clusters) to $\Delta M = 0.29$; we fix the mass loss to $\Delta M = 0.21$ and we increase the spread in He content from mean value estimated by Milone et al. (2018), $\partial Y = 0.03$, to, at least, $\partial Y = 0.05$; we consider both a higher mass loss and an higher spread in He content.

Then, we decided to explore the HB morphology variation in composite stellar populations in nearby dSph galaxies. Indeed, we used homogeneous $UBVRI$ ground-based photometry for nine MW satellite galaxies, while for seven Andromeda satellites we have space-based data from ACS/HST in $F475W(\sim B)/F606W$ ($\sim V$) and $F814W$ ($\sim I$) bands. Moreover, we have data in $F475W$ and $F814W$ also for two isolated dSphs. Firstly, we analysed the HB morphologies of dSph galaxies estimating the classical HBR' index. It ranges from $HBR' \sim 1$ (Andromeda III) to $HBR' \sim 2.5$ (Ursa Minor). This means that the HB morphology is systematically redder than the one characterizing the GGCs.

Since for most of the galaxies, we had data in B and I-bands, we verified the validity of our τ_{HB} index also in the $I, B-I$ diagram. Using the ground-based photometry, we compared $\tau_{HB}(IVI)$ with $\tau_{HB}(IBI)$, estimated for the sample of

GGCs. As expected, thanks to the higher sensitivity to the effective temperature of B–I colour, we found that $\tau_{HB}(IBI)$ is characterized by even a larger dynamical range (of a factor of ~ 2) compared to the one found for $\tau_{HB}(IVI)$. Furthermore, we still found a quadratic anti-correlation with cluster metallicity and a linear correlation with cluster age. Moreover, the 2ndP clusters are peculiar also for their $\tau_{HB}(IBI)$ values. We also found other three globular clusters, characterized by blue HB morphologies, located slightly above the 1σ level in the $\tau_{HB}(IBI)$-[Fe/H]. Therefore, according to the photometric availability, we estimated $\tau_{HB}(IVI)$ and/or $\tau_{HB}(IBI)$ for our sample of 19 dSphs. We found that nearby dSphs are located in a limited ($\tau_{HB} \sim 1-5$) region below the mean value observed for the GGCs. These findings suggest that HB morphologies in dSph galaxies are redder than in GGCs. However, since they show a modest variation both in metallicity and age, this means that we are facing to a relevant environmental effect when moving from GGCs ($M = 10^4 - 10^6 M_\odot$) to dSphs ($M = 10^7 - 10^9 M_\odot$).

We performed an empirical calibration of BC03 SPSMs (Bruzual & Charlot, 2003) on the observed GGC SEDs in an unprecedented wide coverage in wavelength (from FUV to MIR). In particular, we took advantage of GALEX/FUV-NUV (Dalessandro et al., 2012) and ACS/$F275W$ (Piotto et al., 2015b; Nardiello et al., 2018) integrated magnitudes for UV wavelengths. For those clusters for which we did not have data from the literature in FUV and/or NUV, we synthetically estimated the integrated magnitudes in these filters, performing a detailed and complete synthetic CMD using the code described in Salaris et al. (2013) and the bolometric corrections from PARSEC database. In the optical range we took advantage of the $UBVRI$ ground-based data and $F606W$ ($\sim V$), $F814W$ ($\sim I$) space-based photometry together with $grizy$ data from the first data release of Pan-STARRS. In the IR wavelengths, we employed the JHK_s photometry from 2MASS, while we calculated the integrated magnitudes in Spitzer/MIR bands using the same synthetic CMDs estimated for the UV integrated magnitudes. We performed the empirical calibration of BC03 models with Padova 1994 isochrones. Firstly, we fixed the metallicity of the models to the values $Z/Z_\odot$= 0.005, 0.02, 0.2, 0.4, available in BC03. We used the Salpeter IMF and a τ-model SFH with $\tau = 0.01$ to simulate a simple stellar population and we left the age as a free parameter. Using *zphot* code, for each cluster we performed the SED fitting fixing the metallicity to the values estimated by Carretta et al. (2009) to eliminate the age-metallicity degeneracy. We decided to investigate the accuracy of the inferred parameters comparing the age extracted from the SED fitting procedure and the independent measures published by VandenBerg et al. (2013); Leaman et al. (2013). Considering the uncertainties both from SED fitting due to both the χ^2 technique and the photometric errors) and from the observed values by VandenBerg et al. (2013); Leaman et al. (2013), we expected a difference of at most $\sim \pm 2Gyr$. However, we found a difference ΔAge spanning from -2.5 to 11 Gyr. A group of clusters are characterized by $\Delta Age < 3Gyr$, a second sample by $3Gyr < \Delta Age < 7Gyr$ and a

third one characterized by $\Delta Age > 7 Gyr$. Moreover, they seem to have a mild correlation with cluster metallicities. Despite our efforts, so far we did not find any correlation between the clusters in the different groups. Moreover, to verify the validity of our models, we compared them to the models introduced by Conroy & Gunn (2010b). We found that, in the optical-*NIR* wavelength range, they are in quite good agreement with observations (with differences of the order of at most 0.3 mag). On the contrary, in the *FUV* band, they systematically under-estimate colours in the metal-rich regime ([Fe/H]>-1), while they over-estimate *NIR* colours in the metal-poor regime ([Fe/H]<-1). Finally, to find an explanation to the high difference in age we compared inferred and empirical values, through rest-frame colours. We obtained that the observed colours of our GGCs are more compatible to the younger ages predicted by BC03 models.

After the investigation concerning the resolved stellar populations in the nearby Universe, we decide to analyse the unresolved stellar populations in distant galaxies. Indeed, we estimated the GSMF up to $z = 4$ in a total area of $1.65 deg^2$. We combined the deep multi-wavelength (optical to *MIR*) photometry of four Frontier Fields Parallels ($H \sim 29$) and of the five CANDELS fields ($H \sim 27$). together with the large area ($1.38 deg^2$) covered by the UltraVista/COSMOS survey. In this way, we can estimate the GSMF in an unprecedented mass range, from very low masses ($\sim 10^7 - 10^8 M_\odot$, dwarf galaxy stellar mass limit) to the very high-mass end ($\sim 10^{12} M_\odot$) also at high redshift. We infer the stellar masses of the galaxies in our sample from *zphot* SED fitting code using the BC03 SPSMs, the Chabrier IMF and a "delayed" SFH with $\tau = 0.1 - 2.0$. Then, for each field, we estimated in seven different bins in $0.2 < z < 4.0$ redshift range, the GSMF through the $1/V_{max}$ method correcting for incompleteness effects. We calculated the total GSMF obtained considering the ten fields as a whole, and compared them to several MF available in the literature. We found an overall agreement, but, as expected thanks to the FF deep NIR photometry, we reach masses lower of a factor of 1.5-2.0 dex than the ones observed in previous works. Moreover, we fit the total GSMF with a single and a double Schechter functions. We found a progressive steepening of the faintest region of the GSMF, while the "knee" of the Schechter function shows a slight decrease with redshift, suggesting that, probably, the exponential decay observed in the GSMF shape does not depend on redshift. On the contrary, the overall normalization parameter of the Schechter function decreases as redshift increases. Additionally, as already found in previous studies, we confirm that at $z < 2.5$ the GSMF seems to be better constrained by a double Schechter function, while at higher redshift both single and double functions well fit the observed GSMF. Finally, we decided to investigate the GSMF of star-forming and quiescent populations. Firstly, we selected and separated the two populations according to their position in the rest-frame *UVJ* diagram. Then, we estimated the $1/V_{max}$ GSMF for both galaxy populations. We found that, in general, the GSMF of the star-forming population has a similar shape of the one observed for the total

GSMF and it can be fit through a single Schechter function. The low-mass end of the star-forming GSMF is in general steep all the redshift bins and we do not observe a strong evolution of the highest mass galaxies. On the contrary, we found an upturn in the quiescent GSMF for $M < 10^9 M_\odot$, better constrained by a double Schechter function. In the $10^9 M_\odot < M < 10^{10.5} M_\odot$ range the quiescent GSMF is quite flat and the high-mass end does not show a strong evolution. Thanks to our deep photometry, we are now able to observe a bi-modality in the quiescent GSMF for which we had barely an hint from previous works. Moreover, it can be connected to the bi-modality observed also in the Local Universe GSMF and it is consistent with a combination of two different (mass and environment) quenching mechanisms. Finally, since we found that for GGCs we have a significant difference between the values of observed and inferred ages, we expect the same problem in the inferred ages of quiescent galaxies, which, similarly to GGCs, contain old stellar populations. Therefore, we employed a new SED fitting prescription able to eliminate too young, non-physical ages inferred for quiescent galaxies. Hence, we re-calibrated the inferred stellar masses, and so, the quiescent GSMF. As expected, the age estimate mildly (< 0.1 dex) affects the GSMF lowest mass end ($M < 10^8 M_\odot$) at $z < 1.5$.

Future developments

The results presented in this thesis are preliminary results of a larger project concerning the empirical calibration of a number of SPSMs on local objects. Indeed, we plan to extend this analysis on nearby dwarf galaxies and open clusters, which are recognized to be very different in stellar population and dynamics when compared to the much simpler GGCs investigated here. Moreover, we plan to extend the calibration also to other widely used SPSMs, in addition to the Bruzual & Charlot (2003), employing also other more updated SED fitting codes. This remarkable empirical calibration together with the future large photometric and spectroscopic surveys, like EUCLID, James Webb Space Telescope (JWST) and Extremely Large Telescope (ELT) facilities, will allow us to identify the sources of the already observed discrepancies between theory and observations, and thus, to improve our knowledge concerning galaxy formation and evolution.

Appendices

Appendix A

Notation for chemical composition

In astronomy we denote the Hydrogen (H) and Helium (He) abundances by mass as "X" and "Y", respectively, while we call all the elements more massive than He as "metals" ("Z").

The solar total abundance of metals by mass is $Z_\odot = 0.02$.

In general, we usually use the iron as the metal abundance indicator thanks to the fact that it is easy to estimate from stellar spectra. Moreover, we usually specify the star metallicity in units of the solar value through the logarithmic quantity:

$$[Fe/H] = Log\left(\frac{Z}{X_*}\right) - Log\left(\frac{Z}{X_\odot}\right) \tag{A.1}$$

so that for the Sun $[Fe/H]_\odot = 0$.

In general, He and heavier element abundance variations are negligible if compared to the H abundance, so we can consider X as constant, and we can write the metal abundance simply as:

$$[Fe/H] \sim Log\left(\frac{Z_*}{Z_\odot}\right) \tag{A.2}$$

If we assume a universal scaled solar heavy element distribution, we can define the total amount of metals of an object as:

$$[M/H] = Log\left(\frac{Z}{X_*}\right) - Log\left(\frac{Z}{X_\odot}\right) \tag{A.3}$$

We denote the O, Ne, Mg, Si, S, Ca and Ti elements, produced mainly by Type II supernovae, as α elements. Their abundance relative to iron is usually defined as $[\alpha/Fe]$.

Their distribution in the Milky Way halo is $[\alpha/Fe] \sim 0.3 - 0.4$ while in the Magellanic Clouds ($[Fe/H] < -1.0$) it is $[\alpha/Fe] \sim 0.2$. Indeed, in general we find that in external galaxies, for example in massive early-type ones, they are

more abundant than in our Galaxy (Worthey et al., 1992), and we define them as "α-enhanced" populations.

On the contrary, if the distribution of the heavy elements in the stellar population chemical composition is similar to the solar one, we define it as "scaled solar".

Appendix B

Stellar evolution

Stellar evolutionary theory provides synthetic luminosity and effective temperature of the stars allowing to reproduce the Hertzsprung–Russell diagram (HRD), a fundamental plot showing the star bolometric luminosity versus its effective temperature. The evolution of a stellar model in the HRD is denoted as "stellar track" (see Figure B.1). We can interpret and predict the star formation and chemical evolution histories of a stellar population combining stellar tracks of different masses.

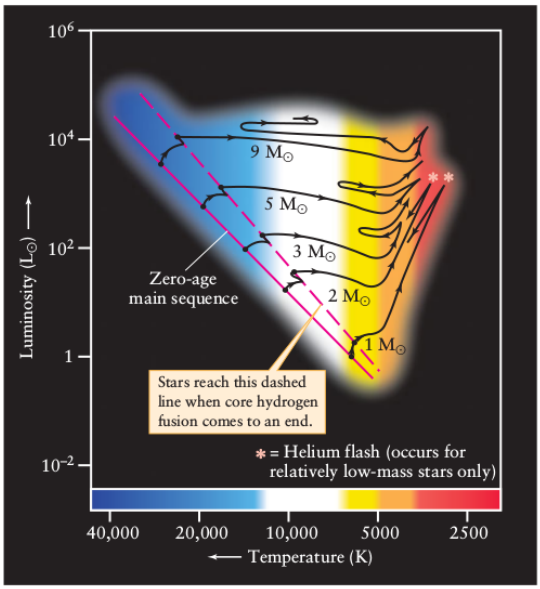

Figure B.1: Evolutionary tracks of five stars with different mass on the HRD (Freedman & Kaufmann, 2007).

Indeed, independently from their chemical composition, stars can be classified in three different groups according to their initial mass: low mass ($0.8M_\odot < M <$

$2.3M_\odot$), intermediate ($2.3M_\odot < M < 10M_\odot$) and massive ($10M_\odot < M < 25M_\odot$) stars. Mass limits depend on the particular physical processes which take place inside the object, like the sequence of nuclear burnings from Hydrogen to heavier elements, the existence of electron degenerate gas inside the nucleus, the values reached by central temperatures and densities, etc.

The first step in stellar evolution is the pre-main sequence (PMS) phase: the star is convective and it contracts at $T_{eff} \sim const$ while its radius and luminosity decrease ($L = 4\pi\sigma T_{eff}^4 R^2$). Therefore, during this phase, the star evolves vertically in the HRD along the "Hayashi track", until a radiative core forms and eventually H-burning ignites in the central regions. At this point, the star evolves along the main sequence (MS) phase when the H is converted into He in the core. The H-burning core gradually develops an He core while the stellar luminosity increases. Low mass stars burn H through the so-called "pp-chain" ($T_c \sim 10^6 K$), which transforms H (protons, p) in He nuclei, while intermediate and high-mass stars are sustained by the C-N-O cycle ($T_c \sim 10 - 20 \cdot 10^6 K$), which transforms Carbon (C), Nitrogen (N) and Oxygen (O) nuclei in He nuclei.

The H-burning time scales depend on the initial mass of the star and they are in general shorter as the star initial mass increases (e.g., for $M = 0.8M_\odot$ $t_{MS} \sim 12 \cdot 10^9 yrs$, for $M = 5M_\odot$ $t_{MS} \sim 100 \cdot 10^6 yrs$, for $M = 15M_\odot$ $t_{MS} \sim 13 \cdot 10^6 yrs$). The time spent along the MS represents the 90% of the entire life of the star.

When the Hydrogen is exhausted the star reaches the highest T_{eff} value at the turn-off (TO) point in the HRD: the star has an He-core surrounded by a H-shell and it is at the base of the red giant branch (RGB). In low-mass stars, the central temperature T_C is too low to ignite the He-burning in the core, which grows thanks to the shell, which is experiencing the H-burning and producing a convective H-envelope. The core contracts and both central and shell temperatures increase. Furthermore, the star climbs the RGB while the convective envelope formed at the RGB base penetrates into layers processed during the previous stages causing a discontinuity in the chemical profile of the star (first dredge-up). In the meanwhile, the He-core grows until $M_C \sim 0.5M_\odot$ and the central density ρ_C is higher than T_C: the gas degenerates and produces neutrinos. When $T_C \sim 10^8 K$, the star ignites He-burning outside the centre in a convective region: the star experiences the so-called He-flash which allows T_C to increase at constant ρ_C, removing the degeneracy. The star reaches the maximum luminosity on the RGB (RGB-tip). At this point, the He-burning begins quiescently in the core and the RGB phase is terminated.

Low-mass stars burns He in their core and H in a shell during the horizontal branch (HB) phase. Their position on the branch depends on their metal content and on the mass lost along the RGB. Metal-rich stars cover a red region on the HRD ~ 3 magnitude below the RGB-tip, while metal-poor stars are characterized by a broad range in T_{eff} to the blue of the RGB.

Intermediate and high-mass stars ignite H-burning in a convective core. When the central hydrogen terminates, they experience a rapid evolution to the RGB

phase burning the hydrogen in a thin shell, surrounding the He-core. Also in this case, a convective envelope develops and penetrates into layers processed through CNO cycles (first dredge-up), causing a chemical variation of the surface elements.

Intermediate and high-mass stars ignites the He-burning in a non-degenerate core when $T_C \sim 10^8 K$, requiring a minimum core-mass of $0.33 M_\odot$, while the H-burning continues in a shell. The early stages of He-burning occur near the Hayashi line, while when the energy released by the He-burning core is equal to the energy released by the H-burning shell, the star experiences a rapid contraction of the envelope and the convective outer layers become radiative. In this phase, the star moves to a bluer region on the HRD (blue loop). In general, as the mass of the star decreases, the blue loop location moves toward the Hayashi line.

He-burning turns Helium into Carbon, Oxygen and traces of heavier elements. When it ends, the star is characterized by a C-O core, which is of equal mass for the low-mass stars, while its mass increases with the stellar mass for more massive ones.

At the end of the He-burning, the star is formed by a C-O core, a He-burning shell, and a H-envelope with a H-burning shell at its base, which, for very massive stars, can be lost because of strong stellar wind mass loss.

After the He-burning phase, low and intermediate-mass stars evolve to the asymptotic giant branch (AGB) phase, which is composed of two stages: early AGB (E-AGB) and thermally pulsing AGB (TP-AGB). During the first stage, while the He content in the core decreases, the star expands and cools, evolving almost parallel to the RGB and experiencing the second dredge-up, bringing fresh Helium and Nitrogen to the surface. The E-AGB lasts until the H-burning shell is re-ignited by the envelope re-contractions. In the second stage, the C-O gas in the core reaches so high temperature and density that the electrons become degenerate. After the re-ignition of the H-shell, the burning in the He-shell becomes thermally unstable and produces a convective region, that gradually re-absorbs. The H-shell and the He-shell alternate as major source of energy for the star, which experiences a series of thermal pulses and a third dredge-up. The TP-AGB stage lasts until the H-envelope is lost due to stellar wind.

Low-mass and intermediate-mass stars end their life as planetary nebulae and white dwarfs since their central temperature is not high enough to burn other elements. On the contrary, after the He-burning phase, massive stars ignite all the burnings until the iron one: the star has now an iron core of $\sim 1.4 M_\odot$. Since the iron burning does not release energy, the core cools down and the fusion suddenly stops. At this point, the star implodes and the external layers rebound on the iron core, producing the explosion known as supernova. The supernova remnant can be a white dwarf, a neutron star, or a black hole, depending on the initial mass of the star.

B.1 From theory to observations

The observational counterpart of the HRD is the colour-magnitude diagram (CMD), displaying the star magnitude in a specific photometric band as a function of the so-called colour index, the difference between two magnitudes of two different photometric bands. In the following, we describe how to transform luminosity and temperature values predicted by theoretical models, to the observed magnitude and colours we need to build the CMD.

If f_λ is the monochromatic flux (energy per unit of area, time and wavelength) received at the top of our atmosphere, we can define the apparent magnitude as the flux collected by a telescope in a generic photometric band A covering the wavelength range between λ_1 and λ_2 as (Salaris & Cassisi, 2005):

$$m_A = -2.5Log\left(\frac{\int_{\lambda_1}^{\lambda_2} f_\lambda S_\lambda d\lambda}{\int_{\lambda_1}^{\lambda_2} f_\lambda^0 S_\lambda d\lambda}\right) + m_A^0 \tag{B.1}$$

where f_λ^0 and m_A^0 are the flux and the magnitude in the photometric band A produced by a reference star, and S_λ is the response function of the filter A.

Therefore, the apparent magnitude is defined on the basis of the choice of a reference star. We define the colour index as the difference of two apparent magnitudes estimated in two different photometric bands: $(m_A - m_B) = A - B$.

Moreover, the apparent magnitude is not directly linked to the intrinsic properties of a star, since it depends on the distance. Therefore, we need to define the absolute magnitude in the given band A, as the magnitude that a source would have if it would be located at a distance of $10pc$:

$$M_A = m_A - 5Log(d) + 5 \tag{B.2}$$

where d is the distance in parsec. We also define the distance modulus as

$$\mu = (m_A - M_A) \equiv (m - M)_A \tag{B.3}$$

Finally, we can relate the flux observed on top of the Earth atmosphere (f_λ) to the one at the stellar surface (F_λ) as:

$$f_\lambda = F_\lambda\left(\frac{R}{d}\right)^2 \tag{B.4}$$

Therefore, we need of F_λ to estimate the magnitude of a stellar source. We can calculate F_λ using the results of models of stellar atmospheres, determined by chemical composition, gravity (g) and effective temperature.

Consequently, we can determine F_λ, and hence the magnitude, from L, T_{eff} and g as estimated by the appropriate atmospheric model.

If we write the absolute magnitude as:

$$M_A = -2.5Log\left[\left(\frac{R}{10pc}\right)^2 \frac{\int_{\lambda_1}^{\lambda_2} F_\lambda S_\lambda d\lambda}{\int_{\lambda_1}^{\lambda_2} F_\lambda^0 S_\lambda d\lambda}\right] + m_A^0 \tag{B.5}$$

and if we assume $S_\lambda = 1$ at all wavelengths, $\lambda_1 = 0$, $\lambda_2 = \mathrm{inf}$ and considering the Sun as the reference star, we can introduce the absolute bolometric magnitude as:

$$M_{bol} = M_{bol,\odot} - 2.5Log(L/L_\odot) = M_{bol,\odot} - 2.5Log(4\pi R^2 F_{bol}/L_\odot) \tag{B.6}$$

where $M_{bol,\odot} = 4.74$.

Finally, we define the bolometric correction in the photometric band A as:

$$BC_A \equiv M_{bol} - M_A = M_{bol,\odot} - 2.5Log(4\pi R^2 F_{bol}/L_\odot) \tag{B.7}$$

The bolometric correction allows to transform the theoretical models into observational quantities. In this way, the stellar track on a HRD can be transformed in various CMDs obtained combining different photometric filters.

Appendix C

Peculiar globular clusters

The classical HB morphology index (*HBR'*) estimations for NGC 6304, NGC 6426, NGC 6624, Lynga 7, and Palomar 2 and the τ_{HB} indices for NGC 6426, NGC 6624, and NGC 6652 were derived using *I*, *V*-bands from ACS-*HST* because we lack ground-based catalogues. For these globulars we considered all the stars in the *HST* field and within the tidal radius in ground-based telescope fields.

Due to the high field contamination in ground observations, for the clusters NGC 6388 and NGC 6441, we used only ACS data. Despite this, the sample is statistically good enough to analyse their HB morphology, even if the ACS FoV does not cover the entire extent of these two clusters.

Owing to the low number of HB stars in Lynga 7 and NGC 6304, we obtain τ_{HB}=0 and so, these clusters have not been included in the analysis of our new index. Finally, we note that ground-based data for NGC 104, NGC 5272, NGC 5466, NGC 5927, NGC 6362, NGC 6397, and NGC 6752 do not reach the tidal radius.

Appendix D

Notes on individual outliers

In the following we give notes about the clusters we can define as outliers either in the τ_{HB}-[Fe/H] plane or in the τ_{HB}-age plane or both.

NGC 6218: outlier of τ_{HB}-[Fe/H], while we cannot consider it an outlier in τ_{HB}-age planes (it is located under the 2.0σ levels). Both ground-based and space data are of good quality. It has been identified as a second parameter cluster.

NGC 288: outlier of τ_{HB}-[Fe/H] and of the τ_{HB}-age planes. Both ground-based and space data are of good quality. It has been identified as a second parameter cluster.

NGC 6205: outlier of τ_{HB}-[Fe/H] and of the τ_{HB}-age planes. Both ground-based and space data are of good quality. It has been identified as a second parameter cluster.

NGC 6254: outlier of τ_{HB}-[Fe/H] and of the τ_{HB}-age planes. Both ground-based and space data are of good quality. It has been identified as a second parameter cluster.

NGC 6426: outlier of τ_{HB}-[Fe/H] and of τ_{HB}-age planes. We have only space photometry. Among the second parameter clusters, it is the one attaining the lowest value in τ_{HB}.

NGC 6752: outlier of τ_{HB}-[Fe/H] and of the τ_{HB}-age planes. Both ground-based and space data are of good quality, but ground data do not reach the globular tidal radius. It has been identified as a second parameter cluster.

NGC 6541: outlier of τ_{HB}-[Fe/H] and of the VandenBerg et al. (2013); Leaman et al. (2013) τ_{HB}-age plane. We have no age estimation from Salaris & Weiss (2002). Both ground-based and space data are of good quality. It has been identified as a second parameter cluster.

NGC 6681: outlier of τ_{HB}-[Fe/H] and of the τ_{HB}-age planes. Both ground-based and space data are of good quality. It has been identified as a second parameter cluster.

NGC 6362: outlier of τ_{HB}-age plane for age estimations from VandenBerg et al. (2013); Leaman et al. (2013). Both ground-based and space data are of good

quality.

NGC 6535: outlier of τ_{HB}-age planes (above 2.5σ limit in the VandenBerg et al. (2013); Leaman et al. (2013) plane and 2.0σ limit in the Salaris & Weiss (2002) one). Both ground-based and space data are of good quality.

NGC 6652: outlier of the Salaris & Weiss (2002) τ_{HB}-age plane. Both ground-based and space data are of good quality.

NGC 7089: outlier of the VandenBerg et al. (2013); Leaman et al. (2013) τ_{HB}-age plane. We have no age estimation from Salaris & Weiss (2002). Both ground-based and space data are of good quality.

NGC 6171: outlier in the τ_{HB}-age planes (above the 2.5σ limit in VandenBerg et al. (2013) and the 2.0σ limit in Salaris & Weiss (2002)). Both ground-based and space data are of good quality.

Appendix E

Additional CMDs of dSph galaxies

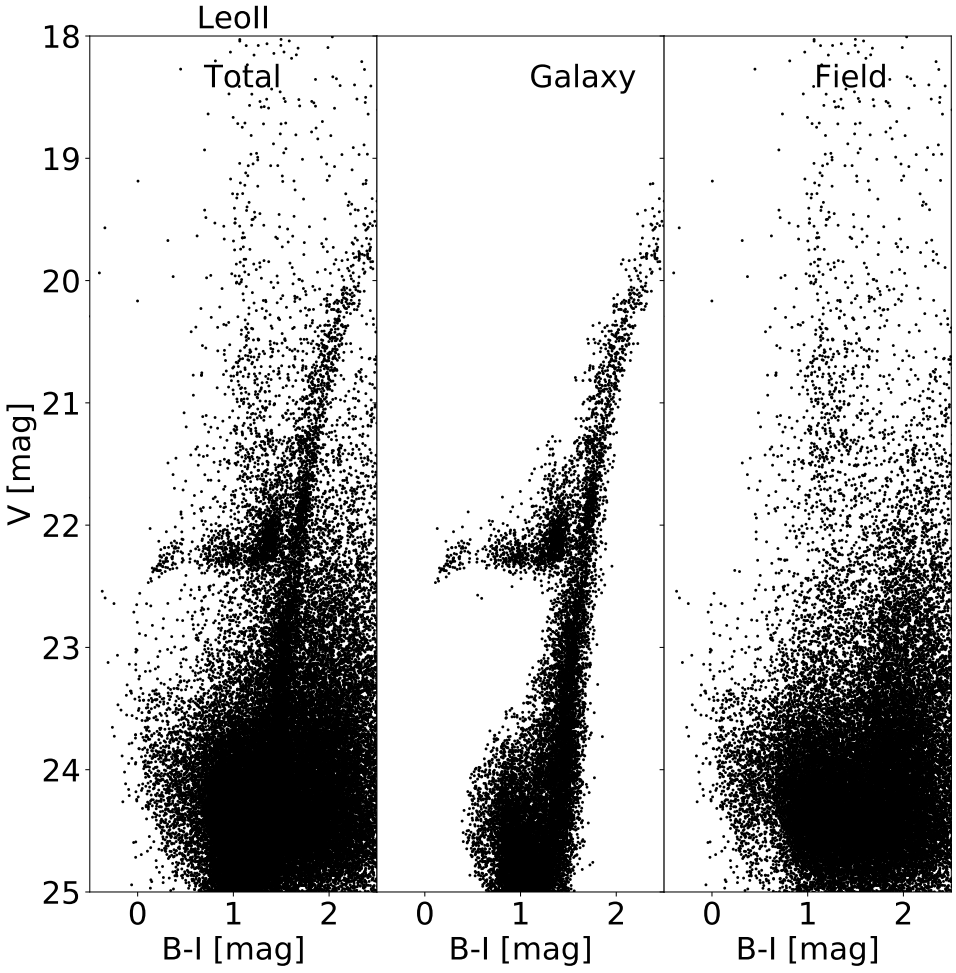

Figure E.1: Leo II V, B–I CMD of the entire catalogue (left panel), candidate galaxy (central panel) and candidate field (right panel) stars.

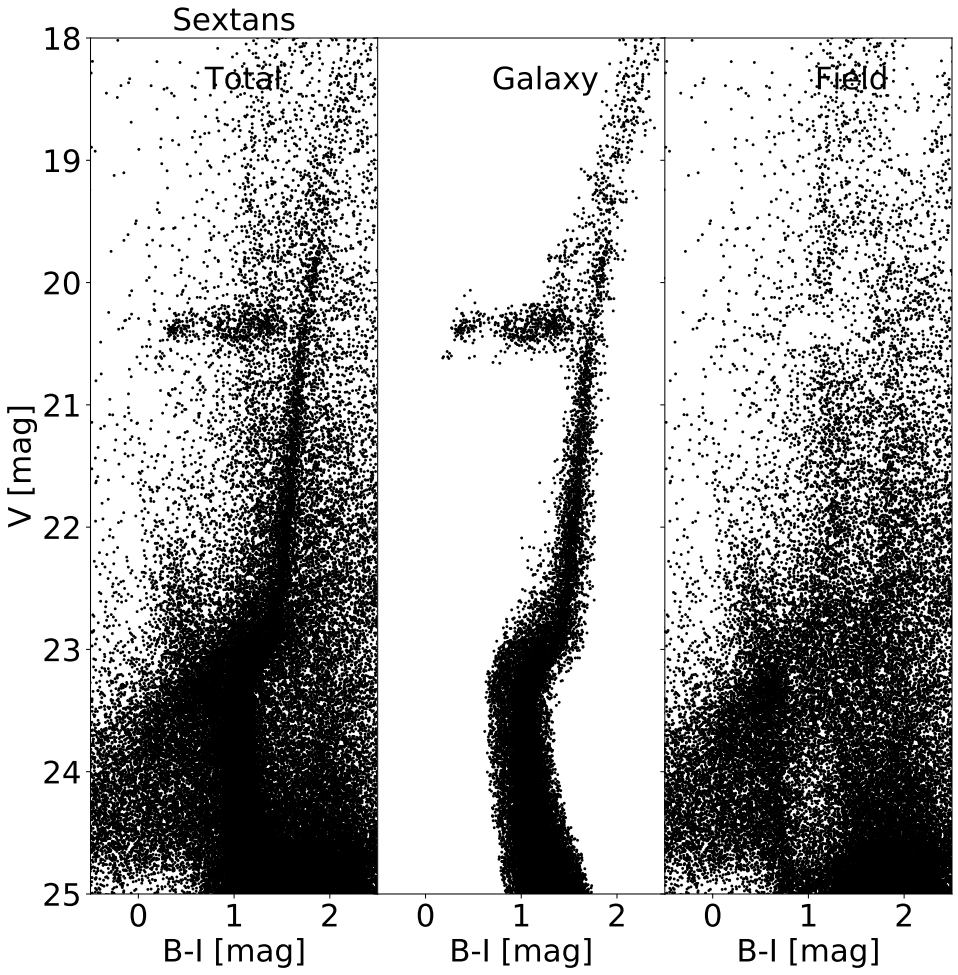

Figure E.2: Sextans V, B–I CMD of the entire catalogue (left panel), candidate galaxy (central panel) and candidate field (right panel) stars.

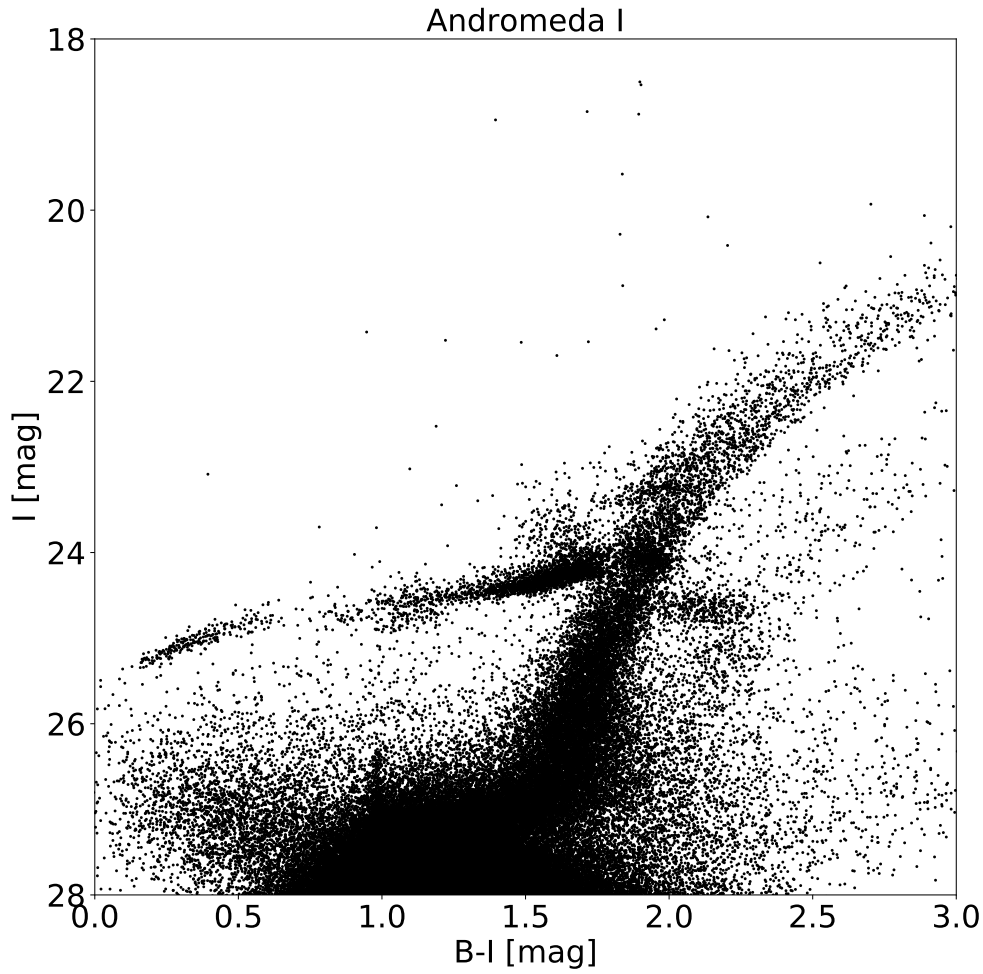

Figure E.3: Andromeda I I, B–I CMD.

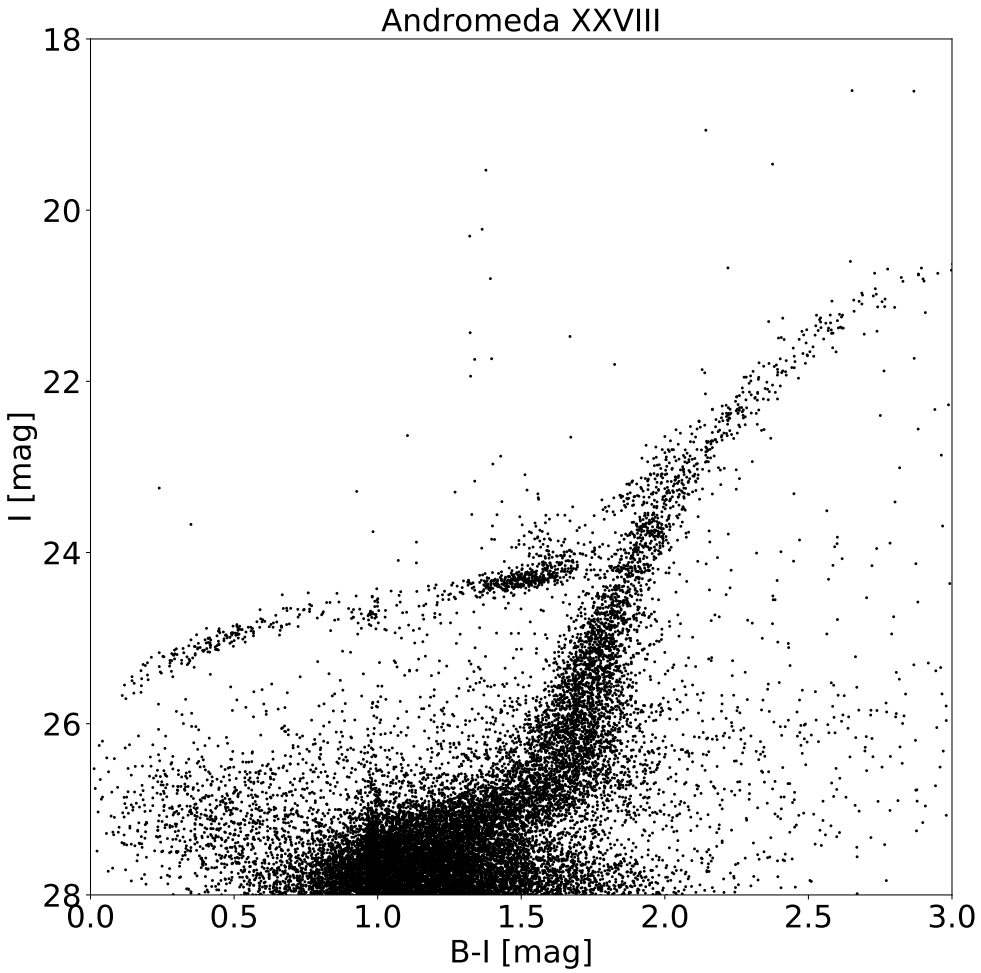

Figure E.4: Andromeda XXVIII *I*, *B–I* CMD.

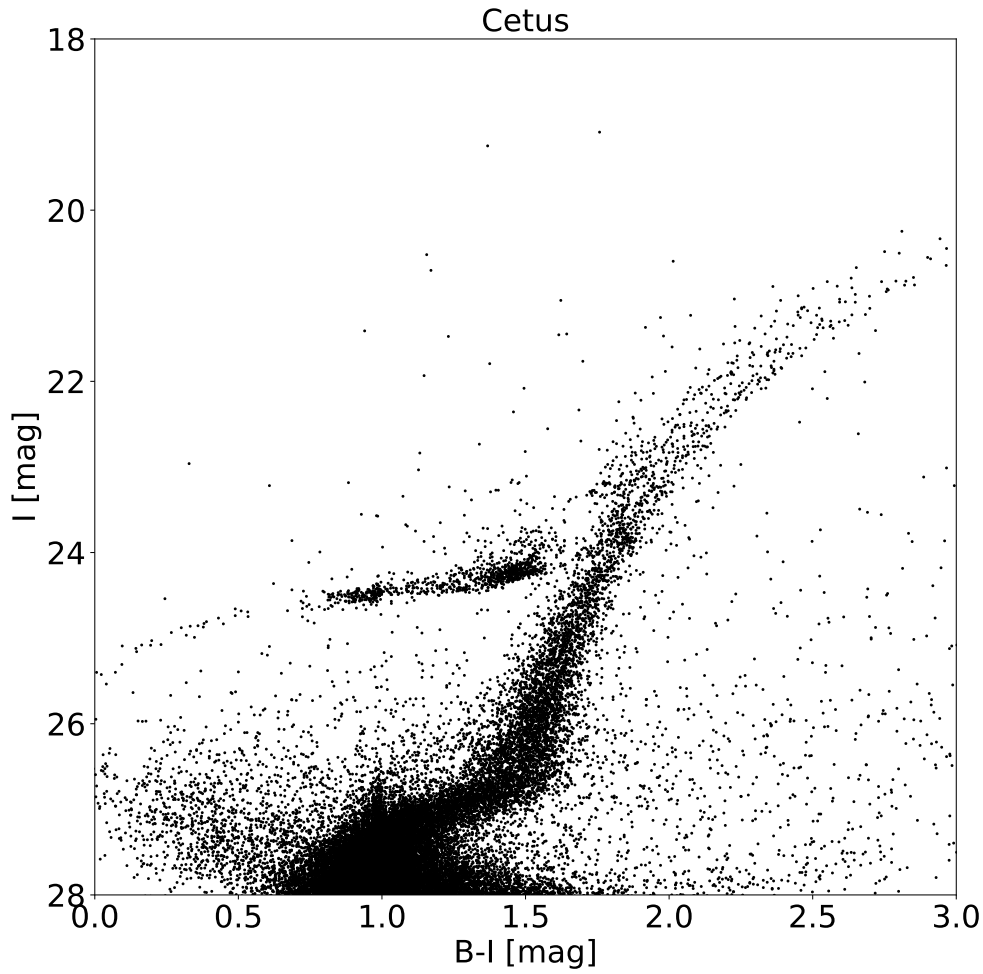

Figure E.5: Cetus *I*, *B–I* CMD.

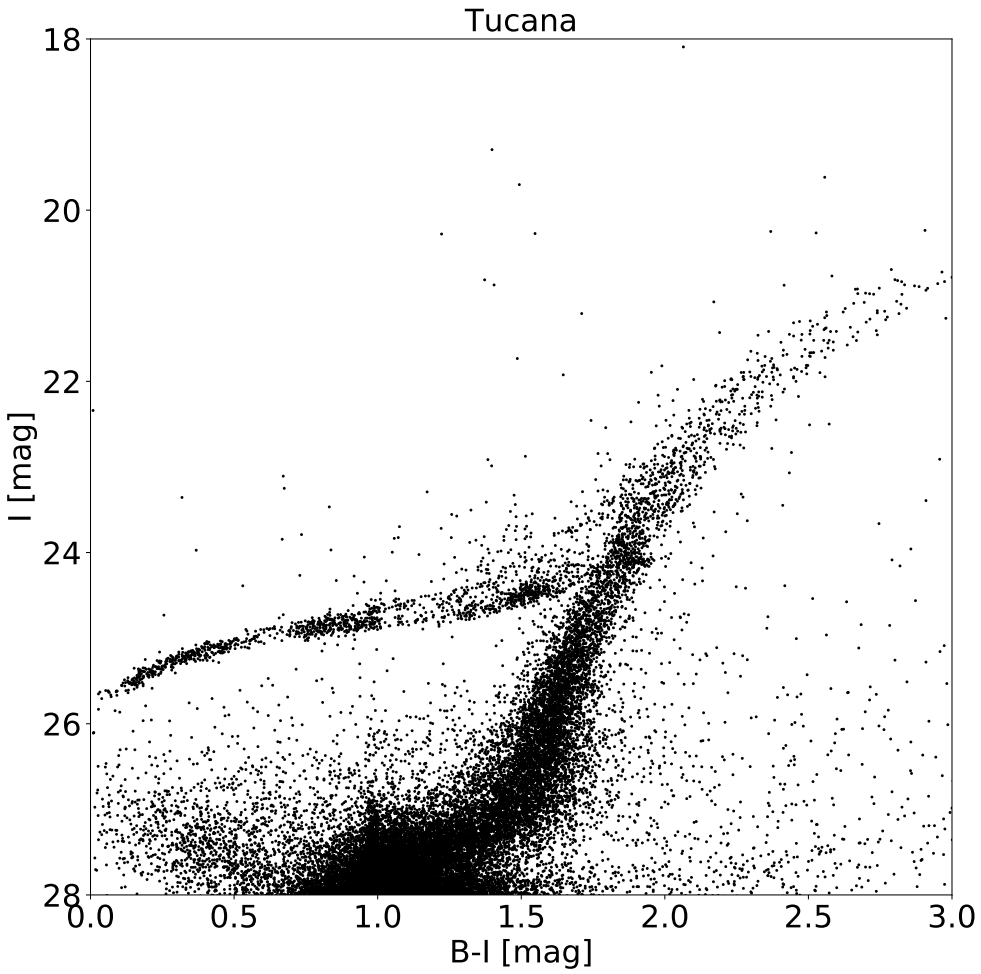

Figure E.6: Tucana *I*, *B–I* CMD.

References

Allard F., Homeier D., Freytag B., 2011, in Johns-Krull C., Browning M. K., West A. A., eds, Astronomical Society of the Pacific Conference Series Vol. 448, 16th Cambridge Workshop on Cool Stars, Stellar Systems, and the Sun. p. 91 (arXiv:1011.5405)
Anderson J., et al., 2008, AJ, 135, 2055
Aringer B., Girardi L., Nowotny W., Marigo P., Lederer M. T., 2009, A&A, 503, 913
Arnouts S., Cristiani S., Moscardini L., Matarrese S., Lucchin F., Fontana A., Giallongo E., 1999, MNRAS, 310, 540:556
Arnouts S., et al., 2007, A&A, 476, 137
Baldry I. K., Glazebrook K., Brinkmann J., Ivezić Ž., Lupton R. H., Nichol R. C., Szalay A. S., 2004, ApJ, 600, 681
Baldry I. K., Glazebrook K., Driver S. P., 2008, MNRAS, 388, 945
Baldry I. K., et al., 2012, MNRAS, 421, 621
Ball N. M., Brunner R. J., Myers A. D., Strand N. E., Alberts S. L., Tcheng D., 2008, ApJ, 684, 12
Barro G., et al., 2019, arXiv e-prints,
Beare R., Brown M. J. I., Pimbblet K., Taylor E. N., 2019, ApJ, 873, 78
Bedin L. R., Piotto G., Anderson J., Cassisi S., King I. R., Momany Y., Carraro G., 2004, ApJ, 605, L125
Bell E. F., McIntosh D. H., Katz N., Weinberg M. D., 2003, ApJS, 149, 289
Bellazzini M., Gennari N., Ferraro F. R., Sollima A., 2004, MNRAS, 354, 708
Benitez N., 2000, ApJ, 536, 571
Bernard E. J., Lcid Team 2007, in Vazdekis A., Peletier R., eds, IAU Symposium Vol. 241, Stellar Populations as Building Blocks of Galaxies. pp 317–318 (arXiv:0705.2667), doi:10.1017/S1743921307008241
Bernard E. J., et al., 2009, ApJ, 699, 1742
Bernasconi P. A., Maeder A., 1996, A&A, 307, 829
Bertelli G., Bressan A., Chiosi C., Fagotto F., Nasi E., 1994, A&AS, 106, 275
Bertelli G., Nasi E., Girardi L., Chiosi C., Zoccali M., Gallart C., 2003, AJ, 125, 770
Blanton M. R., Moustakas J., 2009, ARA&A, 47, 159
Blanton M. R., et al., 2003, AJ, 125, 2348
Bolzonella M., Miralles J., Pellò R., 2000, A&A, 363, 476
Bonanos A. Z., Stanek K. Z., Szentgyorgyi A. H., Sasselov D. D., Bakos G. Á., 2004, AJ, 127, 861
Bono G., Stellingwerf R. F., 1994, ApJS, 93, 233
Bono G., Marconi M., Stellingwerf R. F., 1999, ApJS, 122, 167
Braga V. F., et al., 2016, AJ, 152, 170
Brammer G. B., van Dokkum P. G., Coppi P., 2008a, ApJ, 686, 1503
Brammer G. B., van Dokkum P. G., Coppi P., 2008b, ApJ, 686, 1503
Brammer G. B., et al., 2011, ApJ, 739, 24

Bressan A., Marigo P., Girardi L., Salasnich B., Dal Cero C., Rubele S., Nanni A., 2012, MNRAS, 427, 127
Brott I., Hauschildt P. H., 2005, in Turon C., O'Flaherty K. S., Perryman M. A. C., eds, ESA Special Publication Vol. 576, The Three-Dimensional Universe with Gaia. p. 565 (arXiv:astro-ph/0503395)
Brown T. M., Sweigart A. V., Lanz T., Smith E., Landsman W. B., Hubeny I., 2010, ApJ, 718, 1332
Brunner R. J., Connolly A. J., Szalay A. S., Bershady M. A., 1997, ApJ, 482, 21
Bruzual G., Charlot S., 2003, MNRAS, 344, 1000
Buonanno R., 1993, in Smith G. H., Brodie J. P., eds, Astronomical Society of the Pacific Conference Series Vol. 48, The Globular Cluster-Galaxy Connection. p. 131
Buonanno R., Corsi C. E., Fusi Pecci F., Hardy E., Zinn R., 1985, A&A, 152, 65
Burgarella D., Buat V., Iglesias-Páramo J., 2005, MNRAS, 360, 1413
Buzzoni A., 2015, MNRAS, 449, 296
Calamida A., et al., 2017, AJ, 153, 175
Caloi V., D'Antona F., 2005, A&A, 435, 987
Calzetti D., Armus L., Bohlin R. C., Kinney A. L., Koornneef J., Storchi-Bergmann T., 2000, ApJ, 533, 682
Cannon R. D., Hawarden T. G., Tritton S. B., 1977, MNRAS, 180, 81P
Cardelli J. A., Clayton G. C., Mathis J. S., 1989, ApJ, 345, 245
Cariulo P., Degl'Innocenti S., Castellani V., 2004, A&A, 421, 1121
Carnall A. C., McLure R. J., Dunlop J. S., Davé R., 2018, MNRAS, 480, 4379
Carnall A. C., Leja J., Johnson B. D., McLure R. J., Dunlop J. S., Conroy C., 2019, ApJ, 873, 44
Carrera R., Aparicio A., Martínez-Delgado D., Alonso-García J., 2002, AJ, 123, 3199
Carretta E., Gratton R. G., 1997, A&AS, 121, 95
Carretta E., Bragaglia A., Gratton R., D'Orazi V., Lucatello S., 2009, A&A, 508, 695
Carretta E., et al., 2014, A&A, 564, A60
Cassisi S., Salaris M., 2013, *Old Stellar Populations-How to Study the Fossil Record of Galaxy Formation*. WILEY-VCH
Castellani V., Degl'Innocenti S., Marconi M., Prada Moroni P. G., Sestito P., 2003a, A&A, 404, 645
Castellani M., Caputo F., Castellani V., 2003b, A&A, 410, 871
Castellano M., et al., 2014, A&A, 566, A19
Castellano M., et al., 2016, A&A, 590, A31
Castelli F., Kurucz R. L., 2003, in Piskunov N., Weiss W. W., Gray D. F., eds, IAU Symposium Vol. 210, Modelling of Stellar Atmospheres. p. A20 (arXiv:astro-ph/0405087)
Chaboyer B., et al., 2017, ApJ, 835, 152
Chabrier G., 2003, PASP, 115, 763
Charlot S., Fall S. M., 2000, ApJ, 539, 718
Chen H.-W., Marzke R. O., 2004, ApJ, 615, 603

Chevallard J., Charlot S., 2016, MNRAS, 462, 1415
Clement C. M., et al., 2001, AJ, 122, 2587
Cohen J. G., Huang W., 2010, ApJ, 719, 931
Cole S., et al., 2001, MNRAS, 326, 255
Collins M. L. M., et al., 2015, ApJ, 799, L13
Collister A. A., Lahav O., 2004, PASP, 116, 345
Connolly A. J., Csabai I., Szalay A. S., Koo D. C., Kron R. G., Munn J. A., 1995, ApJ, 110, 2655
Conroy C., 2013, ARA&A, 51, 393
Conroy C., Gunn J. E., 2010a, FSPS: Flexible Stellar Population Synthesis, Astrophysics Source Code Library (ascl:1010.043)
Conroy C., Gunn J. E., 2010b, ApJ, 712, 833
Coppola G., et al., 2015, ApJ, 814, 71
Crosby B. D., O'Shea B. W., Smith B. D., Turk M. J., Hahn O., 2013
D'Antona F., Caloi V., Montalbán J., Ventura P., Gratton R., 2002, A&A, 395, 69
D'Orazi V., et al., 2018, ApJ, 855, L9
Dale D. A., Helou G., Contursi A., Silbermann N. A., Kolhatkar S., 2001, ApJ, 549, 215
Dalessandro E., Schiavon R. P., Rood R. T., Ferraro F. R., Sohn S. T., Lanzoni B., O'Connell R. W., 2012, AJ, 144, 126
Dalessandro E., Salaris M., Ferraro F. R., Mucciarelli A., Cassisi S., 2013, MNRAS, 430, 459
Davidzon I., et al., 2017, A&A, 605, A70
Demarque P., 1997, in Livio M., Donahue M., Panagia N., eds, The Extragalactic Distance Scale. pp 30–48
Desert F.-X., Boulanger F., Puget J. L., 1990, A&A, 237, 215
Di Cecco A., et al., 2015, AJ, 150, 51
Di Criscienzo M., et al., 2017, A&A, 607, A30
Dotter A., Chaboyer B., Jevremović D., Baron E., Ferguson J. W., Sarajedini A., Anderson J., 2007, AJ, 134, 376
Dotter A., Sarajedini A., Anderson J., 2011, ApJ, 738, 74
Draine B. T., Li A., 2007, ApJ, 657, 810
Duncan K., et al., 2014, MNRAS, 444, 2960
Dutra C. M., Bica E., 2000, A&A, 359, 347
Faber S. M., 1972, A&A, 20, 361
Fabrizio M., et al., 2015, A&A, 580, A18
Feldmann R., et al., 2006, MNRAS, 372, 565
Finlator K., Davé R., Oppenheimer B. D., 2007, MNRAS, 376, 1861
Fioc M., Rocca-Volmerange B., 1999, arXiv Astrophysics e-prints,
Fioc M., Rocca-Volmerange B., 2019, A&A, 623, A143
Fiorentino G., et al., 2017, A&A, 599, A125
Fontana A., D'Odorico S., Poli F., Giallongo E., Arnouts S., Cristiani S., Moorwood A., Saracco P., 2000, AJ, 120, 2206

Fontana A., et al., 2004, A&A, 424, 23
Fontana A., et al., 2006, A&A, 459, 745
Fontana A., et al., 2009, A&A, 501, 15
Fraternali F., Tolstoy E., Irwin M. J., Cole A. A., 2009, A&A, 499, 121
Freedman R., Kaufmann W. J., 2007, Universe, 8th edition
Freeman K. C., Norris J., 1981, ARA&A, 19, 319
Galametz A., et al., 2013, ApJS, 206, 10
Geha M., van der Marel R. P., Guhathakurta P., Gilbert K. M., Kalirai J., Kirby E. N., 2010, ApJ, 711, 361
Giallongo E., D'Odorico S., Fontana A., Cristiani S., Egami E., Hu E., McMahon R. G., 1998, AJ, 115, 2169
Girardi L., Bertelli G., Bressan A., Chiosi C., Groenewegen M. A. T., Marigo P., Salasnich B., Weiss A., 2002, A&A, 391, 195
Girardi L., Grebel E. K., Odenkirchen M., Chiosi C., 2004, A&A, 422, 205
Gratton R. G., Carretta E., Bragaglia A., Lucatello S., D'Orazi V., 2010, A&A, 517, A81
Grazian A., et al., 2015, A&A, 575, A96
Greggio L., Renzini A., 2011, *Stellar Populations –A User Guide From Low to High Redshift*. WILEY-VCH
Grogin N. A., et al., 2011, ApJS, 197, 35
Guo Y., et al., 2013, ApJS, 207, 24
Gustafsson B., Edvardsson B., Eriksson K., Jørgensen U. G., Nordlund Å., Plez B., 2008, A&A, 486, 951
Harbeck D., et al., 2001, AJ, 122, 3092
Harrington R. G., Wilson A. G., 1950, PASP, 62, 118
Harris W. E., 1996, AJ, 112, 1487
Herschel W., 1789, Philosophical Transactions of the Royal Society of London Series I, 79, 212
Herschel J. F. W., 1833, Philosophical Transactions of the Royal Society of London Series I, 123, 359
Hidalgo S. L., et al., 2011, ApJ, 730, 14
Hidalgo S. L., et al., 2018, ApJ, 856, 125
Hutchings J. B., 1982, ApJ, 255, 70
Iannicola G., et al., 2009, ApJ, 696, L120
Ibata R., Martin N. F., Irwin M., Chapman S., Ferguson A. M. N., Lewis G. F., McConnachie A. W., 2007, ApJ, 671, 1591
Ilbert O., et al., 2006, A&A, 457, 841
Ilbert O., et al., 2009, ApJ, 690, 1236
Ilbert O., et al., 2010, ApJ, 709, 644
Ilbert O., et al., 2013, A&A, 556, A55
Irwin M. J., Bunclark P. S., Bridgeland M. T., McMahon R. G., 1990, MNRAS, 244, 16P

Kalirai J. S., et al., 2010, ApJ, 711, 671
Karachentseva V. E., 1976, Soobshcheniya Spetsial'noj Astrofizicheskoj Observatorii, 18, 42
Kauffmann G., et al., 2003, MNRAS, 341, 54
Kesseli A. Y., West A. A., Veyette M., Harrison B., Feldman D., Bochanski J. J., 2017, ApJS, 230, 16
Kinemuchi K., Harris H. C., Smith H. A., Silbermann N. A., Snyder L. A., La Cluyzé A. P., Clark C. L., 2008, AJ, 136, 1921
Kirby E. N., Lanfranchi G. A., Simon J. D., Cohen J. G., Guhathakurta P., 2011, ApJ, 727, 78
Klypin A., Kravtsov A. V., Valenzuela O., Prada F., 1999, ApJ, 522, 82
Kodra D., 2019, PhD thesis, University of Pittsburgh
Koekemoer A. M., et al., 2011, ApJS, 197, 36
Koekemoer A. M., et al., 2014, in American Astronomical Society Meeting Abstracts #223. p. 254.02
Kotulla R., Fritze U., Weilbacher P., Anders P., 2009, MNRAS, 396, 462
Kraft R. P., Ivans I. I., 2003, PASP, 115, 143
Kriek M., van Dokkum P. G., Labbé I., Franx M., Illingworth G. D., Marchesini D., Quadri R. F., 2009, ApJ, 700, 221
Kroupa P., 2001, MNRAS, 322, 231
Kurucz R. L., 2011, Canadian Journal of Physics, 89, 417
Laigle C., et al., 2016, ApJS, 224, 24
Lanzoni B., et al., 2018, ApJ, 861, 16
Lavery R. J., 1990, IAU Circ., 5139
Le Borgne J.-F., et al., 2003, A&A, 402, 433
Leaman R., VandenBerg D. A., Mendel J. T., 2013, MNRAS, 436, 122
Lee Y. W., 1989, PhD thesis, Yale University
Lee Y.-W., Demarque P., Zinn R., 1990, ApJ, 350, 155
Lee Y.-W., Demarque P., Zinn R., 1994, ApJ, 423, 248
Lee S.-K., Idzi R., Ferguson H. C., Somerville R. S., Wiklind T., Giavalisco M., 2009a, ApJS, 184, 100
Lee J. C., et al., 2009b, ApJ, 706, 599
Lee S.-K., Ferguson H. C., Somerville R. S., Wiklind T., Giavalisco M., 2010, ApJ, 725, 1644
Leja J., Carnall A. C., Johnson B. D., Conroy C., Speagle J. S., 2019, ApJ, 876, 3
Lejeune T., Cuisinier F., Buser R., 1997, A&AS, 125, 229
Letarte B., et al., 2010, A&A, 523, A17
Li C., White S. D. M., 2009, MNRAS, 398, 2177
Lotz J., et al., 2014, in American Astronomical Society Meeting Abstracts #223. p. 254.01
Mackey A. D., Broby Nielsen P., Ferguson A. M. N., Richardson J. C., 2008, ApJ, 681, L17

Majewski S. R., Siegel M. H., Patterson R. J., Rood R. T., 1999, ApJ, 520, L33
Maraston C., 1998, MNRAS, 300, 872
Maraston C., 2005, MNRAS, 362, 799
Maraston C., Daddi E., Renzini A., Cimatti A., Dickinson M., Papovich C., Pasquali A., Pirzkal N., 2006, ApJ, 652, 85
Maraston C., Pforr J., Renzini A., Daddi E., Dickinson M., Cimatti A., Tonini C., 2010, MNRAS, 407, 830
Marchesini D., van Dokkum P. G., Förster Schreiber N. M., Franx M., Labbé I., Wuyts S., 2009, ApJ, 701, 1765
Marconi M., et al., 2015, ApJ, 808, 50
Marigo P., Girardi L., 2007, A&A, 469, 239
Marigo P., Girardi L., Bressan A., Groenewegen M. A. T., Silva L., Granato G. L., 2008, A&A, 482, 883
Marigo P., Bressan A., Nanni A., Girardi L., Pumo M. L., 2013, MNRAS, 434, 488
Marigo P., et al., 2017, ApJ, 835, 77
Martínez-Vázquez C. E., et al., 2016, MNRAS, 462, 4349
Martínez-Vázquez C. E., et al., 2017, ApJ, 850, 137
Mateo M., 1997, in Arnaboldi M., Da Costa G. S., Saha P., eds, Astronomical Society of the Pacific Conference Series Vol. 116, The Nature of Elliptical Galaxies; 2nd Stromlo Symposium. p. 259 (arXiv:astro-ph/9701158)
Mateo M. L., 1998, ARA&A, 36, 435
McConnachie A. W., 2012, AJ, 144, 4
McConnachie A. W., Irwin M. J., Ferguson A. M. N., Ibata R. A., Lewis G. F., Tanvir N., 2005, MNRAS, 356, 979
McCracken H. J., et al., 2012, A&A, 544, A156
Merlin E., et al., 2016, A&A, 590, A30
Merlin E., et al., 2018, MNRAS, 473, 2098
Merlin E., et al., 2019, MNRAS,
Meynet G., Maeder A., Schaller G., Schaerer D., Charbonnel C., 1994, A&AS, 103, 97
Milone A. P., et al., 2008, ApJ, 673, 241
Milone A. P., et al., 2014, ApJ, 785, 21
Milone A. P., et al., 2017, MNRAS, 464, 3636
Milone A. P., et al., 2018, MNRAS, 481, 5098
Monelli M., et al., 2010a, ApJ, 720, 1225
Monelli M., et al., 2010b, ApJ, 722, 1864
Monelli M., et al., 2015, ApJ, 812, 25
Monelli M., Fiorentino G., Bernard E. J., Martínez-Vázquez C. E., Bono G., Gallart C., Dall'Ora M., Stetson P. B., 2017, ApJ, 842, 60
Moore B., Ghigna S., Governato F., Lake G., Quinn T., Stadel J., Tozzi P., 1999, ApJ, 524, L19
Mortlock A., Conselice C. J., Bluck A. F. L., Bauer A. E., Grützbauch R., Buitrago F., Ownsworth J., 2011, MNRAS, 413, 2845

Muzzin A., et al., 2013, ApJ, 777, 18
Nardiello D., et al., 2018, MNRAS, 481, 3382
Natali F., Natali G., Pompei E., Pedichini F., 1994, A&A, 289, 756
Nayyeri H., et al., 2017, ApJS, 228, 7
Nemec J. M., Wehlau A., Mendes de Oliveira C., 1988, AJ, 96, 528
Pacifici C., Charlot S., Blaizot J., Brinchmann J., 2012, MNRAS, 421, 2002
Pancino E., Galfo A., Ferraro F. R., Bellazzini M., 2007, ApJ, 661, L155
Papovich C., Dickinson M., Ferguson H. C., 2001, ApJ, 559, 620
Peng Y.-j., et al., 2010, ApJ, 721, 193
Peng Y.-j., Lilly S. J., Renzini A., Carollo M., 2012, ApJ, 757, 4
Pietrinferni A., Cassisi S., Salaris M., Castelli F., 2004, ApJ, 612, 168
Pietrinferni A., Cassisi S., Salaris M., Castelli F., 2006, ApJ, 642, 797
Pietrinferni A., Cassisi S., Salaris M., Hidalgo S., 2013, A&A, 558, A46
Pietrzyński G., et al., 2008, AJ, 135, 1993
Pietrzyński G., Górski M., Gieren W., Ivanov V. D., Bresolin F., Kudritzki R.-P., 2009, AJ, 138, 459
Piotto G., et al., 2015a, AJ, 149, 91
Piotto G., et al., 2015b, AJ, 149, 91
Planck Collaboration et al., 2016, A&A, 596, A107
Pozzetti L., et al., 2010, A&A, 523, A13
Pritzl B. J., Smith H. A., Stetson P. B., Catelan M., Sweigart A. V., Layden A. C., Rich R. M., 2003, AJ, 126, 1381
Prugniel P., Soubiran C., 2001, A&A, 369, 1048
Prugniel P., Soubiran C., 2004, arXiv Astrophysics e-prints,
Rauch T., 2003, A&A, 403, 709
Recio-Blanco A., Aparicio A., Piotto G., de Angeli F., Djorgovski S. G., 2006, A&A, 452, 875
Richer H. B., et al., 2013, ApJ, 778, 104
Riess A. G., et al., 2018, ApJ, 861, 126
Salaris M., Cassisi S., 2005, Evolution of Stars and Stellar Populations
Salaris M., Weiss A., 2002, A&A, 388, 492
Salaris M., de Boer T., Tolstoy E., Fiorentino G., Cassisi S., 2013, A&A, 559, A57
Salimbeni S., Fontana A., Giallongo E., Grazian A., Menci N., Pentericci L., Santini P., 2009, in Giobbi G., Tornambe A., Raimondo G., Limongi M., Antonelli L. A., Menci N., Brocato E., eds, American Institute of Physics Conference Series Vol. 1111, American Institute of Physics Conference Series. pp 207–211 (arXiv:0901.3540), doi:10.1063/1.3141545
Salpeter E. E., 1955, ApJ, 121, 161
Sánchez-Blázquez P., et al., 2006, MNRAS, 371, 703
Sandage A. R., 1953, AJ, 58, 61
Sandage A., Wildey R., 1967, ApJ, 150, 469
Santini P., et al., 2009, A&A, 504, 751

Santini P., et al., 2012, A&A, 538, A33
Santini P., et al., 2019, MNRAS, 486, 560
Sarajedini A., et al., 2002, ApJ, 567, 915
Sarajedini A., et al., 2007, AJ, 133, 1658
Savino A., Salaris M., Tolstoy E., 2015, A&A, 583, A126
Schaerer D., de Barros S., 2009, A&A, 502, 423
Schaerer D., de Barros S., Sklias P., 2013, A&A, 549, A4
Schaller G., Schaerer D., Meynet G., Maeder A., 1992, A&AS, 96, 269
Schechter P., 1976, ApJ, 203, 297
Schmidt M., 1968, ApJ, 151, 393
Schneider P., 2015, *Extragalactic Astronomy and Cosmology-An Introduction*. Springer
Searle L., Zinn R., 1978, ApJ, 225, 357
Shapley H., 1938, Harv. Coll. Obs. Bull., 908
Siegel M. H., Majewski S. R., 2000, AJ, 120, 284
Sirianni M., et al., 2005, PASP, 117, 1049
Skillman E. D., et al., 2017, ApJ, 837, 102
Slater C. T., Bell E. F., Martin N. F., 2011, ApJ, 742, L14
Smith L. J., Norris R. P. F., Crowther P. A., 2002, MNRAS, 337, 1309
Stefanon M., et al., 2015, ApJ, 803, 11
Stefanon M., et al., 2017, ApJS, 229, 32
Steidel C. C., Giavalisco M., Dickinson M., Adelberger K. L., 1996, AJ, 112, 352
Stetson P. B., Catelan M., Smith H. A., 2005, PASP, 117, 1325
Stetson P. B., et al., 2014a, PASP, 126, 521
Stetson P. B., Fiorentino G., Bono G., Bernard E. J., Monelli M., Iannicola G., Gallart C., Ferraro I., 2014b, PASP, 126, 616
Stetson P. B., Pancino E., Zocchi A., Sanna N., Monelli M., 2019, MNRAS, 485, 3042
Straatman C. M. S., et al., 2014, ApJ, 783, L14
Taylor E. N., et al., 2015, MNRAS, 446, 2144
Thomas D., Maraston C., Bender R., 2003, MNRAS, 339, 897
Thomas D., Maraston C., Schawinski K., Sarzi M., Silk J., 2010, MNRAS, 404, 1775
Tomczak A. R., et al., 2014, ApJ, 783, 85
Torelli M., et al., 2019, A&A, 629, A53
Valdes F., Gupta R., Rose J. A., Singh H. P., Bell D. J., 2004, ApJS, 152, 251
VandenBerg D. A., Brogaard K., Leaman R., Casagrande L., 2013, ApJ, 775, 134
Vassiliadis E., Wood P. R., 1994, ApJS, 92, 125
Vazdekis A., Casuso E., Peletier R. F., Beckman J. E., 1996, ApJS, 106, 307
Villanova S., Geisler D., Piotto G., Gratton R. G., 2012, ApJ, 748, 62
Vivas A. K., Alonso-García J., Mateo M., Walker A., Howard B., 2019, AJ, 157, 35
Walcher J., Groves B., Budavári T., Dale D., 2011, Ap&SS, 331, 1
Wang Y., Bahcall N., Turner E. L., 1998, ApJ, 116, 2081
Weigel A. K., Schawinski K., Bruderer C., 2016, MNRAS, 459, 2150
Weiss A., Schlattl H., Salaris M., Cassisi S., 2004, A&A, 422, 217

Whitaker K. E., et al., 2011, ApJ, 735, 86
Whiting A. B., Hau G. K. T., Irwin M., 1999, AJ, 118, 2767
Wilson A. G., 1955, PASP, 67, 27
Worthey G., Ottaviani D. L., 1997, ApJS, 111, 377
Worthey G., Faber S. M., Gonzalez J. J., 1992, ApJ, 398, 69
Worthey G., Faber S. M., Gonzalez J. J., Burstein D., 1994, ApJS, 94, 687
Zinn R., West M. J., 1984, ApJS, 55, 45
Zoccali M., Cassisi S., Bono G., Piotto G., Rich R. M., Djorgovski S. G., 2000, ApJ, 538, 289
Zocchi A., Gieles M., Hénault-Brunet V., 2017, MNRAS, 468, 4429
de Boer T. J. L., et al., 2012, A&A, 539, A103
van den Bergh S., 1967, AJ, 72, 70
van den Bergh S., 1972, ApJ, 171, L31